UNIVERSITY OF OKLAHOMA

GRADUATE COLLEGE

RECONFIGURABLE AND MULTIBAND ANTENNAS WITH RESONANT AND REACTIVE LOADS

A DISSERTATION

SUBMITTED TO THE GRADUATE FACULTY

in partial fulfillment of the requirements for the

Degree of

DOCTOR OF PHILOSOPHY

By

PAUL WINNIFORD

Norman, Oklahoma

2020

Downloaded from SHAREOK. Persistent Handle URL: https://hdl.handle.net/11244/326683

RECONFIGURABLE AND MULTIBAND ANTENNAS WITH RESONANT AND REACTIVE LOADS

A DISSERTATION APPROVED FOR THE
SCHOOL OF ELECTRICAL AND COMPUTER ENGINEERING

BY THE COMMITTEE CONSISTING OF

Dr. Jessica Ruyle, Chair

Dr. Hjalti Sigmarsson

Dr. Caleb Fulton

Dr. Nathan Goodman

Dr. Keri Kornelson

© Copyright by PAUL WINNIFORD 2020
All Rights Reserved.

Acknowledgements

I'd like to give an enormous thanks to my advisor, Dr. Jessica Ruyle, for her vision, patience and guidance over the last seven years. I'm also very grateful to Dr. Sigmarsson and Dr. Saeedi for their frequent advice and help. I appreciate the contribution of my other committee members, Dr. Fulton, Dr. Goodman, and Dr. Kornelson, for their availability and input throughout my time at OU.

A special thanks goes out to Adrian Bauer and David Mitchell for fabrication and measurement of many antenna designs. Thanks also to Ian Kennedy and Runsha Long for their help with analytical design tasks. Thanks also to Alex Moreno, Stephen Bass, Drew Schaeffer, Marc Thibodeau, Lucasz Szolc, Ashley Palmer, Garrett Robinson, Javier Lujan, Austin Saunders, Blake James, and many other students who helped in making my time as a grad student a positive time.

Thanks also to Bill Liles for help with moving the Robert Hansen archives to OU. Without that contribution I likely would never have written the second half of this dissertation.

I'd like also to thank my wife Catherine and the rest of my family for their constant support.

Table of Contents

List of Figures **ix**

Abstract **xvii**

1 Introduction **1**

2 Theory of Resonators, Waveguides, and Coupling Structures **7**
2.1 Introduction 7
2.2 Aperture Coupled Waveguide 8
2.3 Modelling of Evanescent Mode Coaxial Cavity 10
2.3.1 Coaxial Transmission Lines and Resonators 14
2.4 Slotline 16
2.4.1 Short Discontinuity 18
2.4.2 Electric Field and Magnetic Current 19
2.4.3 Coupling 19
2.4.4 Simulated Fields Analysis 22
2.5 Conclusion 24

3 Design of Reconfigurable Cavity Loaded Slot Antennas **25**
3.1 Introduction 25
3.2 End Loaded Slot Antenna 26
3.2.1 CPW Fed End-Loaded Slot Antenna 31
3.3 Center Loaded Slot Antenna 31
3.3.1 Center Loaded Slot with Center Feed 34
3.4 Middle Loaded Slot Antenna 35
3.5 Microstrip Coupled Loads 38
3.5.1 End Loads 38
3.5.2 Mid Loads 40
3.6 RLC Loaded Slot 42
3.7 Dual Band L-Slots Coupled to CPW and Reconfigurable Loads 42
3.8 Conclusion 43

4 Design of Cavity Backed Slots **46**
4.1 Introduction . . . 46
4.2 Traditional Cavity Backing . . . 46
4.2.1 Cavity Backed Slot, Eigenmode Simulation . . . 48
4.3 Reconfigurable Slot and Backing Cavity . . . 54
4.3.1 Thin Cavity Backing . . . 54
4.4 Conclusion . . . 57

5 Theory of Trap Dipoles **61**
5.1 Introduction . . . 61
5.2 Resonant and Reactive Loading Literature Review . . . 63
5.3 Calculation of Basic Trap Dipole Behavior . . . 66
5.3.1 Unloaded Dipole . . . 66
5.3.2 Trap Dipole . . . 69
5.4 Modal Analysis and Loss in Trap Dipole Antennas . . . 71
5.4.1 Network Parameter Analysis . . . 71
5.4.2 Current Analysis . . . 75
5.4.3 Inductively Loaded Dipole . . . 79
5.4.4 Current past the loads and ratios . . . 83
5.4.5 Loss Conclusions . . . 84
5.5 Parametric Investigations . . . 85
5.5.1 Load Placement . . . 86
5.5.2 Resonator Q . . . 95
5.5.3 Inductor and Capacitor Tolerance . . . 101
5.5.4 Multiple Load Pairs and Distributed Loads . . . 102
5.5.5 Parametric Conclusions . . . 104
5.6 Conclusion . . . 104

6 Traps Expanded **106**
6.1 Introduction . . . 106
6.2 A Note on Loading Higher Order Modes . . . 107
6.3 Changing Feed Location . . . 109
6.4 Off-Resonant . . . 109
6.5 Series RLC Trap Dipole . . . 111
6.6 Stub Loading on Dipoles . . . 112
6.7 Resonator Terminated Stubs . . . 116
6.8 Conclusion . . . 118

7 Trap Loaded Slot Antennas **120**
7.1 Introduction . . . 120
7.2 Unloaded Slot Antenna . . . 123
7.3 Feed Options . . . 125
7.4 Capacitor and Inductor Loads on Slot . . . 126

7.5 Parallel RLC, CPW Feed . . . 127
7.6 Series RLC, CPW Feed . . . 128
7.7 Stub Loading on Slots . . . 133
7.8 Conclusion . . . 137

8 Trap Measurements 139
8.1 Introduction . . . 139
8.2 Design Process . . . 140
8.3 Fabrication Concerns . . . 142
8.4 Parallel LC Trap Monopole . . . 143
8.4.1 Time Gating . . . 149
8.4.2 Wheeler Cap . . . 153
8.5 Series LC Trap Monopole . . . 154
8.6 Inductor Loaded Dual Band Monopole . . . 155
8.7 Series LC Trap Slot Antenna . . . 161
8.8 Parallel LC Trap Slot Antenna . . . 162
8.9 Conclusion . . . 163

9 Reconfigurable Trap Antennas 167
9.1 Introduction . . . 167
9.2 Revised Design Process . . . 168
9.3 Reconfigurable Trap Dipole and Trap Slot Antennas . . . 170
9.4 Slot Antenna Loaded with Cavity Terminated Stubs . . . 172
9.5 Conclusion . . . 177

10 Conclusions and Future Work 179
10.1 Conclusions . . . 179
10.2 Future Work . . . 181

Bibliography 183

A Multiline Coupling 196
A.1 Introduction . . . 196
A.2 Telegrapher's Equations (TE) . . . 197
A.3 TE for Two Coupled Lines . . . 199
A.4 Capacitance for Coupled Multiline Microstrip . . . 203
A.5 Network Parameters for a Two Line System . . . 205
A.6 Network Parameters for n-Coupled Line System . . . 209
A.7 Conclusions and Future Work . . . 213

B Measurement Calibration and Accreditation 214

List of Tables

5.1 Minimum efficiency values as second resonance of trap dipoles changes . . 88
5.2 Calculated cases of component tolerance variance 102

6.1 Loading trap dipole in MoM with SC 4 GHz quarter-wavelength stubs, lower stub characteristic impedance causes f_2 to be closer to f_{trap} 114

A.1 Example eigenvoltage calculation for a system of four coupled lines defined as $w_1 = w_2 = w_4 = 0.2286mm$, $w_3 = 2.286mm$, $s_1 = s_2 = s_3 = 0.2286mm$, $h = 2.286mm$, $\epsilon_r = 2.2$ 210

List of Figures

1.2 Slot antenna end-loaded with piezo-tunable resonant cavities, total length of 47.9 mm, which is a half wavelength at 2.3 GHz for an equivalent unloaded slotline, side-view of piezo reconfigurable cavity also shown 3
1.3 Dual frequency dipole loaded with resonant bandstop "traps" redefining the location of the open boundary conditions 5

2.1 Side view of a reconfigurable coax cavity 10
2.2 Resonant frequencies of three different cavity sizes across capacitive gap size 11
2.3 Q of a sealed dielectric resonator with an inner to outer radius ratio of 3.6 is about 1000 12
2.4 Reconfigurable cavity and parallel RLC with comparable a) resonance and b) Q values 12
2.5 Coupling into cavity with slotline requires a cutout in the side wall of the cavity, which acts as a shorted length of slotline in parallel with the slot antenna, E-field transverse to the slot 13
2.6 Slotline coupled to cavity through cutout in cavity ceiling: quarter arc, half arc, split half arc, full annulus, offset annulus 20
2.7 Reactance measured on a slotline coupled to a reconfigurable coax resonator, real part of impedance omitted for clarity, resonance at input to slotline tuned by changing cavity capacitive gap 21
2.8 Coupling slot, quarter arc (preferred), with range of design parameters labelled 22
2.9 Magnetic field in cavity rotates around z-axis, aligns with curved slotline, H-field normal to ground plane at slotline short circuit 23
2.10 Electric field in coax cavity, concentrated in capacitive region, slotline E-field aligns with cavity E-field elsewhere 23

3.1 Initial slot antenna end-loaded with coax cavity resonators and a center lumped port feed 26
3.2 Frequency tunable input impedance of end loaded slot antenna, tuned from 1.7 GHz to 3.7 GHz by changing cavity capacitive gap 27
3.3 The cutout in the sidewall of the cavity is a shorted slotline in parallel with the radiating slot, approximate reactance of X jΩ at f GHz 28

3.4 Significant loss at cavity resonance, efficiency 8% at 1.75 GHz and 29% at 3.65 GHz . . . 29
3.5 Impedance measured from the center of the slotline for the lower Q loaded slot antenna, resonance tuned from 2.22 GHz to 3.65 GHz . . . 30
3.6 Antenna with wider cavity post radius for lower Q, simulated to investigate cavity Q impact on radiation efficiency . . . 30
3.7 Radiation efficiency for the lower Q slot antenna, 49% at 2.2 GHz and 58% at 3.65 GHz . . . 31
3.8 CPW fed slot antenna with cavity end loads . . . 32
3.9 CPW fed slot antenna with cavity loads is reconfigurable across frequency . 32
3.10 CPW fed slot antenna with cavity end loads has poor efficiency at the operating frequency, as predicted by simulations of the antenna without a feed structure . . . 33
3.11 Center loaded slot antenna with different radiation efficiency trends, cavity loading excites third order radiating mode. . . . 33
3.13 Microstrip center feed to center loaded slot . . . 35
3.14 Center fed and center loaded slot, tunes from -10.7 dB at 2.36 GHz to -13.4 dB at 3.23 GHz . . . 36
3.15 Radiation efficiency ranges from 69% at 2.35 GHz to 95% at 3.25 GHz . . 36
3.16 Radiation pattern at lowest operating frequency . . . 37
3.17 Radiation pattern at highest operating frequency . . . 37
3.18 Slot antenna with reconfigurable cavity loads, total length 45.20mm, which would be half wavelength at 2.5GHz for a straight unloaded slot . . . 38
3.20 Microstrip line on superstrate above radiating slot, microstrip couples to cavity apertures and slotline, cavities are a multimode evanescent mode cavity with split posts [42] . . . 39
3.22 Slot with cavity loads coupled through microstrip. . . . 41
3.24 Two L-shaped slots coupled to CPW with cavity loads, longer leg radiates at S-band, shorter leg radiates at X-band, both tuned by proximity coupling to cavity loaded CPW . . . 43

4.1 TE cavity modes, resonant frequency of transverse electric modes in 76.2x50.8x3.175mm rectangular cavity cavity . . . 48
4.3 Parametric analysis of slot length and location against cavity resonant frequency . . . 49
4.4 Slot loaded cavity, excitation of slot and resonance of cavity altered by changing slot length and offset from cavity wall . . . 50
4.8 Slot radiator with evanescent mode cavity loads and $\lambda/4$ cavity backing . . 54
4.9 Input impedance of reconfigurable slot antenna with $\lambda/4$ cavity backing, resonance tuned from 1.73 GHz to 3.75 GHz by changing capacitive gap in evanescent cavities . . . 55
4.10 Radiation efficiency of reconfigurable slot antenna with $\lambda/4$ cavity backing 55

4.11 Thin cavity backed reconfigurable slot antenna with a variable capacitor loaded post added to tune the outer backing cavity. Antenna element is 40 mm x 40 mm, making it λ/2 at 3.75 GHz. 56
4.12 Layers for cavity backed slot fabrication 58
4.13 Reflection of cavity backed slot antenna, tunable across S-band with potential for higher order filtenna response. The separate dips on each trace can be tuned by individual control of each of the three piezo tuning elements. . 59
4.14 Radiation efficiency of tunable cavity backed slot antenna 59
4.15 Single sided radiation pattern, realized gain at 3.67 GHz 60

5.1 Trap dipole antenna with d_1 half a wavelength at lower operating frequency and d_2 half a wavelength at upper operating frequency 63
5.2 Trap dipole lower and upper operating frequencies with dashed line representing the commonly assumed current distributions. The trap adds slight inductive loading at f_1 and is antiresonant at f_2. 65
5.3 Off-resonant trap dipole at key frequencies, dashed line current distributions. Unlike the conventional trap dipole, the entire dipole radiates at both operating frequencies 65
5.4 Comparing unloaded dipole input impedance between HFSS, FEKO, and a hybrid FEKO/MatLab MoM solution 67
5.5 Reflection coefficient and radiation efficiency of unloaded dipole, λ/2 resonance at 2 GHz and 3λ/2 resonance at 6 GHz 68
5.6 Input impedance and radiation efficiency of unloaded dipole, efficiency around 100% over the frequency range covering the first three resonances . 68
5.7 Comparing trap dipole input impedance between HFSS, FEKO, and a hybrid FEKO/MatLab MoM solution 70
5.8 Trap dipole reflection coefficient comparison between HFSS, FEKO, and a hybrid FEKO/MatLab MoM solution 70
5.9 Trap dipole radiation efficiency agrees well between HFSS, FEKO, and a hybrid FEKO/MatLab solution 71
5.10 Reflection and efficiency of trap dipole, dip in efficiency near upper operating frequency 72
5.11 Input impedance and efficiency of trap dipole, resonances and minima and maxima marked 72
5.12 Slope of real and imaginary input impedance, plotted to easily identify the frequencies of the input imepdance minima and maxima (zero crossings of the slope). The minimum radiation efficiency lines up exactly with the minima of the input resistance. 73
5.13 Matlab calculated currents at resonances and η_{rad} minima. First-mode current distribution at first resonance, second-mode at first antiresonance, third-mode at η_{rad} minimum, first-mode over inner dimensions of dipole at second resonance. 76

5.14 Trap dipole at key frequencies, approximate current distribution as blue dashed line, based on Figure 5.13 78
5.15 Current on inductor loaded dipole. The inductor loads are tuned to have the same reactance value as the parallel LC traps at the minimum η_{rad} frequency. current distribution at the first resonance is first-mode, second-mode at at first antiresonance, and third-mode at η_{rad} minima. The second resonance in this case has a greater excitation on the outer length 80
5.16 Reflection coefficient of inductor loaded dipole, replicating trap dipole radiation efficiency minima 80
5.17 Input impedance of inductor loaded dipole, replicating trap dipole radiation efficiency minima 81
5.18 Current on inductor loaded dipole. The inductors are tuned to have the same reactance as the parallel LC traps at the frequency of the second series resonance, which is a first-mode current distribution between the loads . . . 82
5.19 Reflection coefficient of inductor loaded dipole, replicating trap dipole second series resonance 82
5.20 Input impedance of inductor loaded dipole, replicating trap dipole second series resonance 83
5.21 Load and feed current magnitude across frequency, 4 GHz trap 84
5.22 Trap load spacing is 0.475λ at 4 GHz trap resonant frequency, unoptimized, only a -6.5 dB match at 3.93 GHz 87
5.23 Trap load spacing is 0.475λ at 4 GHz trap resonant frequency, unoptimized, no resonance in input reactance at second operating frequency band 88
5.24 Load spacing optimized, 0.56λ at 3.84 GHz resonance, -19.2 dB match . . 89
5.25 Load spacing optimized, 0.56λ load spacing at 3.84 GHz resonance 89
5.26 Inner load location, 4.74 GHz trap related resonance, minimal radiation efficiency dip 90
5.27 Outer load location, 2.91 GHz trap related resonance, greater dip in radiation efficiency as trap loads tuned lower and moved outwards on dipole . . 91
5.28 Tuning f_2 closer to f_1 increases the amount of loss at the input resistance minima because it also tune the $3\lambda/2$ mode lowerin frequency. With a fixed RLC tuning, moving the load inwards on the dipole increases the amount of loss at input resistance minima. 91
5.29 Impact of load placement and loss value R on input impedance and radiation efficiency, "Middle Load" is a conventional dual-band trap dipole design 93
5.30 Minimum radiation efficiency of trap dipole over a range of parallel resistance values 95
5.31 Second operating frequency (second series resonance) S_{11} match vs trap Q, sweeping R, calculated with the hybrid MatLab MoM approach. Trap Q over 400 has negligible impact on impedance match. 96

5.32 Second operating frequency (second series resonance) S_{11} match vs trap Q, sweeping R and C/L separately, simulated in HFSS. Trap Q has negligible impact on impedance match. 97
5.33 Input resistance at second series resonance vs trap Q, with Q based on variable R, calculated in MatLab. 98
5.34 Input resistance at second series resonance vs Q, with Q based on variable R and on variable L/C ratio, calculated in HFSS. 98
5.35 Corresponding to Figure 5.33, the radiation efficiency at resonance vs Q, with Q based on a varying R value, calculated in MatLab. The antenna has better than 80% η_{rad} at resonance for all Q values. 99
5.36 Minimum radiation efficiency of trap dipole over a range of trap Q values based on variable trap loss resistance, based on Figure 5.30 99
5.37 Radiation efficiency at antenna resonance over a range of trap Q, based on variable R and on variable L/C ratio, simulated in HFSS. The antenna has better than 92% η_{rad} at resonance across all Q values. 100
5.38 Fine parametric variation of trap location and spacing between "distributed" loads 103
5.39 Reflection and radiation efficiency for a dipole with four trap loads, half the magnitude of the double trap design, Figure 5.38, showing an overlap of radiation efficiency dip and possible operating frequency 103

6.1 It is well known that loading an electrically small monopole closer to the feed will more heavily load the monopole. However, when loading higher order modes, placing a load at the current maximums will more heavily load the specific load. This can result in a higher order mode being more heavily loaded than the fundamental load. 108
6.3 Series RLC load impedance and radiation efficiency of dual band trap dipole loaded with series RLC loads 111
6.4 Dual band trap dipole with series rather than parallel RLC loads 112
6.5 Input impedance of dual band trap dipole with series RLC loads, η_{rad} lines up with R_{in} minima 113
6.6 Monopole with series short circuit stub to create a trap dual band response . 113
6.7 Monopole with short circuit stub, dual band response 114
6.8 Monopole with short circuit stub, radiation efficiency over 90% at both operating frequencies 115
6.9 Monopole with short circuit stub, typical monopole realized gain pattern at lower frequency, suggesting straight length of monopole has normal current distribution and stub doesn't contribute negatively towards radiation 115
6.10 Monopole with short circuit stub, typical realized gain pattern at upper frequency, suggests stub doesn't contribute negatively towards radiation 116

7.1 a) Slot antenna with lumped port feed at center and parallel LC loads. b) near LC antiresonance is high impedance f_1, and c) is intended to be a slightly capacitive short at f_2. Approximate currents as blue dashed lines. . 121
7.2 a) Slot antenna with lumped port feed center and series LC loads b) high impedance capacitive load at f_1 c) low impedance at f_2 near to f_{trap} 122
7.3 Slot antenna with CPW center feed and RLC traps (blue) 123
7.4 Input impedance of lumped port fed unloaded slot antenna, comparing center fed 28 mm slot, center fed 48 mm slot, and 48 mm slot with feed near the slot end. 28 mm slot is approximately the same as the inner length defined in subsequent trap slot antennas. 124
7.5 Comparison of CPW fed slots, with inductor load, capacitor load, and unloaded. The unloaded antenna has the same length as the inner length between the loads. The loaded slot antennas are terminated in shorts, but have very little difference compared to open ended slots 126
7.6 Reflection coefficient of CPW fed slot antenna with parallel LC traps 129
7.7 Input impedance of CPW fed slot antenna with parallel LC traps 129
7.8 Radiation efficiency of CPW fed slot antenna with parallel LC traps 130
7.9 Reflection of slot antenna with series LC loads, operating frequencies at 1.99 GHz and 3.43 GHz 131
7.10 Input impedance of slot antenna with series LC loads 131
7.11 Radiation efficiency of slot antenna with series LC loads 132
7.12 H field across slot, slot antenna with series LC loads 132
7.13 E field across slot, slot antenna with series LC loads 133
7.14 E field, rescaled with just minimum η_{rad} trace 134
7.15 CPW fed slot antenna with open circuit CPW stubs to create a trap dual-band response 134
7.16 CPW fed slot antenna with OC CPW stubs, dual-band response 135
7.17 CPW fed slot antenna with OC CPW stubs, good radiation efficiency at both operating frequencies, significant dip in between 135
7.18 CPW fed slot antenna with OC CPW stubs, typical slot realized gain pattern at lower operating frequency 136
7.19 CPW fed slot antenna with OC CPW stubs, typical slot realized gain pattern at upper operating frequency 136

8.1 Fabricated monopole with parallel LC trap, 1.6 pF and 1 nH 144
8.2 Measured and simulated parallel trap S11. The measured lower operating frequency is -17.49 dB at 2.372 GHz, and the upper operating frequency is -10.79 dB at 3.772 GHz. The HFSS simulation predicted a -15.83dB match at 2.36 GHz, and a -18.20 dB match at 3.94 GHz. 145
8.3 Elevation measurement in anechoic chamber, 3D printed mount 145
8.4 Elevation cut at f_1 146
8.5 Elevation cut at f_2 147

8.6 Azimuth measurement . . . 147
8.7 Azimuth cut at 2.37 GHz . . . 148
8.8 Azimuth cut at 3.77 GHz . . . 148
8.9 Max realized gain over frequency of trap monopole antenna, decrease at 3.78 GHz . . . 149
8.10 Radiation pattern at 3.68 GHz, the frequency at which realized gain is a minimum. The gain at all angles is reduced, indicating increased loss, rather than a change in directivity over angle. . . . 150
8.11 Radiation efficiency of trap monopole antenna from Wheeler cap measurement . . . 150
8.13 Fabricated series LC trap monopole . . . 155
8.14 Measured and simulated reflection coefficient of dual-band monopole with series LC load. The LC is tuned to be a short at the 1.44 GHz, and provides the same reactance magnitude at 3.22 GHz as a more conventional parallel LC trap, proving that trap dipoles operate at finite reactive loads rather than open circuits. . . . 156
8.16 Realized gain across frequencies at the angle of maximum directivity, $\theta = -54^\circ$ . . . 158
8.17 Fabricated dual band $\lambda/4$ monopole with inductor load . . . 158
8.18 Measured and simulated reflection coefficient of dual-band monopole with only an inductor load. The inductor value is chosen to provide the same reactance magnitude at the upper operating frequency as would be caused by a more conventional parallel LC trap, again emphasizing that trap dipoles operate at finite reactive loads rather than at the trap antiresonance open circuit. . . . 159
8.20 Inductor loaded monopole realized gain, sharp decrease in gain at GHz . . . 161
8.21 Slot antenna with series LC trap loads . . . 162
8.22 Slot antenna with series LC trap loads, operating frequencies at GHz and GHz. . . . 163
8.24 Series LC trap slot antenna, realized gain at broadside over frequency . . . 165
8.25 Fabricated trap slot antenna with parallel LC loads, 2 nH and 3 pF . . . 165
8.26 Measured reflection of parallel LC loaded slot antenna compared with measurement . . . 166

9.1 Sweeping trap resonance on dipole, higher Q loads tune antenna resonance a higher percentage of the trap resonance sweep . . . 171
9.2 Radiation efficiency is also tuned across frequency, still offset from antenna operating frequencies. . . . 172
9.3 Useful range of reactive load values are closer in frequency to load resonance with higher Q loads . . . 173
9.4 Trap slot with static load location, varied load resonance and Q . . . 173
9.5 Reconfigurable trap slot antenna, trap stub terminated in reconfigurable cavity 174

9.6 The reactance of the cavity terminated stub can be tuned by simulating the CPW and cavity separately to reduce simulation time 175
9.7 S11 of CPW fed slot antenna with cavity end loads, static low frequency at 2.24 GHz, and tunable upper frequency at 2.52 GHz and 3.02 GHz and 3.41 GHz, varying capacitive gap in cavities 175
9.8 Radiation efficiency over 90% at low static frequency, varies from 88% to 59% at the upper frequencies 176
9.9 2.52 GHz realized gain pattern, 30 μm capacitive gap 176
9.10 3.41 GHz, 70 μm capacitive gap 177

A.1 Even and odd mode excitations for two coupled lines, (a) Even mode excitation and (b) capacitance seen by the lines, and (c) Odd mode excitation and (d) capacitance seen by the lines 199
A.2 Superposition of two line capacitance calculations use to approximate an n-line structure 205
A.3 New closed-form analytical calculation compared to commercially available MoM solver, for two lines. s=2.286mm, w=2.286mm, l=50mm, h=0.762mm, ϵ_r=2.2. Zero crossings with less than 0.3% error compared to a MoM solution. 208
A.4 Port currents and voltages labelled for four coupled lines 211
A.5 Z11 for 4 coupled symmetric width lines, $w = 2.286mm$, $s = 2.286mm$, $h = 0.762mm$, $\epsilon_r = 9.2$, $l = 25mm$, showing a frequency shift of less than 1.4% frequency shift error compared to MoM calculation 212
A.6 Z11 for 4 coupled asymmetric lines, $w_1 = w_2 = w_4 = 0.2286mm$, $w_4 = 2.286mm$, $s_1 = s_2 = s_3 = 0.2286mm$, $h = 2.286mm$, $\epsilon_r = 2.2$, $l = 50mm$, showing a frequency shift of less than 5.9% error compared to MoM calculation 212

Abstract

Reactive and resonant loads have been used from the very beginning of antenna design to improve impedance matching, bandwidth, and current distributions on antennas, and to create multiband and reconfigurable antennas.Trap loaded dipoles are one of the simplest resonator-loaded antennas and are traditionally loaded with either an inductor-capacitor pair or a quarter wavelength stub integrated into a dipole or monopole to create a second operating frequency at the trap resonant frequency. Adding resonant loads to antennas will only increase in popularity and practicality as filtennas are more often used for their SWaP improvements, better noise performance, and potential for additional degrees of reconfigurability. In this dissertation, I demonstrate that resonant loads can introduce lossy modes, and I significantly revise and expand the theory of the basic trap dipole antenna, which is a valuable aid in designing resonator loaded antennas with higher degrees of complexity. Based on the new analysis, I demonstrate novel series LC trap dipoles, dual-band inductor loaded trap dipoles, and parallel and series LC trap slots. The newly developed design process also allows for the integration of any kind of resonator or reactive load to be used to create trap style antennas. A reconfigurable load is also used to demonstrate novel tunable trap antennas. The design procedure is ultimately adaptable to any resonators that can be practically fabricated and physically incorporated into the antenna structure.

Chapter 1

Introduction

Modern antenna systems face many significant obstacles in a wide variety of applications. Uncertain environments, congested spectrum, and the proliferation of interferers challenge an antenna's ability to radiate and receive effectively. Making antennas reconfigurable with operating frequency, radiation pattern, and bandwidth is a powerful method to alleviate these problems. While reconfigurable antennas have been a research topic for some time [1]–[4], the antennas typically have limitations, such as low power handling due to a reliance on varactors and switches. These components can fail at power levels necessary for radar systems. Reconfigurable antennas are often not conformal, which can limit application. Slot antennas are a planar antenna structure that can be made conformal and even radiate well on metallic structures by adding cavity backing.

In wideband systems, tunable filters can eliminate the need for banks of multiple filters, which reduces the necessary size of the filter elements. Microelectromechanical (MEMS) devices, p-i-n diodes, and varactors are commonly used in tunable filters. An increasingly popular approach to increasing antenna selectivity while reducing SWaP is to combine the antenna and filter in a combined "filtenna". By combining these elements, the overall system size can be made smaller. The antenna itself acts as the final resonator in the

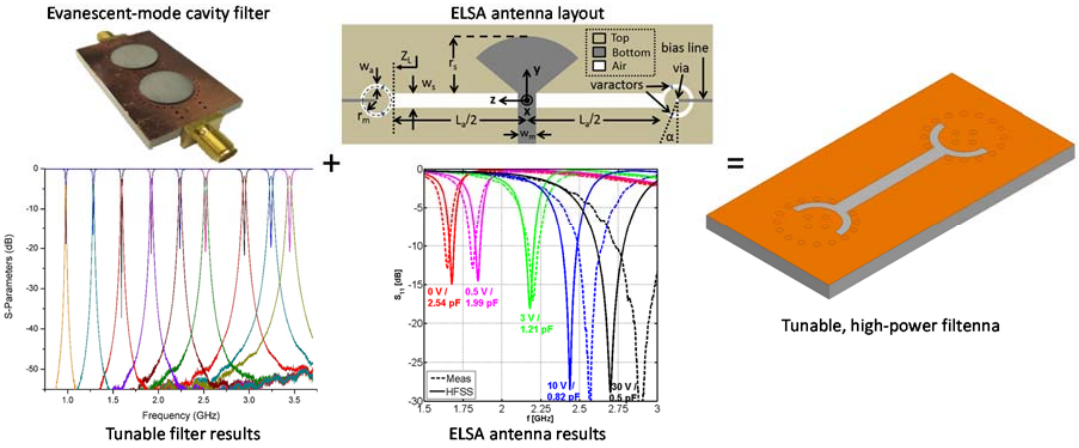


Figure 1.1: Overview of the proposed filtenna implementation. It will be based on a combination of tunable cavity-based filter technology [5] and tunable slot antennas [6]. The wide tuning and power handling capabilities of the cavity filters and the low-profile and efficiency of the slot antenna will be combined into a widely-tunable filtenna with potential power handling improvement for radar systems. The proposed, integrated filtenna element is on the right.

filter design. Combining the filter and antenna can reduce system size and reduce loss by eliminating the interconnect between filter and antenna and improving both filtering and radiating capability. By combining the antenna to the filter, the filter's order is raised without adding any additional resonators. By integrating the filter into the antenna, the antenna selectivity is improved and better prevents unwanted signals from entering the system. Designing filtennas inevitably involves adding resonators to the antenna. Trap dipoles are among the simplest examples of resonator loaded antennas, and I will study them in depth in this dissertation to develop guidelines for loading antennas with resonators.

Resonantly loaded antennas can be made more selective and reconfigurable. Several coupled structures and resonators are used in later chapters, and Chapter 2 has an initial overview of circuit modeling of waveguide structures, boundary conditions, surface equivalence, reaction, polarizability, and general waveguide discontinuities. In early work, many slotline coupling geometries were investigated to effectively couple into the cavity. Aper-

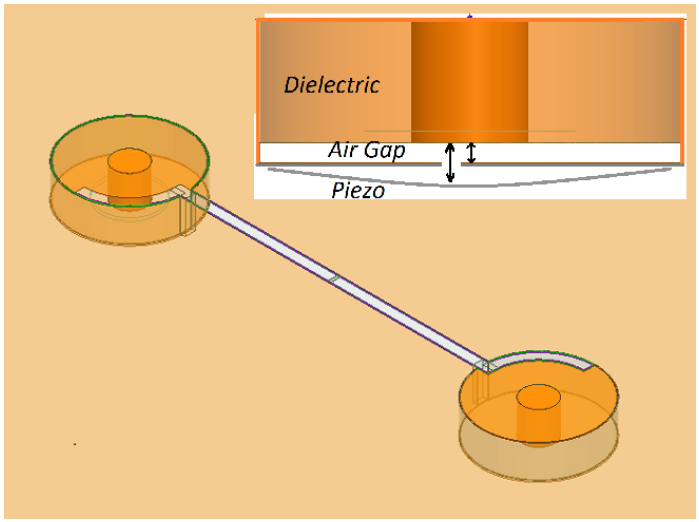


Figure 1.2: Slot antenna end-loaded with piezo-tunable resonant cavities, total length of 47.9 mm, which is a half wavelength at 2.3 GHz for an equivalent unloaded slotline, side-view of piezo reconfigurable cavity also shown

ture coupling in rectangular waveguides is relatively well-understood and can be used as a reference for other coupled structures. An evanescent mode coaxial cavity resonator is described and modeled, followed by slotline and coupling between the two.

Several new designs for a reconfigurable loaded slot antenna element for use in congested and contested spectrum are presented in Chapter 3. In past work, tunable cavity resonators for reconfigurable filters have been designed and implemented [5], [7]–[11] as well as tunable and reconfigurable antennas using multiple technologies [6], [12], [13]. This work combines these efforts into one tunable antenna capable of handling high transmit power.

In [6], [14], varactors were used to vary the reactive loading on slot antennas. Slot radiators can be thin, high-efficiency radiators, fairly simple to design, and relatively inexpensive. Traditionally slot antennas are terminated in shorts at the end of the slots, requiring an offset probe feed point as the simplest way to impedance match the feed. Previously in [6], ring resonator structures created reconfigurable boundary conditions on a slot antenna.

The reactive structures allowed the slot to be loaded with short-circuit, open-circuit, inductive, or capacitive loads, providing a wide tuning range. However, varactors are limited in their power-handling capability. Therefore, this work uses coaxial cavity resonators with reconfigurable capacitive gap loading to provide a comparable reactive load with potentially for higher power handling [15]. The cavity power handling is heavily dependent on the capacitive gap size in the cavity [16].

Chapter 4 will extend the design of the cavity loaded slot antenna to include cavity backing, which brings the added benefits of a single radiation direction, suitability for array integration, and new options for feeding the antenna elements. Probe feed location, cavity size, and additional loading structures will be investigated to establish a cavity design that tunes across the same frequency range as the radiating slot with a good impedance match and radiation pattern.

Across all of the cavity loaded slot antennas that I designed, there were consistently always dips in radiation efficiency either at the antenna operating frequencies, or near the operating frequencies. It is well known that resonators introduce loss into filters [17]. The existing literature for resonator loaded antennas does not explain the prevalence of lossy frequencies, and frequently ignores discussion of radiation efficiency. I decided to investigate loss in resonator loaded antennas and answer whether resonant loading is necessarily lossy due to resonator loss. I focused my investigation on the trap dipole, which is the simplest of resonator loaded antennas, and the rest of the chapters significantly revise and expand the theory of trap dipoles into a broad design framework for a new class of trap style antennas.

In Chapter 5, I start with a review of the literature on wire antennas with discrete reactive and resonant loads, Section 5.2, and I emphasize the load impact on radiation efficiency. I use several different simulation tools for analysis and explain dipole modes and resonance while comparing the accuracy of solutions from different software tools in Sec-

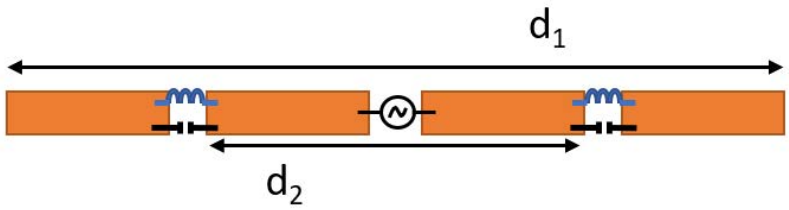


Figure 1.3: Dual frequency dipole loaded with resonant bandstop "traps" redefining the location of the open boundary conditions

tion 5.3. Trap loaded dipoles are one of the simplest resonator-loaded antennas. Traditionally, the resonant load is an inductor-capacitor "trap" integrated into a dipole or monopole to create a second operating frequency at the trap resonant frequency, as shown in Figure 1.3. The literature on trap-loaded and inductor-loaded wire antennas can guide more complicated resonator-loaded antenna designs. I demonstrate high loss frequency bands on loaded antennas and explain them in terms of characteristic modes, Section 5.4. This new explanation of load-related loss results from comparing parameter sweeps of several antenna dimensions and component values. Additional design guidelines based on these parametric sweeps are presented in Section 5.5.

The design of trap dipoles will be expanded in Chapter 6 by demonstrating that the loads in any basic parallel LC trap dipole antenna can be replaced with another resonator calculated to have the same load reactance. I will demonstrate a novel series LC trap loaded dipole, as well as stub loaded antennas. My analysis that traps work by providing a reactive load is further validated by demonstration of these novel designs.

The design of trap dipoles will be applied to slot antennas in Chapter 7. There are no examples of multibanding slot antenna by use of traps in the literature. Slot antennas are planar, inexpensive, and easy to fabricate, offer broad radiation pattern coverage, and can be made more directional by cavity backing. A slot antenna accommodates the addition of discrete components or stubs and is a planar structure, which makes it an ideal antenna type to integrate into arrays and monolithic systems.

Several antennas were fabricated and measured in Chapter 8. This chapter will briefly review the design process for trap antennas before presenting measurements for several monopoles and slot trap antennas. The reflection coefficient, realized gain radiation patterns, and realized gain across frequency was measured for all antennas.

The trap antenna is made reconfigurable across frequency in Chapter 9. I demonstrate both reconfigurable trap dipoles and trap slots, and conclude with a simulated reconfigurable trap slot that uses cavity terminated stubs as its reconfigurable loading mechanism.

In this dissertation I develop a framework for resonator loaded trap antennas as a broad new class of high-efficiency multiband and reconfigurable antennas. I summarize the results in Chapter 10.

Chapter 2

Theory of Resonators, Waveguides, and Coupling Structures

2.1 Introduction

Antennas can be made more selective and reconfigurable with resonant and reactive loads. Several coupled structures and resonators are used in later chapters, and the individual elements are first described in this chapter. Aperture coupling in rectangular waveguides is relatively well-understood and can be used as a reference for other coupled structures. It is discussed in Section 2.2. An evanescent mode coaxial cavity resonator is described and modeled in Section 2.3, followed by slotline and coupling between the two in Section 2.4. Appendix A contains an overview of coupled multiconductor transmission lines and their application.

2.2 Aperture Coupled Waveguide

Circuit models for coupled structures have been developed in many papers [18]–[24]. Many of them are based on computational methods, while some are based on analytical field analysis.

In general, a normal waveguide mode incident on a waveguide discontinuity excites an infinite number of scattered modes[25], most of which are evanescent modes. In practice, a discontinuity can often be well modeled by only considering a single propagating scattered mode and the first evanescent mode. Far from the discontinuity, the evanescent modes can be treated as a lumped reactance that exists only at the discontinuity.

Bethe [26] models waveguide coupling through electrically small apertures with induced electric and magnetic dipoles in the aperture. Power is not conserved in this model because there are no conductance terms for radiation, and radiation reaction fields can be a dominant mechanism in critical waveguide to cavity coupling. A method of moments (MoM) solution for aperture coupling is given in [19]. The field distribution in the aperture can be replaced with an equivalent magnetic source over a PEC wall. The magnetic source is equal in magnitude and opposite in sign on either side of the conductor. The fields in both regions A and B can be solved. The field distribution can be represented with a moment method solution, which can also be described in terms of a region A and region B admittance matrix (or scalar) for the aperture admittance.

Dual fed coupled patch antennas are analyzed in [20]. There is some interesting discussion of multiport analysis and MoM techniques for this problem. This paper was also a precursor to [21], which contains circuit models for microstrip to slotline coupling, multilayer microstrip to microstrip coupling, microstrip-slotline-microstrip coupling, and slotline-stripline-slotline coupling. The paper starts with a general MoM analysis of structures and then derives the circuit models. Pozar [23] applies MoM techniques to an aperture coupled

patch antenna, with a circuit model for the microstrip with an aperture in the ground plane, which is seen as a series impedance.

Modeling of small aperture coupling is further refined in [22], for circuit models for small aperture coupling between half-space and rectangular cavity with an arbitrary elliptic aperture. The paper includes concise details on setting up the testing and expansion function used for the region admittance matrices' MoM solution.

Reactance functions for coupling aperture are given in [24], which are dependent on knowing the resonant frequency and physical dimensions of the aperture. The formula for the resonant length of a narrow rounded slot is given, with stated bounds on the accuracy. Several references are given for theoretical resonant frequency calculations for alternative slot shapes. Q and wall thickness are discussed, and experimental slot reactance is shown to agree with theory. Magnetic polarizabilities of different aperture shapes can be found from the citations, and an expression for the attenuation from the aperture is given. Pozar also discusses electric and magnetic aperture polarization in [25]. Aperture polarization is usually written α_e for electric polarization and α_m for magnetic polarization, not to be confused with the attenuation constant for wave propagation. The polarizabilities are proportionality constants that depend on aperture geometry and have been derived for various aperture shapes in the literature.

Evanescent mode waveguides and cavities can be used for miniaturized filter design and still achieve full power transfer over a limited bandwidth when the load is conjugate matched. A network of pure reactive inductances can represent a waveguide below resonance. Several papers [27]–[29] give design guidelines for realizing high Q reactive networks for various microwave components. Generally, a decrease in volume can be traded for an increase in loss, and obstacles in waveguides are often represented in terms of the energy they store. Coupled resonators can be divided into resonator regions and coupling regions and analyzed separately. The resonator region constrains the bulk of the stored

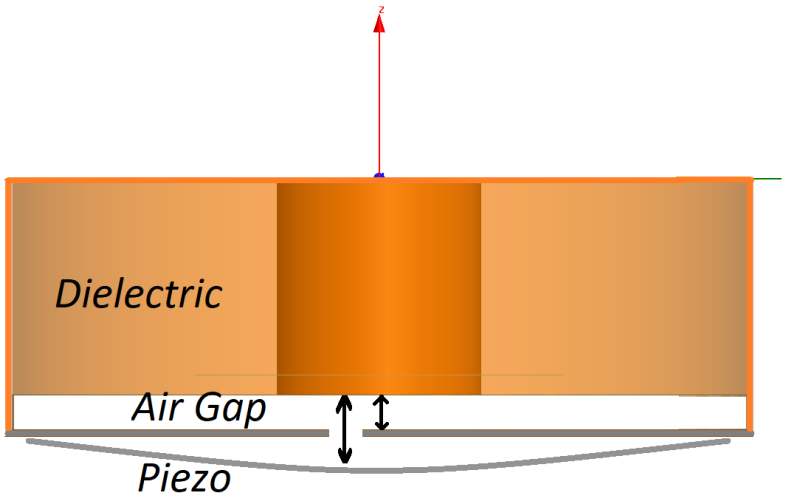


Figure 2.1: Side view of a reconfigurable coax cavity

fields, and as such, any loss in this region has a big impact on the system's performance. The coupling region usually has less intense stored fields, and loss has less of an impact there. Waveguide obstacles above cutoff can be represented as capacitances and inductances depending on whether they store electric and magnetic energy. Normal H-step, E-step, and aperture irises all appear inductive below cutoff [30].

2.3 Modelling of Evanescent Mode Coaxial Cavity

I will be using piezo reconfigurable evanescent mode coax resonators, Figure 2.1 to change the resonant frequency of a resonant slot antenna. The coax cavity resonator can handle higher power than available with the varactor based design in [14]. The cavity design resonates at a lower frequency than usual due to capacitive loading from a variable air gap between the center conductor and the cavity floor. The gap distance can be varied $\pm$ 20 μm with a piezo, as seen in Figure 2.1. The coax cavity resonators were tuned primarily using the HFSS eigenmode simulator. Setting the post radius to 1.5 mm, and the cavity radius to 1.5 mm*3.6 = 5.4 mm, with capacitive gaps of 10 μm-50 μm, results in tunable resonance

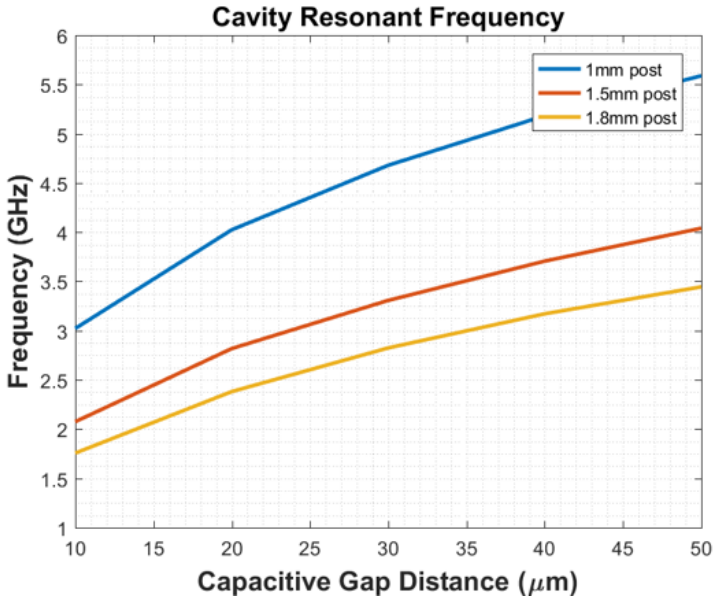


Figure 2.2: Resonant frequencies of three different cavity sizes across capacitive gap size

from 2-4 GHz, as seen in Figure 2.2. The Q stays around 1000, as seen in Figure 2.3.

The center value of the capacitive gap size is dependent on readily available thicknesses of Pyralux, which is used to bond together multiple substrate layers. The available thicknesses are 1/2, 1, and 2 mil, which translates to 12.7, 25.4, and 50.8 μm.

In [31], the piezo-reconfigurable cavity resonator was modeled as a simplified parallel RLC circuit, with L=1 nH and C=1.6-6.2 pF, which tunes from 2-4 GHz. A parallel loss resistor R=20kΩ gives a Q of about 1000, which is similar to the Q value for the original coax cavity resonator design for the slot antenna (which also was tuned 2-4 GHZ). In Figure 2.4a and 2.4b, the eigenmode simulation of the reconfigurable cavity load is compared with the simple RLC model. Both tune across S-band with similar Q. Though there are differences, the parallel RLC is a reasonably simplified case for all resonant loads. The resonant frequency of an RLC is

$$f_{res} = (2\pi\sqrt{LC})^{-1}, \tag{2.1}$$

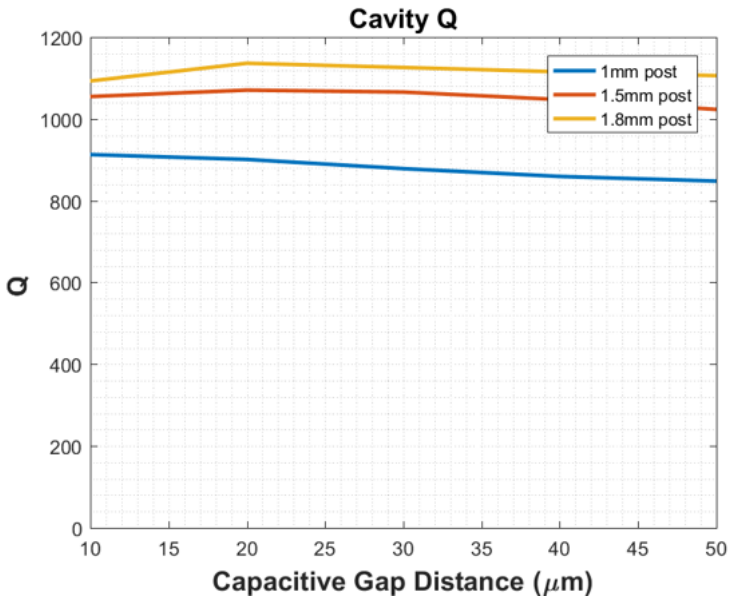
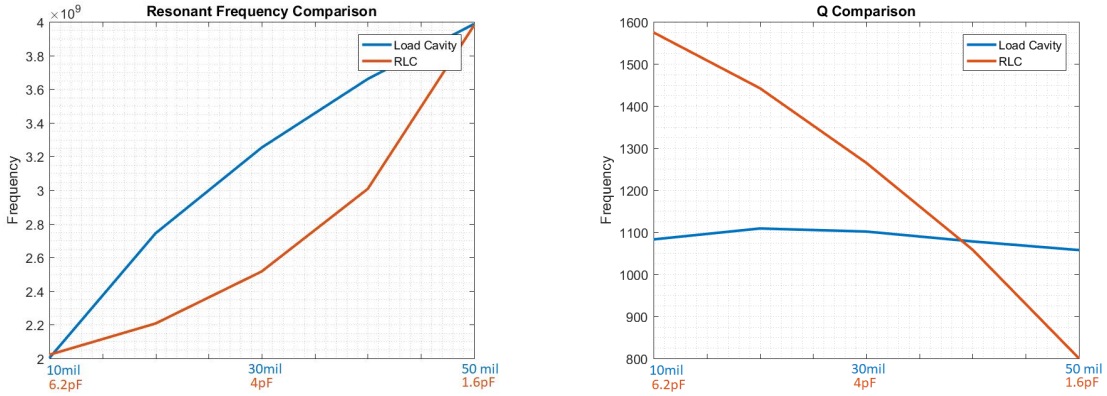


Figure 2.3: Q of a sealed dielectric resonator with an inner to outer radius ratio of 3.6 is about 1000



(a) (b)

Figure 2.4: Reconfigurable cavity and parallel RLC with comparable a) resonance and b) Q values

and the Q of a parallel RLC can be defined as

$$Q = R\sqrt{\frac{C}{L}}. \tag{2.2}$$

The characteristic impedance can also be useful to define the L/C ratio and is defined as

$$Z_c = \sqrt{\frac{L}{C}}. \tag{2.3}$$

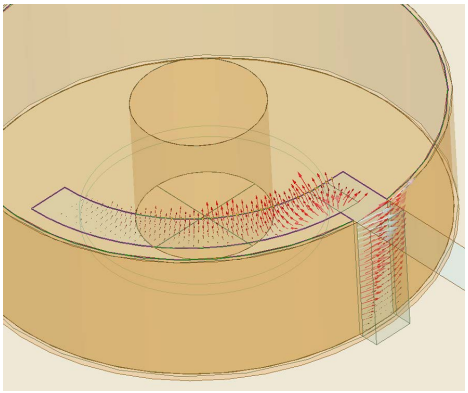


Figure 2.5: Coupling into cavity with slotline requires a cutout in the side wall of the cavity, which acts as a shorted length of slotline in parallel with the slot antenna, E-field transverse to the slot

Cutouts in the cavity sidewall are necessary to avoid disrupting the slot fields, Figure 2.5. Previously in [15], [31], it was discussed that the cutouts form shorted slotline segments, and these reactive stubs likely dominate the reactive loading of the antenna when the load cavities are not near resonance. Interestingly, the wall cutouts present parallel slotline stubs, Figure 2.5, but conventional slotline can usually only have series stubs.

RLC loaded antennas will be investigated in greater detail in Chapters 5 and 7, and the cavity resonator will be applied in Chapter 3.

2.3.1 Coaxial Transmission Lines and Resonators

A circuit model for the coupling between slotline and coax cavity resonators is desired. According to [32], the coaxial cavity is best approximated by the inductance of a section of coaxial line and by the parallel plate capacitance and coax capacitance in parallel. According to [33], the bottom of the cavity is a short circuit, and the top is heavily capacitively loaded. Formulas for stored energy and resonant frequency are also given in [7].

Coaxial transmission line supports Transverse Electromagnetic (TEM) wave propagation. According to [25], the scalar potential can be written as

$$\Phi(\rho, \phi) = \frac{V_0 \ln b/\rho}{\ln b/a}. \tag{2.4}$$

From earlier in [25], the E- and H-fields can be found from the scalar potential, according to

$$\mathbf{e}(\rho, \phi) = -\nabla_t \Phi(\rho, \phi) = \frac{\delta \Phi}{\delta \rho}\hat{\rho} + \frac{1}{\rho}\frac{\delta \Phi}{\delta \phi}\hat{\phi} \tag{2.5}$$

and

$$\mathbf{h}(\rho, \phi) = \frac{1}{Z_{TEM}}\hat{z} \times \mathbf{e}(\rho, \phi) = \frac{1}{Z_{TEM}}[-\frac{1}{\rho}\frac{\delta \Phi}{\delta \phi}\hat{\rho} + \frac{\delta \Phi}{\delta \rho}\hat{\phi}] \tag{2.6}$$

Substituting in

$$\mathbf{e} = \frac{V_0}{-\rho \ln b/a}\hat{\rho} \tag{2.7}$$

and

$$\mathbf{h} = \frac{1}{Z_{TEM}}\frac{V_0}{-\rho \ln b/a}\hat{\phi}. \tag{2.8}$$

where V_0 is the voltage across the slot.

For TEM propagation, the transverse component of the electric and magnetic field is zero.

$$\mathbf{E} = [\mathbf{e_t} + \mathbf{e_z}]e^{-j\beta z} \tag{2.9}$$

$$\mathbf{H} = [\mathbf{h_t} + \mathbf{h_z}]e^{-j\beta z} \tag{2.10}$$

Use the E and H solutions and apply boundary conditions in z to solve for the cavity field expressions, with a short on one end and a capacitive load on the other. [7] states that 90% of the E-field energy is in the capacitive gap.

From [34], the capacitance and inductance of the coaxial cavity are best approximated by the inductance of a coaxial line section and by the parallel plate capacitance and coax capacitance in parallel.

From [35], the capacitance of a parallel plate capacitor is

$$C = \epsilon\frac{S}{d}, \tag{2.11}$$

where S is the surface area of the parallel plates, and d is the distance between them. The capacitance of a cylindrical capacitor, which exists between the center conductor and the wall of the coax structure, is

$$C = \frac{2\pi\epsilon L}{\ln b/a}. \tag{2.12}$$

In the above, a is the inner conductor radius, b is the outer wall radius, and L is the coax's length. According to [25], the inductance per unit length is

$$L = \frac{\mu}{2\pi} \ln b/a(H/m) \tag{2.13}$$

2.4 Slotline

Slotline was first proposed by Cohn in [36] as a new class of structures for transmission lines, filters, and radiators. The field distribution in slotline at a distance $r >> W$ in the air above the slot can be written as [37]

$$H_x = AH_0^{(1)}(k_c r), \tag{2.14}$$

$$H_r = -\frac{\gamma_x}{k_c^2}\frac{\delta H_x}{\delta r} = \frac{A}{\sqrt{1-(\lambda_s/\lambda_0)^2}} H_1^{(1)}(k_c r), \tag{2.15}$$

and

$$E_\phi = \frac{j\omega\mu}{k_c^2}\frac{\delta H_x}{\delta r} = -\eta H_r \lambda_s/\lambda_0. \tag{2.16}$$

Propagation is in the x-direction, and the fields are expressed in a cylindrical coordinate system.

$$k_c = j\frac{2\pi}{\lambda_0}\sqrt{(\frac{\lambda_0}{\lambda_s})^2 - 1} \tag{2.17}$$

Alternately, Cohn expresses the fields above the slot in [38] as

$$H_x = -\frac{j2V_0}{\eta b}(\frac{\lambda}{\lambda'})^2 \frac{b}{\lambda} \sum_{n=1/2,3/2,\ldots} [\frac{1-(\lambda'/\lambda)^2}{nF_n}] \cdot \frac{\sin \pi n\delta}{\pi n\delta} \cdot \cos\frac{2\pi n y}{b} \cdot e^{-\gamma_n|z|} \tag{2.18}$$

and

$$H_z = \frac{2V_0}{\eta b} \cdot \frac{\lambda}{\lambda'} \sum_{n=1/2,3/2,\ldots} \frac{\sin \pi n\delta}{\pi n\delta} \cos \frac{2\pi ny}{b} e^{-\gamma_n |z|}. \tag{2.19}$$

The fields inside the substrate are

$$\begin{aligned} H_x = \frac{j2V_0}{\eta b} (\frac{\lambda}{\lambda'})^2 \frac{b}{\lambda} \sum_{n=1/2,3/2,\ldots} \frac{1}{nF_{n1}} \cdot \frac{\sin \pi n\delta}{\pi n\delta} \cdot \cos \frac{2\pi ny}{b} \\ \cdot \{[\frac{F_{n1}^2 \coth q_n - \epsilon_r(\lambda'/\lambda)^2 \tanh r_n}{1 + (b/n\lambda')^2}] \cosh \gamma_{n1} z - [1 - \epsilon_r(\lambda'/\lambda)^2] \sinh \gamma_{n1} z\} \end{aligned} \tag{2.20}$$

and

$$H_z = \frac{2V_0}{\eta b} \cdot \frac{\lambda}{\lambda'} \sum_{n=1/2,3/2,\ldots} \frac{\sin \pi n\delta}{\pi n\delta} \cos \frac{2\pi ny}{b} \cdot [\cosh \gamma_{n1} z - \coth q_n \sinh \gamma_{n1} z]. \tag{2.21}$$

And the fields beyond the substrate are defined as

$$\begin{aligned} H_x = \frac{j2V_0}{\eta b} (\frac{\lambda}{\lambda'})^2 \frac{b}{\lambda} \sum_{n=1/2,3/2,\ldots} \frac{\sin \pi n\delta}{\pi n\delta} \cdot \cos \frac{2\pi ny}{b} \\ \cdot \{[\frac{F_{n1}^2 \coth q_n - \epsilon_r(\lambda/\lambda')^2 \frac{b}{\lambda}}{1 + (b/n\lambda')^2} \cosh \gamma_{n1} d \\ - [1 - \epsilon_r(\lambda'/\lambda)^2] \sinh \gamma_{n1} d\} \frac{e^{-\gamma_n (z-d)}}{nF_{n1}} \end{aligned} \tag{2.22}$$

$$\begin{aligned} H_z = \frac{2V_0}{\eta b} \cdot \frac{\lambda}{\lambda'} \sum_{n=1/2,3/2,\ldots} \frac{\sin \pi n\delta}{\pi n\delta} \cos \frac{2\pi ny}{b} \\ \cdot [\cosh \gamma_{n1} d - \coth q_n \sinh \gamma_{n1} d] e^{-\gamma_n (z-d)} \end{aligned} \tag{2.23}$$

and $\delta = w/d$.

A closed-form expression for the characteristic impedance of a dielectric backed slotline was first given in [36]. The stated accuracy range is within 2% for $9.7 < \epsilon_r < 20$ and $0.02 < W/h < 1$, but the accuracy decreases very gradually for thicker and lower permittivity substrates. A slotline with 1mm width, ϵ_r=3.27, f_c=3 GHz, and dielectric substrate width of 125mil has a characteristic impedance of 111.2 Ω. The slot's input impedance, fed by a differential feed, can be calculated across the slot's length as a simple transmission line with the specified characteristic impedance.

2.4.1 Short Discontinuity

At a short discontinuity, the current circles around the end, creating an extra inductance. Depending on the slot width and substrate thickness, short end-discontinuities also lead to radiation and surface wave propagation, both of which lend to a resistance. With both of these mechanisms, a short end-discontinuity can be represented as series resistance and inductance.

Simple expressions for the short reactance and resistance can be found in [39], and are repeated here:

$$L = 0.2w_s(\ln(\frac{4w_s}{d}) + \frac{d}{2w_s} - 1)[nH] \tag{2.24}$$

$$d = \frac{w_s + h_m}{20p^2} \tag{2.25}$$

$$p = \frac{\lambda_0}{\lambda} \tag{2.26}$$

$$R = (2.63x10^{-}3)\frac{w_s}{d}\sqrt{f} \tag{2.27}$$

$$Z_L = R + j\omega L \tag{2.28}$$

2.4.2 Electric Field and Magnetic Current

The slot electric field is a function of the voltage distribution divided over the width of the slot [39],

$$E = \frac{V(x)}{w_a} = \frac{-V_0 \sinh(\gamma(\frac{L_a}{2} - \left|x\right|))}{\sinh(\gamma\frac{L_a}{2})}\hat{y}, \tag{2.29}$$

which can be replaced with a magnetic current according to the equivalence principle [40],

$$\mathbf{M} = -2\hat{z}xE_a = -2\frac{V_0}{w_a}\frac{\sinh(\gamma(\frac{L_a}{2} - \left|x\right|))}{\sinh(\gamma\frac{L_a}{2})}\hat{x}. \tag{2.30}$$

2.4.3 Coupling

Coupling between waveguiding structures typically works best when an aperture junction between the two structures is located at a point of field symmetry, where the fields are symmetric on either side of the aperture.

A slotline width of 1 mm had been arbitrarily chosen, so that was not a design variation. Moving the slot further from the post and closer to the cavity wall increased cavity coupling, as evidenced by a more evident change in Z parameters across capacitance gap size. The radial length of the coupling was also varied, as seen in Figure 2.6. The quarter arc and half arc both performed similarly well. Most of the other designs did not couple as strongly. Having an arc length of less than 90°was also explored and did not work well.

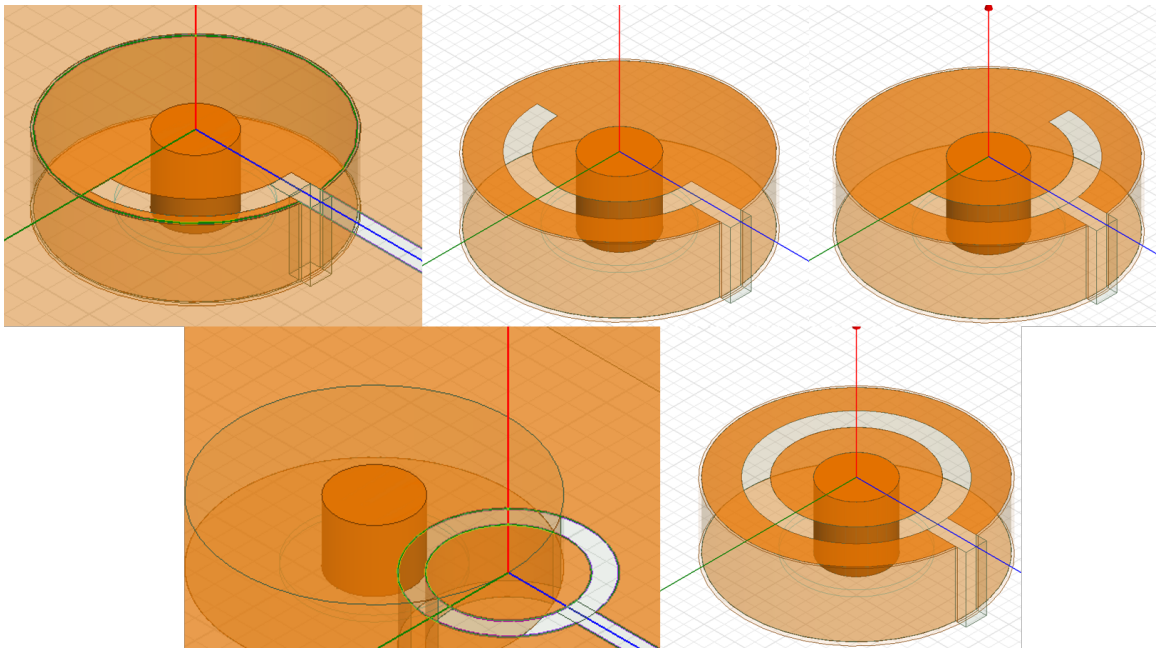


Figure 2.6: Slotline coupled to cavity through cutout in cavity ceiling: quarter arc, half arc, split half arc, full annulus, offset annulus

The offset annulus is inspired by coplanar to slotline transitions, [37], which are sometimes used for coupling into coax resonators (usually along with SIW coupling).

The coupling into the cavities is primarily H-field, creating a short at the slot's ends. Different metrics can be used to examine the reconfigurability and coupling of the cavity. Reactance tuning across frequency, being able to cover the outer circle of the Smith chart (or at least the negative portion), and phase of the Z parameters (being able to provide any negative phase at any frequency) were the main parameters being examined. The reactance seen by a lumped port exciting a slotline coupled to a cavity with a quarter arc is given in Figure 2.7. The anti-resonance at 2.27 GHZ is due to the length of the slot feedline. The sharper resonances are due to the cavity tuning, 1.8-3.75 GHZ. The resonances have shifted down from the original 2-4 GHZ tuning due to coupling.

It was briefly assumed that coupling could be more directly measured by defining the bottom of the cavity as a wave port with an impedance of 0 Ω (a short) and then calculating

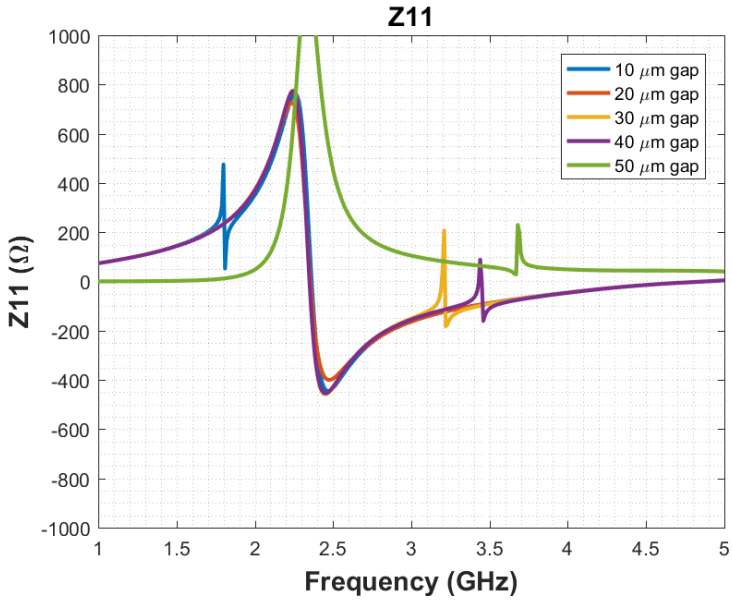


Figure 2.7: Reactance measured on a slotline coupled to a reconfigurable coax resonator, real part of impedance omitted for clarity, resonance at input to slotline tuned by changing cavity capacitive gap

the S21 between the cavity wave port and the lumped port excitation of the slotline. However, S parameters are defined by a chosen reference impedance, so there was no real way to get meaningful quantities from a 0 Ω port and a 111 Ω port. Moreover, HFSS probably would struggle to accurately model the wave port with a coax center conductor 10 μm away from the wave port's face.

Moving the slot further from the post and closer to the cavity wall increased cavity coupling, as evidenced by a more apparent change in Z parameters across capacitance gap size. Coupling slot arcs of 90°, 135°, and 180°each showed a reconfigurable resonant frequency range of about 2 GHZ. Radial arc length does make an expected impact on shifting the overall range of tunable frequencies lower with increasing arc length. The tunable range of the 180°arc is about 25 MHz lower than the 90°coupling arc.

The slot's voltage is known, and the slot's electric field can be approximated based on the slot divided by the width. If desired, the known electric field tangential to the slot

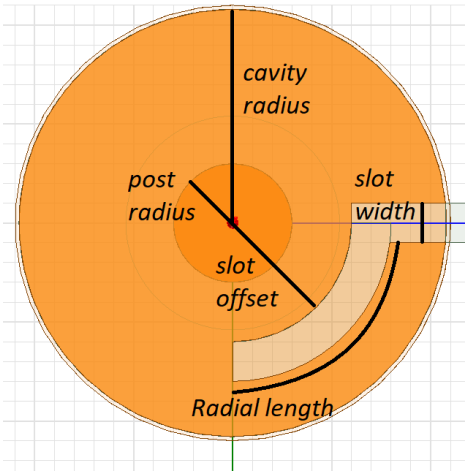


Figure 2.8: Coupling slot, quarter arc (preferred), with range of design parameters labelled

surface can be replaced by a PMC slot surface with an equivalent magnetic current defined on it by the uniqueness theorem.

2.4.4 Simulated Fields Analysis

The $\hat{\phi}$ and $\hat{z}$ components of the H-field in the cavity can be seen in Figure 2.9. Also, there is a significant field response in the sidewall aperture underneath the slotline, which can probably best be understood as several local evanescent modes excited by the discontinuity. The $\hat{z}$ component of the magnetic field comes from the short termination behavior of the slotline. The radial component of the cavity E-field can be seen in Figure 2.10, as well as the large-magnitude of the parallel plate electric field distribution. The radial component has a notably large magnitude near the start of the slotline curvature, a distance from the short end of the slot, where the E-field in the slot goes to null. The simulated fields align between the slot fields and cavity fields and indicate strong coupling.

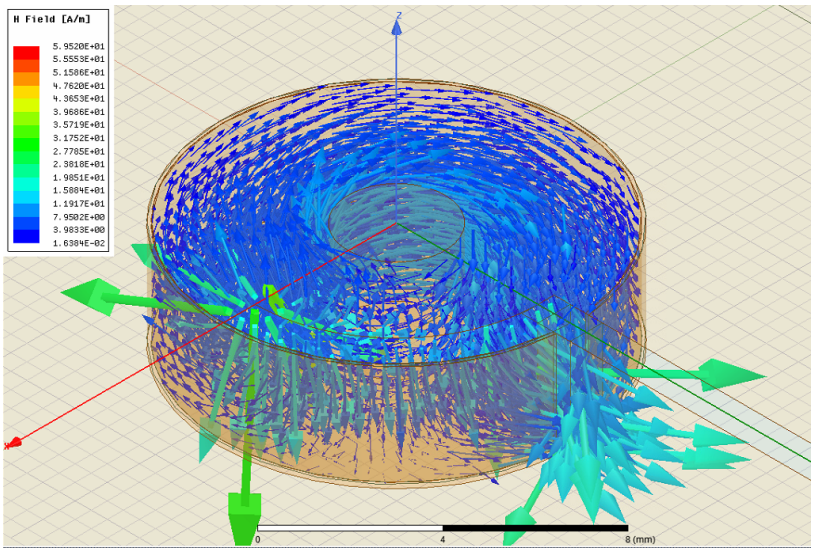


Figure 2.9: Magnetic field in cavity rotates around z-axis, aligns with curved slotline, H-field normal to ground plane at slotline short circuit

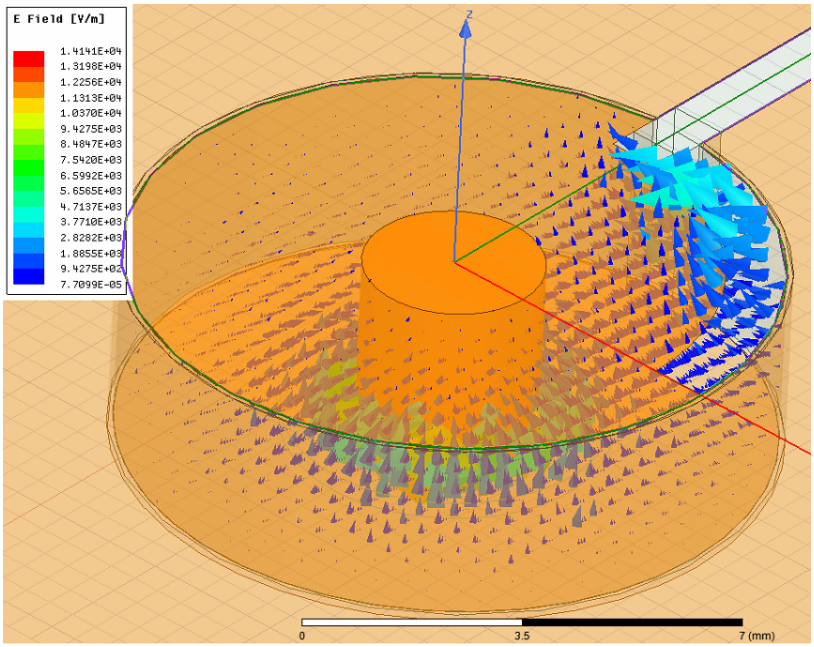


Figure 2.10: Electric field in coax cavity, concentrated in capacitive region, slotline E-field aligns with cavity E-field elsewhere

2.5 Conclusion

Evanescent mode cavities have a known field distribution, can be retuned with a piezo disc, and can be coupled to slotline. Slotline coupled to the evanescent mode cavity is a type of aperture coupling into waveguides and cavities. A slot antenna coupled to reconfigurable cavities is demonstrated in Chapter 3. The theoretical basis for this design has been first developed in this chapter.

Chapter 3

Design of Reconfigurable Cavity Loaded Slot Antennas

3.1 Introduction

In the introduction, I mentioned combining cavity loads with a resonator end-loaded slot design. In the previous chapter, I included an overview of slotline coupling to reconfigurable cavities. A slot antenna is end loaded with reconfigurable coaxial evanescent mode cavities in place of the ring resonator loads. Further design modifications are also included, to preserve frequency tuning while minimizing the effects of the loss caused by resonant loading.

The reconfigurable coax cavity resonator tunes the antenna across frequency. Special attention will be given to each antenna's input impedance to measure frequency reconfigurability and feed matching potential. Input impedance peaks that are similar in magnitude will be easier to match with a single feed. The radiation efficiency at the operating frequency will also be a primary consideration. Antennas that are frequency reconfigurable with acceptable radiation efficiency will also be evaluated for their radiation patterns.

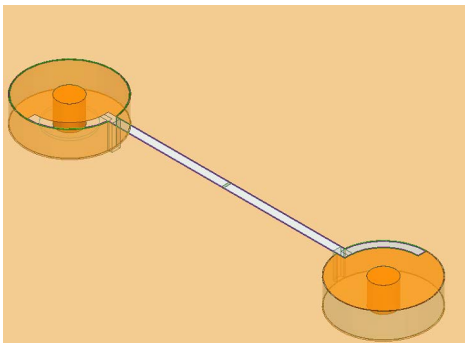


Figure 3.1: Initial slot antenna end-loaded with coax cavity resonators and a center lumped port feed

The initial designs are simulated with only a lumped port excitation and no realistic feed. For these designs, only the input impedance is shown, and the tuning of resonances is evidence of frequency reconfigurability. Impedance transformers can be incorporated into the feed structure for the antenna. For this reason, the exact magnitude of the input impedance response will not be focused on in this chapter. Instead, the parameters of interest are to see that the complex impedance can be reconfigured across frequency and that the radiation efficiency can still be high with a lumped port feed across the slot in HFSS.

3.2 End Loaded Slot Antenna

The initial antenna design was based on [6] with the distinction that the slot antenna is end-loaded with tunable resonant reactive loads, as shown in Figure 3.1. The cavity structures used here have a theoretical Q of about 1000 and a realizable fabricated Q of about 600, whereas the ring resonators in [6] have a Q on the order of 78 [41]. The theoretical Q is calculated from an HFSS model with solid cavity walls, and the fabricated antenna has cavity walls made from a ring of closely spaced vias, leading to a reduced Q. The antenna is excited in simulation with a lumped port across the narrow dimension of the slot.

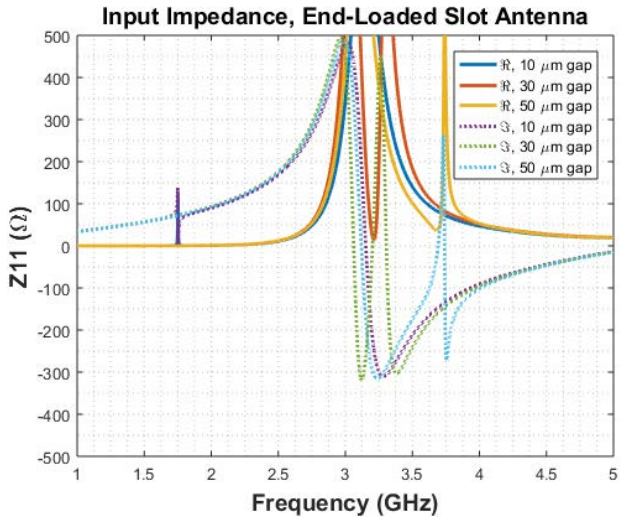


Figure 3.2: Frequency tunable input impedance of end loaded slot antenna, tuned from 1.7 GHz to 3.7 GHz by changing cavity capacitive gap

The reconfiguration of the antenna's input impedance when the cavity is tuned is shown in Figure 3.2. The resonance of the antenna is being tuned across frequency by varying the capacitive gap in the cavity. The impedance varies sharply only at the cavity resonances, as it can be seen that the traces in Figure 3.2 match nearly exactly off of resonance. Inadvertently, the cutout in the sidewall of the cavity behaves as a shorted stub in parallel with the coupled cavity, shown in Figure 3.3. The stub creates a strong inductance such that the tunable cavity reactance is significant when near resonance, and the antenna input impedance becomes reconfigurable only near the cavity resonances.

Though the antenna resonance can be swept across frequency, the radiation efficiency is unusable at resonance, seen in Figure 3.4. The low-efficiency value is possibly due to the cavity load combined with the dielectric and conductor loss, resulting in significant loss at resonance. It is well established in [17] that bandstop resonators will introduce maximum dissipation at resonance, which raises questions about radiation efficiency in resonator loaded antennas. The antenna does not need to operate at cavity resonance. If possible to vary the load reactance away from the cavity resonance significantly, the an-

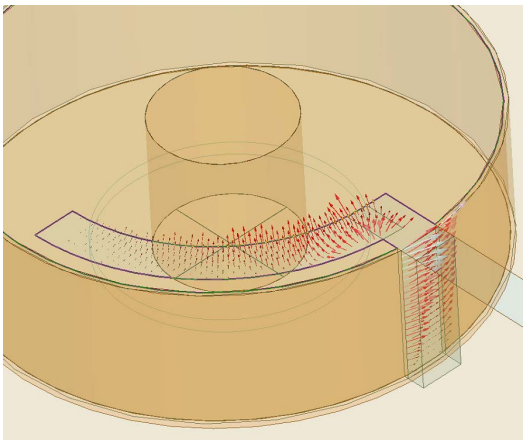


Figure 3.3: The cutout in the sidewall of the cavity is a shorted slotline in parallel with the radiating slot, approximate reactance of X jΩ at f GHz

tenna could reconfigure across frequency with less resonant loss. The current design is reconfigurable only near resonance due to the short circuit presented by the cavity wall's cutout.

A slot antenna with coax cavity loads was simulated in HFSS, Figure 1.2. The antenna was excited with a lumped port element in the center of the slot. The impedance of the antenna with varying capacitive gap sizes is seen in Figure 3.2. The range of resonances is from 1.75-3.67 GHz, which is very close to the frequency bounds shown in Figure 2.7. Most of the resonances are much higher impedance than the slotline characteristic impedance of $111\ \Omega$, so an impedance matching mechanism is needed. Unfortunately, more significant than the impedance matching is a dip in radiation efficiency at cavity resonance, as seen for the lowest resonance value in Figure 3.12b. The same trend holds for the higher resonances, with a somewhat improved efficiency of 40% at the highest resonance. Power dissipation in both dielectric and conductor loss in the cavities is responsible for the low radiation efficiency.

The cavities do not need to be resonant at the radiating slot resonance. Ideally, the tuning mechanism could vary the slot loads without cavity resonance, still allowing for

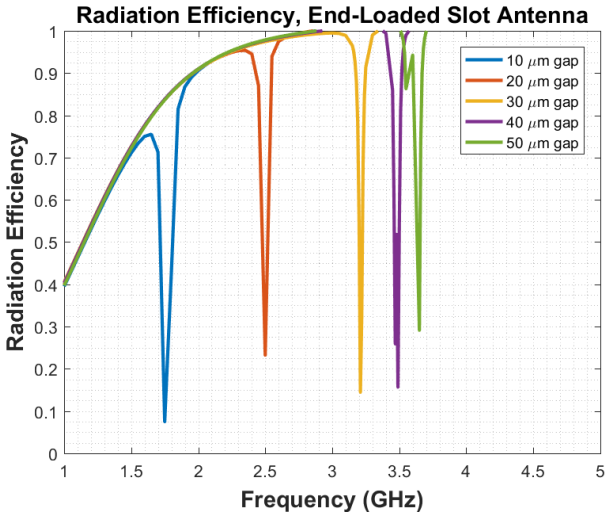


Figure 3.4: Significant loss at cavity resonance, efficiency 8% at 1.75 GHz and 29% at 3.65 GHz

tuning the slot's resonance. Unfortunately, the coupled load impedance seems to only vary significantly across capacitive gap sizes near resonance.

A new set of cavities with theoretical Q around 400 was designed and added to the slot antenna. These cavities were designed to investigate whether a lower Q could lead to a better radiation efficiency at cavity resonance. The input impedance for the slot with lower Q end loads still is reconfigurable across the desired frequency range, but the radiation efficiency with lower Q end loads is comparable to its higher Q counterpart.

Increasing cavity height and increasing post radius will both lower the resonant frequency. A larger post radius means there will also be a larger capacitive area in the post-gap. Q remains nearly constant for changes in cavity height. Changes in post radius have a slight effect on cavity Q. For a cavity with a 5.4 mm outer radius, changing the post radius from 1.4 mm to 2 mm changes the Q less than 10%. There is a small change in Q for different piezo positions/ post gaps, and a larger post results in a wider range of Q values across piezo reconfiguration. The change is still moderate, within $\pm 10\%$. The substrate thickness is changed to 30 mils.

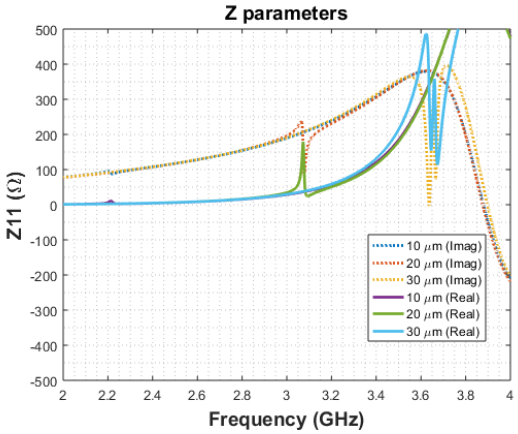


Figure 3.5: Impedance measured from the center of the slotline for the lower Q loaded slot antenna, resonance tuned from 2.22 GHz to 3.65 GHz

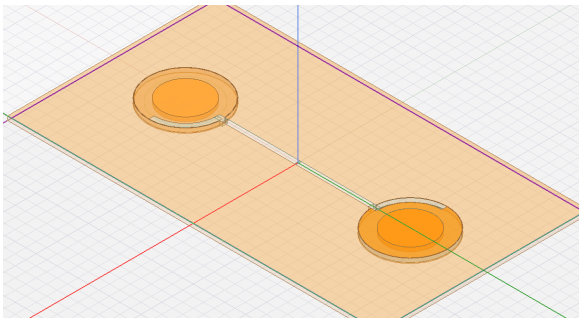


Figure 3.6: Antenna with wider cavity post radius for lower Q, simulated to investigate cavity Q impact on radiation efficiency

An antenna with lower Q cavities has been simulated with the antenna's impedance shown in Figure 3.5 and the radiation efficiency shown in Figure 3.7. The impedance is calculated from a lumped port simulated at the center of the slot. The cavity Q has been decreased by increasing the post radius size relative to the outer cavity wall radius. This particular design shows a wider range of frequency reconfiguration, with a post-gap of 10μm to 50μm tuning from 2.24-4.67 GHz. The radiation efficiency appears to be significantly higher with the lower Q cavity design, with the lowest simulated value of about 13%.

A lower Q cavity may slightly improve the efficiency, and the larger post radius in-

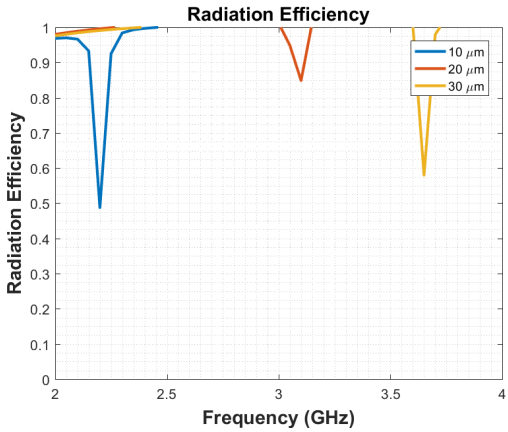


Figure 3.7: Radiation efficiency for the lower Q slot antenna, 49% at 2.2 GHz and 58% at 3.65 GHz

creased the reconfigurable resonant frequency range. The resonant bandwidth seems to have increased with lower Q, which can be inferred from the wider dips in the radiation efficiency in Figure 3.7 compared to Figure 3.12b.

3.2.1 CPW Fed End-Loaded Slot Antenna

Figure 3.8 and 3.9 show the cavity end-loaded slot antenna with a capacitively coupled CPW feed that can be easily manufactured with either milling or etching with photolithography. The design does not have a satisfactory match, and the radiation efficiency minima line up exactly with the matches, as expected from an end-loaded design, as shown in Figure 3.10.

3.3 Center Loaded Slot Antenna

Since the cavity influences field distribution, it significantly controls which radiating mode is excited on the slot. Placing a cavity in the center of the antenna, as shown in Figure 3.11, excites the third radiating slot mode and achieves a radiation efficiency of 20-80%. A slot

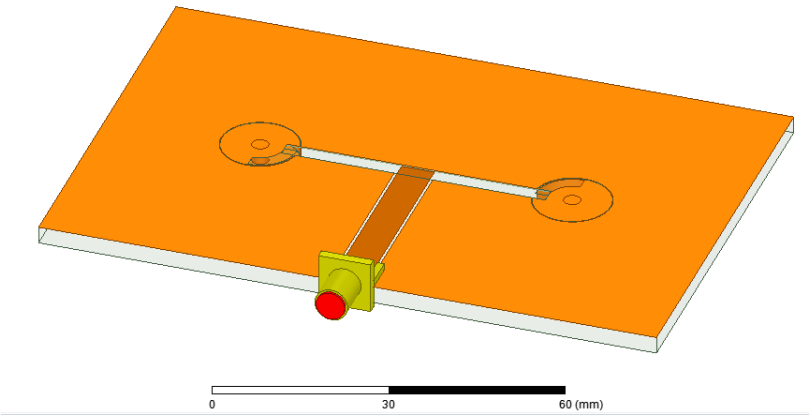


Figure 3.8: CPW fed slot antenna with cavity end loads

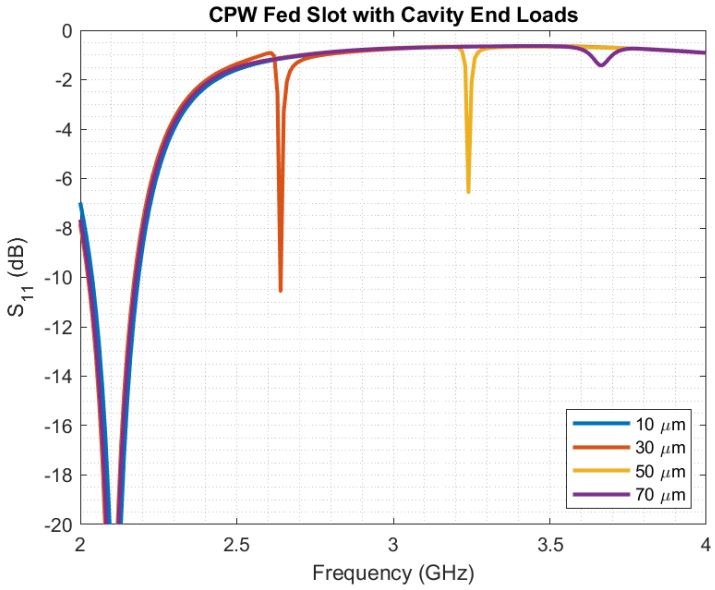


Figure 3.9: CPW fed slot antenna with cavity loads is reconfigurable across frequency

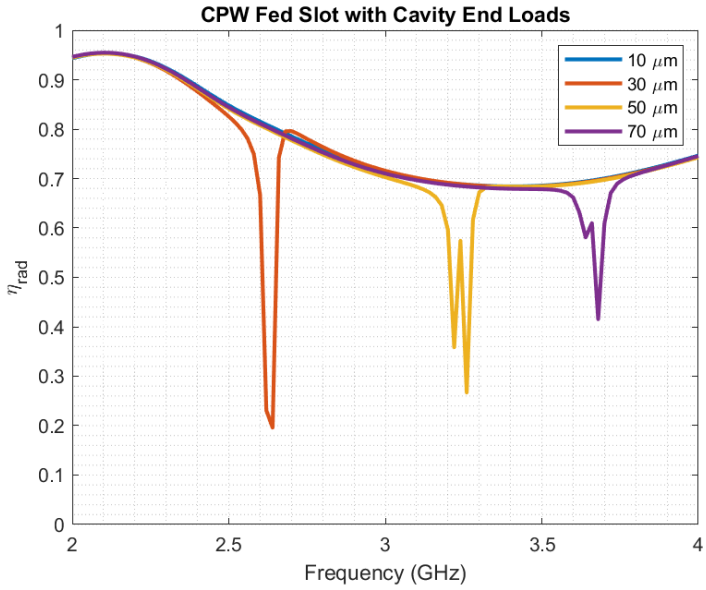


Figure 3.10: CPW fed slot antenna with cavity end loads has poor efficiency at the operating frequency, as predicted by simulations of the antenna without a feed structure

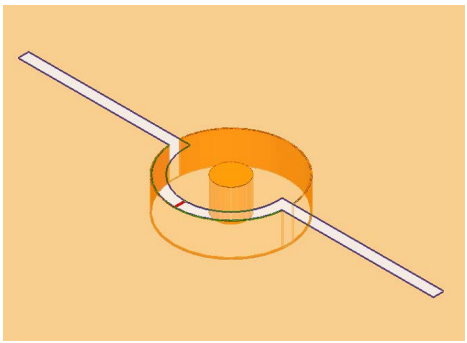
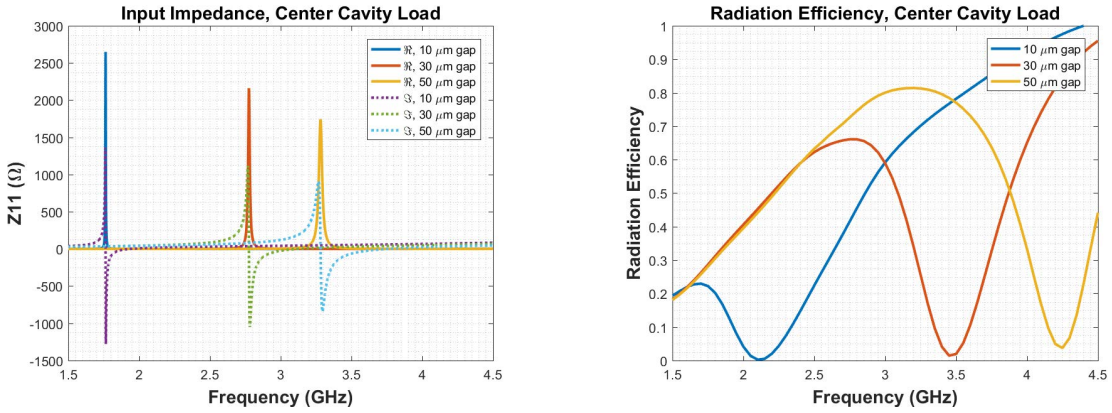


Figure 3.11: Center loaded slot antenna with different radiation efficiency trends, cavity loading excites third order radiating mode.



(a) (b)

Figure 3.12: a) Impedance at center of the slot antenna shown in Figure 3.11, resonant frequency changes with piezo gap distance. b) Radiation efficiency of slot antenna shown in Figure 3.11, efficiency of 20%, 60%, and 80% at antenna resonances.

antenna's radiation pattern varies depending on which mode is excited, and the first three modes offer comparable omnidirectional patterns. Higher-order modes become problematic.

The input impedance at the center of the slot antenna is shown in Figure 3.12a and the impedance is clearly shown to reconfigure across frequency with varying capacitive gap size. The radiation efficiency, which has improved from the double cavity model, is shown in Figure 3.12b.

It would be ideal to feed the slot with an aperture in the floor of the reconfigurable cavity. However, the cavity floor is the piezo actuator and cannot have an aperture.

3.3.1 Center Loaded Slot with Center Feed

Loading the slot directly with a cavity without any stub is still a matter of adding reactance at a point, although the loading is slightly more distributed. The center loaded slot has the best frequency separation between resonance and radiation efficiency dips. The trap dipole had the worst efficiency when the load was moved to the ends of the dipole. The antenna

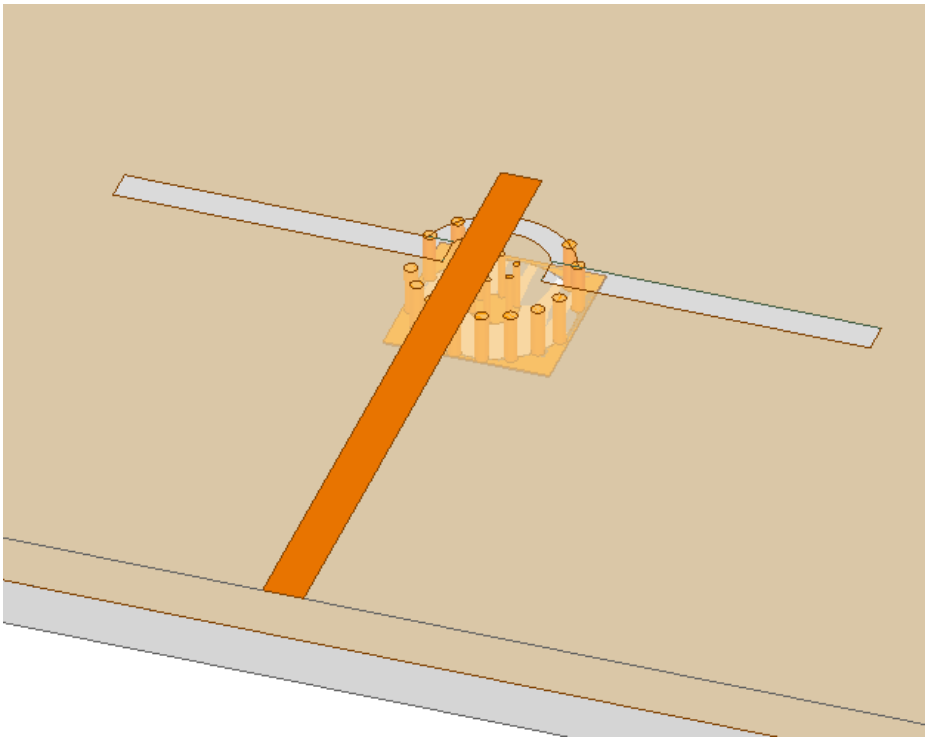


Figure 3.13: Microstrip center feed to center loaded slot

in Figure 3.13 can be tuned from -10.7 dB at 2.36 GHz to -13.4 dB at 3.23 GHz over a realistic range of piezo values, as shown in Figure 3.14.

The radiation efficiency dips near the operating frequencies, but the operating frequencies have efficiency of 69% to 95%, seen in Figure 3.15. The radiation pattern is shown in Figures 3.16 and 3.17.

3.4 Middle Loaded Slot Antenna

Previously, the sidewall cavity transmission line short prevented off-resonant tuning, but an off-resonant design is the best way to improve radiation efficiency. A new set of slot antennas was designed to operate away from cavity resonance from the design rules gathered above. In keeping with trap dipole guidelines, the loads were placed near the midpoint of

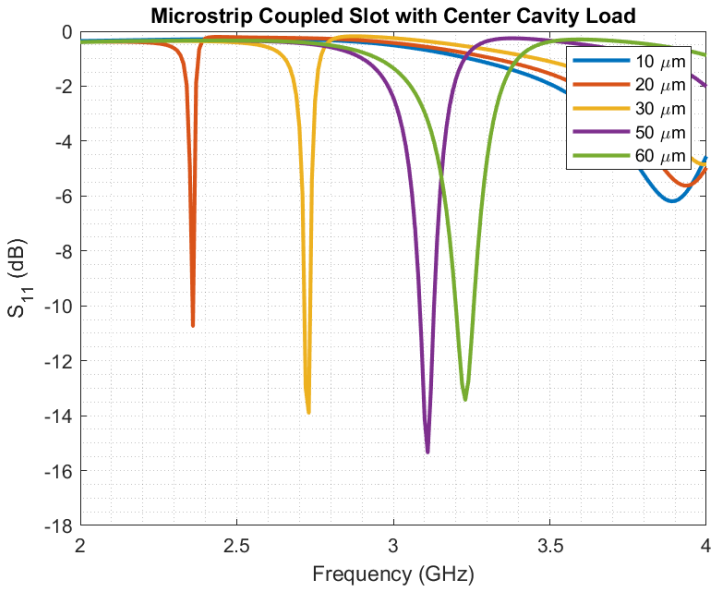


Figure 3.14: Center fed and center loaded slot, tunes from -10.7 dB at 2.36 GHz to -13.4 dB at 3.23 GHz

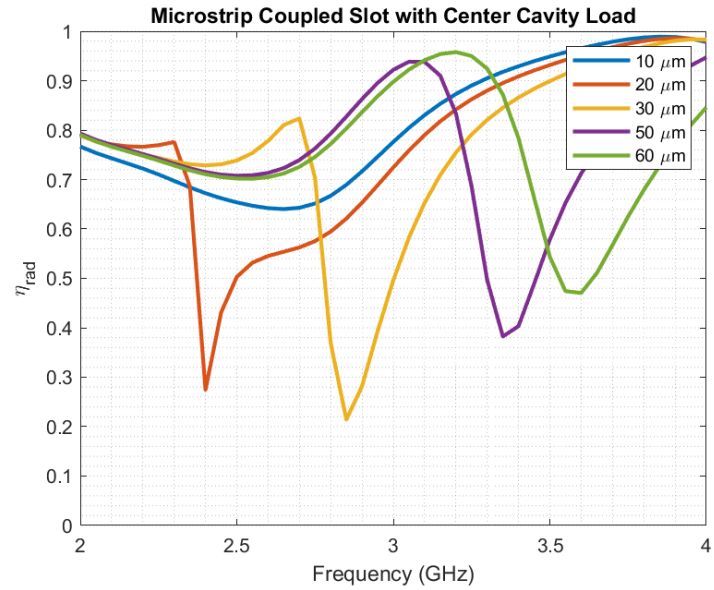


Figure 3.15: Radiation efficiency ranges from 69% at 2.35 GHz to 95% at 3.25 GHz

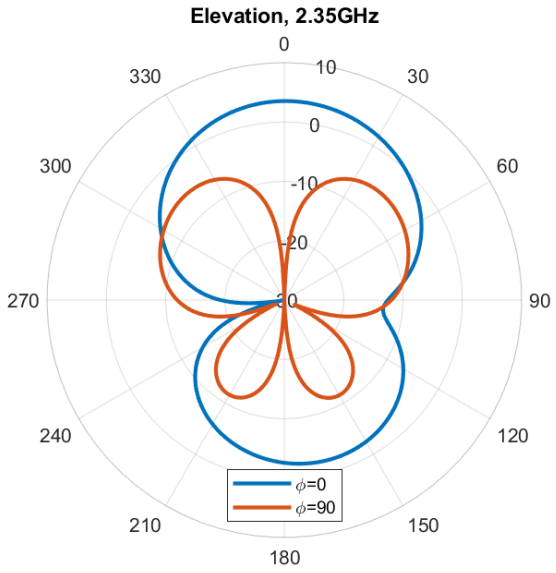


Figure 3.16: Radiation pattern at lowest operating frequency

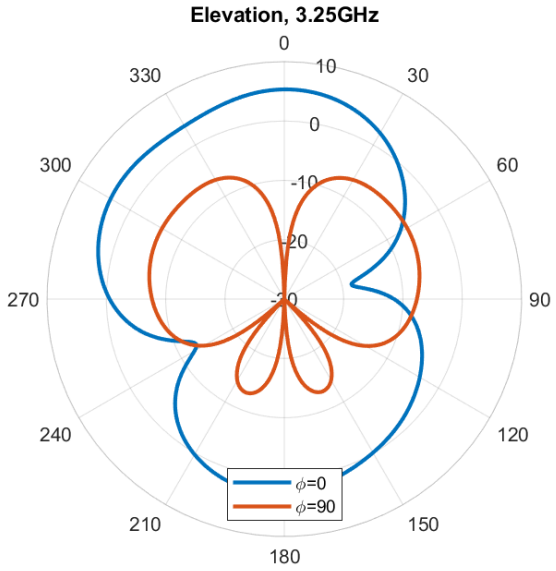


Figure 3.17: Radiation pattern at highest operating frequency

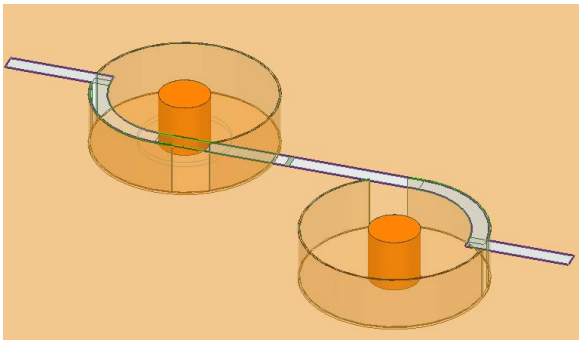


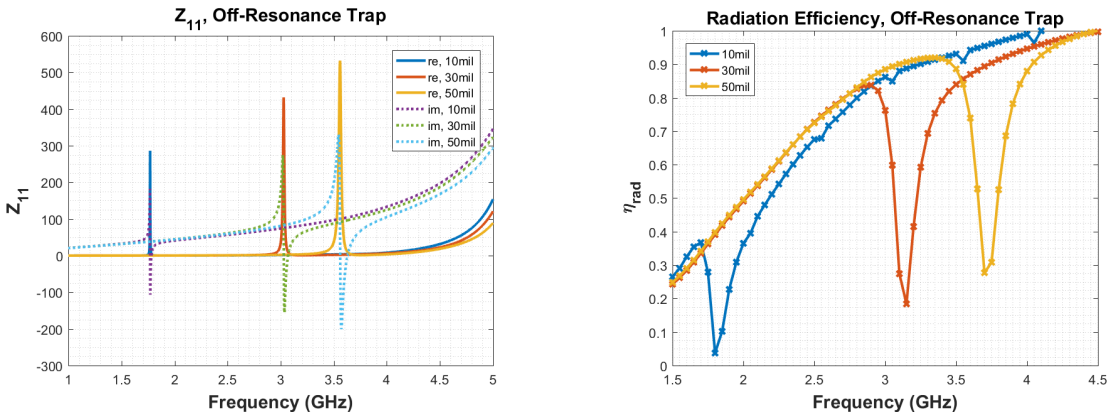
Figure 3.18: Slot antenna with reconfigurable cavity loads, total length 45.20mm, which would be half wavelength at 2.5GHz for a straight unloaded slot

each slot "arm" (between the ends and the center point), Figure 3.18. The location is away from the current maxima at the slot ends. As previously discussed, direct slot to cavity coupling necessitates sidewall cutouts that act as parallel transmission line shorts, Figure 2.5. The parallel shorts dominate the reactive loading away from the cavity resonance. However, the reactance provided by the cavity may be significant enough just off of resonance to allow for impedance match points that line up with the "knee location" of each radiation efficiency dip, rather than being located directly at the efficiency low-point. Improved efficiency at resonance is shown in Figure 3.19a, which demonstrates impedance tuning across S-band, and Figure 3.19b shows the improved radiation efficiency. The current design tunes from 1.77GHz to 3.55GHz with a radiation efficiency of 20%-84%, which is a significant improvement over the end-loaded slot antenna that had a simulated efficiency range of 8% to 29%.

3.5 Microstrip Coupled Loads

3.5.1 End Loads

Figure 3.20 avoids the sidewall cutout shorted transmission line by using a microstrip line on a superstrate above the radiating slot to aperture couple to the cavity resonators. Effec-



(a) (b)

Figure 3.19: Input impedance and radiation efficiency of off-resonant loaded cavity loaded slot design (a) anti-resonances tuned to 1.77GHz (20%), 3.03GHz (65%), 3.55GHz (84%) (b) black circles correspond to anti-resonance frequencies

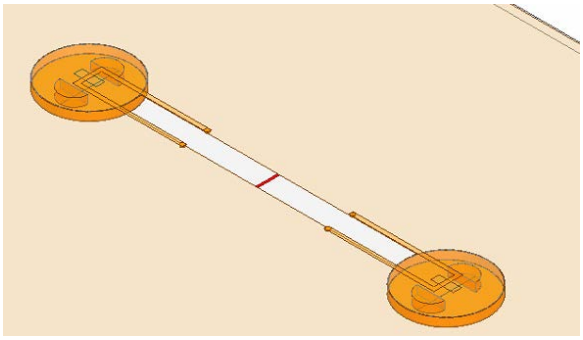
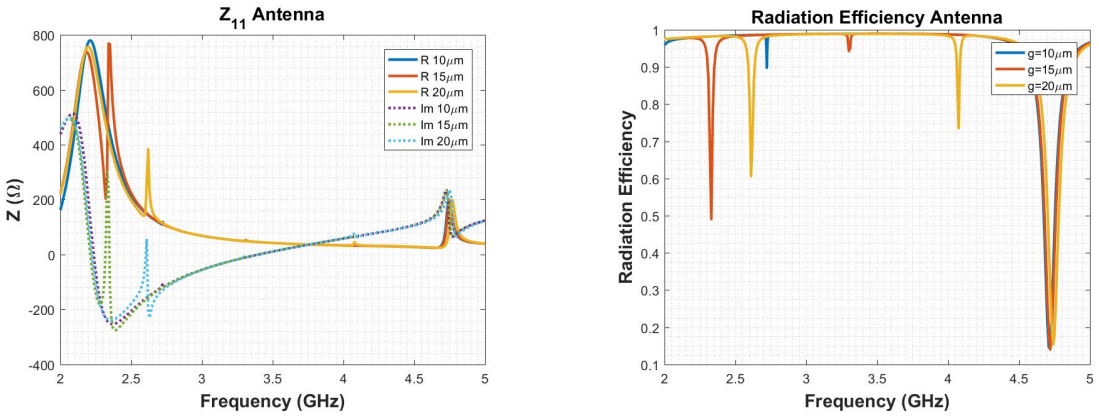


Figure 3.20: Microstrip line on superstrate above radiating slot, microstrip couples to cavity apertures and slotline, cavities are a multimode evanescent mode cavity with split posts [42]



(a) (b)

Figure 3.21: a) Input impedance of slot antenna with microstrip coupled cavities, Figure 3.20, first-mode resonance tuned from 2.34 GHz to 2.6 GHz by changing the cavity capacitive gap from 15 μm to 20 μm b) Radiation efficiency of slot antenna with microstrip coupled cavities, Figure 3.20, efficiency is 49% at 2.33 GHz and 61% at 2.61 GHz

tive coupling only occurs if the via shorts from the microstrip terminate immediately next to the slot, where the slot surface current maximum exists.

Input impedance and radiation efficiency are shown in Figure 3.21a and Figure 3.21b. Though the antenna can be tuned across frequency, the radiation efficiency drops significantly at the tunable resonances.

3.5.2 Mid Loads

Figure 3.22 shows another slot antenna that uses a microstrip on a superstrate to couple into the loading cavities. Unlike the design in Figure 3.20, the coupled load point can be placed anywhere along the length of the slot. Figure 3.23a shows that the high-capacitance tuning shows several resonances at 1.59, 2.13, 2.34, and 3.72GHz. The middle tuning is 1.59, 1.68, and 3.24 GHz. Low-capacitance is 1.59 and 1.85 GHz. The radiation efficiency has a broad dip from 2.5 to 3.5 GHz.

High capacitance radiation efficiency dips at 2.1-2.15, 2.35, and 3.8 GHz, which line

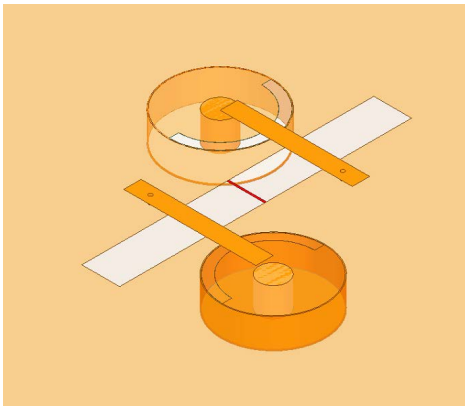
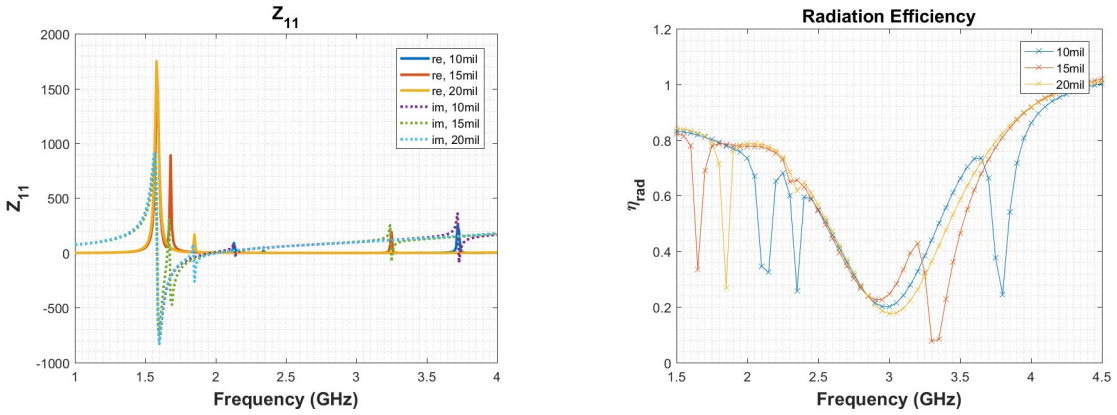


Figure 3.22: Slot with cavity loads coupled through microstrip.



(a) (b)

Figure 3.23: a) Input impedance, anti-resonances tuned by varying capacitive gap in cavity b) Radiation efficiency of antenna in Figure 3.22, 34% at 1.65 GHz and 26% at 2.35 GHz

up with the anti-resonances, Figure 3.23b. None of the anti-resonances are good radiators. Middle tuning is 1.65, maybe around 2.3, and 3.3-3.35 GHz. The low capacitance tuning is 1.85 and maybe 2.35. All bands show a 1.59 GHz anti-resonance, which appears to be unrelated to the cavity tuning. This has good efficiency and is high-impedance. None of the points can radiate on the middle tuning, although the 3.24 GHz point is almost to the knee of the radiation efficiency null. The high-frequency tuning appears to radiate at 1.85 GHz.

3.6 RLC Loaded Slot

A new set of slot antennas designed to operate off of cavity resonance were investigated from the design rules gathered above. In keeping with trap dipole guidelines, the loads were placed near the midpoint of each slot "arm" (between the ends and the center point). To initially test the concept, lumped RLC ports were simulated on a slot antenna, with an equivalent resistance value to simulate the cavity loss. The lumped RLC loaded slot with off-resonant traps had above 68% efficiency at all tunable input impedance resonances.

Direct slot to cavity coupling necessitates sidewall cutouts that act as parallel transmission line shorts, Figure 3.3. The cavity's reactance can be significant enough just off-of resonance to allow for impedance match points that line up with each radiation efficiency dip's "knee location" rather than being located directly at the efficiency low-point.

3.7 Dual Band L-Slots Coupled to CPW and Reconfigurable Loads

Finally, a proximity coupled design with a bent slot and a reconfigurable CPW load is shown in Figure 3.24. The long section of the slot is meant to have a fundamental resonance in S-band, while the slot's short arm aligns the field distribution to proximity coupled to

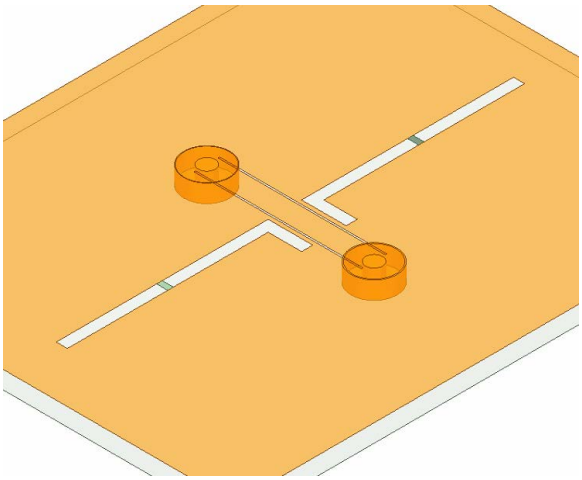


Figure 3.24: Two L-shaped slots coupled to CPW with cavity loads, longer leg radiates at S-band, shorter leg radiates at X-band, both tuned by proximity coupling to cavity loaded CPW

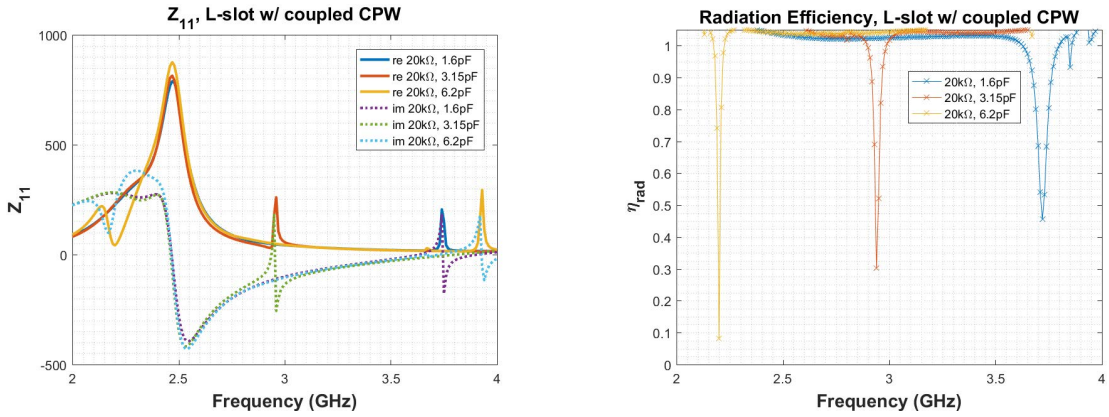
a length of CPW terminated in cavity loads. The slot's short arm is also made to have a fundamental resonance in X-band so that this design is the first attempt at a single tunable element for both the S and X band. As shown in Figure 3.25a, the slot input impedance can be tuned via the proximity coupled loads at S-band, but the same load values tune less significantly in X-band, Figure 3.26a.

The input impedance has a tunable resonance from 2.96, 3.74, and 3.93 GHz. There are simulated overlapping radiation efficiency nulls at 2.94 and 3.72 GHz.

At X-band, the input impedance does not reconfigure very much with the same load values, and similarly, there is very little radiation efficiency loss.

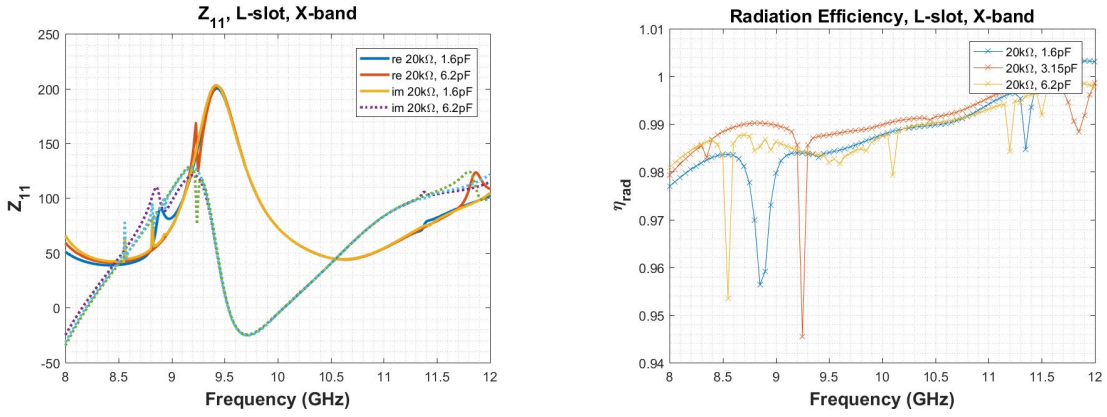
3.8 Conclusion

The evanescent mode cavity was combined with the ring resonator end-loaded slot antenna, and the cavity loads can tune the slot resonance across S-band with a realistic range of piezo reconfigurable capacitive gap sizes in the cavity loads. However, there is a large



(a) (b)

Figure 3.25: L-slot at S-band a) input impedance b) radiation efficiency



(a) (b)

Figure 3.26: L-slot at X-band a) little reconfigurability with current load values b) radiation efficiency

increase in the loss at or near the antenna resonances. Since there is little or no frequency separation between the antenna resonances and steep declines in radiation efficiency, the efficiency cannot be fully evaluated without a realistic feed structure. The impedance match frequencies might be exactly at antenna resonance or might be near antenna resonance, as is true of the dips in radiation efficiency. I demonstrated designs with increased frequency separation between the antenna resonance and loss by moving the cavity locations and changing the coupling mechanisms. The simulation data in this chapter strongly indicates that radiation efficiency should continue to be a primary concern with the addition of a feed structure and cavity backing.

Chapter 4

Design of Cavity Backed Slots

4.1 Introduction

Standard slot antennas have radiation above and below the slot. It is often desirable to add a cavity backing to a slot radiator to radiate in only one direction. In this chapter, I present field analysis and design principles of cavity backed slots in Section 4.2, and then the design process for cavity backing with additional load structures for reconfiguration in Section 4.3.

4.2 Traditional Cavity Backing

A design for a circularly polarized cavity-backed slot is presented in [43]. Sievenpiper explains the frequency response in terms of 4 different cavity modes that are excited, two of which are radiating. The radiating modes can be identified as the ones that excite a significant E-field differential across the slot radiators. The fourth mode provides an E-field differential, but the slot ends are out of phase with each other and cancel out significantly. The particular modes differ from those excited in our structure, but the common principle

remains of analyzing antenna behavior across frequency in terms of which modes provide a proper E-field differential over the radiating slot's narrow dimension. Sievenpiper achieves circular polarization (and a slightly wider impedance bandwidth) by making one slot slightly shorter than the other, such that they have a phase difference of 90 degrees.

The cavity is fed with a coax probe feed. The impedance is matched by moving the probe along a diagonal between the corner short and the open at the cavity center. The cavity impedance (and bandwidth) is also significantly dictated by the cavity thickness. The slot width impacts the antenna bandwidth to a lesser extent. Design formulas are given for the crossed slot design, and there are extensive references on crossed slot antennas.

[44] presents measurements of the impedance of three different variations of a cavity-backed slot. [45] contains a theoretical model for the impedance of a cavity-backed slot, which is mathematically fitted to the previous paper's measurement data. In [44], measurements are taken of the slot antenna impedance by splitting the slot lengthwise with a highly conductive image plane. This method could be repeated for Wheeler cap measurements if desired, assuming that the cavity mode is symmetric about the image plane. Additionally, [44] explores the impedance impact of varying the cavity depth and adding an inductive post. These papers' initial significance is that cavity backing a slot should invalidate the Babinet assumptions for finding a slot's impedance as the inverse of a dipole. These papers present experimental data and theoretical equations for the impedance. The cavity back appears as a short some distance away from the slot.

The difference between the open slot impedance and cavity-backed slot impedance is a function of cavity depth, width, height, and frequency. The open slot impedance is doubled since it radiates in only one half-space. Part of the difference can be approximated by a lossless transmission line short (the cavity back). The mathematical models in [45] are acknowledged not to be precise enough to predict resonant frequency or behavior near resonance accurately, but they do display the general trends in impedance.

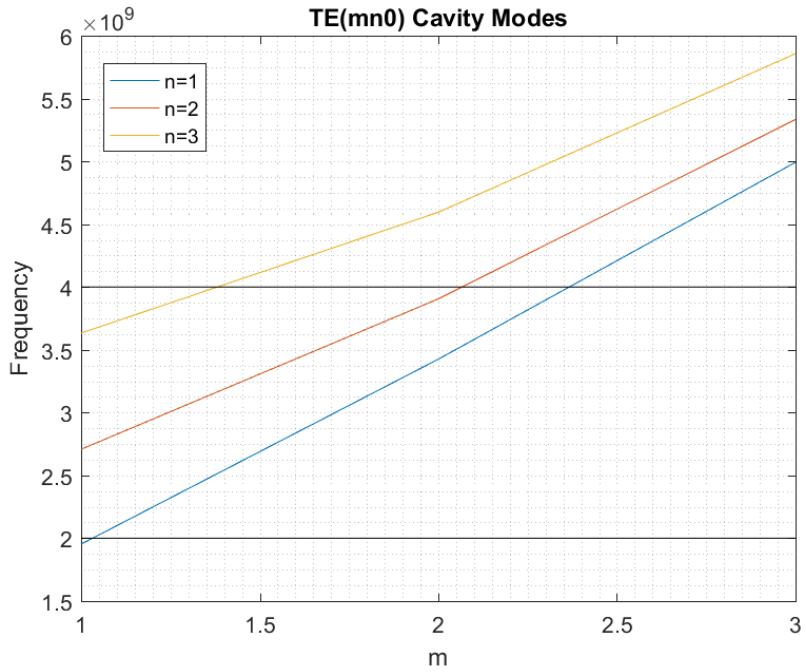


Figure 4.1: TE cavity modes, resonant frequency of transverse electric modes in 76.2x50.8x3.175mm rectangular cavity cavity

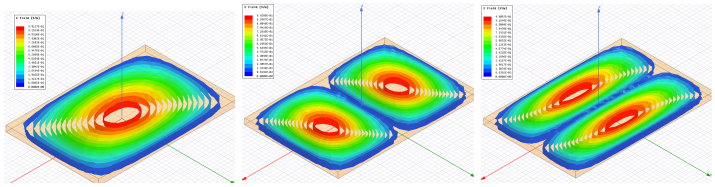
4.2.1 Cavity Backed Slot, Eigenmode Simulation

Figure 4.1 shows the theoretical resonant frequencies of TE cavity modes for a 76.2x50.8x3.175mm cavity.

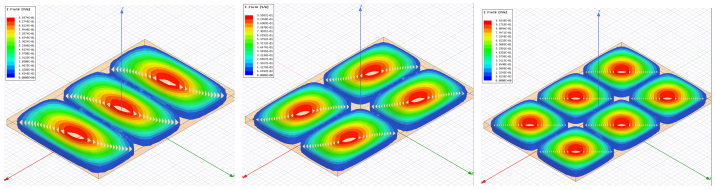
The HFSS simulation of this cavity gives a Q of 500. The first five modes, which cover S-band, are resonant at 1.96GHz, 2.72 GHz, 3.44 GHz, 3.65 GHz, and 3.92 GHz. The 6th mode, which is out of band, is at 4.62 GHz.

Figure 4.3 shows eigenmode simulation results for the first three modes of the same cavity size, but with an added slot with varied length and location. The slot is modeled as a perfect H boundary in an eigenmode solution in HFSS. The simulation model is shown in Figure 4.4.

An off-center slot can lower the resonant frequency of the cavity. Alternatively, it encourages higher-order modes at a lower frequency. The theoretical cavity analysis should



(a) 1.96 GHz (b) 2.72 GHz (c) 3.44 GHz



(d) 3.65 GHz (e) 3.92 GHz (f) 4.62 GHz

Figure 4.2: Cavity modes in S-band, electric field of first six modes in 76.2x50.8x3.175mm rectangular cavity

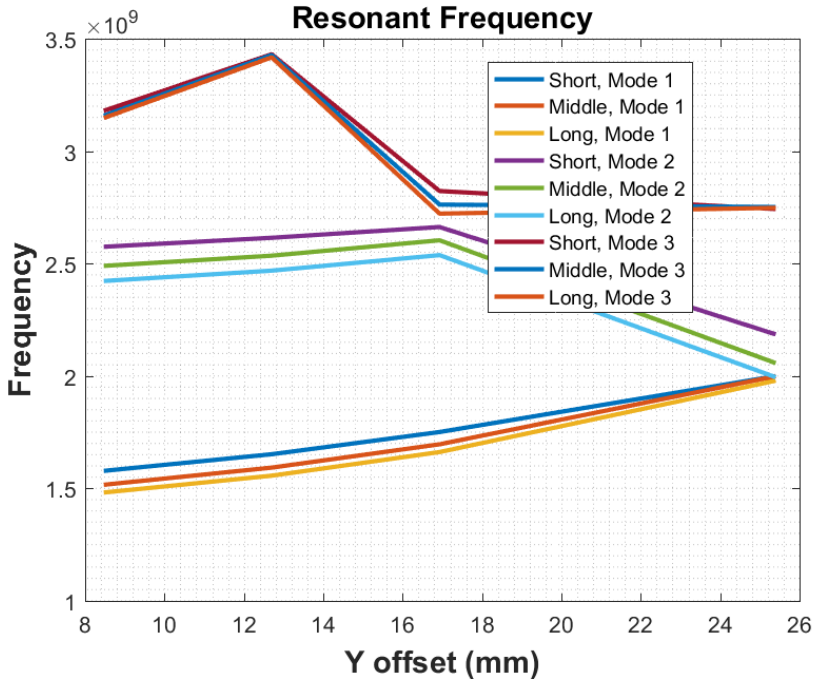


Figure 4.3: Parametric analysis of slot length and location against cavity resonant frequency

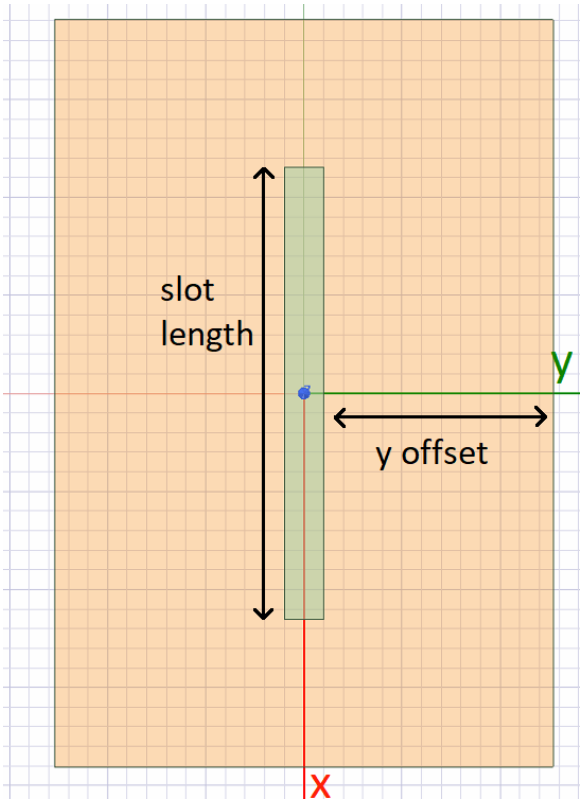
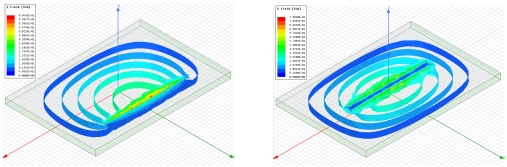
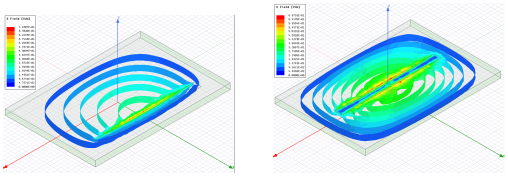


Figure 4.4: Slot loaded cavity, excitation of slot and resonance of cavity altered by changing slot length and offset from cavity wall



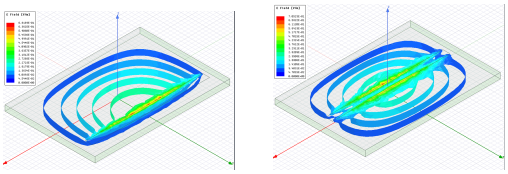
(a) Short Slot, 8mm offset

(b) Short Slot, 25mm offset



(c) Medium Slot, 8mm offset

(d) Medium Slot, 25mm offset



(e) Long Slot, 8mm offset

(f) Long Slot, 25mm offset

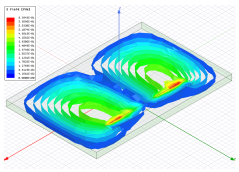
Figure 4.5: 1st mode electric field in slot-loaded cavity, varied by changing slot length and offset from cavity wall

support TE110, TE210, TE310, TE120, TE220 in the 2-4GHZ range. Q is 500.

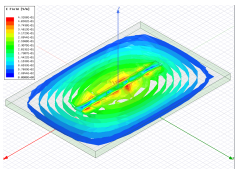
It can be seen in Figure 4.5, that for the first mode, when the slot is near the wall of the cavity, the perfect H boundary of the slot can increase the electrical size of the cavity in the y dimension.

In Figure 4.6, the centered slot can disrupt a higher mode slot distribution.

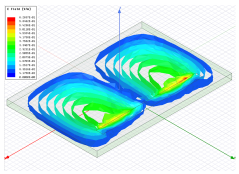
In Figure 4.7, the centered slot can again prevent a higher-order mode from forming.



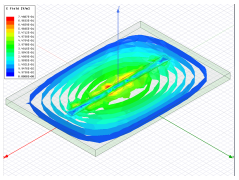
(a) Short Slot, 8mm offset



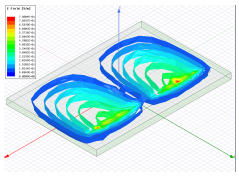
(b) Short Slot, 25mm offset



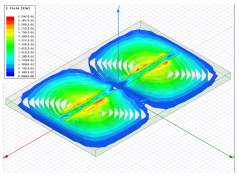
(c) Medium Slot, 8mm offset



(d) Medium Slot, 25mm offset

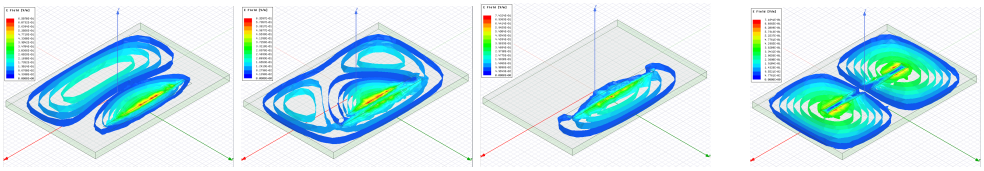


(e) Long Slot, 8mm offset

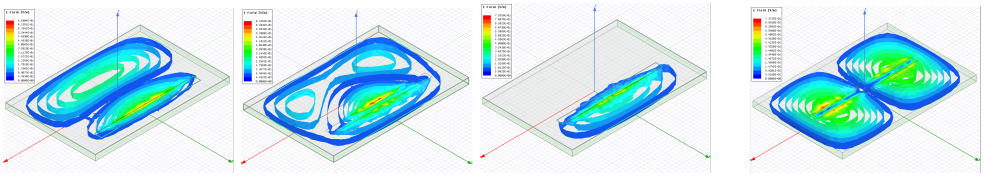


(f) Long Slot, 25mm offset

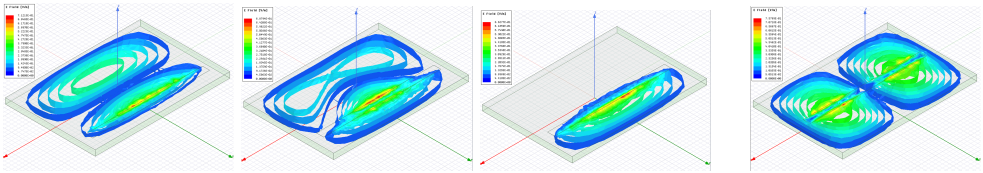
Figure 4.6: 2nd mode electric field in slot-loaded cavity, varied by changing slot length and offset from cavity wall



(a) Short Slot, 8mm offset (b) Short Slot, 13mm offset (c) Short Slot, 17mm offset (d) Short Slot, 25mm offset



(e) Medium Slot, 8mm offset (f) Medium Slot, 13mm offset (g) Medium Slot, 17mm offset (h) Medium Slot, 25mm offset



(i) Long Slot, 8mm offset (j) Long Slot, 13mm offset (k) Long Slot, 17mm offset (l) Long Slot, 25mm offset

Figure 4.7: 3rd mode electric field in slot-loaded cavity, varied by changing slot length and offset from cavity wall

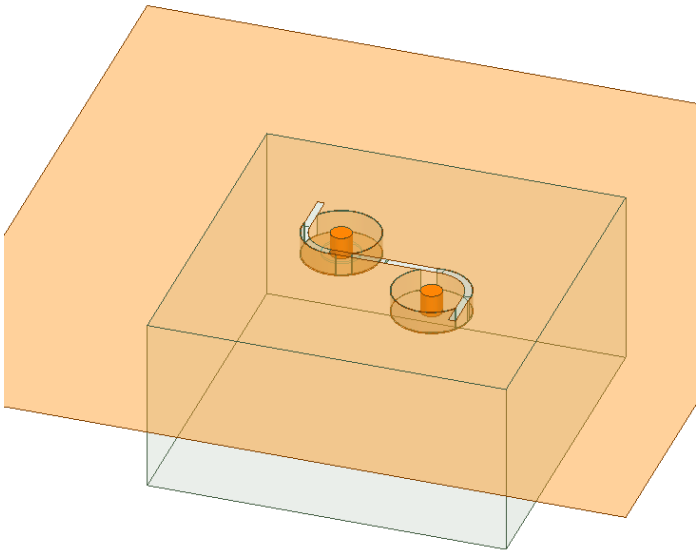


Figure 4.8: Slot radiator with evanescent mode cavity loads and $\lambda/4$ cavity backing

4.3 Reconfigurable Slot and Backing Cavity

The design in Figure 4.8 has a quarter wavelength backing cavity on one of the designs from the previous chapter. The slot is still fed with a lumped port feed, and the antenna is still tunable across much of S-band, Figure 4.9, but there is also a static higher-order resonance at the top of the band.

4.3.1 Thin Cavity Backing

A thinner substrate improves cost and weight. The backing cavity should be able to fit into half-wavelength spacing for array integration. It is also essential that the backing cavity field distribution does not disturb the antenna's far-field radiation pattern. The cavity backing is an additional resonator on the antenna. The cavity could possibly be designed to keep the resonances out of band. Because the backing cavity is must be physically larger than the slot, the unloaded cavity will have a lower first resonance than the antenna, and

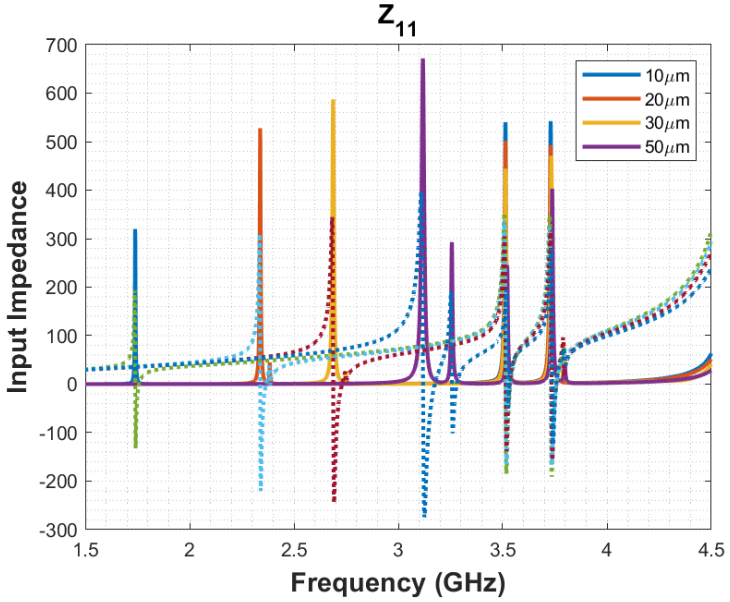


Figure 4.9: Input impedance of reconfigurable slot antenna with $\lambda/4$ cavity backing, resonance tuned from 1.73 GHz to 3.75 GHz by changing capacitive gap in evanescent cavities

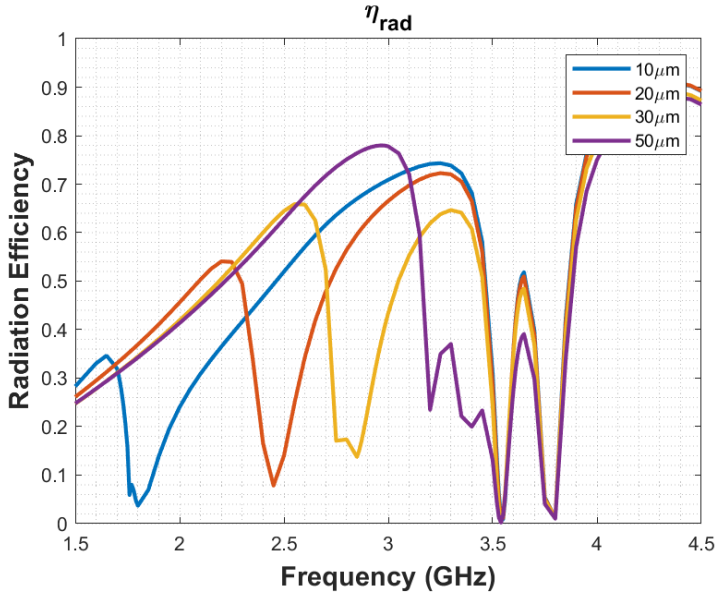


Figure 4.10: Radiation efficiency of reconfigurable slot antenna with $\lambda/4$ cavity backing

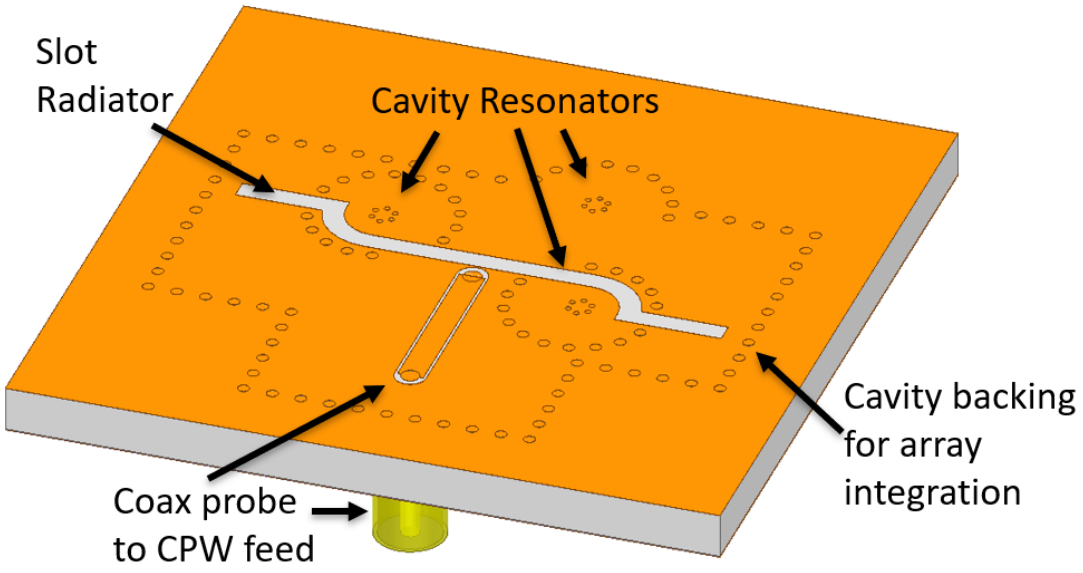


Figure 4.11: Thin cavity backed reconfigurable slot antenna with a variable capacitor loaded post added to tune the outer backing cavity. Antenna element is 40 mm x 40 mm, making it $\lambda/2$ at 3.75 GHz.

will support additional higher modal resonances. I added inductive loading by removing the corners of the cavity, which can also be thought of as simply reducing the cavity volume, in order to raise the fundamental backing cavity resonance, as seen in Figure 4.11. I also added an additional piezo reconfigurable capacitor load to the backing cavity to tune the backing cavity resonance. Since each piezo reconfiguration mechanism probably requires its own DC bias line and fine-tuning, it is better from a simplicity and cost stand-point to have as few as possible. With this design, a single capacitor loaded post can tune the outer backing cavity, and the whole antenna shows near-usable impedance matching across tuning, as shown in Figure 4.13.

The antenna element would take several steps to fabricate, and the layer by layer design is shown in Figure 4.12. The cavity measures 40 mm x 40 mm and the substrate is 125 mil

TMM3 with 17.5 μm copper cladding on both sides of the boards. The capacitive posts are drilled and plated as 0.4 mm diameter vias through the substrate and top and bottom copper layers. The rubout pattern is milled on the bottom copper layer for the air gap area of the three cavities in addition to a rubout for the probe feed. Circular copper pads are retained on underside of the post vias, with the pads having 0.2 mm of extra copper radius beyond the edge of the post vias. Bondply is patterned to leave air gaps in the reconfigurable cavities, and copper foil and bondply are laminated to the underside of the board. Following this, the remaining cavity vias are drilled and plated. The rubout for the broad feed is defined on the copper foil layer, as well as the slot radiator on the top copper layer. Finally, the SMA feed can be soldered on.

The cavity backed slot antenna has a tuning range of about 2 GHz, and the three tunable resonators can possibly be calibrated to create a third order response in S_{11}. The antenna also has improved radiation efficiency, from 20% to 84% across the tuning range, Figure 4.14. The design has typical single sided slot radiation patterns, as shown in Figure 4.15. However, there are still dips in radiation efficiency near to the antenna operating frequencies. Since there are no answers in the literature about what is causing the dips in radiation efficiency that have persisted across all of my resonator loaded antenna designs, I will focus on the trap dipole, which is the simplest resonator loaded antenna.

4.4 Conclusion

Cavity backed slot antennas radiate in a single direction. The simplest cavity backing has a depth of a quarter wavelength. The cavity was made thinner to decrease weight and size for array integration, with additional loading introduced to adjust the cavity resonance. I incorporated a probe feed into the cavity, which can be incorporated with a feed network for an array design. The cavity backed element is small enough to be incoporated into an

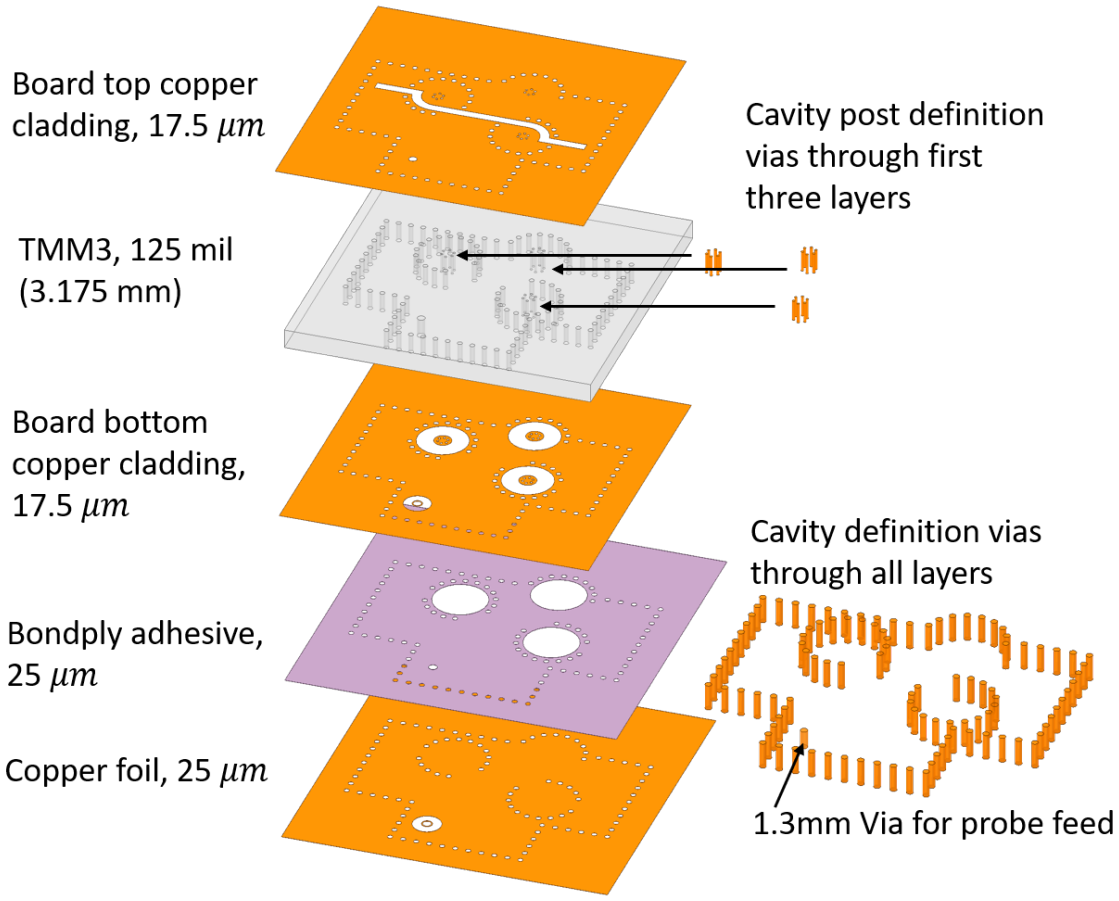


Figure 4.12: Layers for cavity backed slot fabrication

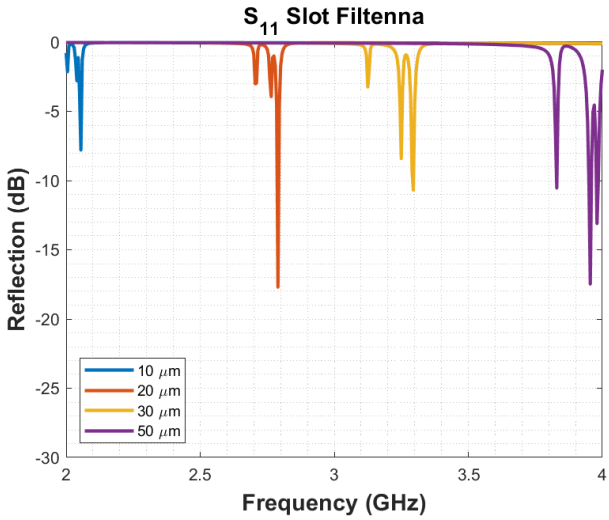


Figure 4.13: Reflection of cavity backed slot antenna, tunable across S-band with potential for higher order filtenna response. The separate dips on each trace can be tuned by individual control of each of the three piezo tuning elements.

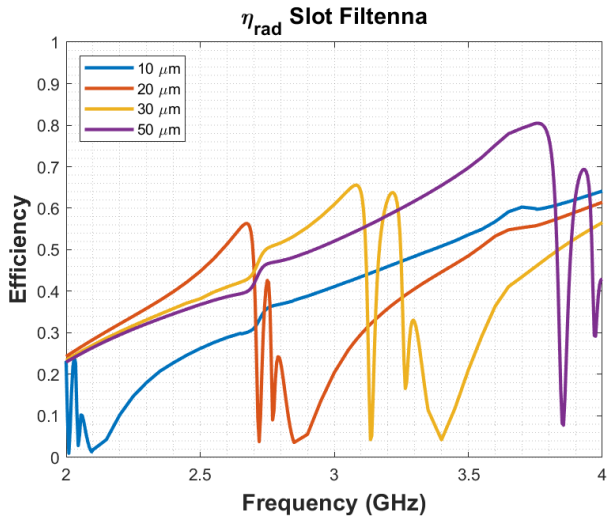


Figure 4.14: Radiation efficiency of tunable cavity backed slot antenna

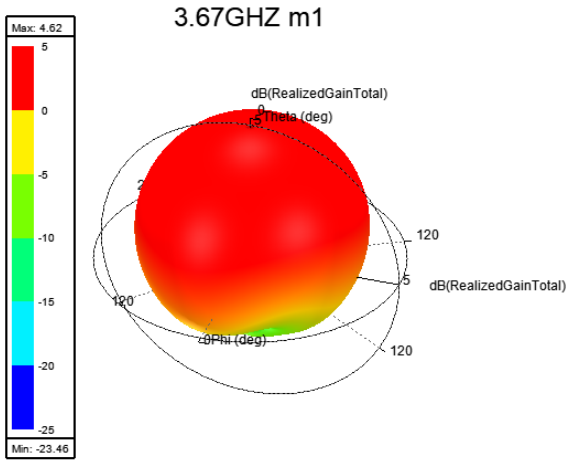


Figure 4.15: Single sided radiation pattern, realized gain at 3.67 GHz

array, and shows potential for a higher order filter response with appropriate calibration of the resonators. Furthermore, radiation efficiency has been improved from the original end-loaded slot antenna design but is not well understood. In the next chapter, I will investigate LC resonator loads on simple wire radiators to investigate the impact of resonant loads on antenna radiation efficiency and reconfigurability.

Chapter 5

Theory of Trap Dipoles

5.1 Introduction

Reactive loads have been used since the origination of antennas, with Heinrich Hertz' first demonstration of radio waves using a dipole with capacitive ball end loads on the antenna [46]. Reactive and resonant loading has been used since then for improving radiation resistance [47], impedance matching [48], bandwidth [49], electrical length[50], current distribution [51], and multiband antennas [52]. Adding loads can mitigate performance restrictions from limits on antenna size, weight, and cost. Newer technologies, like varactors, MEMS, and pin diodes as loads [53]–[56] allow for reconfiguration and continuous tuning of operating frequencies. Filtennas are a more recent development in resonantly loaded antennas, have improved selectivity and out of band rejection, and can potentially decrease size, weight, and cost by coupling an antenna with resonators in a filter design [57]. In short, resonant and reactive loading of antennas has always been used, and will continue to be used to improve antenna performance, especially as advancements in semiconductor devices, miniaturization of mechanical devices, and new fabrication techniques such as 3D printing allow for integrating new load types with antennas for continuing improve-

ments in Q, power handling, and upper frequency limit. However, the well-documented resonator dissipation in filter design [17] raises questions about radiation efficiency in resonator loaded antennas.

Previously, the authors presented a resonator-loaded slot antenna [15]. The resonant loads are the same evanescent mode coaxial cavity resonators with a piezo-reconfigurable air gap under the center post of the cavity, described in Section 2.3. The antenna's resonance can be tuned across S-band via a piezo-controlled variable capacitance in the cavity loads, but initial simulations suggested low radiation efficiency associated with the tunable load resonance. The goal of this chapter is to develop design principles for maintaining high radiation efficiency with resonant loads.

Trap loaded dipoles are one of the simplest resonator-loaded antennas. Traditionally, the resonant load is an inductor-capacitor "trap" integrated into a dipole or monopole to create a second operating frequency at the trap resonant frequency. The literature on trap-loaded and inductor-loaded wire antennas can guide more complicated resonator-loaded antenna designs.

In this chapter, I start with a review of the literature on wire antennas with discrete reactive and resonant loads, Section 5.2, and I emphasize the load impact on radiation efficiency since antenna radiation efficiency and loss is a particular focus of this chapter. I use several different simulation tools for analysis and explain dipole modes and resonance while comparing the accuracy of solutions from different software tools in Section 5.3. After explaining the analysis methods, I demonstrate high loss frequency bands on loaded antennas and explain them in terms of characteristic modes, Section 5.4. This new explanation of load-related loss results from comparing parameter sweeps of several antenna dimensions and component values. Additional design guidelines based on these parametric sweeps are presented in Section 5.5.

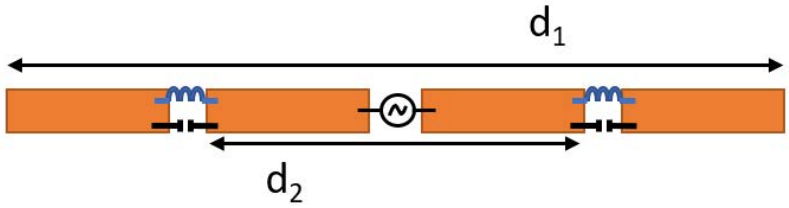


Figure 5.1: Trap dipole antenna with d_1 half a wavelength at lower operating frequency and d_2 half a wavelength at upper operating frequency

5.2 Resonant and Reactive Loading Literature Review

Trap-loaded dipoles are a well-known antenna from the literature [58] and are conveniently similar to our cavity loaded slot antenna [15]. The conventional trap loaded dipole is a half-wavelength long at frequency f_1 and has a pair of bandstop resonators spaced a half-wavelength apart at a higher frequency f_2, as in Figure 5.1. Usually, the bandstop resonators are either discrete parallel LC circuits or quarter-wavelength stubs. One of the first publications on trap dipole design comes from the amateur radio community and uses four traps to operate at three bands [52]. The authors of [52] focus on the performance in terms of SWR and do not discuss radiation efficiency. However, in the same year, [59] mentions that the capacitors' thermal breakdown can be a significant problem in trap dipole antennas, indicating that loss in the trap circuit, and consequently low efficiency, is a common problem for trap dipoles.

Inductively loaded dipoles and monopoles are more commonly discussed in the literature than trap antennas and can give insight into general principles for loaded antennas. Reactive loading on linear wire antennas can offer broad and multi-frequency impedance matching, often in electrically small antennas, with reduced radiation efficiency compared to a design with an optimal resonant length [49]. Radiation efficiency in electrically small monopoles decreases as the antenna length decreases and necessary inductive load magnitude increases. A balance must be struck between achieving an impedance match at the

desired frequencies and achieving an acceptable radiation efficiency, often with limits on the antennas size and the number of elements.

The ideal loading point on an inductively loaded monopole is where the necessary reactive loading is equal to the input unloaded reactance [50]. Loading inductance needed for an electrically small monopole (triangular current distribution) can be calculated [60]. A loaded $\lambda/4$ dipole can achieve 50% radiation efficiency. Radiation efficiency peaks with the load 0.4 of the length from the feed, and radiation resistance is highest with the load at the end, so a good compromise is 2/3 of the length from the feed placement [61]. Radiation efficiency is also impacted by the ratio of radiation resistance to reactive load resistance [61]. Loading is most often used to lower the resonant or operating frequency when size is a limiting factor. Monopoles and dipoles are capacitive below the fundamental series resonance or when the radiator is electrically small. Inductive loading then cancels out some of the capacitance and shifts the series resonance lower in frequency. The general loading case is not confined to positive reactances below an antenna fundamental series resonance, but rather any load reactance may be useful to create antenna resonance behavior above or below a natural series or parallel antenna resonance.

In contrast to the typical method of designing trap dipoles around enforcing an open boundary condition at a new resonant length, Figure 5.2, [62] suggests designing a trap loaded dipole antenna to be operated at a frequency above and a frequency below the trap resonance, thereby dramatically improving the radiation efficiency. The unloaded dipole antenna is capacitive below its first natural resonance, and the trap loads are inductive below the trap resonance, which can cancel out the antenna reactance at the lower frequency, Figure 5.3. Above the first resonance, the dipole is inductive, and the trap presents a capacitive reactance, which again cancels out for an efficient impedance match. The antenna design does not have an operating frequency at the trap resonance, which is still associated with high loss. With this "off-resonant" design, the trap-dipole becomes similar to the

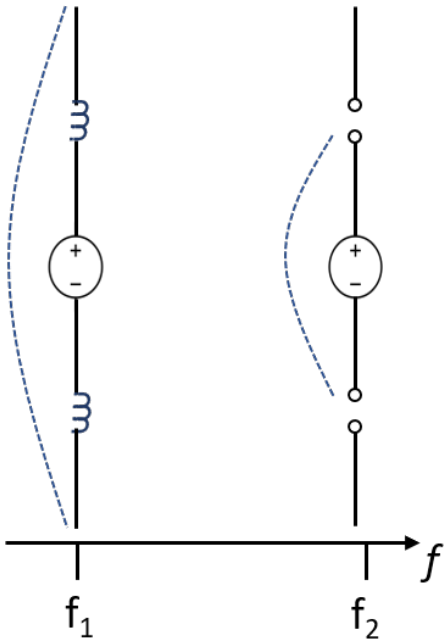


Figure 5.2: Trap dipole lower and upper operating frequencies with dashed line representing the commonly assumed current distributions. The trap adds slight inductive loading at f_1 and is antiresonant at f_2.

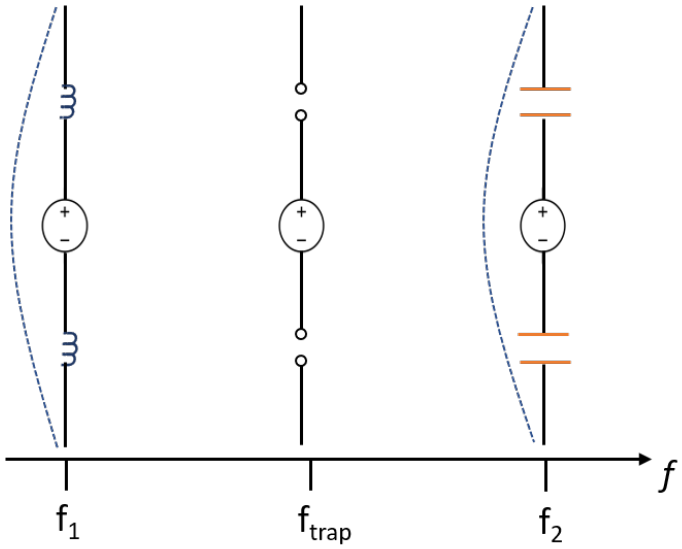


Figure 5.3: Off-resonant trap dipole at key frequencies, dashed line current distributions. Unlike the conventional trap dipole, the entire dipole radiates at both operating frequencies

more broadly investigated design of an inductor loaded monopole and benefits from the same design principles.

Loaded dipoles are still a current topic, as in [63]–[71], but it's very seldom that papers mention radiation efficiency. Since the literature does not conclusively answer whether trap loaded dipoles are lossy, I will focus on loss in the design of resonantly loaded antennas.

5.3 Calculation of Basic Trap Dipole Behavior

In other parts of this dissertation, I typically use HFSS to simulate antennas. In this chapter, I am mostly interested in loading wire dipoles. To save time and allow for greater flexibility in scripting analysis, I used FEKO to generate a Method of Moments impedance matrix for an unloaded wire radiator and then exported FEKO's matrix to MatLab for further simulation and analysis. The load location and excitation are defined in MatLab, and the reactive and resonant loads are added to the antenna. With the data in MatLab, it is very convenient to define arbitrary parametric sweeps and write scripts to save and report on key data points automatically. The simulation time is much shorter because the same starting unloaded wire impedance matrix can be reused.

5.3.1 Unloaded Dipole

The input impedance of an unloaded dipole that is $\lambda/2$ at 2 GHz agrees very well between FEKO, HFSS, and the FEKO + MatLab solution, Figure 5.4. The HFSS model differs slightly from the other two due to parasitic capacitance in the port definition. The pure FEKO and the hybrid FEKO MatLab solution agree almost exactly. Note the presence of several resonances. A series resonance occurs at 1.8 GHz, and a parallel resonance at 2.7 GHz. The input impedance is near to a second series resonance at 6 GHz.

A center-fed unloaded dipole at the λ antiresonance is not well matched to a 73 Ω

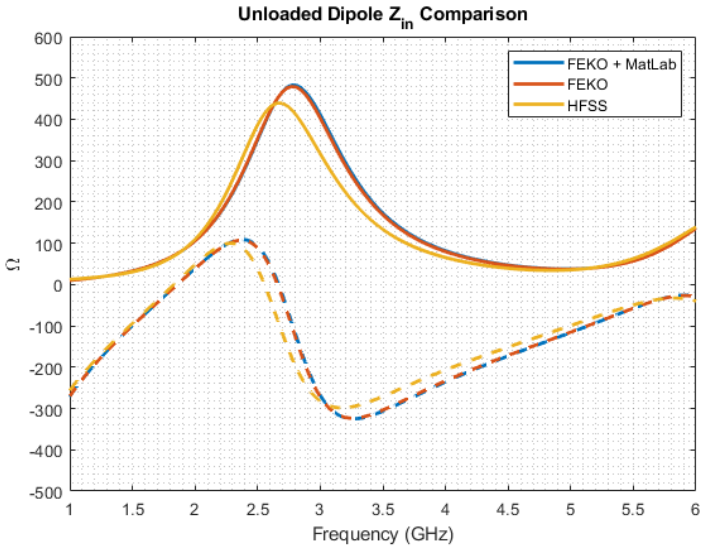


Figure 5.4: Comparing unloaded dipole input impedance between HFSS, FEKO, and a hybrid FEKO/MatLab MoM solution

differential voltage source at the center of the dipole, but the $3\lambda/2$ resonance is relatively well matched.

The 2 GHz λ/2 unloaded dipole has an efficiency of over 98% from 1 to 6 GHz, Figures 5.5 and 5.6. The unloaded dipole impedance matrix is used for almost all of the loaded trap dipole results in this chapter. Adding trap LC loads to the dipole will introduce additional resonance and change the radiation efficiency behavior.

HFSS calculates radiation efficiency as the ratio of radiated power to accepted power,

$$\eta_{rad} = P_{rad}/P_{in}. \tag{5.1}$$

Radiation efficiency is a ratio of radiation resistance and loss resistance (conductor and dielectric loss), defined in [72] as

$$\eta_{rad} = \frac{R_r}{R_L + R_r}. \tag{5.2}$$

The MatLab calculation of efficiency is according to equation 5.1, but equation 5.2 is par-

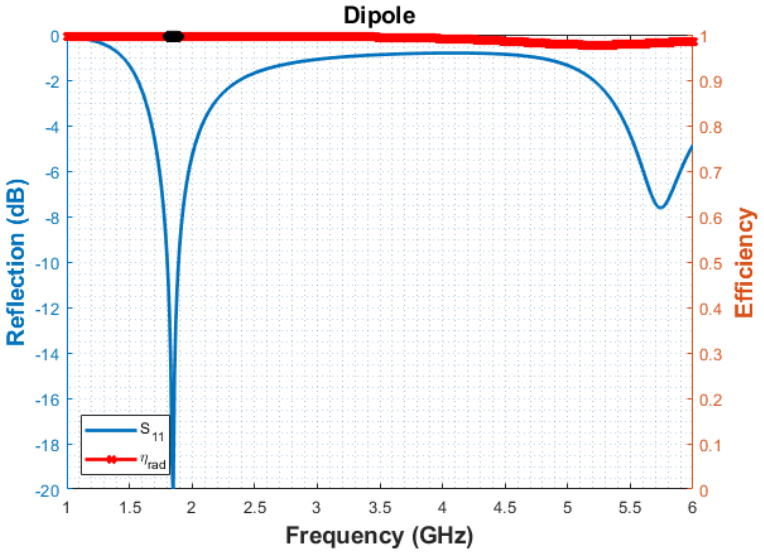


Figure 5.5: Reflection coefficient and radiation efficiency of unloaded dipole, $\lambda/2$ resonance at 2 GHz and $3\lambda/2$ resonance at 6 GHz

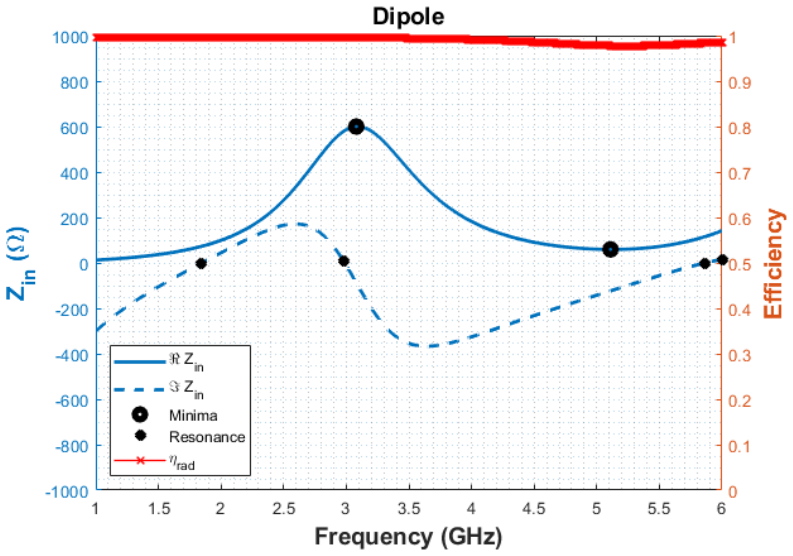


Figure 5.6: Input impedance and radiation efficiency of unloaded dipole, efficiency around 100% over the frequency range covering the first three resonances

ticularly helpful for theoretical explanation of the loss.

5.3.2 Trap Dipole

The calculation of trap dipole behavior is demonstrated to be accurate compared with FEKO and HFSS. In Figure 5.7, I compare the input impedance of a trap dipole, simulated in HFSS, FEKO, and a FEKO + MatLab variation that involves taking the impedance matrix from FEKO, loading it with traps in MatLab, and calculating the behavior in MatLab. The HFSS data has a first antiresonance resistance of 574 Ω at 2.7 GHz, while the FEKO antiresonance is 634 Ω at 2.83 GHz. The FEKO model is a wire dipole with a meshed cylinder radius of 1 mm. The HFSS model is a cylindrical dipole with a radius of 1 mm. Both use a lossy copper metal definition for the radiator, and both have the same lengths, trap locations, and trap values. L_1 = 75 mm, L_2 = 43.8 mm, 1 nH inductor, 1.6 pF capacitor, and a 20 $k\Omega$ resistor.

The unloaded dipole model has a fundamental series resonance at 1.9 GHz, but the trap dipole's first resonance is tuned down to 1.8 GHz due to the trap's inductive loading. The second series resonance is at 3.84 GHz, even though the trap open circuit antiresonance is tuned to 4 GHz. The antenna antiresonances have a high impedance magnitude and are not well matched to our feed, as is typical.

The hybrid solution is in good agreement with the HFSS and FEKO solutions. In the FEKO calculation, automatic meshing was enabled. In the hybrid data source, the mesh has been limited to only 37 elements. A reflection coefficient plot is also included in Figure 5.8 for easy comparison.

Finally, FEKO, HFSS, and MatLab all have similar efficiency results, Figure 5.9. The hybrid design efficiency dips at 3.68 GHz (match at 3.84 GHz), HFSS dips at 3.7 GHz, and FEKO dips at 3.7 GHz. All solutions agree that the second operating frequency at

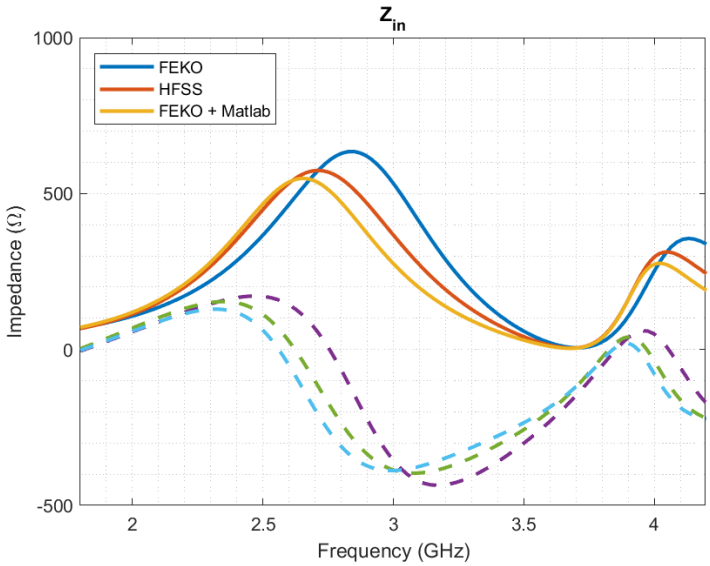


Figure 5.7: Comparing trap dipole input impedance between HFSS, FEKO, and a hybrid FEKO/MatLab MoM solution

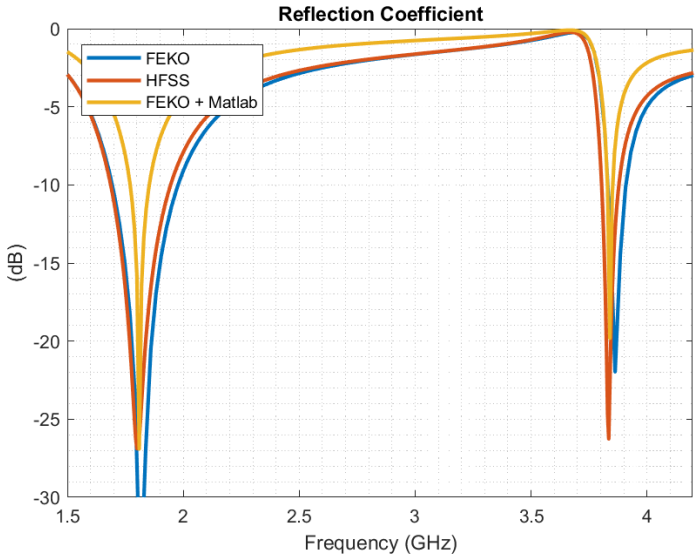


Figure 5.8: Trap dipole reflection coefficient comparison between HFSS, FEKO, and a hybrid FEKO/MatLab MoM solution

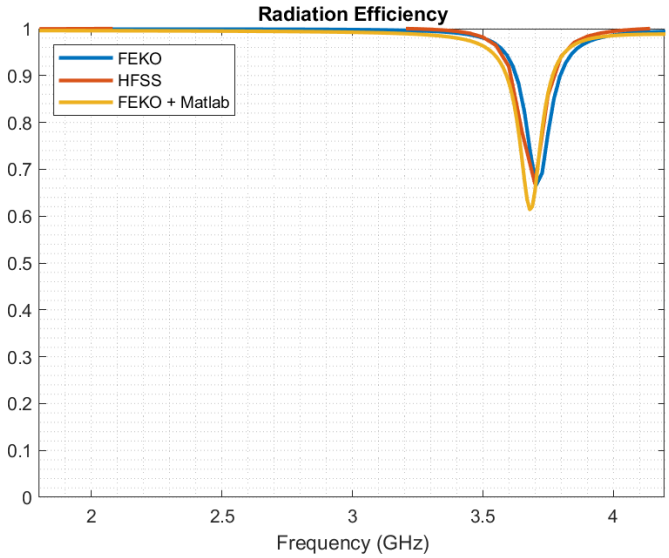


Figure 5.9: Trap dipole radiation efficiency agrees well between HFSS, FEKO, and a hybrid FEKO/MatLab solution

3.84 GHz has a radiation efficiency of over 90%.

5.4 Modal Analysis and Loss in Trap Dipole Antennas

Trap-related loss has been acknowledged in the literature, [59], [62]. To the author's knowledge, there is no study or explanation of loss in trap dipoles beyond implied thermal loss in trap components. Trap loss can be considered a simplified example of the load cavities' impact in Section 2.3, and other resonant loads on antenna performance. I will start by focusing on the relationship between network parameters and loss and then examining current distributions on the dipole at resonant frequencies.

5.4.1 Network Parameter Analysis

In Figures 5.10-5.12 I've overlaid the input impedance and reflection coefficient with the radiation efficiency. The reflection coefficient is plotted with radiation efficiency in Figure

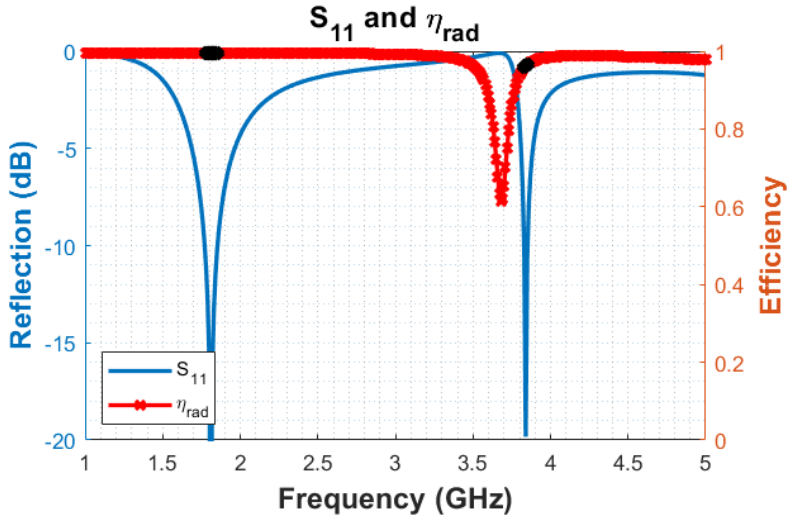


Figure 5.10: Reflection and efficiency of trap dipole, dip in efficiency near upper operating frequency

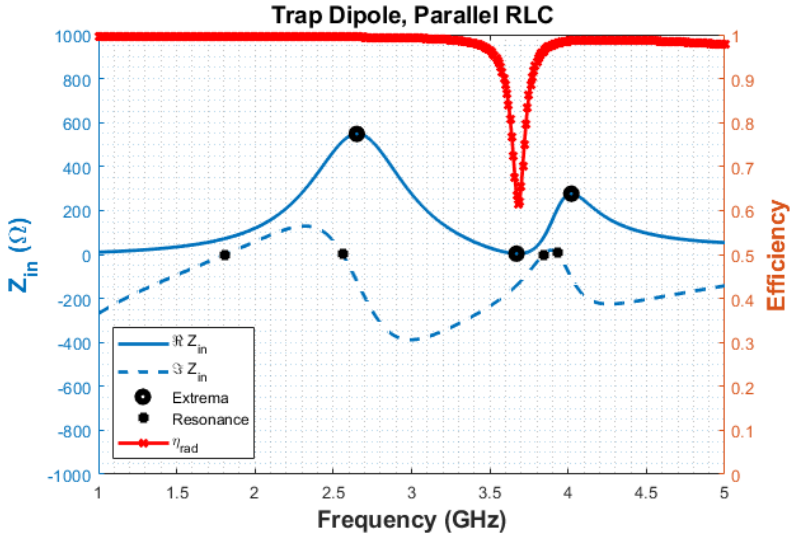


Figure 5.11: Input impedance and efficiency of trap dipole, resonances and minima and maxima marked

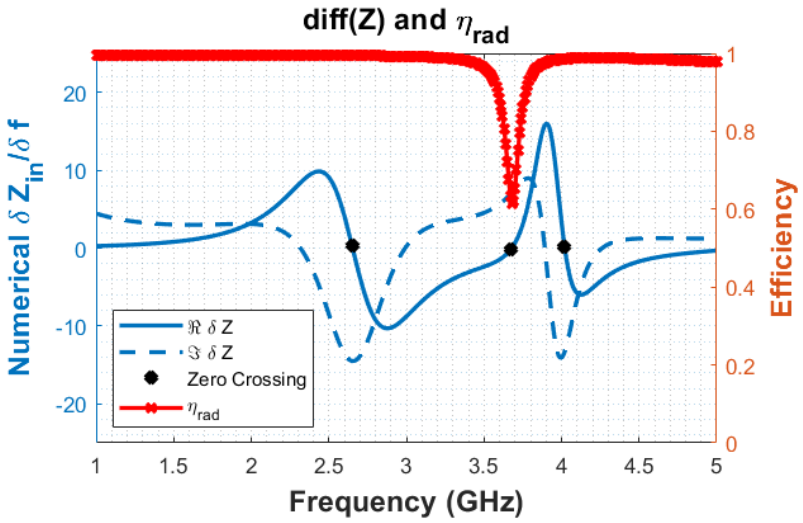


Figure 5.12: Slope of real and imaginary input impedance, plotted to easily identify the frequencies of the input imepdance minima and maxima (zero crossings of the slope). The minimum radiation efficiency lines up exactly with the minima of the input resistance.

5.10, the input impedance and radiation efficiency in Figure 5.11, and a computational derivative of input impedance is plotted with radiation efficiency in Figure 5.12. It is clear in the overlay of reflection coefficient and radiation efficiency, Figure 5.10, that the dip in radiation efficiency does not occur at either of the operating frequencies. It is subsequently clear that the efficiency dip does not line up with any of the antenna input resonances (zero crossings of the reactance), Figure 5.11. The frequency differential of input impedance, Figure 5.12, was plotted to aid if the input resistance and reactance points of minimum slope (minima and maxima) or steepest slope have any bearing on low radiation efficiency. The real part zero crossing lines up in frequency with the radiation efficiency minimum, as shown in Figure 5.12. The zero-crossing is the local minimum in the real part of the input impedance.

With the loss tied to the minimum value in the real part of the input impedance, the radiation efficiency could be explained in terms of the ratio of radiation resistance (at a minimum) to loss resistance (fixed) becoming unfavorable. I will examine the currents

on the trap dipole at the resonances and the real input resistance minimum to investigate further.

The real input impedance and radiation efficiency minimum at 3.67 GHz is above the first dipole antiresonance (parallel resonance) at 2.56 GHz and below the trap created antenna second series resonance operating frequency at 3.84 GHz, which is in turn below the RLC resonance at 3.98 GHz, Figure 5.11. It has been reported that all antiresonances are due to the interaction of two neighboring modes, and series resonances are due to the excitation of a pure mode [73]. The parallel RLC trap's antiresonant frequency occurs at 3.98 GHz, above the trap-induced antenna series resonance at 3.84 GHz, and the trap induced antenna antiresonance at 3.93 GHz. The trap antiresonance frequency is not substantially lossy, nor are the nearby antenna series resonances and antiresonances. The radiation efficiency minimum at 3.67 GHz, while near a resonance, does not typically occur at a resonance. Fine-tuning the trap location over exact mesh edge location impacts the impedance match at the antenna second resonance (trap induced resonance).

The radiation efficiency minimum in Figure 5.11 is at the same frequency as an input resistance minima. An antenna's input resistance is a combination of radiation resistance and loss resistance, and dielectric and conductor loss is usually nearly constant across an antenna frequency band. Low radiation resistance can be explained in terms of the electrical size of the dipole antenna. For electrically small to half-wavelength dipoles, the radiation resistance increases with increasing dipole length. The first trap antenna resonance occurs 1.81 GHz, and the inductance of the trap loads both cancels some of the antenna capacitance to shift the unloaded antenna resonance from 1.9 GHz to 1.81 GHz and also improves the current distribution on the antenna, which is slightly undersized at 1.81 GHz and slightly improves radiation resistance by improving the current distribution. Below the upper resonance at 3.84 GHz, the radiating length is about λ full length with inductive loading. At the operating frequency, the radiator's effective electrical length changes to

about $\lambda/2$ between the j350Ω load discontinuities. Above the trap resonance, the radiating length is again about λ, but with capacitive loads.

In Section 5.5, I discuss trends as several different design variables for the trap dipole are changed, and all simulations confirm that the radiation efficiency minimum value is at the minimum real input impedance frequency.

5.4.2 Current Analysis

Figure 5.13 shows the currents on the trap dipole at all resonances and at the radiation efficiency minimum, which were also compared with FEKO and HFSS. The lower operating frequency (first series resonance) at 1.81 GHz is a first-mode excitation, in Figure 5.13. At the antiresonance at 2.56 GHz, the current distribution looks like a second-mode current distribution, which has a very high impedance at the center of the dipole due to being at a current minimum and voltage maximum. The dipole current distribution at the radiation efficiency minimum, 3.67 GHz, is a third-mode distribution, considered in length below. 3.84 GHz is the second resonance upper operating frequency and looks like a typical λ/2 mode between the traps, combined with a 3λ/2 mode over the whole antenna. The amount to which the third mode appears in the second series resonance current is a good indicator of the second series resonance efficiency.

An unloaded dipole has a first-mode resonance at 2 GHz and third-mode resonance at 5.6 GHz. On an unloaded dipole, the third mode is resonant or near-resonant when the dipole is around 3λ/2 and has better than 98% radiation efficiency. The dipole first-mode resonance is typically only slightly compressed with a trap and is still near 2 GHz. Radiation resistance on electrically small wire antennas is tied to the size of the radiator. The shorter the wire, the smaller the radiation resistance is, which causes worse radiation efficiency. With a trap on the dipole, the radiation efficiency dip is at a third-mode current

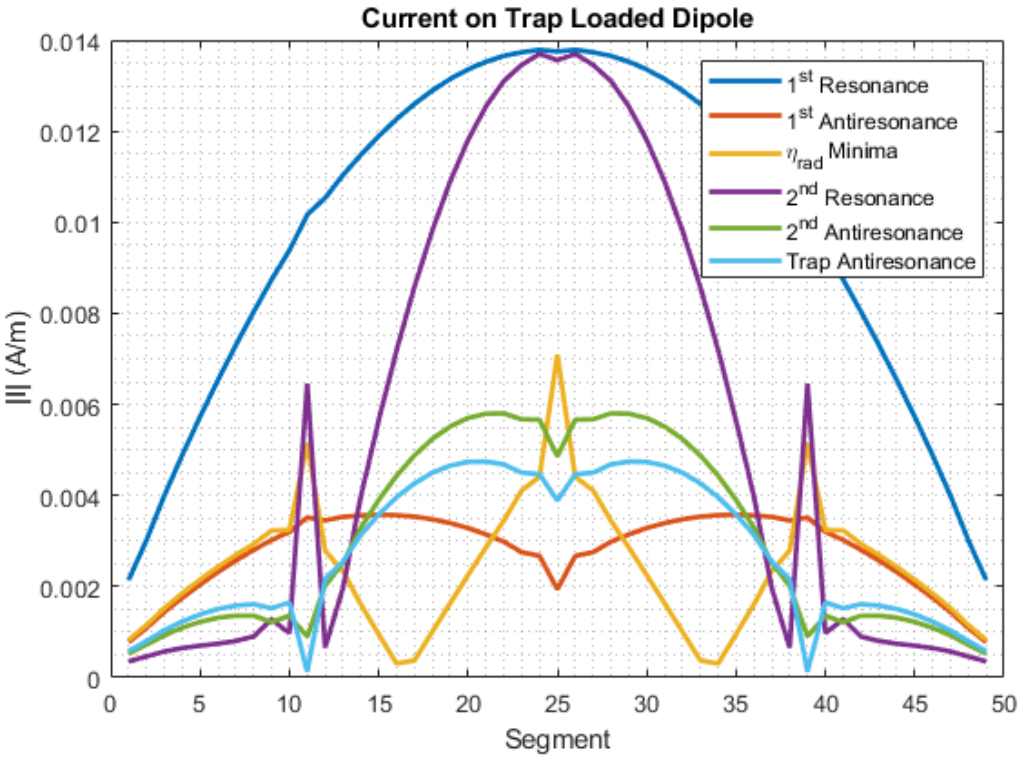


Figure 5.13: Matlab calculated currents at resonances and η_{rad} minima. First-mode current distribution at first resonance, second-mode at first antiresonance, third-mode at η_{rad} minimum, first-mode over inner dimensions of dipole at second resonance.

at 3.6 GHz, when the dipole is less than λ in size. On an unloaded dipole, the dipole is $3\lambda/2$ size at the third-mode resonance and has very high efficiency. Since the mode is compressed, the radiation resistance decreases, and R_{loss} stays nearly constant, so radiation efficiency decreases. The first mode's radiation efficiency degrades slowly as the electrical length is compressed, but there is little discussion in the literature about compressing higher-order modes [74]. The third-mode currents occur at significantly smaller electrical sizes than the optimal $3\lambda/2$ size of the unloaded dipole at third-mode operation. The compressed third mode has poor radiation efficiency, low real input impedance, and is loaded (tuned lower in frequency) to a much greater extent than the first resonance and antiresonance.

The third mode is highly compressed by the trap inductance, especially when the trap resonance is tuned closer towards the fundamental resonance. The third mode also creates a current maximum at the load locations by definition, enabling heavier loading effects on the third mode than on the first mode. The load impact and current distribution is illustrated in Figure 5.14. With electrically small inductor loaded dipoles, the efficiency worsens as the loads are moved toward the center because the loads will keep tuning the antenna lower in frequency, making the antenna electrically smaller. Furthermore, the load's resistive loss will increase when the load is closer to the feed, where there is a current maximum. I have found that while moving the trap loads towards the dipole ends and tuning the loads to match the approximate half-wavelength frequency, the minimum efficiency value decreases as the loads move outwards. On the surface, this seems counter to the inductor loaded dipole trend since the directions of low efficiency are reversed. However, in both instances, the radiation efficiency decreases as the reactively loaded radiator becomes electrically smaller. Placing the load in the first-mode current max increases load resistive loss and increases load impact, but placing the load at the third-mode current max also increases loading and loss. The max location just happens to be different between the first and third

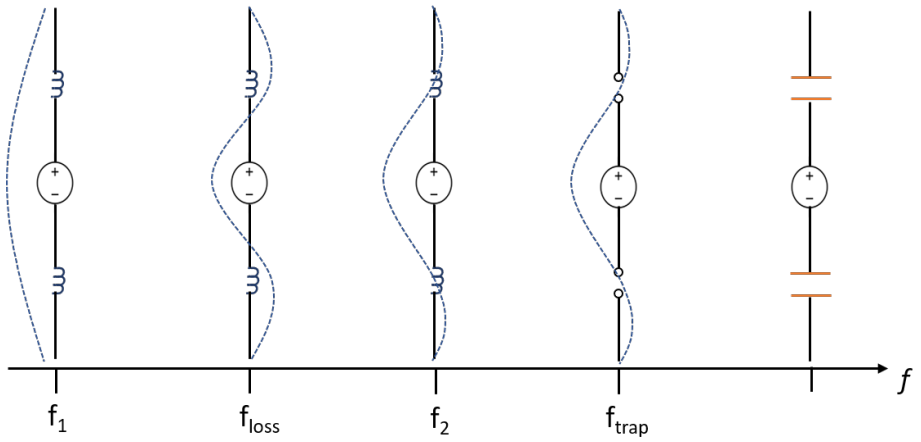


Figure 5.14: Trap dipole at key frequencies, approximate current distribution as blue dashed line, based on Figure 5.13

modes.

There are several significant findings based on the current distributions at frequencies of interest. There will be a radiation efficiency null somewhere near the trap resonance. The trap dipole antenna second resonance is not at the frequency of the RLC antiresonance. At the second resonance, the trap loads have a surprisingly low magnitude reactance (j350Ω) rather than an actual open circuit. The second series resonance behavior will be replicated with an inductively loaded dipole. There is usually a current maxima at the trap loads and current on the outside of the traps at the operating frequency. There is current on the other side of the traps, even for lossless (infinite Q) traps.

The traps are located at segments 12 and 39, which both have a relative maxima in the current magnitude at the antenna resonance rather than a trend toward zero, indicating an open circuit boundary condition. The current on the outer lengths of the dipole beyond the traps is also nonzero. The relative maxima at the traps in Figure 5.13 is about 1/6 the magnitude of the current at the feed.

5.4.3 Inductively Loaded Dipole

If the radiation efficiency minimum is due to a compressed third mode instead of just trap resonator loss, the modal behavior should also be attainable with just an inductive load. Likewise, if the trap dipole upper resonance depends on a reactive open from the trap rather than an actual open, an inductor load should replicate the upper resonance response. Both of those scenarios are simulated below. While inductor loaded dipoles and monopoles are common in the literature, they are typically electrically small, while both of these scenarios are with dipoles that are more than half a wavelength long.

At the frequency of the radiation efficiency minima of the example trap loaded dipole, the trap load has a reactance of 160 Ω. At 3.68 GHz, the reactance corresponds to an inductance of 6.92 nH. I am interested in whether the same third mode can be replicated with low efficiency on an inductor loaded dipole rather than a resonator loaded dipole. To test this, I loaded a dipole with a 6.92 nH inductor to lower the frequency of the resonances. The current distribution at the first resonance is a first-mode distribution, and is a third-mode distribution at the radiation efficiency minimum frequency, Figure 5.15. The reflection and input impedance are also shown in Figures 5.16 and 5.17.

The radiation efficiency minimum occurs with the characteristic third-mode distribution. The second series resonance resembles that of the trap loaded dipole, with a combination of the first- and third-mode current distributions. With a series 0.2 Ω resistor (the resonator had a parallel resistor), the radiation efficiency dips to 88%. 0.2 Ω was chosen as a typical value for discrete inductors rated for RF frequencies. With no added resistor, the impedance behavior changes little, and the efficiency dips at the same frequencies, but only to 96%. Later, with trap loaded slots, conductor and dielectric loss increases, and lossless trap designs can still have radiation efficiency dip to 40%.

The second operating frequency of the trap dipole is at 3.84 GHz. At 3.84 GHz, the

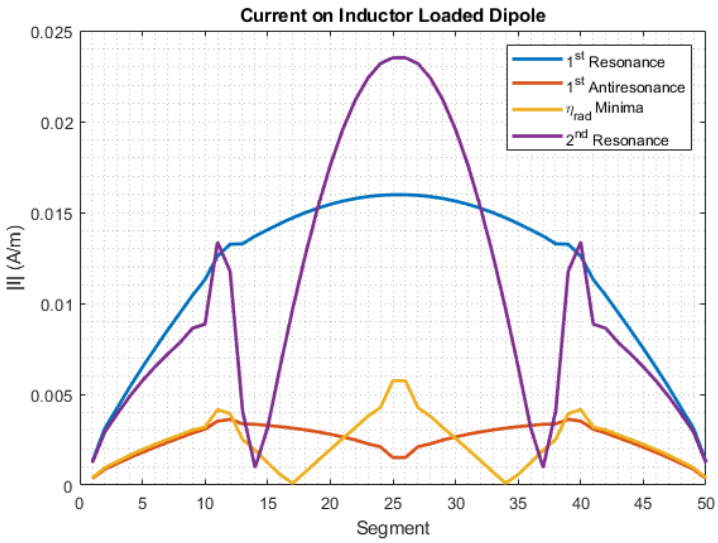


Figure 5.15: Current on inductor loaded dipole. The inductor loads are tuned to have the same reactance value as the parallel LC traps at the minimum η_{rad} frequency. current distribution at the first resonance is first-mode, second-mode at at first antiresonance, and third-mode at η_{rad} minima. The second resonance in this case has a greater excitation on the outer length

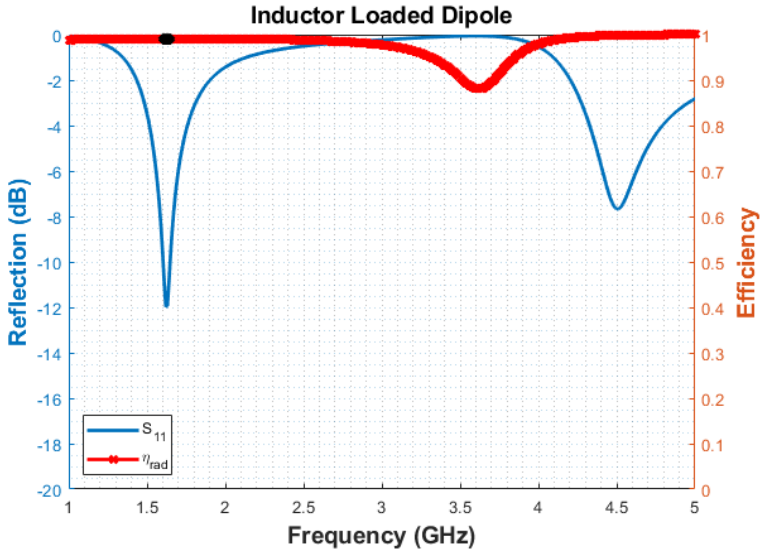


Figure 5.16: Reflection coefficient of inductor loaded dipole, replicating trap dipole radiation efficiency minima

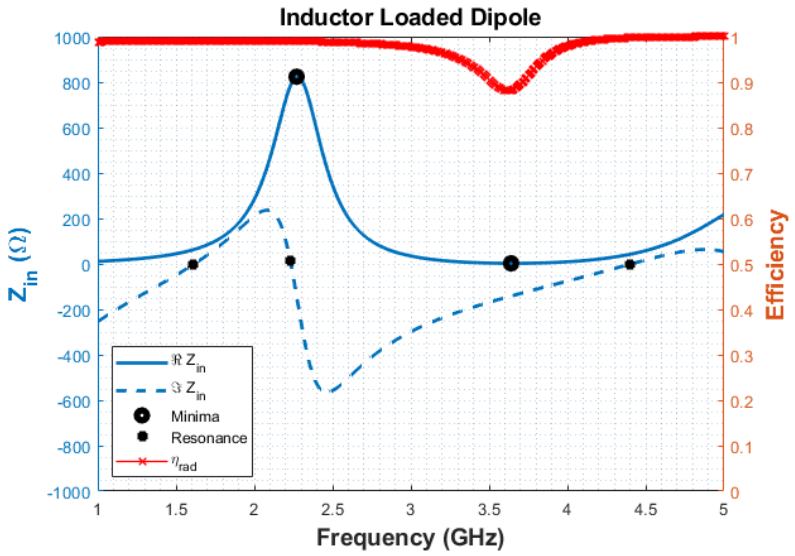


Figure 5.17: Input impedance of inductor loaded dipole, replicating trap dipole radiation efficiency minima

RLC resonator has a reactance of 351.7 jΩ, which can be replicated with a 14.6 nH inductor. The unloaded dipole has a reactance of -258 jΩ at 3.84 GHz, which is canceled by the 351.7 jΩ loads located ±21.9 mm on either side of the center feed. The first series resonance is tuned lower than in the trap dipole, down to 1.41 GHz, due to the increased inductance, Figure 5.20. A radiation efficiency minimum occurs at 2.72 GHz. The upper passband is shown in Figure 5.19, and the currents are shown in Figure 5.18 with the same modes are prevalent as on the trap loaded dipole. At 3.84 GHz, an inductor resistor load recreates the impedance match and current distribution of the trap load. Typically, inductor loads are used only for tuning the first-mode of wire radiators.

The inductor loaded models prove that the trap loaded dipole experiences a strongly reactive discontinuity from the trap loads at second resonance rather than an actual open circuit condition. There is also a significant reactance at the radiation efficiency minima. The general principle that trap dipoles are designed by creating an open circuit still yields approximately correct designs, subject to fine-tuning. However, this new understanding

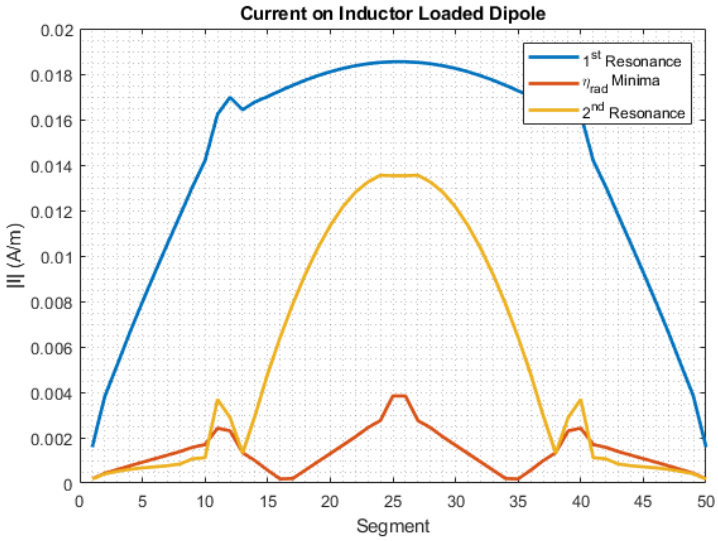


Figure 5.18: Current on inductor loaded dipole. The inductors are tuned to have the same reactance as the parallel LC traps at the frequency of the second series resonance, which is a first-mode current distribution between the loads

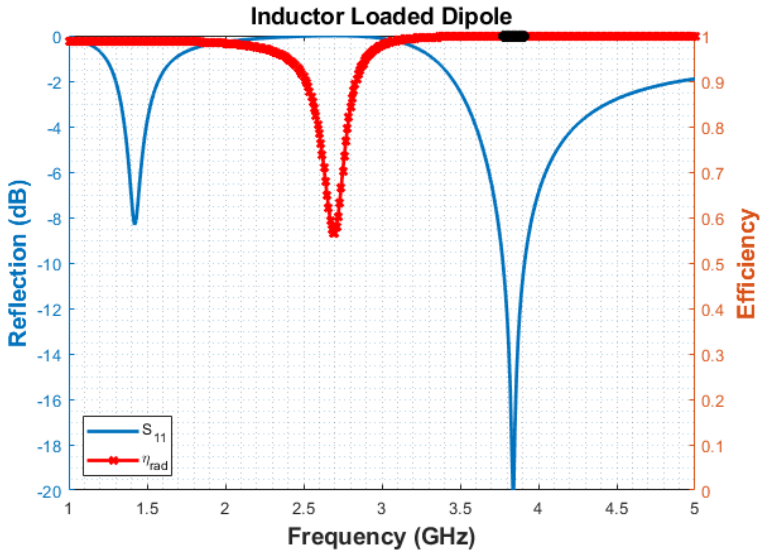


Figure 5.19: Reflection coefficient of inductor loaded dipole, replicating trap dipole second series resonance

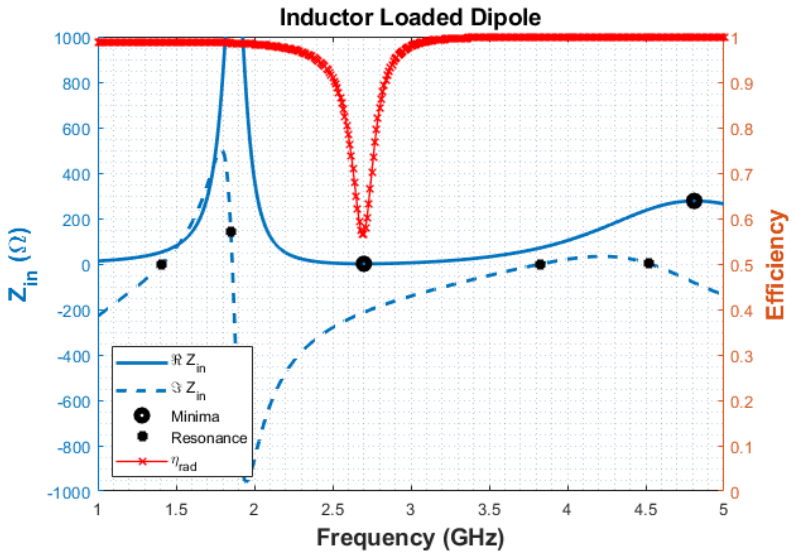


Figure 5.20: Input impedance of inductor loaded dipole, replicating trap dipole second series resonance

allows for more precise designs. Regular dipoles are resonant at slightly less than half a wavelength in size, usually at about 0.475λ, depending on width. Empirically it appears that 0.52λ is a better starting rule of thumb for trap load placement.

5.4.4 Current past the loads and ratios

There seems to be a trend that when comparing the dipole current distributions at radiation efficiency minima, second resonance, and trap antiresonance, the ratio of current at the loads to at the feed is a predictor of the radiation efficiency. When the current magnitude is much greater at the feed than at the loads, the radiation efficiency is better. If the resistive trap loss were the primary loss mechanism in trap dipoles, I would expect that the feed to trap current ratio would be a good indicator of overall antenna loss. However, this does not hold when comparing load current and trap current continuously across frequency, Figure 5.21. There are typically frequency bands where the magnitude of current at the traps is greater than at the feed, yet the radiation efficiency is still above 98%.

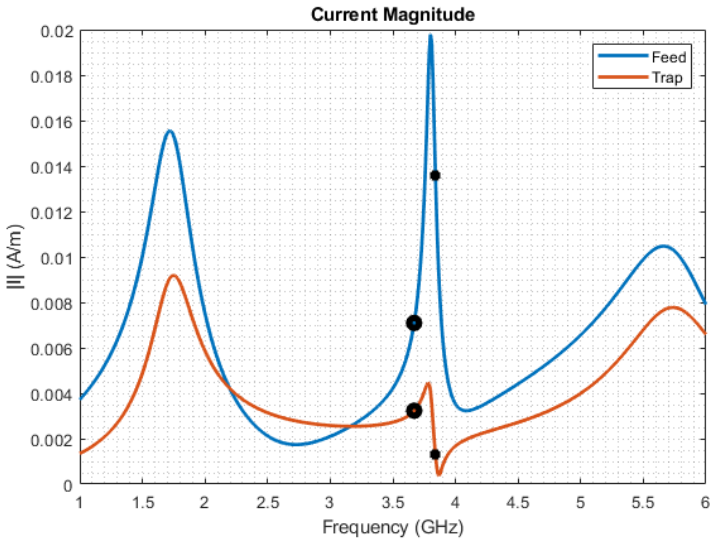


Figure 5.21: Load and feed current magnitude across frequency, 4 GHz trap

Current distribution on the trap dipole typically looks like a combination of $\lambda/2$ and $3\lambda/2$ modes. The clearest indicator is that the lowest radiation efficiency occurs at the same frequency as the minima of the real input impedance. Also, the efficiency decreases as loads tuned and moved outwards, which is counter to the suggestion that traps follow the principles of inductively loaded monopoles. The electrical length of the distance between the loads varies from 0.56λ with the 3GHz load to 0.59λ with the 5 GHz load.

This behavior could be better calculated using a characteristic impedance representing the wire as a transmission line for computation of the input impedance into the trap followed by a transmission line open circuit.

5.4.5 Loss Conclusions

Trap dipoles do have significant loss near the trap-related operating frequency, but the loss does not overlap with most designs' actual operating band. The loss is due to a higher-order mode being excited in a compressed state with low radiation resistance that compares unfavorably with a virtually static loss resistance. Decreasing the resonator loss will improve

the overall antenna loss, but the compressed higher-order mode will still have a radiation efficiency dip even with a lossless trap. This dip can be especially significant if there is dielectric on the antenna, as demonstrated with slot antennas in the next chapter.

While trap dipoles with a single pair of loads usually have high radiation efficiency, adding multiple pairs of loads, or having distributed loading can result in a lossy operating frequency. It is important to check for lossy modes in general resonator loaded antenna design.

The solution accuracy agrees well with FEKO and HFSS. In the next section, I analyze several variations on the ideal trap dipole design to document the precise relationship between input impedance and possible lossy frequencies.

5.5 Parametric Investigations

As previously stated, the existence of a lossy compressed higher-order mode is supported by trends consistent across several parametric sweeps and alternate trap designs. The parametric sweep analysis is presented more fully in this section. The most basic parameter sweep is changing the load locations. Load locations can be changed slightly to fine-tune the design or move across the dipole's entire length to change the dipole behavior drastically.

Changing the L to C ratio changes the Q and characteristic impedance of the resonator. The Q of a parallel RLC circuit is

$$Q = R\sqrt{\frac{C}{L}}, \tag{5.3}$$

and characteristic impedance of the resonator is

$$Z_c = \sqrt{\frac{L}{C}}. \tag{5.4}$$

The parallel RLC is inductive below the RLC resonance. The trap inductance will load any antenna resonances below the RLC resonance, causing the antenna resonances to be tuned lower in frequency. Perhaps the most significant aspect of changing the L/C ratio is that it will alter how much reactive loading occurs at antenna resonances below the RLC resonance.

The tolerance of discrete RF inductors and capacitors will change the Q and resonance of the traps. The detuning due to tolerance can also result in different load values on each dipole arm, which is investigated.

Moving the feed location on an unloaded dipole alters the impedance magnitude at the fundamental resonance and changes the resonant frequency and impedance magnitude of subsequent resonances. Moving the feed off-center is investigated with trap loads. Even with the increasingly complicated impedance response across frequency, the radiation efficiency minima still lines up with the real input impedance minima.

5.5.1 Load Placement

Changing the load location has a very significant impact on the response of a loaded dipole. Load location can be varied from the traditional trap dipole design by moving the loads symmetrically or asymmetrically. The loads can have fixed component values, or the components can be varied with load location to maintain dual-band trap dipole behavior. Additionally, more than two loads could be added to the radiator, or the feed could be offset from the center and only a single load added to the antenna. I am primarily focused on moving the loads symmetrically, with both fixed and tuned component values.

Load Placement Fine Tuning

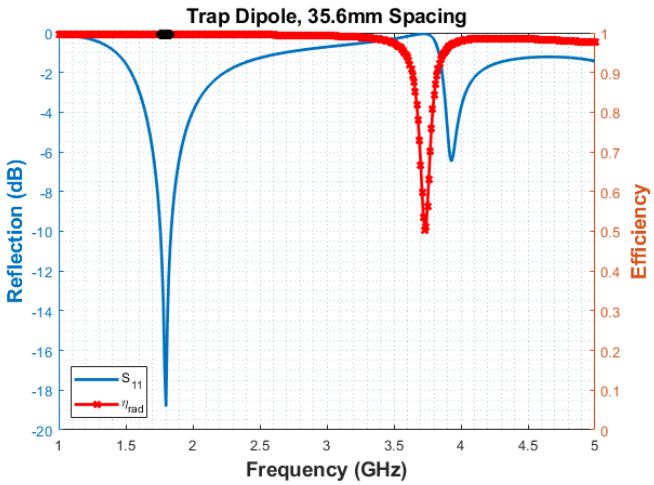


Figure 5.22: Trap load spacing is 0.475λ at 4 GHz trap resonant frequency, unoptimized, only a -6.5 dB match at 3.93 GHz

Fine-tuning the load locations can improve the impedance match of the operating frequencies for a given load. An unloaded dipole is slightly less than half a wavelength at the fundamental resonance, typically about 0.475 λ. Following this principle, the loads on a trap dipole are resonant at a frequency f_{LC} and are spaced 0.475λ apart at f_{LC}. However, the trap dipole second resonance has been proven in this chapter to be at a different frequency than f_{LC}. For instance, a 75 mm dipole with loads tuned to 4 GHz would initially be designed with a load spacing of 35.6 mm. With that spacing, the second operating frequency only has a match of -6.5 dB at 3.93 GHz, Figure 5.22. The input reactance never goes through a true resonance around this frequency (-j33Ω at 3.93 GHz), Figure 5.23. The typical dipole design method and approximation of trap loads as open circuits get close to a working design, but the match needs further optimization, and the actual frequency is subject to further change.

The actual spacing between the loads is not optimal because the trap related operating frequency is at a different frequency than the load resonance, and the loads are inductive at the operating frequency. A simple sweep of load location was performed, and a 75 mm

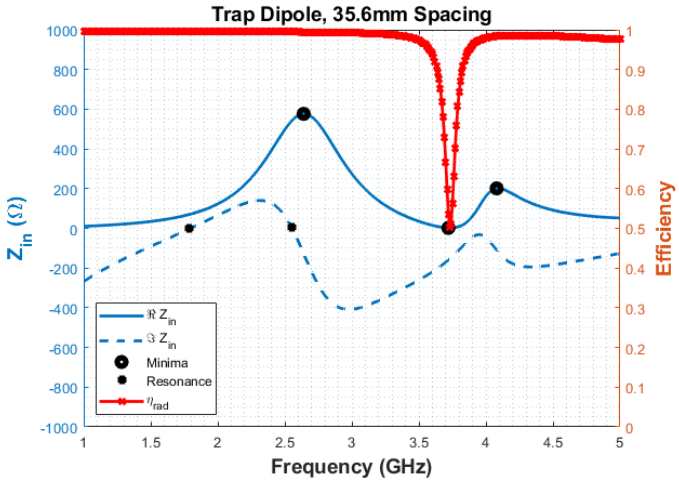


Figure 5.23: Trap load spacing is 0.475λ at 4 GHz trap resonant frequency, unoptimized, no resonance in input reactance at second operating frequency band

f_{res}	$\eta_{rad,min}$	Match	Spacing (mm)	Spacing (λ)
4.74 GHz	89%	-12.6 dB	37.5	0.59
4.29 GHz	78%	-16.0 dB	40.6	0.58
3.84 GHz	61%	-19.8 dB	43.8	0.56
3.37 GHz	38%	-14.1 dB	50.0	0.56
2.91 GHz	18%	-13.6 dB	56.3	0.54

Table 5.1: Minimum efficiency values as second resonance of trap dipoles changes

dipole with a load spacing of 43.8 mm has the best match (for a mesh resolution of about 1.5 mm) at the upper operating frequency. The match significantly improves to -19.2 dB, and the resonant frequency and match frequency drops further to 3.84 GHz, Figures 5.24-5.25. The load spacing is 0.56λ at 3.84 GHz. The load spacing was increased by 8.2 mm from the starting design.

Matching Load Placement and Resonance Tuning

A range of load tunings from about 3 to 5 GHz was simulated, and the best spacing between the loads in terms of impedance match was found for all of them. The results are summarized in Table 5.1.

Figures 5.26 and 5.27 show a 5 GHz load and 3 GHz load. The locations are optimized

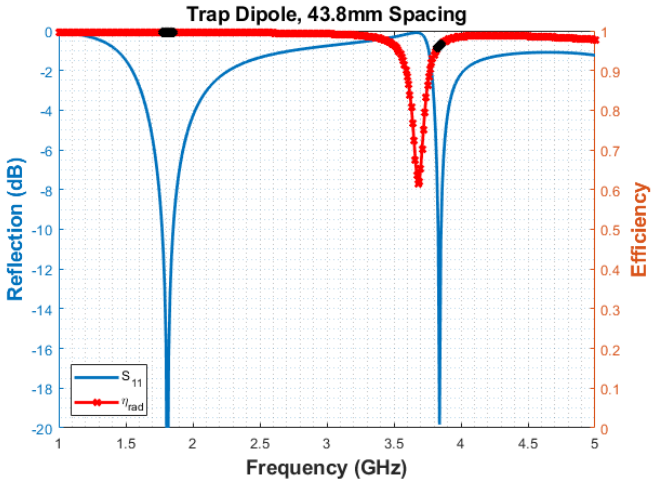


Figure 5.24: Load spacing optimized, 0.56λ at 3.84 GHz resonance, -19.2 dB match

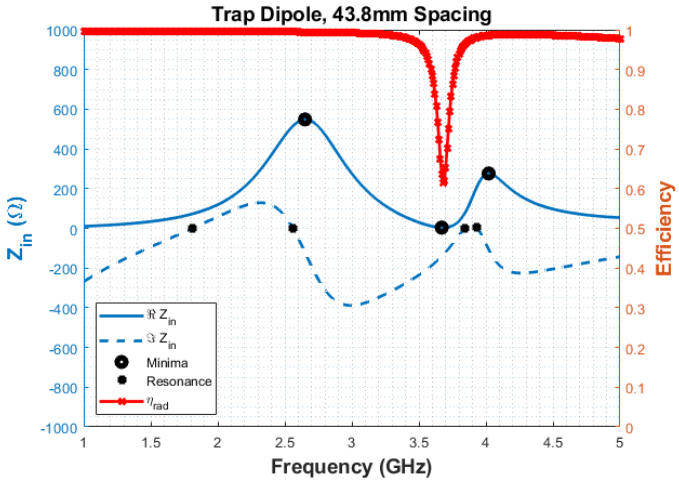


Figure 5.25: Load spacing optimized, 0.56λ load spacing at 3.84 GHz resonance

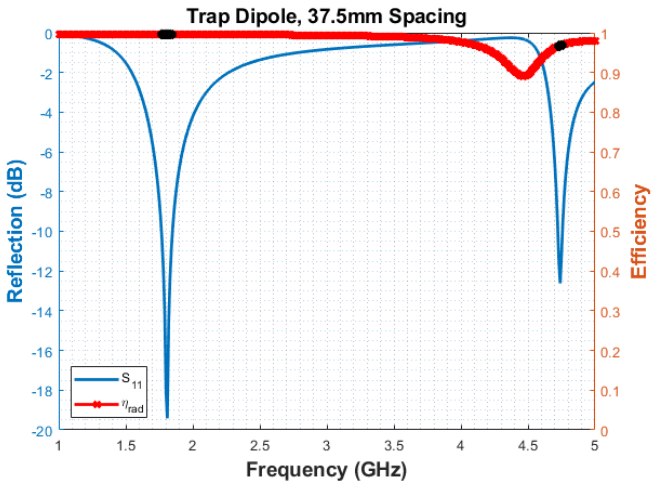


Figure 5.26: Inner load location, 4.74 GHz trap related resonance, minimal radiation efficiency dip

for the best match. The dip in radiation efficiency does not overlap with the operating frequencies. The efficiency is always over 95% at the matched operating frequencies. However, the actual radiation efficiency minimum decreases as the tuned loads move outwards.

The minimum value of the radiation efficiency decreases as the tuned loads are moved towards the antenna's ends. As detailed in the earlier section on loss, tuning the trap lower results in greater compression of the third mode that corresponds to low input resistance and radiation efficiency. Figure 5.28 summarizes the results.

Moving the loads inwards on the dipole while retuning them increases the frequency separation between the real input impedance minima and the second resonance, Figure 5.28. The second resonance frequency increases as the loads move inward. Also, the efficiency decreases as the loads are tuned and moved outwards, which is counter to the suggestion that traps follow the principles of inductively loaded monopoles. The electrical length of the distance between the loads varies from 0.56λ with the 3 GHz load to 0.59λ with the 5 GHz load.

Fixed Load, Variable Location

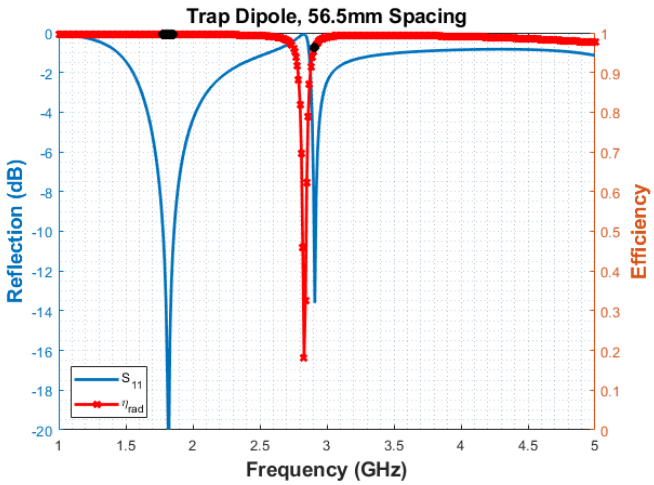


Figure 5.27: Outer load location, 2.91 GHz trap related resonance, greater dip in radiation efficiency as trap loads tuned lower and moved outwards on dipole

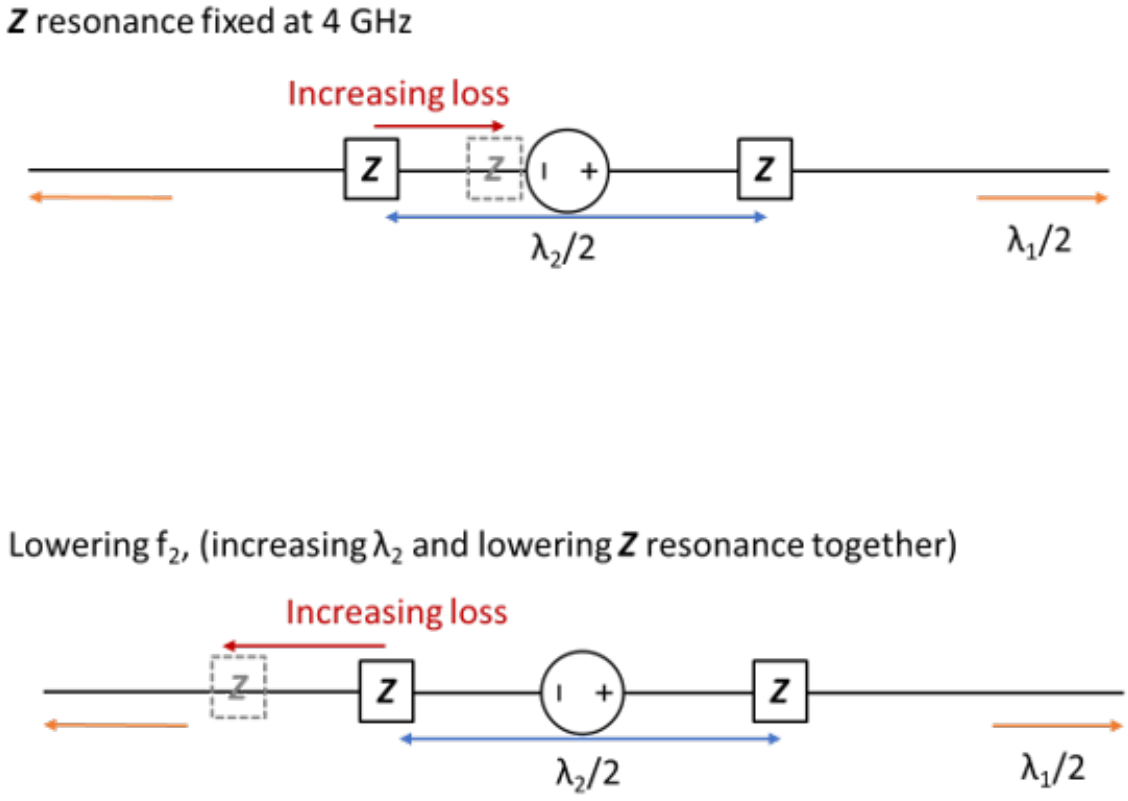


Figure 5.28: Tuning f_2 closer to f_1 increases the amount of loss at the input resistance minima because it also tune the $3\lambda/2$ mode lowerin frequency. With a fixed RLC tuning, moving the load inwards on the dipole increases the amount of loss at input resistance minima.

If a trap load with static tuning is placed closer to the dipole center, the minimum radiation efficiency value will move closer to 0%. If the load value is fixed, the resonance frequency will not move very much even as the load placement changes, Figure 5.28. Since the load is antiresonant, it provides infinite inductance below resonance and infinite capacitance above resonance. If the load would cause the antiresonance to resonate at shorter than half a wavelength, the load provides reactance to cancel out the dipole reactance. When the trap is placed nearer to the center of the dipole, it loads more effectively. This should mean that a portion of the trap impedance curve with a less steep slope will provide reactive cancellation for resonance, ultimately making the match more broadband. Similarly, if the trap is closer to its optimal location for a half-wavelength resonance, less reactance is needed to create resonance, and the match might be more broadband.

A trap dipole is designed for S-band. The dipole's outer length is about half a wavelength at 2 GHz, or d_1 = 64.5 mm. An RLC boundary in HFSS was used to model a lumped element parallel LC circuit. The RLC boundary is also a simplified model of real resonant loading structures and loss. The RLC boundaries are spaced to create an inner dipole length of about half a wavelength at 4 GHz, or d_2 = 32.5 mm. Capacitance was simulated at 6.2 pF and 1.6 pF, while induction is constant at 1 nH, resulting in resonance at 2 GHz and 4 GHz. Going forward, this design will be labeled as the "middle load" design.

Additionally, two other load placements were simulated for comparison to investigate how significant load location is in incurring loss. The "outer load" will be nearly at the dipole ends, 0.5 mm from each end. The "inner load" is closer to the feed, with d_2=16.5 mm. The dipole is center-fed with a lumped port. Every combination of location, capacitance, and resistance values was simulated in HFSS, with convergence on imaginary impedance and radiation efficiency.

A typical capacitor insulation resistance is 10^4 MΩ, modeled in parallel with the capacitor. The inductor loss is usually more significant, and a series 2 mΩ resistor is a reasonable

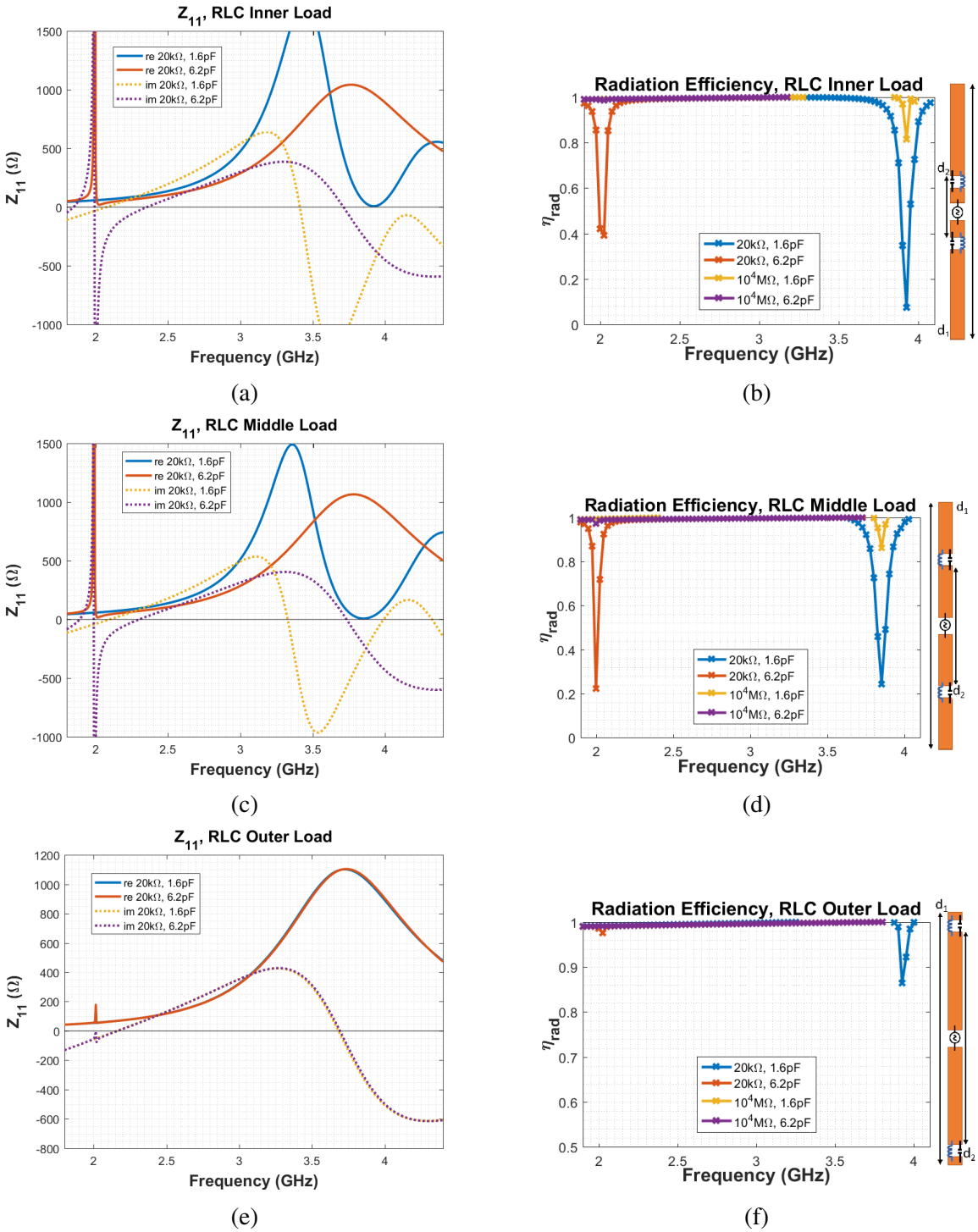


Figure 5.29: Impact of load placement and loss value R on input impedance and radiation efficiency, “Middle Load” is a conventional dual-band trap dipole design

low loss value. Since the trap circuit is parallel LC, it would simplify simulations to have a single parallel R value that maintained the same Q value. Compared to the parallel inductor loss, the capacitor loss is negligible. A series LC circuit resonant at 4 GHz with 2 mΩ loss resistor would have an associated Q value of 12,000. Coincidentally, our reconfigurable load cavities have a simulated Q value of about 11,000. For simplicity, letting the equivalent parallel loss resistance be 20 kΩ is a good approximation for both a realistic discrete component trap circuit and the load cavities. I also include simulation data with R=10^4 MΩ to examine just the impact of capacitor loss.

The "middle" and "inner" load placements show a similar tuning range to each other, as shown in Figures 5.29a and 5.29c, and similar radiation efficiency. Radiation efficiency for the 20 kΩ inner load circuits dips to 39% and 7% for the 2 and 4 GHz circuits, respectively, as shown in Figure 5.29d. Radiation efficiency for the 20 kΩ middle load circuits dips to 22% and 14% for the 2 and 4 GHz circuits, respectively, as shown in Figure 5.29d. The radiation efficiency for R=10^4MΩ remains over 82% for all variations, although a smaller frequency step could reveal a deeper null in the efficiency. The "outer load" introduces less loss than the inner and middle load placements. Figure 5.29f shows 86% radiation efficiency at 4 GHz with the 4 GHz resonant circuit and 98% efficiency at 2 GHz with the 2 GHz circuit. The "outer load" placement is more appropriate for the 2 GHz circuit but introduces higher loss with the 4 GHz trap circuit. The 4 GHz circuit likely redefines the boundary conditions to excite a higher-order mode on the antenna. This interpretation is substantiated by a resonance seen in the impedance in Figure 5.29e.

Figure 5.29 shows that the dipole resonance can be reconfigured with varying capacitance when the load is near the feed point or the midpoint of each dipole arm but does not reconfigure for the same reactance values when placed at the end of the dipole. However, the radiation efficiency drops drastically at any load resonance unless placed at the dipole ends. This reinforces the literature findings that end-loading requires higher reactance val-

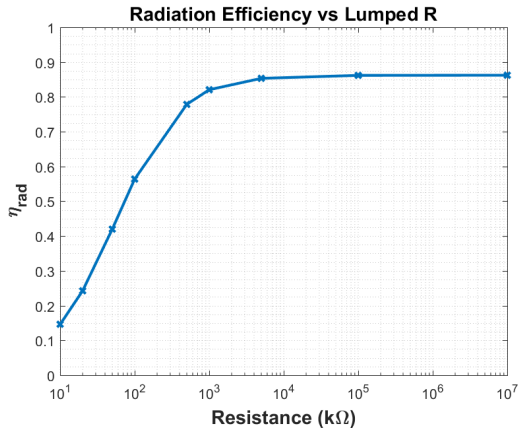


Figure 5.30: Minimum radiation efficiency of trap dipole over a range of parallel resistance values

ues and highlights even further that trap dipoles have significant loss.

To further highlight the impact of the load loss resistance, a simulation of equivalent load resistance versus radiation efficiency at the trap resonance is shown in Figure 5.30, using the "middle load" design. The radiation efficiency ranges from 15% to 86% over a wide range of R values. For any practical R value, there will be non-negligible loss near the load resonance.

To summarize, RLC loads on a dipole result in significant loss near resonance for any practical R value.

5.5.2 Resonator Q

Next, I consider the impact of the resonator Q value on loaded dipoles. I expect that higher Q loads will result in less antenna loss The Q of a parallel RLC resonator is defined by both the resistance and the ratio of capacitance to inductance, or

$$Q = R\sqrt{\frac{C}{L}}. \tag{5.5}$$

Increasing the load parallel R value causes the trap to have higher Q, and increasing

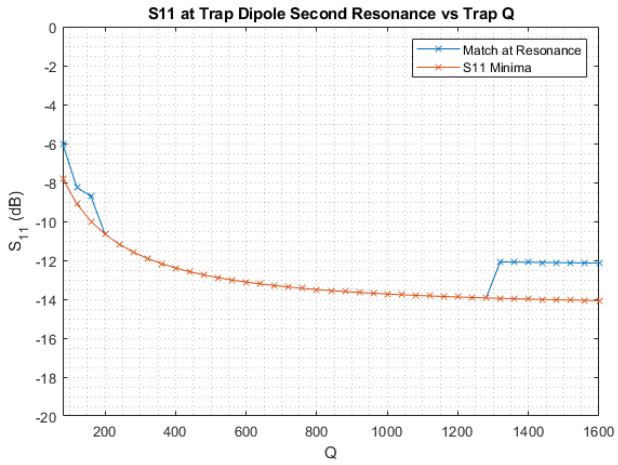


Figure 5.31: Second operating frequency (second series resonance) S_{11} match vs trap Q, sweeping R, calculated with the hybrid MatLab MoM approach. Trap Q over 400 has negligible impact on impedance match.

the capacitance to inductance ratio (while keeping resonant frequency constant) also increases load Q. The MatLab MoM solutions variable Q have noticeable resolution artifacts from frequency and mesh resolution limits. Trends in efficiency, match, and impedance are discernible, but the trends have oscillatory behaviors. I simulated the same Q sweeps in HFSS, which applies adaptive meshing to its solutions and is simulated with a finer frequency resolution. The trap dipoles used in both are nearly identical, as was shown in Figure 5.7.

I am interested in whether a particular trap Q value improves the impedance match (by changing input resistance and resonance), and whether higher trap Q corresponds to better radiation efficiency at the antenna resonance.

In the MatLab calculations higher Q trends towards a better (73Ω) match, Figure 5.31, but in HFSS a higher Q trends towards a slightly worse match, Figure 5.32. The actual match values disagree significantly between MatLab and HFSS, which is likely due to a coarse frequency resolution in MatLab. Both trends are slight, and the change in match is fairly constant above 800 Q. Trap Q does not appear to have a significant effect on the

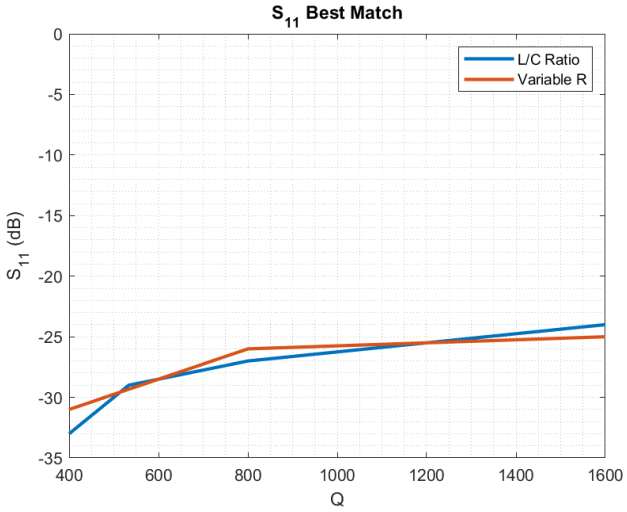


Figure 5.32: Second operating frequency (second series resonance) S_{11} match vs trap Q, sweeping R and C/L separately, simulated in HFSS. Trap Q has negligible impact on impedance match.

antenna impedance match for a practical range of trap Q values.

The input resistance at resonance does not change significantly with trap Q in HFSS, but it decreases in the MatLab MoM calculation, Figures 5.33 and 5.34. These results are just an alternate way of viewing the match at resonance trends of Figures 5.31 and 5.32. The only new insight gained here is that MatLab calculates the low Q trap antennas to have a higher than 73 Ω efficiency, and the HFSS simulation calculates the antenna to have a lower than than 73 Ω resistance at resonance.

Decreasing the trap Q by decreasing the trap parallel resistance slowly decreases the antenna radiation efficiency, Figure 5.35, as expected. In HFSS I recorded both the minimum radiation efficiency value, as well as the efficiency at the antenna resonance, Figure 5.37. A dipole with lower Q trap has a lower minimum radiation efficiency, Figure 5.37. However, the efficiency at resonance remains very high for a practical range of trap Q values. If the Q is changed by varying the L/C ratio, the efficiency at resonance stays constant, and if the R value is lowered the efficiency at resonance decreases slightly. As Q decreases, the fre-

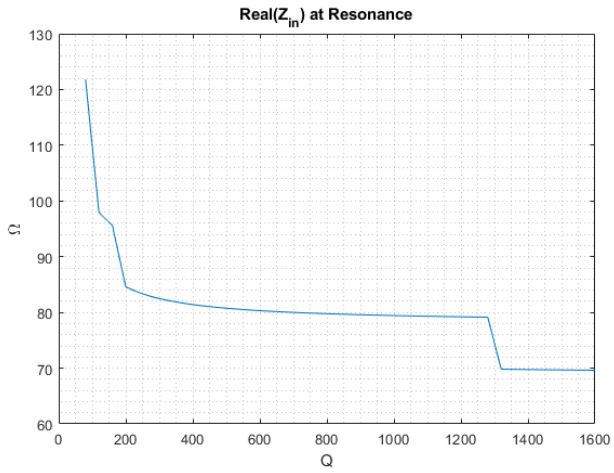


Figure 5.33: Input resistance at second series resonance vs trap Q, with Q based on variable R, calculated in MatLab.

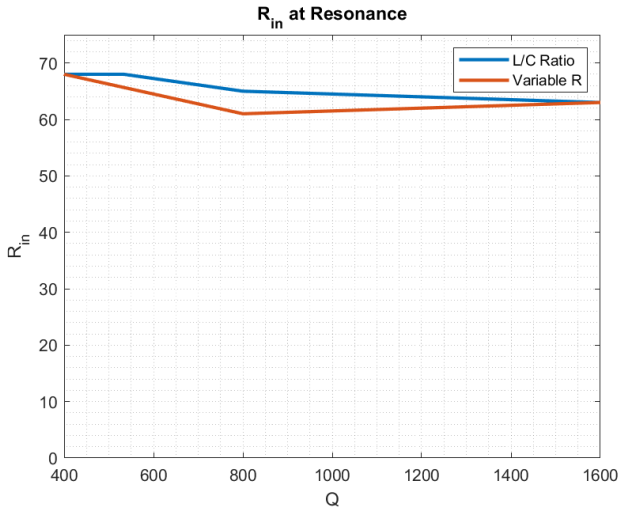


Figure 5.34: Input resistance at second series resonance vs Q, with Q based on variable R and on variable L/C ratio, calculated in HFSS.

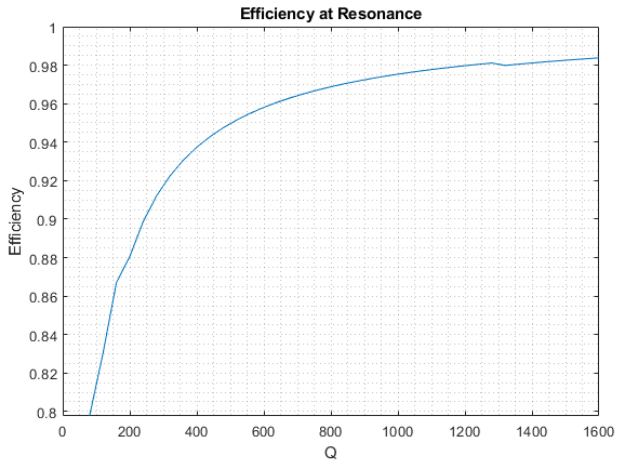


Figure 5.35: Corresponding to Figure 5.33, the radiation efficiency at resonance vs Q, with Q based on a varying R value, calculated in MatLab. The antenna has better than 80% η_{rad} at resonance for all Q values.

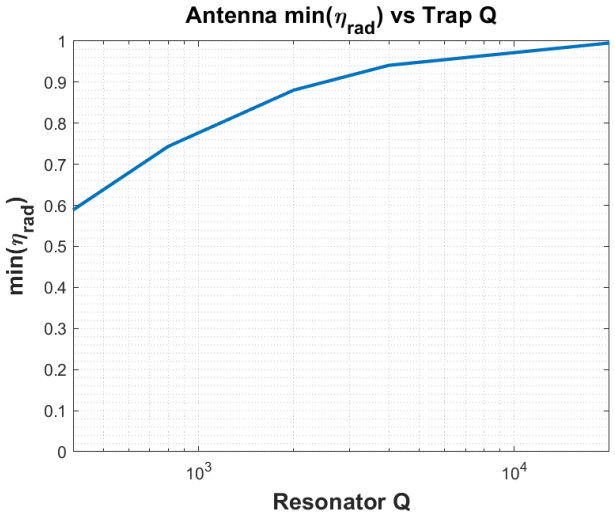


Figure 5.36: Minimum radiation efficiency of trap dipole over a range of trap Q values based on variable trap loss resistance, based on Figure 5.30

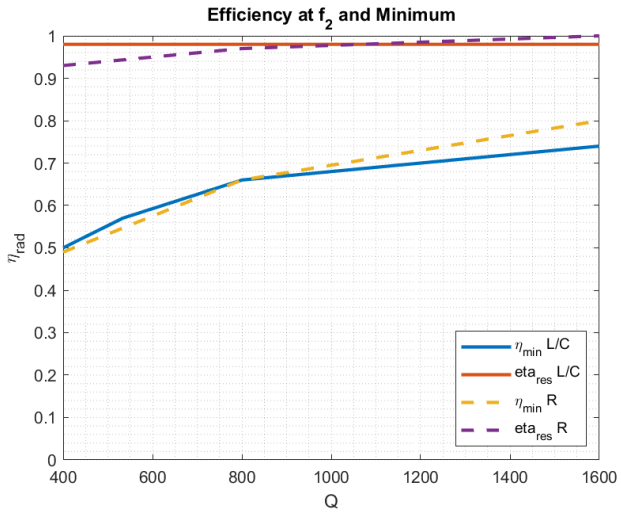


Figure 5.37: Radiation efficiency at antenna resonance over a range of trap Q, based on variable R and on variable L/C ratio, simulated in HFSS. The antenna has better than 92% η_{rad} at resonance across all Q values.

quency separation increases between real impedance minima and second resonance, which moves the deeper dip in radiation efficiency further away from the second series resonance. The overall result is that the second resonance operating frequency has high efficiency for a wide range of practical Q values.

Increasing the ratio of L/C lowers the frequency of f_2. Increasing the ratio of L/C increases the positive reactance of the resonator at a given frequency (below the trap resonance). This trend is seen in Figure 4-24 in [75], although the trace was not commented on and was not included in the accompanying paper [58].

With varying Q values and standard trap dipole design, the loss does not overlap with match frequencies. Across all of the R and L/C variations, the efficiency at resonance was over 80%. The Q of the trap does not significantly impact either the efficiency or the impedance match of the antenna at resonance.

5.5.3 Inductor and Capacitor Tolerance

In practice, small deviations in load values will occur. For trap dipoles with lumped component loads, it is not uncommon for components to have a 5% tolerance. For antennas with reconfigurable loads, deviations in the tuning process or drift from the loading mechanism will cause the loads to deviate from their ideal values. Past simulations show that asymmetric antennas often produce more complex responses (a greater number of resonances) than perfectly symmetric ones. With each trap related resonance, there seems to be a nearby dip in radiation efficiency. Increasing the number of trap related resonances in close proximity (due to asymmetry) may likely increase the odds that a resonant, possibly matched frequency is also the site of a dip in radiation efficiency. It is necessary to verify that loss frequencies do not overlap with operating frequencies. It is also more computationally efficient to solve (or measure) only reflection and not radiation efficiency or realized gain. If possible, determining loss frequencies from just reflection would simplify both simulation and measurement.

A given inductor and capacitor have stated tolerances of 0.95 - 1.05 nH and 1.55 - 1.65 pF. Working with only the extreme values, a simple trap dipole could be loaded with four different loads, and any combination of two loads (including repeats) could end up on the antenna. If both the inductor and capacitor are at their lowest probable value (0.95 nH and 1.55 pF), then the trap load has a slightly higher resonant frequency. If one component is high and the other is low, then the trap load will remain at approximately the same resonant frequency but with a different characteristic impedance and bandwidth. If both components are high, then the load will have a lower resonant frequency. A shift in the trap's resonant frequency paired with no change in trap location will detract from the impedance match at the upper operating frequency.

From the data, the trap related radiation efficiency is lower in frequency than the an-

Case	C_1 (pf)	L_1 (nH)	C_2 (pF)	L_2 (nH)
1	1.6	1	1.6	1
2	1.55	0.975	1.55	0.975
3	1.55	0.975	1.65	0.975
4	1.55	0.975	1.55	1.025
5	1.55	0.975	1.65	1.025
6	1.65	0.975	1.55	1.025
7	1.65	0.975	1.65	1.025
8	1.55	1.025	1.65	1.025

Table 5.2: Calculated cases of component tolerance variance

tenna resonance and match frequency, which is lower in frequency than the trap resonance. A possible worst-case asymmetry scenario would be that the load with a lower resonant frequency creates an impedance match that overlaps in frequency with a radiation efficiency minima caused by the slightly higher frequency trap.

For all asymmetric scenarios, the match degrades, and the efficiency degrades at the match frequencies compared to the ideal case. The match frequency shifts higher and lower with different cases.

5.5.4 Multiple Load Pairs and Distributed Loads

Trap dipole antennas can operate at more than two bands if more pairs of traps are added. One of the earliest trap dipole papers was a three-band design with two pairs of traps [52].

My original motivation to study trap loaded antennas was to simplify the design of a slot loaded with a cavity resonator. The cavity loading can have multiple sites of strong coupling and loading on each cavity. Multiple RLC loads may be a better model for cavity loads and other more complex load structures. Possibly it could be helpful to imagine a single load value tuned to a design frequency, and then split the load into parts that still sum to the same response, and distribute them on adjacent segments of the dipole, or with some close spacing to better approximate the distributed nature of larger load structures.

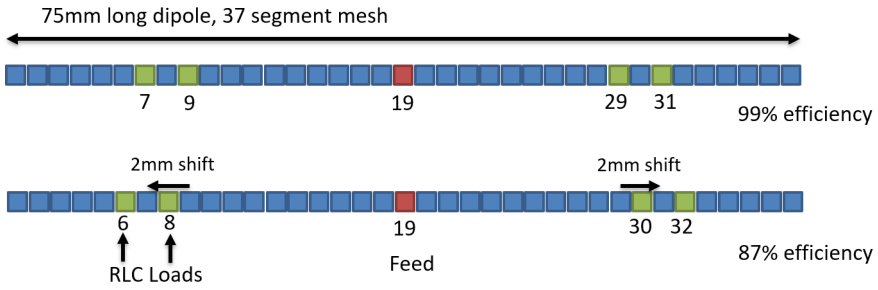


Figure 5.38: Fine parametric variation of trap location and spacing between "distributed" loads

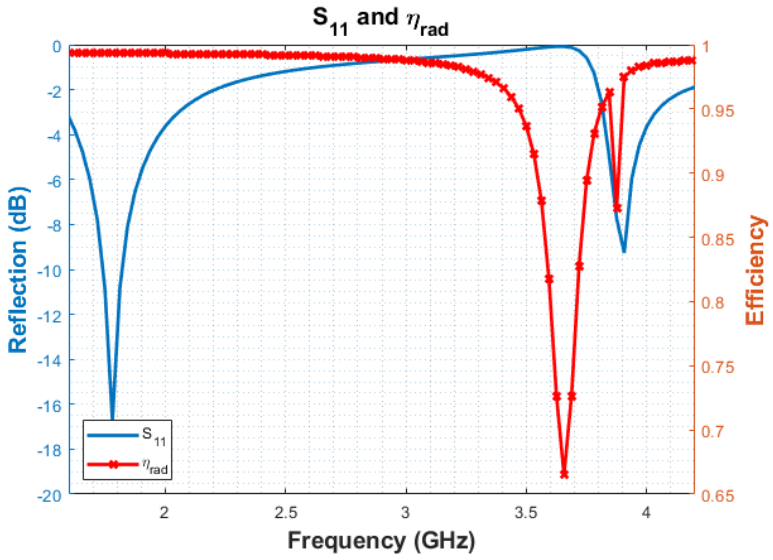


Figure 5.39: Reflection and radiation efficiency for a dipole with four trap loads, half the magnitude of the double trap design, Figure 5.38, showing an overlap of radiation efficiency dip and possible operating frequency

With an increasing number of loads, there is an increasing likelihood that an antenna operating frequency can suffer from low radiation efficiency, as shown in Figures 5.38 and 5.39.

5.5.5 Parametric Conclusions

Fine-tuning of the load location is useful for improving the impedance match. Changing the Q changes the frequency separation between antenna resonance and the minimum real input impedance. Moving the loads inwards on the dipole increases the frequency separation between real input impedance minima and the second resonance. The second resonance frequency increases as the loads move inwards. Reconfigurable loading in trap antennas is likely to work because the impedance match degrades slowly as the load value and placement is changed. The efficiency decreases as the loads are tuned and moved outwards on the antenna. If the load tuning is kept constant, the minimum efficiency value will decrease as the loads are moved inwards. Increasing trap Q will improve efficiency and move the efficiency dip closer in frequency to the trap related operating frequency.

5.6 Conclusion

In this chapter, the essential operation and literature background of the trap dipole was summarized. There is very little attention to trap related loss in the literature, but multiple simulation methods demonstrate that there are significant loss bands excited by the trap loads. The trap loading excites a heavily loaded and electrically compressed $3\lambda/2$ mode with poor efficiency. In most cases, the trap related operating frequency will not overlap with low radiation efficiency. This understanding of loaded higher order modes introducing loss should have a widespread application in the design of antennas with reactive and resonator loads.

Additionally, the trap is not resonant at the upper operating frequency of trap dipoles, contrary to the accepted explanation of trap antennas. The traps have a finite reactance at the upper operating frequency, and a pure inductive load can recreate the current distribution and impedance match at the upper operating frequency. The antenna current distribution is a quasi-first order mode at the upper operating frequency. The trap Q should be over a minimum threshold to create a second series resonance, and this Q value will depend on the specific design, but was around 200 for the designs that were simulated. Reconfigurable loading in trap antennas is likely to work because the impedance match degrades slowly as the load value and placement is changed. New design principles for wire radiators and slots with traps were developed. I will continue to expand trap dipole design principles in the next chapter.

Chapter 6

Traps Expanded

6.1 Introduction

In the previous chapter I developed a new explanation of how trap dipoles operate and how to design them. It was particularly interesting that the trap load is a finite reactance and not antiresonant at the trap associated operating frequency. In the previous chapter I also demonstrated that an inductor calculated to present the same reactance as the trap load can recreate the trap dipole response at a single frequency. I will continue that idea in this chapter and demonstrate that the loads in any basic parallel LC trap dipole antenna can be replaced with another resonator calculated to have the same load reactance. I will demonstrate a novel series LC trap loaded dipole, as well as the classic stub trap antenna. My analysis that traps work by providing a reactive load is further validated by demonstrating the series LC loaded trap antenna.

6.2 A Note on Loading Higher Order Modes

Inductive loads on electrically small monopoles more heavily load the antenna when moved closer to the feed [61]. Hansen explains this as being due to the increased current magnitude at the feed of the monopole. Based on [61] alone it was unclear whether proximity to the input or proximity to current maxima has a more significant loading impact on the resonances of the input impedance. Higher order modes can have multiple current maxima and minima on the dipole or monopole, so it is possible to move a load further from the feed and still be moving it closer to a current maxima of a higher order mode. The authors in [74] claim that higher order modes on dipoles are more significantly impacted by loading than lower order modes. If load proximity to modal current maxima changes the apparent loading of each mode, then it would only sometimes be true that higher order modes would be more significantly loaded than lower order modes.

I simulated an inductor loaded monopole and recorded the shift in the first and second series resonance as I changed the load locations. The reults are shown in Figure 6.1. The well-documented first mode response is shown, with the load moving closer to the single current max at the feed causing the the resonance to move lower in frequency. The second series resonance (the third mode) matches my prediction, that moving the load to the current maxima increases loading, even if the maxima is further from the feed.

This is a novel result as far as I am aware, and a key theme of [74] is that there is a lack of literature attention on loaded antennas operating at a higher order mode. However, with resonator loads on antennas it is inevitable that more higher order modes will be excited in band. I have particularly focused on how the third order mode is electrically compressed and lossy on the trap dipole. I do not design the antenna to match to the third order mode. I describe the upper resonance on the trap antenna as a quasi-first order mode, but it is certainly due to an unknown combination of higher order modes. This new understanding

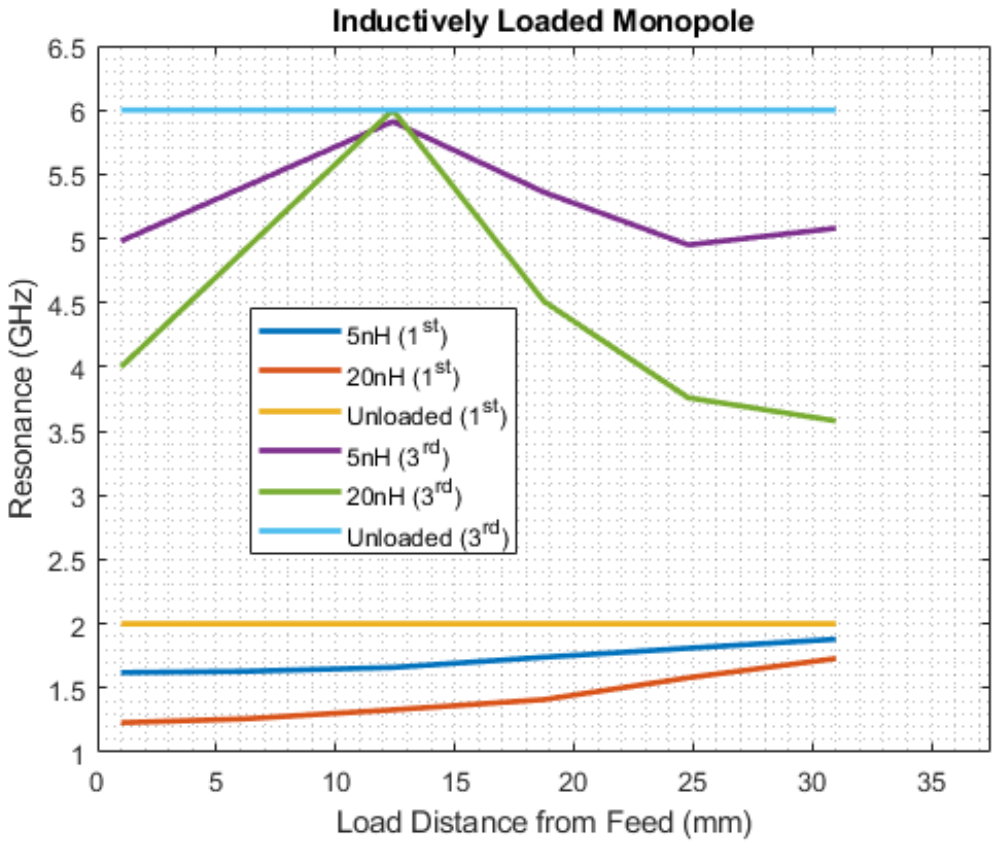


Figure 6.1: It is well known that loading an electrically small monopole closer to the feed will more heavily load the monopole. However, when loading higher order modes, placing a load at the current maximums will more heavily load the specific load. This can result in a higher order mode being more heavily loaded than the fundamental load.

of current maxima impact on higher modes is not directly applicable to trap dipoles since the revised analysis still does not directly track the combination of higher modes that create the antenna upper resonance. However, this is certainly a helpful principle for the general design of resonator loaded antennas.

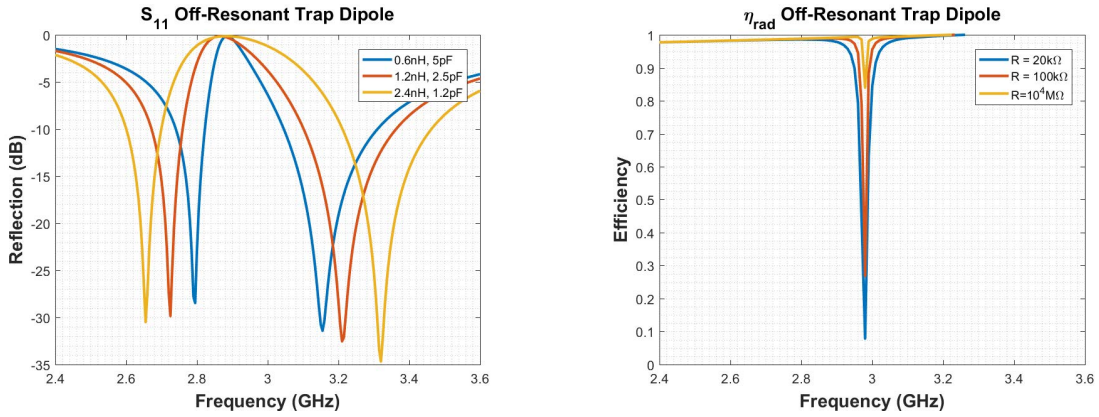
6.3 Changing Feed Location

Moving the feed off-center can add a new resonance. The distance between minima and resonance remains essentially static if the feed location is moved. The second resonance frequency also remains nearly static. When moving the feed location, a new resonance and match point can be shaped that occurs in frequency below the radiation efficiency dip rather than above it. Even with the increasingly complicated impedance response, it is still true that the radiation efficiency minima lines up with the real input impedance minima.

Moving the feed location does not change the frequency separation between the radiation efficiency minima and the trap related resonance. The second resonance frequency also remains nearly static. When moving the feed location, a new resonance and match point can be shaped that occurs in frequency below the radiation efficiency dip rather than above it. Even with the increasingly complicated impedance response, it is still true that the radiation efficiency minima lines up with the real input impedance minima.

6.4 Off-Resonant

The off-resonant trap dipole mentioned in [62] avoids the trap resonance loss by operating away from the trap resonance. Rather than using the trap to define a second open-circuit boundary condition for a half wavelength at a higher frequency, the load inductance below trap resonance and capacitance above trap resonance can be used to retune the antenna to



(a) (b)

Figure 6.2: Off-resonant trap dipole design from [62] (a) parametric of L/C ratio, R=20kΩ (b) R loss parametric (L= 0.56 nH,C=5 pF), data from HFSS

impedance matches above and below the trap resonance. I designed the off-resonant trap dipole with a 3 GHz trap circuit in HFSS to create two different passbands at S-Band, seen in Figures 6.2a and 6.2b. The reflection coefficient matched to 73 Ω in Figure 6.2a shows two passbands. The corresponding radiation in Figure 6.2b shows significant loss at the trap resonance, but not at the antenna match frequencies. Bandwidth and distance between radiation bands can be adjusted by the ratio of lumped L to lumped C, shown in Figure 6.2a. Figure 6.2b shows that for fixed L and C, varying R directly impacts the radiation efficiency at trap resonance, in agreement with conventional trap antennas. Conveniently, this loss is no longer located at the operating frequencies of the antenna.

This design is similar to some of the load placement parametric results. With the loads moved to the ends of the antenna and the RLC resonance tuned to match, a similar response is created, but not with quite as good of a match.

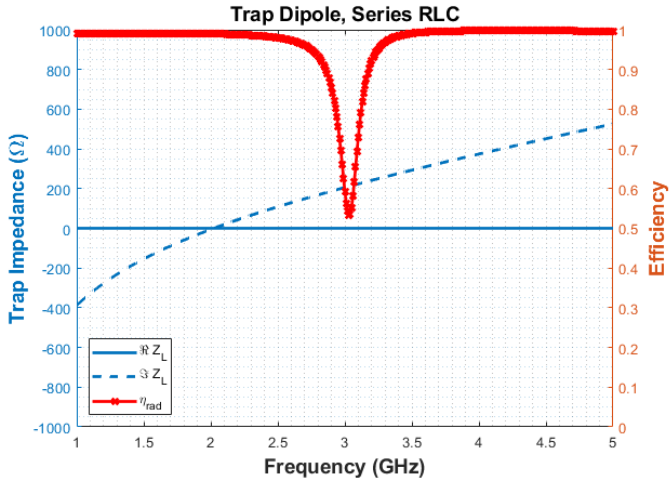


Figure 6.3: Series RLC load impedance and radiation efficiency of dual band trap dipole loaded with series RLC loads

6.5 Series RLC Trap Dipole

Trap dipoles in the literature are always created with parallel RLC loads. Since I proved that the upper operating frequency is caused by a reactive load value rather than an actual open circuit boundary condition, it should also be possible to use a series RLC tuned to have the same reactance value at the upper operating frequency. The primary trap dipole that has been discussed extensively already had a load reactance value of +j351.7Ω at the 3.84 GHz upper operating frequency. A series RLC resonator is inductive above resonance, so if the resonant frequency is tuned below 3.84 GHz there will be some ratio of inductance to capacitance that will make the load have the required +j351.7Ω reactance at 3.84 GHz. Since a series RLC is a short circuit at resonance, it is preferable to tune the RLC resonance to match the unloaded dipole fundamental resonance at 2 GHZ so that the resonator does not reactively retune the fundamental resonance.

A starting resonator tuning with a 1 nH inductor and 6.2 pF capacitor is resonant at 2 GHz. After sweeping the L/C ratio (keeping a constant resonant frequency), a 20 nH and 0.31 pF series combination has a reactance of +348.8jΩ at 3.84 GHz, Figure 6.3. As

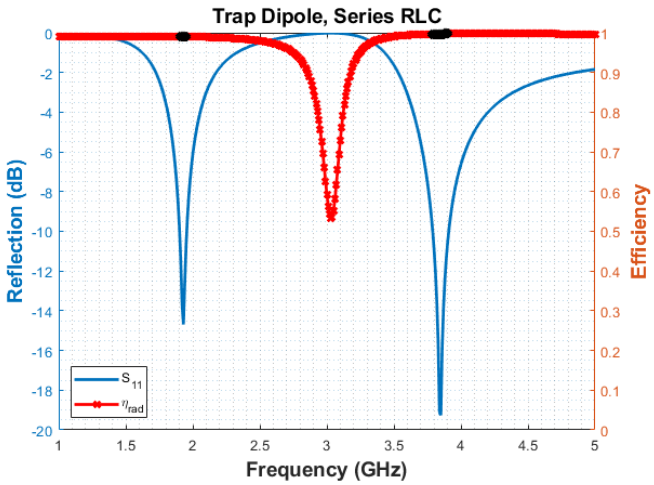


Figure 6.4: Dual band trap dipole with series rather than parallel RLC loads

expected, this design has an excellent dual-band behavior, Figure 6.4. The radiation efficiency minimum still lines up with the input resistance minimum, Figure 6.5. A series resistance of 0.5Ω is included for a realistic discrete component loss approximation.

6.6 Stub Loading on Dipoles

Trap dipoles have long been made with stub loads. Like LC traps, stubs have been explained as enforcing an OC boundary condition on the dipole. Again like LC traps, stubs in simulation are not actually resonant at the trap-created operating frequency. They have a finite reactance. However, it is still easy to design stub trap dipoles according to the traditional explanation. Quarter wavelength stubs terminated in a short circuit will enforce an open circuit at the input. If the stub is in series with the dipole wire, an open circuit is created on the dipole. (The dipole is not a transmission line structure.)

I simulated a 4 GHz stub load on a trap dipole with 25, 50, and 73 Ω stub characteristic impedances. The simulation is done in the Matlab, so the stubs are defined generally by their length and characteristic impedance, although twin-wire and coax line can be used

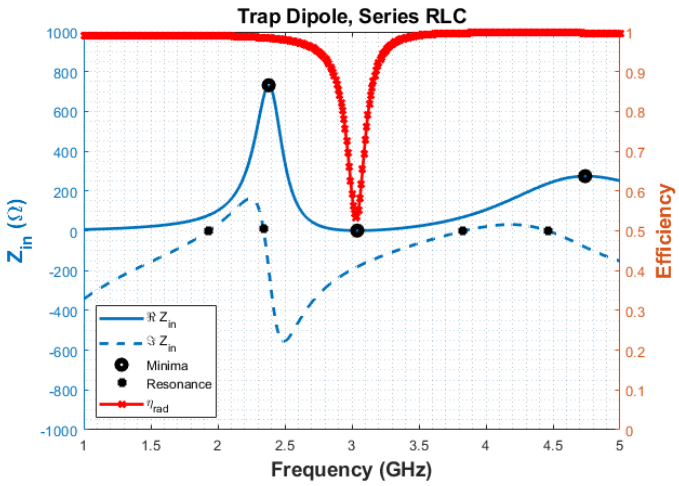


Figure 6.5: Input impedance of dual band trap dipole with series RLC loads, η_{rad} lines up with R_{in} minima

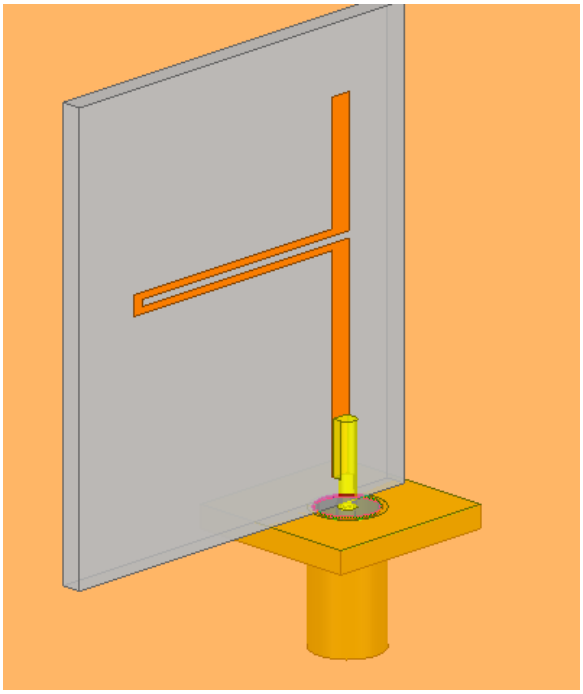


Figure 6.6: Monopole with series short circuit stub to create a trap dual band response

$Z0$	f_1	f_{loss}	f_2
25	1.78	3.62	3.86
50	1.71	3.33	3.72
73	1.66	3.14	3.69

Table 6.1: Loading trap dipole in MoM with SC 4 GHz quarter-wavelength stubs, lower stub characteristic impedance causes f_2 to be closer to f_{trap}

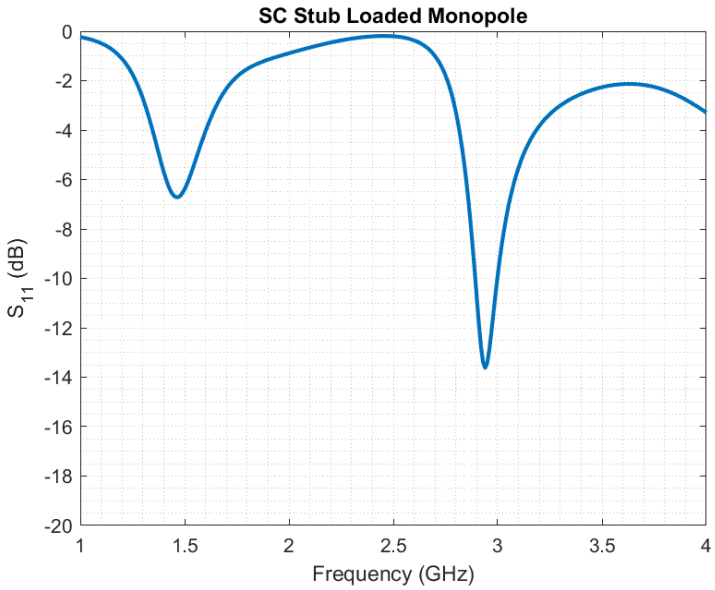


Figure 6.7: Monopole with short circuit stub, dual band response

in practice. The results are summarized in Table 6.1, and it can be seen that stub with lower characteristic impedance creates an antenna operating operating frequency closer to the stub resonance (f_{trap}).

The off-resonant design from [62] can be replicated with stubs by adding a 2 GHz tuned SC stub on a 2 GHz dipole. The calculated antenna had operating frequencies at 1.37 GHz and 2.41 GHz. The frequency separation can be adjusted by changing the characteristic impedance of the stub.

Tuning an open circuit stub to the lower frequency means that that at an octave up there will be a half wavelength OC stub, which is like a quarter wavelength SC stub. The reactance at the lower stub resonance is probably smaller than with the SC stub tuned to

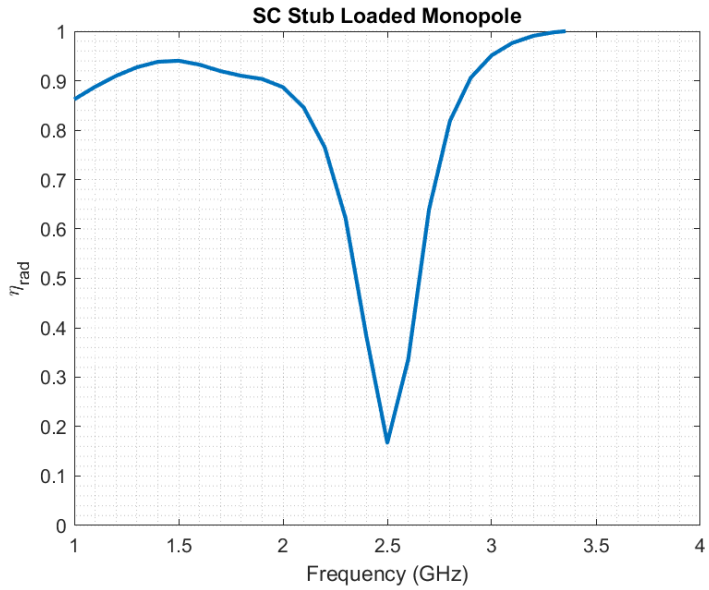


Figure 6.8: Monopole with short circuit stub, radiation efficiency over 90% at both operating frequencies

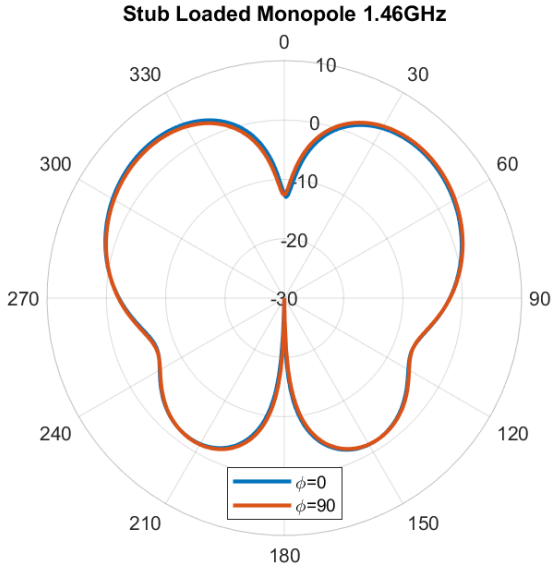


Figure 6.9: Monopole with short circuit stub, typical monopole realized gain pattern at lower frequency, suggesting straight length of monopole has normal current distribution and stub doesn't contribute negatively towards radiation

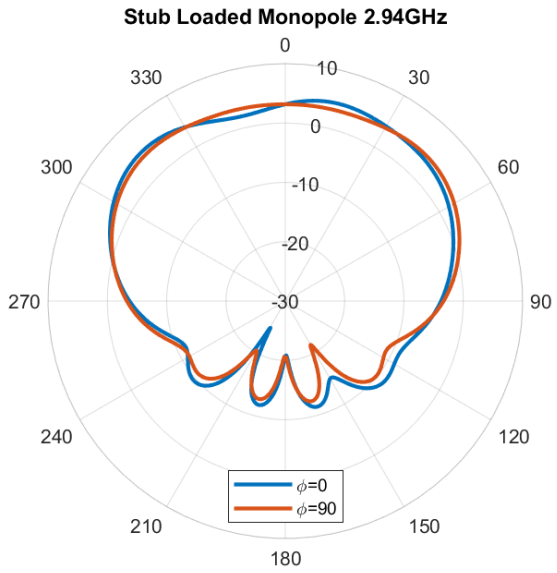


Figure 6.10: Monopole with short circuit stub, typical realized gain pattern at upper frequency, suggests stub doesn't contribute negatively towards radiation

4 GHz, so this option can be nice because it adds less loading to the lower frequency, but at the cost of having physically larger stubs on the antenna. The simulated open circuit stub created operating frequencies at 1.88 GHz and 3.81 GHz with a 73 Ω OC stub tuned to 2 GHz on a 2 GHz dipole. The radiation efficiency minimum is at 3.5 GHz.

Starting from a working LC loaded design, the reactance of the LC loads can be recreated with a stub.

6.7 Resonator Terminated Stubs

Adding a resonator to the stub can change the end condition of the stub from OC to SC at different frequencies. Suppose there is a quarter wavelength stub at 4 GHz. If a series RLC is added to the end (to ground) and tuned to 4 GHz, we recreate the previous results of a simple SC stub, and a dual band antenna results. In this case the antenna has a dual band match of -19.5 dB at 1.85 GHz (1 Ω), and -10.5 dB at 3.83 GHz (474 Ω). Radiation

efficiency dips at 3.58 GHz (176 Ω). Unlike the simple short circuit stub, there is an additional series resonance at 1.81 GHz.

If the stub length is changed, I still expect that the short circuit condition will be enforced when the series RLC is resonant, but the stub will no longer present an open circuit at the antenna loading point. However, the RLC will reactively load the stub to be antiresonant at a different frequency. To start with I've tuned the stub to be an eight of a wavelength at 4 GHz. The stub is electrically too small to provide an open circuit in band (2-4 GHz). However, we can add electrical length (or phase change) to the stub at 4 GHz to make it antiresonant. The series RLC tuned to 4 GHz provides no reactive loading because it is at a short at 4 GHz. If I tune the RLC higher than 4 GHz, the RLC will provide capacitance, which will shorten the stub and exacerbate the problem. If I tune the series RLC lower than 4 GHz, the RLC will provide inductance and should electrically lengthen the stub. As a first guess, I tune the RLC to 2 GHz, combined with a stub that is one eighth of a wavelength at 4 GHz. The result is a dual-band response with a match of -21.4 dB at 1.8 GHz, and -9.6 dB at 4.63 GHz. The results are very similar to what has been presented so far. The stub itself is antiresonant at 5.33 GHz.

Just as was true with the RLC loaded dipole, the upper operating frequency is not at the antiresonance of a short circuit stub, but merely near the antiresonance. When loading a stub, I am not aiming to achieve resonance at a certain frequency, but I am instead aiming to recreate the reactive load that a resonant stub would create at the operating frequency. The design is tied to ideal SC or OC stubs, or to the already existing cases of parallel and series RLC designs. To limit the number of solutions, an acceptable stub length should be decided, and then the RLC load value can be solved for so that the stub provides the required reactance. The RLC load then is a problem that typically has multiple solutions, but that is also true for the simple RLC loaded dipole. The shorter the stub is, the stronger the reactive loading needed, probably.

The one eighth wavelength stub with a heavier load of 4 nH and 6.2 pF series RLC has an upper operating frequency at 3.14 GHz (-8.2 dB), and the stub antiresonance is also exactly at 3.14 GHz, which is interesting. The radiation efficiency dip is at 2.68 GHz. If the inductance is retuned to 1 nH, the match is -21.4 dB at 1.8 GHz and -9.6dB at 4.63 GHz. If the inductance is changed to 6 nH, the match is -10.5 dB at 1.57 GHz and -8.1 dB at 2.8 GHz. If the capacitance is changed, the combination of 1.6 pF and 4 nH has a match of -20.3 dB at 1.82 GHz and a match of -8.7 dB at 3.43 GHz. In all of these designs the physical dimensions remain constant, which is partly to blame for some of the impedance matching to be worse than -10 dB.

A one eighth wavelength stub with a parallel RLC load of 20 Ω, 1 nH, and 1.6 pF has matches of -15 dB at 1.73 GHz and -8.3 dB at 3.27 GHz. If the capacitor is changed to 6.2 pF, the match is -12 dB at 1.64 GHz and -11.5 dB at 2.08 GHz.

If an undersized stub is loaded with a parallel RLC, the stub will still need an inductive load, so the RLC should be tuned above the upper operating frequency.

6.8 Conclusion

Since the trap has a finite reactance at the antenna operating frequency, the trap LC circuit can be replaced with any other resonator that has a matching reactance value at the same frequency. This principle is new to the literature and can assist broadly in designing multi-band and reconfigurable loaded antennas. Designing parallel LC trap dipoles in terms of the traditional theory of open circuits at key electrical lengths results in reasonably accurate design that can be fine tuned in simulation. However, trap dipoles belong to the broader category of reactively and resonantly loaded antennas and the design process can be unified with existing theory, especially trends for inductor loaded monopoles. I demonstrated that loads impact higher order modes based on proximity to current maxima.

The parallel LC trap dipole antenna is a useful prototype on which to base more complex resonator loaded antennas. These results have been found for loading dipoles with discrete resistors, capacitors, and inductors, but the findings can be extrapolated to resonant and reactive loading of other structures with analogous current distributions, such as loaded slotline [53], [76], [77]. In Section 2.3, I approximate the evanescent mode coaxial cavity resonator as a discrete RLC so that I can apply the trap dipole investigation to the loaded slot antenna. In the next chapter, I will design and demonstrate multiband trap slot antennas using the wire-based design principles from this chapter.

Chapter 7

Trap Loaded Slot Antennas

7.1 Introduction

Reactive and resonant loads have been added to slot antennas to create electrically small slots [78], [79], multiband slots [80], [81], and reconfigurable designs [54], [55]. In [81], an ultra-wideband slot was loaded with elliptical short-circuited slot stubs to improve radiation pattern stability at the higher frequencies. The trap stubs were shown to suppress ground plane currents that contributed to end-fire radiation in the upper portion of the operating band. One of the significant advantages of the multiband trap loaded dipole antenna is that it creates first-mode like field distributions at the antenna operating frequencies, which results in radiation patterns free of beam splitting [58], [59] at multiple operating bands. In contrast to dipoles, slot antennas are planar, can be cavity backed for unidirectional radiation and array integration, and can be easily integrated with a wider variety of resonator structures because they are planar. In this paper, discrete inductor-capacitor traps are added across slots to create a novel dual-band trap slot antenna.

The trap dipole design principle can be replicated with slot antennas. A slot that is half a wavelength at 2 GHz can be loaded with parallel RLC loads spaced half a wavelength apart

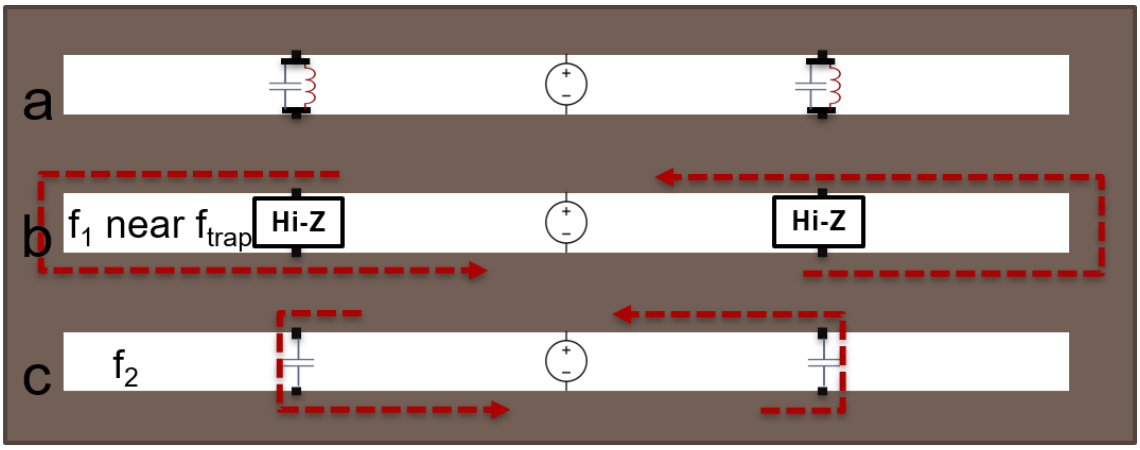


Figure 7.1: a) Slot antenna with lumped port feed at center and parallel LC loads. b) near LC antiresonance is high impedance f_1, and c) is intended to be a slightly capacitive short at f_2. Approximate currents as blue dashed lines.

at some higher operating frequency, 4 GHz, for example. The parallel RLC should be tuned to 2 GHz to create an open circuit across the trap and not disturb the 2 GHz slot resonance. At around 4 GHz, the load can function as a new current path that defines a shorter slot antenna and creates a higher operating frequency, Figure 7.1. The reactance magnitude at the upper operating frequency can be controlled by adjusting the L/C ratio. An improper L/C ratio could cause the upper frequency reactance to be large enough reactance to act as a reactive open rather than a new current path.

Both series or parallel resonators can be used for trap antenna design. A series resonator load (bandpass) should be tuned to the upper operating frequency as shown in Figure 7.2, and a parallel resonator (bandstop) should be tuned to the lower operating frequency seen in Figure 7.1. Further tuning of the other frequency can be adjusted by changing the L/C ratio. A parallel resonator allows current through across a broad range of frequencies on either side of the antiresonance. Across this range of frequencies, the parallel resonator would be both a short and a reactance. The load is capacitive below its antiresonance and lengthens the electrical length. Above antiresonance, the load is inductive and shortens the electrical length. In either case, the load is an alternative current path that circumvents the

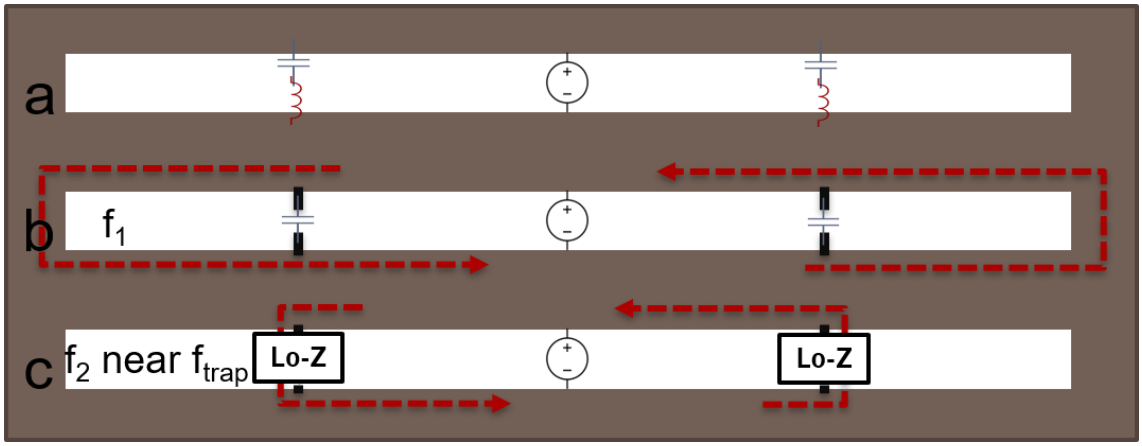


Figure 7.2: a) Slot antenna with lumped port feed center and series LC loads b) high impedance capacitive load at f_1 c) low impedance at f_2 near to f_{trap}

full slot length. The bandstop antiresonance should be tuned to the unloaded slot antenna's fundamental mode response so that the LC pair does not short out the slot. Depending on the placement and then on the reactance values, the LC will define a shorter length slot with reactive loading that can operate at a higher frequency than the fundamental unloaded slot response.

The off-resonant dual-band design from [62] can be also be created with series RLC loads. A slot that is half a wavelength at 2 GHz can be loaded with 4 GHz series RLC loads to short out the slot to a smaller resonant length at 4 GHz. Adding loads across the slot's narrow dimension creates a new short path and resizes the slot length. The series RLC loads will be capacitive below the 4 GHz resonance. With the right L/C ratio, the capacitance across the slot will be effectively a reactive open at 2 GHz to allow the full slot length to resonate. Adding LC traps to slot antennas hasn't been demonstrated in the literature.

I designed a capacitively coupled CPW feed for both the series and parallel LC trap slot antennas, as shown in 7.3. The parallel RLC loads were tuned near to 2 GHz to create a high impedance at the slot's fundamental unloaded resonance. The series RLC loads were

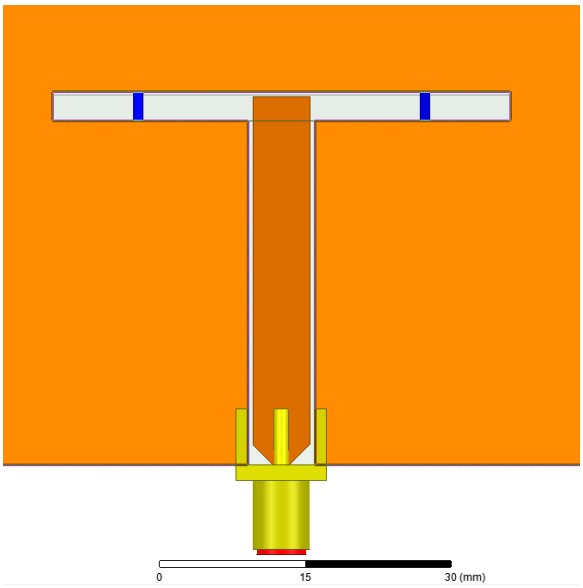


Figure 7.3: Slot antenna with CPW center feed and RLC traps (blue)

tuned near to 4 GHz with a half-wavelength spacing at 4 GHz.

7.2 Unloaded Slot Antenna

Basic resonant slot antennas are typically designed to be $\lambda/2$ in length and typically have a narrowband response with a dipole-like radiation pattern. An unloaded 48 mm slot has a first antiresonance at 2.15 GHz, regardless of feed location, Figures 7.4. The slot is 3 mm wide, and the substrate is 120 mil TMM3 ($\epsilon_r = 3.66$). Copper loss is included in the metallic ground.

For the center-fed slot, the antiresonance (2.15 GHz) has magnetic field maxima at both ends of the slot and the feed (middle), so it appears to be the third mode. However, the end feed shows a second mode, so I will refer to this as a second-mode distribution. The series resonance (at 3.65 GHz) adds a magnetic field maxima at the center, third-mode distribution.

Planar slot antennas are commonly fed with a coax probe, and a 50 Ω impedance match

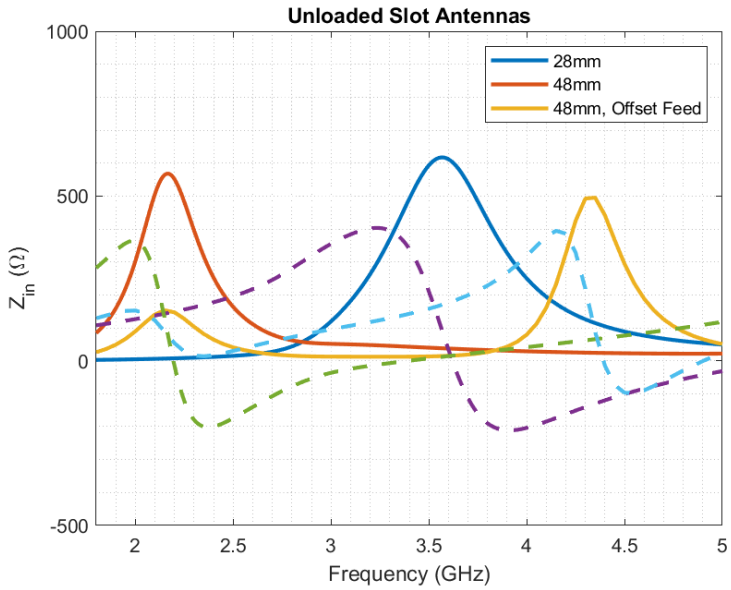


Figure 7.4: Input impedance of lumped port fed unloaded slot antenna, comparing center fed 28 mm slot, center fed 48 mm slot, and 48 mm slot with feed near the slot end. 28 mm slot is approximately the same as the inner length defined in subsequent trap slot antennas.

point typically exists about $\lambda/20$ away from the end of a $\lambda/2$ slot. For the end-fed model, the input is inductive, so simulation does not show any true resonances. There is a faux antiresonance at 2.15 GHz and again at 4.32 GHz. The 4.32 GHz antiresonance appears to have a third-mode distribution. Radiation efficiency is above 98% over the frequency band of interest.

End feeding changes the impedance magnitude of the first antiresonance and changes the magnitude AND frequency value of the first series resonance. The first antiresonance has a magnetic field maxima at both ends. The first series resonance adds a magnetic field maxima in the middle.

I will also consider several loaded 48 mm slots. Unless noted otherwise, the loads will be at -14 mm and +14 mm from the slot center, and in many cases, the loaded slot should be thought of as both a 48 mm and a 28 mm slot depending on the frequency and the behavior of the loads. For comparison purposes, I have also simulated a 28 mm unloaded slot. Its

first antiresonance is at 3.55 GHz, Figure 7.4, and first series resonance around 5.6 GHz.

7.3 Feed Options

CPW feed has the advantage of being in the center, so it should work with a wide variety of load placements. Near end feeding with coax or coupled microstrip gets tricky with the OC created by the loads potentially isolating the feed from most of the radiator. It is worth looking at center loads to see whether they work well with end feeding. Interesting array spacing if the center load and end feed cuts antenna to half size.

Loss occurs in RLC loaded slots at real Z_{in} minima, which is not due to resonator loss primarily but is due to the combination of dielectric, conductor, and resonator loss on a higher order electrically compressed mode. This fits the trap dipole finding that a higher-order mode is electrically compressed by disproportionate reactive loading, loses its radiation resistance, and the ratio of R_{rad} to R_{loss} becomes unfavorable. The slot antenna adds a new factor of dielectric loss. If the resonator can be lossless and efficiency dips to 30%, the higher-order compressed mode seems like a good explanation. However, proving this is not easy because a center lumped port feed and lumped loads disturb the field distribution. There seems to be evidence that a center 50 Ω feed creates an artificial H-field spike at the center of the slot for the $\lambda/2$ resonance. E differential across slot is nearly constant around the center of the slot for the first-mode, so the drop in impedance at the feed (to 50 Ω, from 150) probably causes the H-field to spike unnaturally.

The CPW center feed excites a first-mode distribution, but it does not excite a very clear third-mode distribution. Center 73 Ω voltage source is a good feed choice for dipoles, but not the only option. Moving the feed off-center changes the upper resonances. Feed choice matters similarly for slots and impacts resonances.

Dipoles with an RLC load have multiple sources of reactances. The RLC loads add

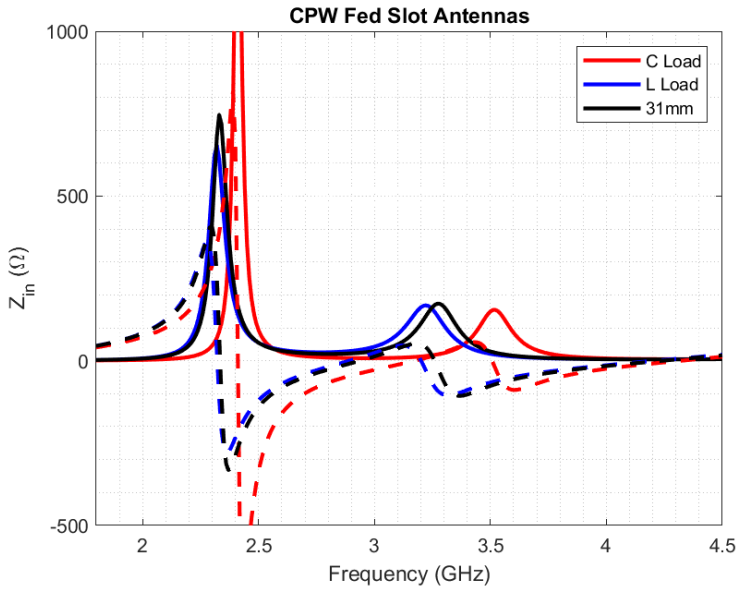


Figure 7.5: Comparison of CPW fed slots, with inductor load, capacitor load, and unloaded. The unloaded antenna has the same length as the inner length between the loads. The loaded slot antennas are terminated in shorts, but have very little difference compared to open ended slots

reactance, but the dipole open ends also add reactance, specifically capacitance. The feed for the dipole can also add reactance. I have to take into account multiple reactances to analyze the trap slot. This could seem over-complicated for the dual of a simple dipole, but dipole analysis is commonly restricted to simple cases. The CPW fed RLC loaded slot is reactively loaded by the RLC loads, is capacitively loaded by the CPW transition, and the outer length of the slot can act as a short stub. When the RLC loads serve as a short current path, they are not true shorts but still have some reactance, which should serve to couple into the shorts.

7.4 Capacitor and Inductor Loads on Slot

A reactive load across the slot will add a new current path that circumvents the slot's full length. The shorter current path/ electrical length will raise the first antiresonance fre-

quency. Additionally, if the reactive load is a capacitor, it will lengthen the electrical length and lower the current path's resonant frequency. Figure 7.5 shows the input impedance of a slot with centered 1.6 pF loads at 28 mm spacing (20 mm outside). Antiresonances are at 1.36 and 3.83 GHz, and series resonance at 1.7 GHz.

An inductor across the slot should create a new length definition and shorten the electrical length (raise the first antiresonance frequency). A capacitor would lengthen the electrical length. Figure 7.5 shows antiresonance at 3.21 GHz and series resonance at 5.14 GHz. At 1 GHz, radiation efficiency is 40%. It seems that the inductor lowers the resonances of the 28 mm antenna (originally 3.55 GHz and 5.6 GHz).

Again, an altered model with open-circuit end conditions was simulated. With OC slot ends, the resonance shifts from 3.2 to 2.9 GHz. Again, the unloaded 28mm slot is resonant at 3.55 GHz, so the inductor current path shifts the resonance down by 0.65 GHz. The inductor loaded monopole literature suggests that the inductor more heavily loads an antenna at a current maxima. The end load position on a slot is optimal load placement for heavy loading because the current is maximum at the end. The radiation efficiency drops to 0.65 at 2.15 GHz. Loss can come from the conductor and dielectric loss and the 0.2 Ω resistor in series with each inductor. The radiation efficiency dip is near the minimum value of the real input impedance. Despite the antiresonance location tuning down, there is a well-matched series resonance at 4 GHz.

7.5 Parallel RLC, CPW Feed

The traditional trap-style antenna creates a quasi-first mode field distribution at both frequencies, which in turn creates an even radiation pattern without splits. A general resonator loaded slot antenna is likely to excite additional modes in band, due to loading of higher order modes [74]. The higher order modes have poor radiation efficiency when electrically

compressed [50], and can cause unwanted distortion in the far-field pattern [81]. The trap style antenna avoids these problems and creates a multiband response.

I arbitrarily pick 60 mil TMM3 ($\epsilon_r = 3.3$) for the substrate and choose the slot to be 3 mm wide. The trap slot antenna will have an outer length of 48 mm, which has an unloaded resonance at about 2.2 GHz. To minimally disturb the unloaded resonance of the antenna, parallel 1.3 pF and 4.9 nH LC loads are tuned to be resonant at 2 GHz, near the slot unloaded resonance, in order to present a high impedance across the slot. The loads short across the slot at the higher frequency to mimic a shorter length slot, as per the traditional idea of trap dipoles, sketched out in Figure 7.1. The loads are spaced 31 mm apart, which is about the resonant length of a 3.2 GHz slot antenna, but the different end conditions between the low impedance trap current path and a true short circuit termination will alter the effective resonant length.

The parallel LC trap-loaded slot antenna was simulated and has a dual-band response at 2.12 GHz and 3.74 GHz, as shown in Figure 7.6. The lower antenna operating frequency is not coincident in frequency with the 2 GHz trap resonance. The loads have an impedance of -j524Ω across the slot at the lower operating frequency, which I replicate with a series load below. As expected, the antenna has a dip in radiation efficiency centered at 2.55 GHz, but the operating frequencies have high efficiency.

The lower operating frequency is near the 2 GHz trap operating frequency, and the radiation efficiency, shown in Figure 7.8, indicates that the efficiency is over 90%.

7.6 Series RLC, CPW Feed

Since the parallel LC load value at the lower operating frequency is finite, the parallel LC load can be replaced with a series LC load. The series LC load is selected to have a short circuit resonance near the desired upper operating frequency. The L/C ratio is adjusted to

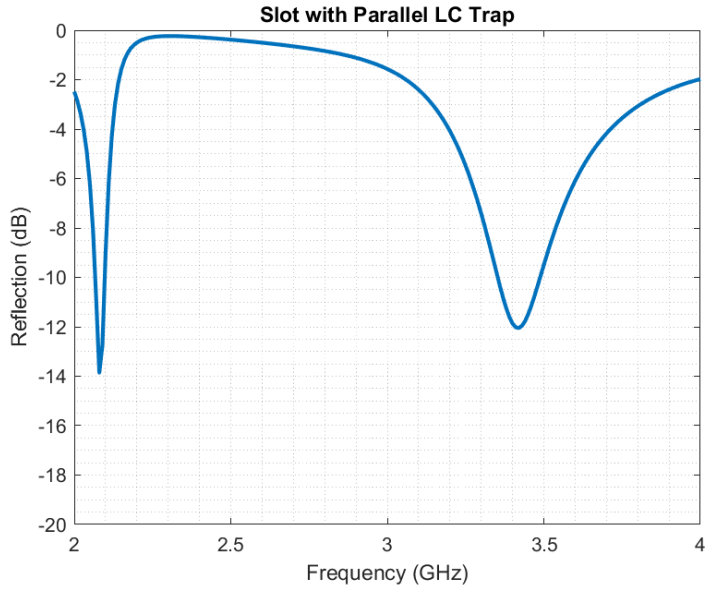


Figure 7.6: Reflection coefficient of CPW fed slot antenna with parallel LC traps

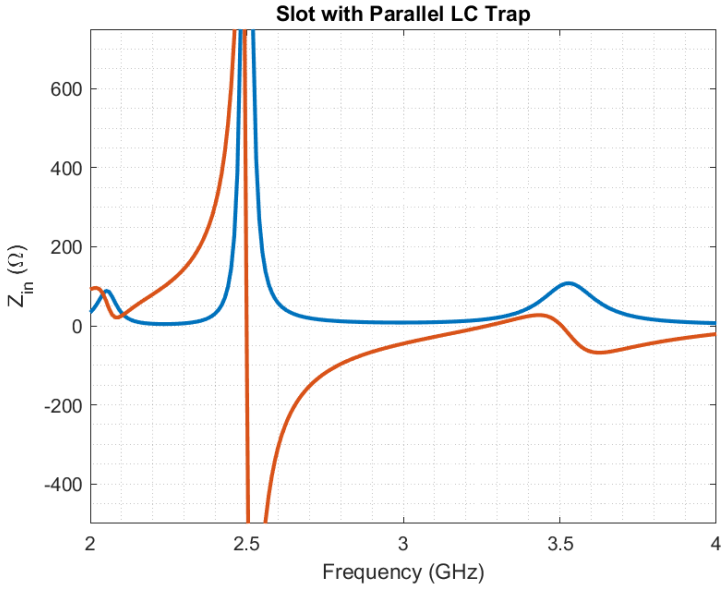


Figure 7.7: Input impedance of CPW fed slot antenna with parallel LC traps

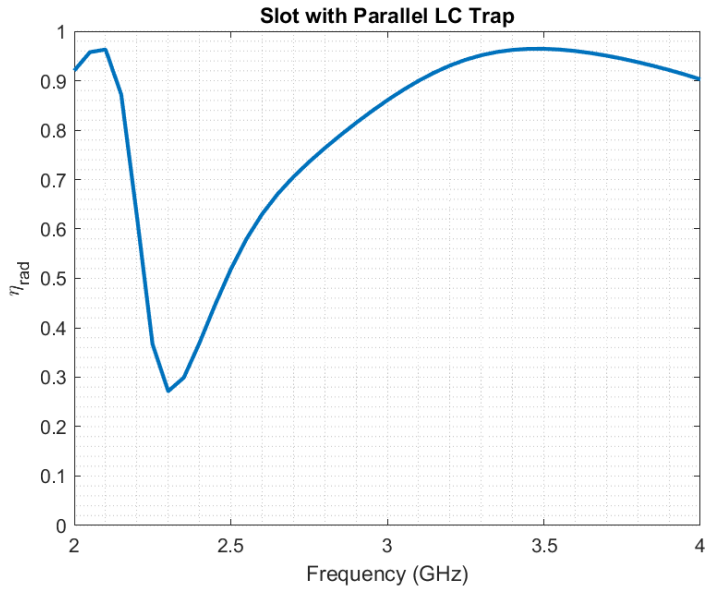


Figure 7.8: Radiation efficiency of CPW fed slot antenna with parallel LC traps

provide the same reactance of the parallel LC at the lower operating frequency, -j524Ω at 2.12 GHz. An LC pair of 0.1 pF and 17 nH is resonant at 3.98 GHz and has a matching impedance of -j524Ω at 2.12 GHz. The CPW fed trap slot antenna was resimulated with all of the same dimensions, and with the parallel LC loads swapped with the series LC loads. The antenna has operating bands at 1.99 GHz and 2.91 GHz, seen in Figure 7.9. The loads are -j587Ω at 1.99 GHz and -j236Ω at 2.91 GHz. The upper operating frequency has been significantly lowered compared to the first design, due to the increased capacitance at the upper operating frequency. There is also an expected dip in radiation efficiency between the bands, but the operating frequencies have high efficiency.

The radiation efficiency dips to 14% at 3 GHz, which is in line with the minimum R_{in} value.

The magnetic field magnitude is shown in Figure 7.12 and confirms that at f_1, the primary short (H field max) is at the outer ends of the slot and is at the LC loads at f_2.

The E-field behavior in Figure 7.13 clearly shows a high E value across the thin CPW

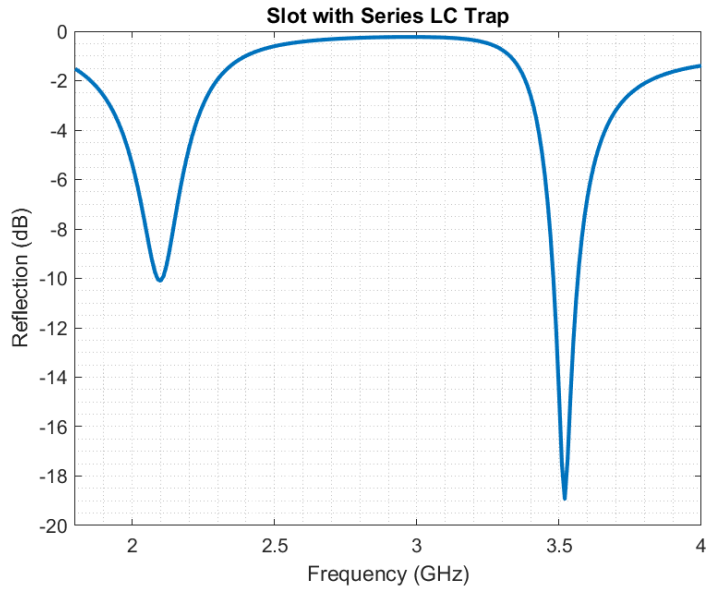


Figure 7.9: Reflection of slot antenna with series LC loads, operating frequencies at 1.99 GHz and 3.43 GHz

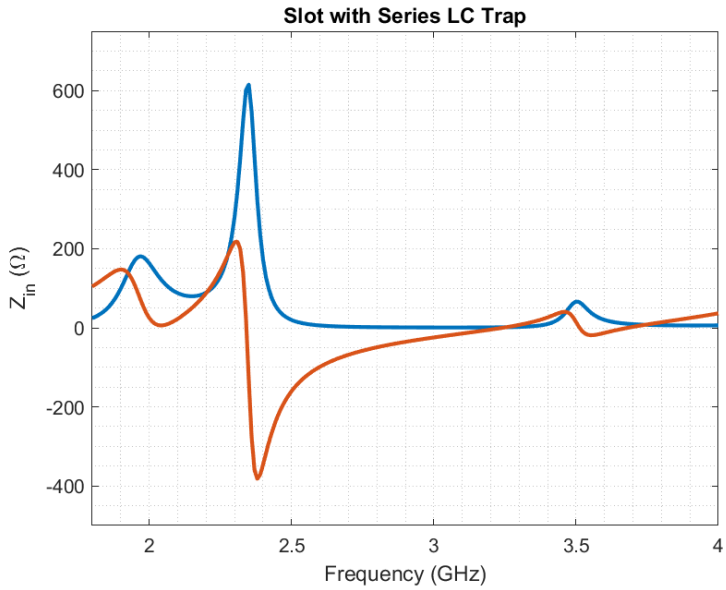


Figure 7.10: Input impedance of slot antenna with series LC loads

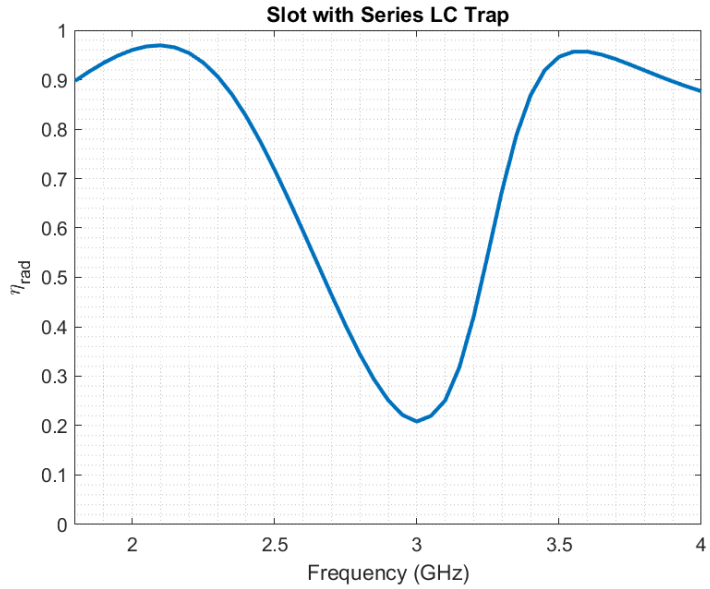


Figure 7.11: Radiation efficiency of slot antenna with series LC loads

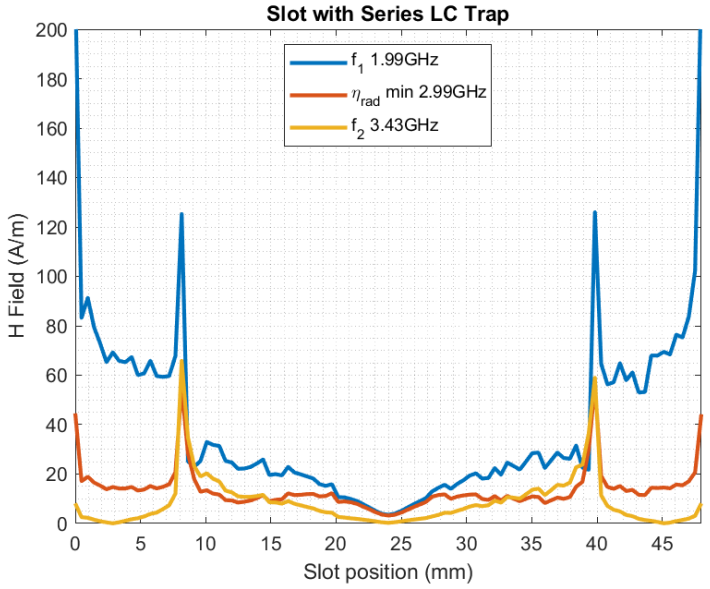


Figure 7.12: H field across slot, slot antenna with series LC loads

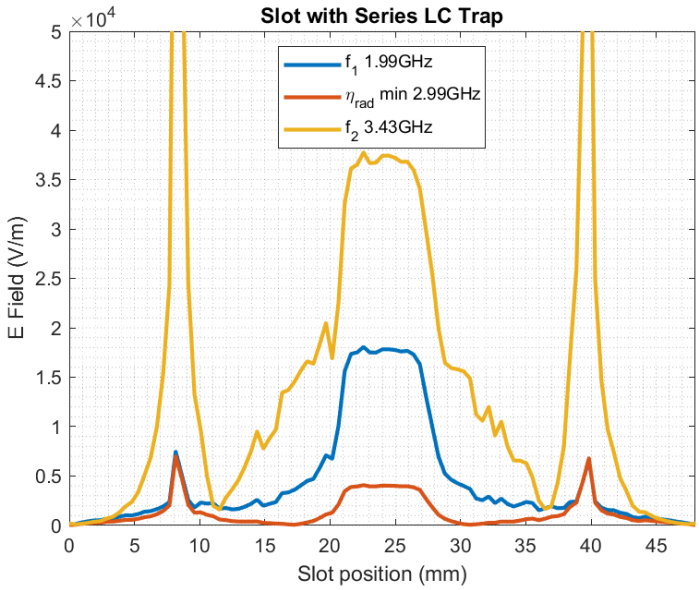


Figure 7.13: E field across slot, slot antenna with series LC loads

to slotline transition, as well as spikes at the LC loads. Despite the data being affected by these features, it seems reasonable to interpret f_1 as a first-mode distribution across the whole slot length and f_2 as a first-mode across the inner length. The η_{rad} min trace, isolated in Figure 7.14, shows a gradual, continual slope around each trap, as well as the max in the middle, which could be interpreted as a $3\lambda/2$ mode.

7.7 Stub Loading on Slots

A 14 mm CPW stub is λ/4 (90 degrees) at 3.8 GHz. The lower passband is tuned down to 1 GHz. With an open circuit, the stub's input impedance is +6 jΩ at 3.8 GHz(β = 115, Z0 = 153), which is very close to enforcing an SC, and there is a passband at 3.8 GHz in HFSS simulation (-13 dB). (Just for fun, SC stub is 3,900 jΩ at 3.8 GHz.) At 1 GHz, β is 30, and OC Zin is -343 jΩ, which is a significant reactive load and lowers the resonance of the slot. (SC stub is +68 jΩ.)

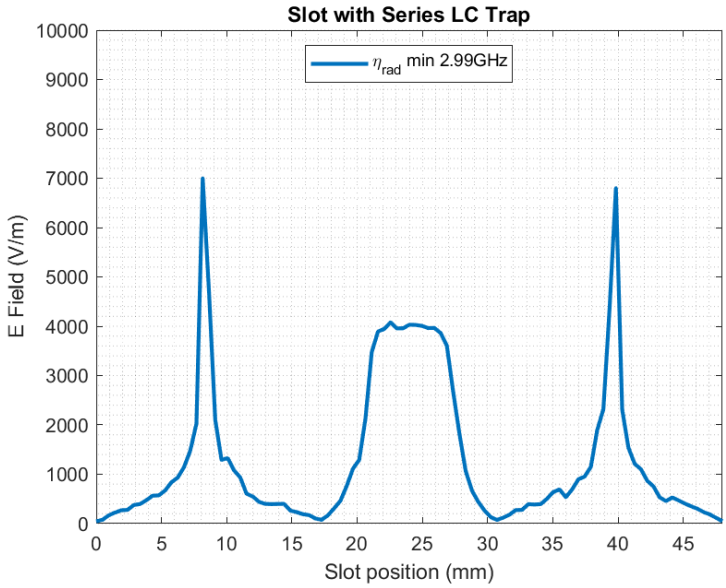


Figure 7.14: E field, rescaled with just minimum η_{rad} trace

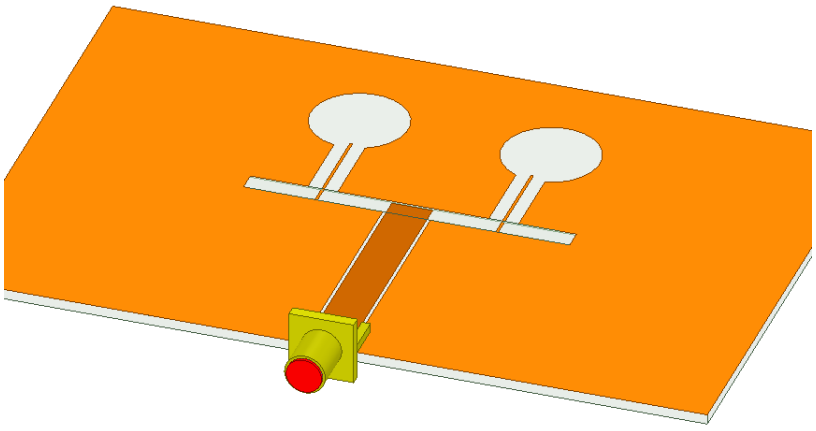


Figure 7.15: CPW fed slot antenna with open circuit CPW stubs to create a trap dual-band response

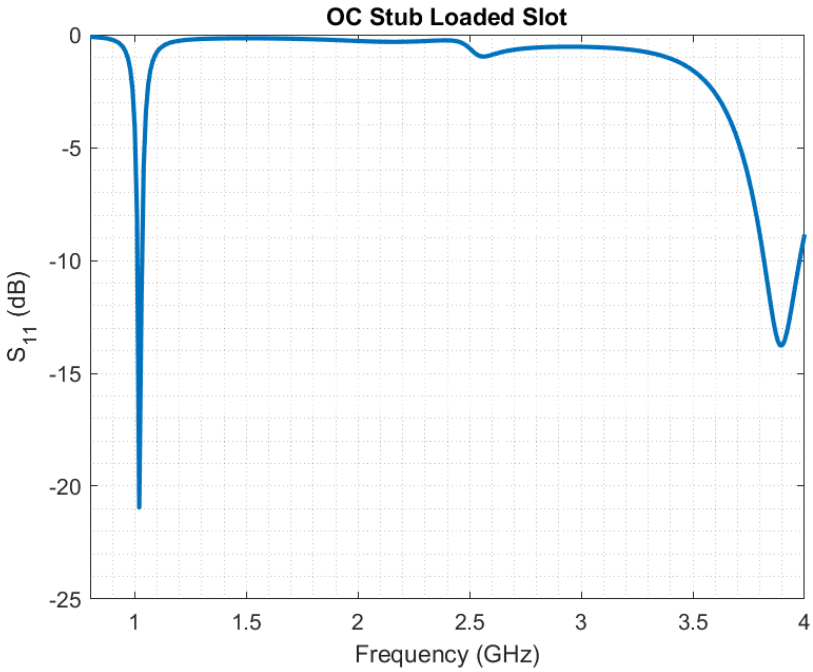


Figure 7.16: CPW fed slot antenna with OC CPW stubs, dual-band response

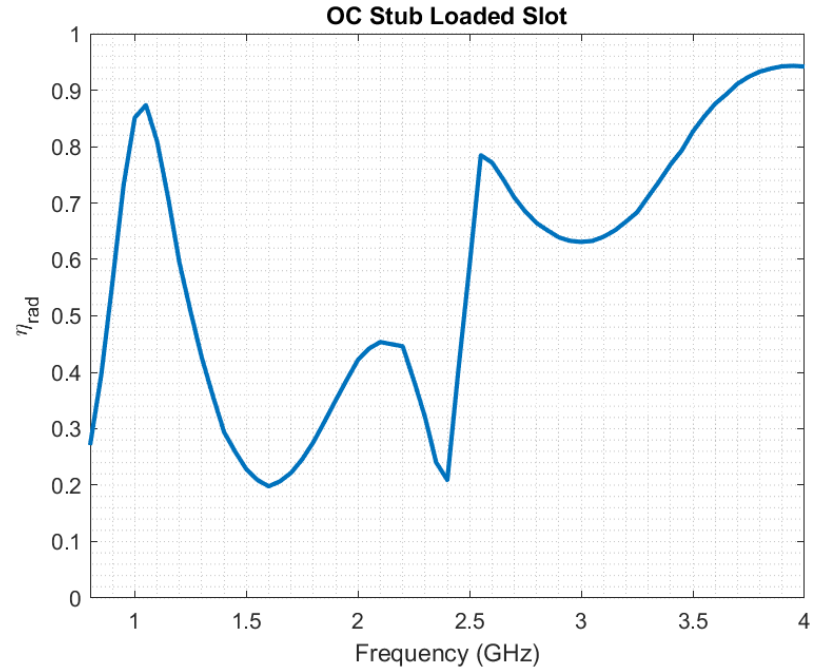


Figure 7.17: CPW fed slot antenna with OC CPW stubs, good radiation efficiency at both operating frequencies, significant dip in between

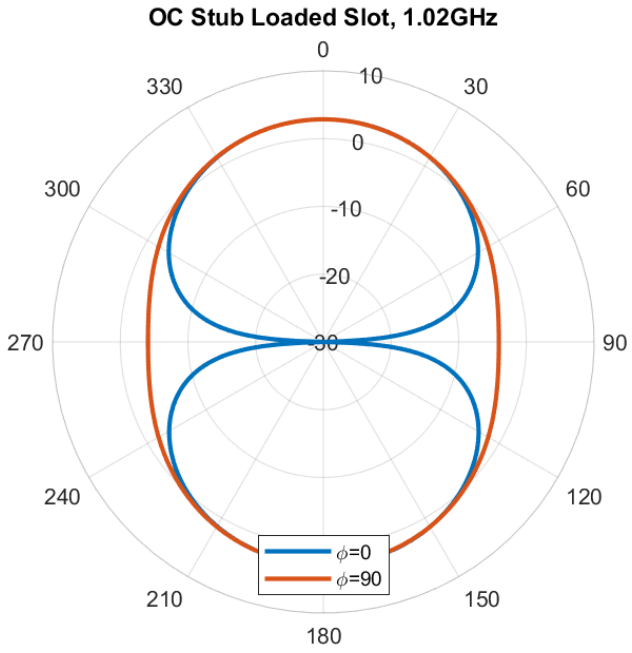


Figure 7.18: CPW fed slot antenna with OC CPW stubs, typical slot realized gain pattern at lower operating frequency

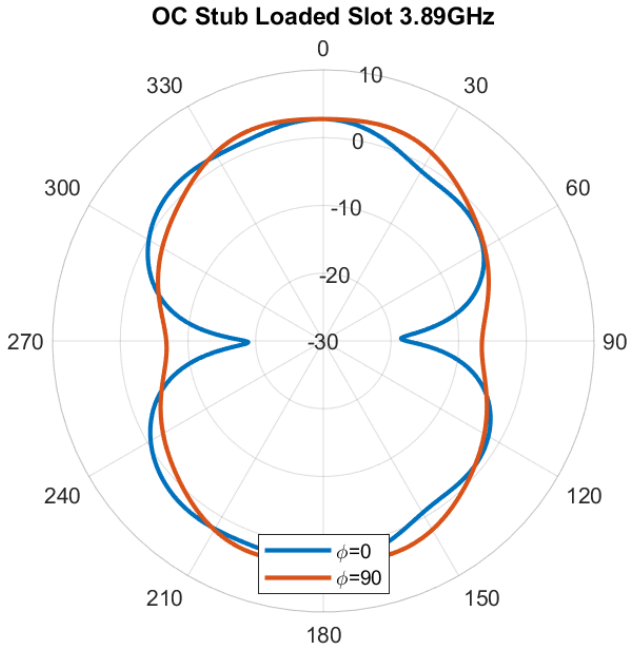


Figure 7.19: CPW fed slot antenna with OC CPW stubs, typical slot realized gain pattern at upper operating frequency

I've demonstrated a slot antenna with OC stubs to enforce a dual-band trap behavior. The series CPW stubs are $\lambda/4$ at 3.9 GHz and create an SC condition at the slot radiator. The lower frequency of the antenna was originally meant to be 2 GHz but has been lowered to 1 GHz. The stubs present a reactive load of -343 jΩ at 1 GHz, which makes sense that it would substantially lower the resonance. This could also be explained by saying that the slot length increased due to the stubs.

If an antenna has point loads with a known reactance, it stands to reason that the loads can be arbitrarily replaced with any other load that provides the same reactance at the same point and frequency. If a slot antenna is designed to be dual-band through the addition of series LC traps, the LC resonators can be replaced with stubs or any other resonator that provides the same reactive loading at the same point and frequency. Substituting loads will be more complicated if the loads need to have the same impedance across frequency.

7.8 Conclusion

In the previous chapters, I demonstrated that trap loaded dipoles operate based on reactive discontinuities and demonstrated new designs, such as the series LC loaded dipole and the dual-band resonant length inductor loaded dipole. This chapter demonstrated novel trap slot antennas, which are the dual of trap dipole antennas.

RLC loads short across the slot and create a new smaller current path than the full perimeter of the slot. Adding stubs to the slot increases the total perimeter of the current path around the slot. The circuit model for the cavity resonator indicates that it can be a short to ground (whether strongly reactive or not depends on whether the connections are bandpass or bandstop). However, the voltage differential and current return path created by the cavity (reactively) shorting to ground is not necessarily the same as the RLC loads shorting across the slot gap.

I demonstrated novel dual-band trap slot antennas with discrete LC loads. The trap slot antenna has a quasi-first mode response at both frequencies which guarantees a radiation pattern free of beam splitting and other unwanted distortions that occur from higher order modes. The antennas are cheap and easy to fabricate, and the demonstrated series and parallel LC loads can be substituted with other resonator structures with equivalent reactance. The trap slot antenna can be used as a design framework for a broad variety of multiband slot antennas.

In the next chapter, I present measurements for trap dipoles and slots. After that, I design a reconfigurable resonator loaded slot antenna based on this chapter's analysis.

Chapter 8

Trap Measurements

8.1 Introduction

This chapter will briefly review the design process for trap antennas before presenting measurements for several monopoles and slot trap antennas. The reflection coefficient, realized gain radiation patterns, and realized gain across frequency was measured for all antennas. Realized gain is easier to measure than radiation efficiency, although it can be tricky to separate increases in loss versus directivity changes.

Neither the unloaded dipole or the unloaded slot has a significant increase in loss at a narrow range of frequencies. A 2 GHz ribbon dipole with 5880 substrate backing (equivalent to the fabricated monopoles) has a simulated radiation efficiency of near 100% over the range of its first three resonances (two series resonances and one parallel resonance). The broadside realized gain only varies between +2.3dB to -2.3dB.

An unloaded slot with 60 mil TMM3 backing has a first resonance at 2.3 GHz and a second resonance associated with the $3\lambda/2$ mode at 4.8 GHz. The simulated radiation efficiency is over 92% from 2 to 5 GHz. The direction of max gain from a slot antenna changes significantly based on the ground plane's electrical size. Even with an infinite

ground plane, the beam still splits at the second series resonance, so a constant angle cannot be used to evaluate broadside realized gain over frequency. Any decreases in radiation efficiency shown in measurements result from adding loads to the dipoles and slots.

8.2 Design Process

Both series and parallel trap loads can always be used to create dual-band behavior. There are existing design equations for inductively loaded wire radiators, but they cannot be directly applied to trap loaded wire radiators because trap antennas have resonant lengths instead of being electrically small. Inductor loads lower the fundamental resonance of a wire radiator and are often used to enforce resonance on electrically small radiators. The inductor loading design process assumes that the operating frequency, f_1, is below the unloaded antenna's first resonance. The unloaded antenna would then be capacitive at f_1, and the inductor load would cancel out the capacitance to enforce a new resonance at f_1. This does not match either the series or parallel trap dipoles, and it also does not describe the use of a single inductor to create a trap-like discontinuity.

Series RLC loads can be used to create a dual-band trap dipole, which has not been demonstrated in the literature. It is not any more complicated and can be done with realistic RF component inductor and capacitors (20 nH and 0.31 pF). Furthermore, the series trap dipoles' design only makes sense because traps provide finite reactive discontinuities rather than true open circuits. I proved that a dual-band trap dipole-like antenna can be made with just inductor loads, and I also created a dual-band trap dipole with series RLC loads.

In the parallel case, the unloaded dipole has a fundamental resonance at f_1, and the addition of parallel LC resonators introduces a slight inductance around f_1 that will tune the resonance lower in frequency. At the upper operating frequency f_2, the trap has a much larger inductance value but is also at the end of the effective radiator, so the impact of its

loading is lessened.

In the series case, the unloaded dipole has a fundamental resonance at f_1, and the series trap load is tuned to present a short at that frequency and introduces minimal loading. At the upper operating frequency f_2, the series trap is designed to introduce a discontinuity of the same magnitude of inductive reactance that the corollary parallel trap dipole would have. This would again mean that the effective radiating length would have a large inductive load at the very end of the radiator, so its impact on tuning would be minimal.

In the dual-band inductor case, the inductor would lower the first resonance of the antenna. However, the inductor is chosen to have the same magnitude of reactance as the parallel and series traps have at f_2. At this upper frequency, the inner length radiator has a strongly inductive load located at a point of minimal impact (the open ends). In all of these cases, the load inductance also significantly lowers the $3\lambda/2$ mode's resonance and tunes it to be between f_1 and f_2.

In theory, monopole impedance is half of the dipole 73 Ω or 36.5 Ω. I increased the ground plane $\lambda/2$ square to λ, and the impedance increased from 25 to 33 Ω, which gives a match of -17 dB to a 50 Ω SMA connector. Note that in simulation, de-embedding through the SMA connector is necessary to view the monopole impedance.

To demonstrate, I will outline the design of all three types of loaded antennas with dual-band 1.2 and 2.4 GHz resonances. The design starts with an unloaded antenna with a resonance of 1.2 GHz, 0.475λ=118.75 mm at 1.2 GHz. The inner length is estimated to be about 0.52λ at 2.4 GHz, or 65 mm. The trap should be antiresonant slightly above 2.4 GHz, so the design starts with L=1 nH and C=4 pF, which is resonant at 2.5 GHz.

A quick HFSS simulation confirms the design is basically accurate, with operating frequencies at f_1=1.16GHz and f_2=2.46GHz. A 3mm ribbon width was used for the dipole.

The parallel trap design can be converted to a series trap quite simply. The resonator is first retuned to 1.2 GHz to define a short at f_1. In this case, I start with values of C = 4.5 pF

and L = 3.9 nH. The L to C ratio is then retuned to have the same reactance X_{trap} at f_2 that the parallel 1 nH and 4 pF trap had. Parallel X_{trap} = 348 jΩ at 2.46 GHz, and the same reactance is required from the series trap. The first guess of 4.5 pF and 3.9 nH is 46 jΩ at 2.46 GHz. Increasing the ratio of L/C will increase impedance. A range of impedances can be quickly calculated in Matlab by creating a vector of L to C ratios with a constant resonance. With L = 31.2 nH and C = 0.56pF, the series trap has an impedance of 367 jΩ at 2.46 GHz. HFSS simulation predicts operating frequencies of 1.44 GHz and 2.42 GHz. Practically, it might not be possible to source an RF inductor of 30nH with a high enough SRF to use in this design.

The inductor on the dual-band inductor loaded dipole must have the same reactance at 2.46 GHz. 22.5nH is 348jΩ at 2.46 GHz. The pure inductor load will lower the resonance of f_1, but the dipole's outer length can be made shorter to compensate. HFSS simulation predicts the operating frequencies to be 0.95GHz and 2.7GHz.

8.3 Fabrication Concerns

RF inductors and capacitors have a specified self-resonant frequency (SRF). Data sheets will often include measurements of the reactance value at several frequency points, but it is usually unclear how close to the SRF the component can be used before the expected value changes significantly. This depends on the specific technology used for a capacitor or inductor. The self-resonance shape depends on the Q of that effective resonator, so the higher the Q, the sharper the transition, which means that the component values hold longer (or closer to the SRF) [82]. The best way is to look at the measured component data (hopefully provided) and draw a line representing the maximum deviation acceptable. I have 15 nH inductors from Coilcraft with a stated SRF of 3.9 GHz. It is possible that the 15nH inductor would work okay at 3 GHz, but likely not at 3.5 GHz.

8.4 Parallel LC Trap Monopole

The fabricated parallel LC trap monopole antenna has an 0402 sized inductor, and capacitor hand soldered to a ribbon radiator on a 31mil 5880 substrate, which was etched through a photolithography process, Figure 8.1. Duroid 5880 is a low dielectric constant substrate, so it minimally loads the radiator. The trap junction is closer to ideal point loading when there is less dielectric loading because the dielectric minimally increases the junction's electrical length. A thinner board also decreases loading, but the board must still be thick enough to remain rigid. The trap has a 1 nH inductor (16 GHz SRF) and a 1.6 pF capacitor (6.7 GHz SRF).

The ground plane substrate is a 60 mil 4350 board and is 6x6", which is approximately λ x λ. The ground plane substrate thickness and material have minimal impact on the antenna. Again, the substrate material and thickness should be selected to be rigid. The ground plane's length and width have a significant impact on the input resistance magnitude at resonance. In simulation, a monopole with a $\lambda/2$ x $\lambda/2$ ground plane is only 25 Ω at resonance. By increasing the ground plane size to λ x λ, the input resistance increases to 33 Ω, which is near to the ideal value of 36.5 Ω and is a better impedance match to a 50 Ω connector. Ideally, monopoles have half the input resistance as dipoles at resonance or 73 Ω/2=36.5 Ω.

The capacitor has a tolerance of $\pm$0.02 pF and a series resistance of 155 mΩ. The inductor has a tolerance of 5% ($\pm$0.025 nH) and a series resistance of 30 $m\Omega$. The loads could be 1.62 pF and 1.025 nH or 1.58 pF and 0.975 nH in reasonable worst-case scenarios. The 3.98 GHz trap resonance would shift down to 3.91 GHz or up to 4.05 GHz. In simulation, changing the component values shifts the upper operating frequency from -18 dB at 3.86 GHz to -17.6 dB at 4 GHz. The lower resonance is not visibly changed. In both cases, the match is not significantly degraded, and even the realized gain magnitude re-

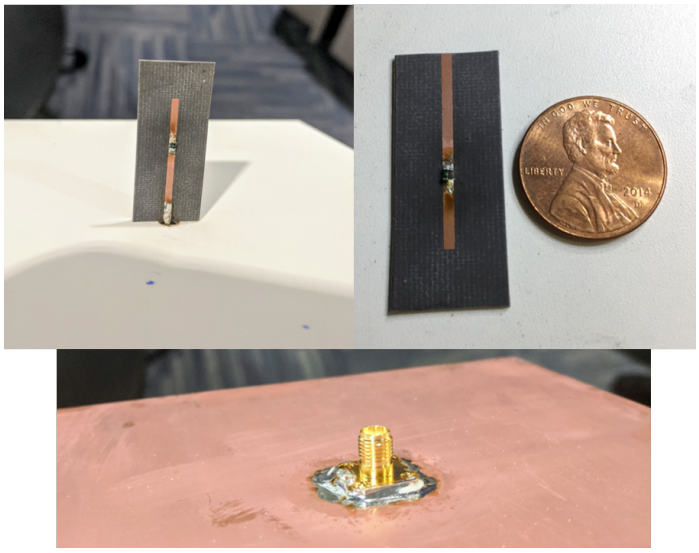


Figure 8.1: Fabricated monopole with parallel LC trap, 1.6 pF and 1 nH

mains mostly unchanged while the frequency shifts from -36.6 dB at 3.72 GHz to -32.2 dB at 3.85 GHz.

The fabricated trap monopole was measured on a network analyzer, Figure 8.2. The measured lower operating frequency is -17.49 dB at 2.372 GHz, and the upper operating frequency is -10.79 dB at 3.772 GHz. The HFSS simulation predicted a -15.83dB match at 2.36 GHz, and a -18.20 dB match at 3.94 GHz, with a range from 3.86 dB to 4 GHz. The fabricated antenna upper operating frequency is 88 MHz below the simulated lower tolerance bound.

A 3D printed mount was used for the elevation cut and shown in Figure 8.3. The maximum measured realized gain value at the lower operating frequency is 1.98dB at -52°, compared with simulated values of 0.24dB at -54°. At the upper operating frequency, the maximum realized gain is 2.41dB at -54°, compared with a simulated value of 2.9dB at -55°.

The maximum measured gain at the lower operating frequency is 1.6dB at 60°, compared with simulated -0.92dB at -135°. The maximum measured gain at the upper operating

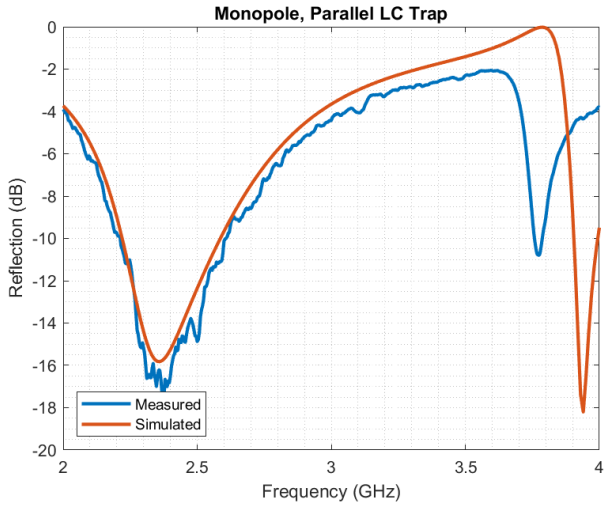


Figure 8.2: Measured and simulated parallel trap S11. The measured lower operating frequency is -17.49 dB at 2.372 GHz, and the upper operating frequency is -10.79 dB at 3.772 GHz. The HFSS simulation predicted a -15.83dB match at 2.36 GHz, and a -18.20 dB match at 3.94 GHz.

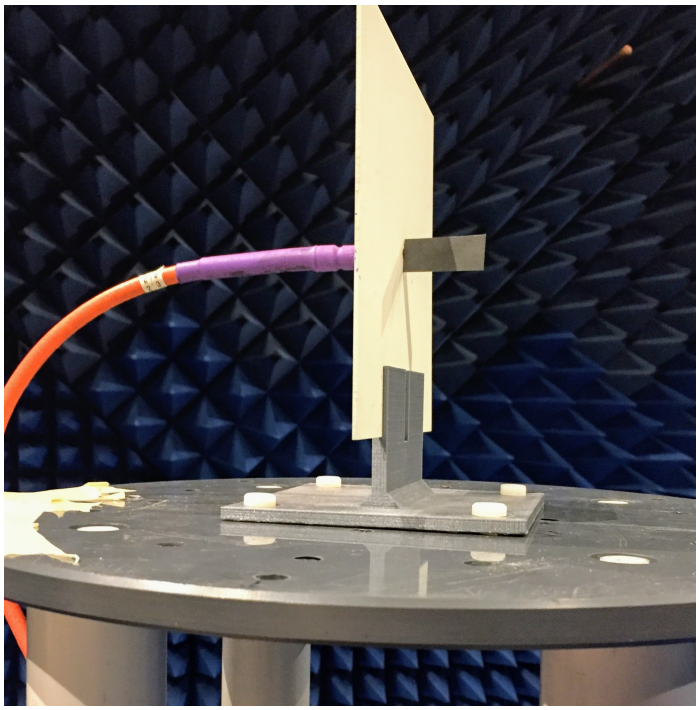


Figure 8.3: Elevation measurement in anechoic chamber, 3D printed mount

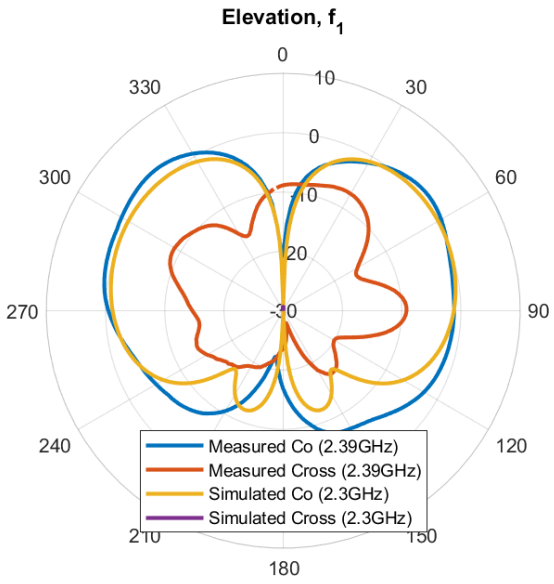


Figure 8.4: Elevation cut at f_1

frequency is -2.65dB at -10°, compared with simulated -0.28dB at -68°.

The monopole has a measured realized gain dip to -9.3 dB at 3.682 GHz, compared with a simulated value of -25.7 dB at 3.78 GHz, Figure 8.9. In simulation, the capacitor and inductor detuned within the specified range of component tolerances shifts the realized gain dip from -36.6 dB at 3.72 GHz to -32.2 dB at 3.85 GHz. The measured dip is 38 MHz below the lower tolerance bound, which is likely due to parasitic capacitance in the trap junction. I was concerned that measurement values were near the chamber's noise floor, but measurements of subsequent antennas go much lower in magnitude. The only remaining solutions are excessive parasitic capacitance, component loss, and cable currents. However, the realized gain reduction is more significant than the limited range that the simulated unloaded dipole had.

Subsequent calculation of the load values revealed that the loads have lower than recommended Q. The load impedance at 2.372 GHz is 0.3+j17 Ω, with a range of 0.3+j16 Ω to 0.3+j19 Ω due to component tolerance. The load impedance at 3.776 GHz is 5+j85.21 Ω,

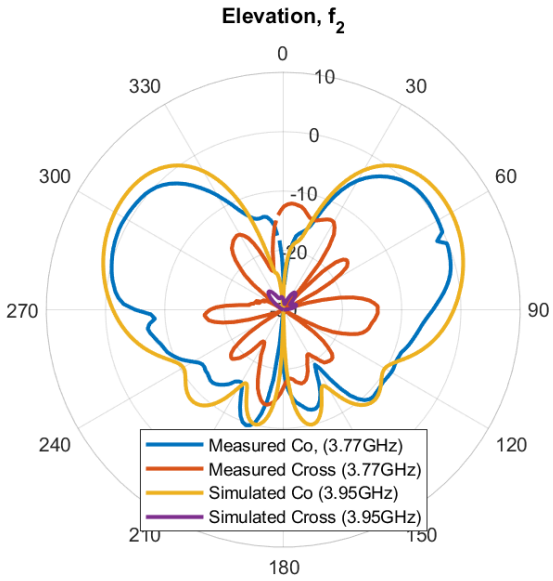


Figure 8.5: Elevation cut at f_2

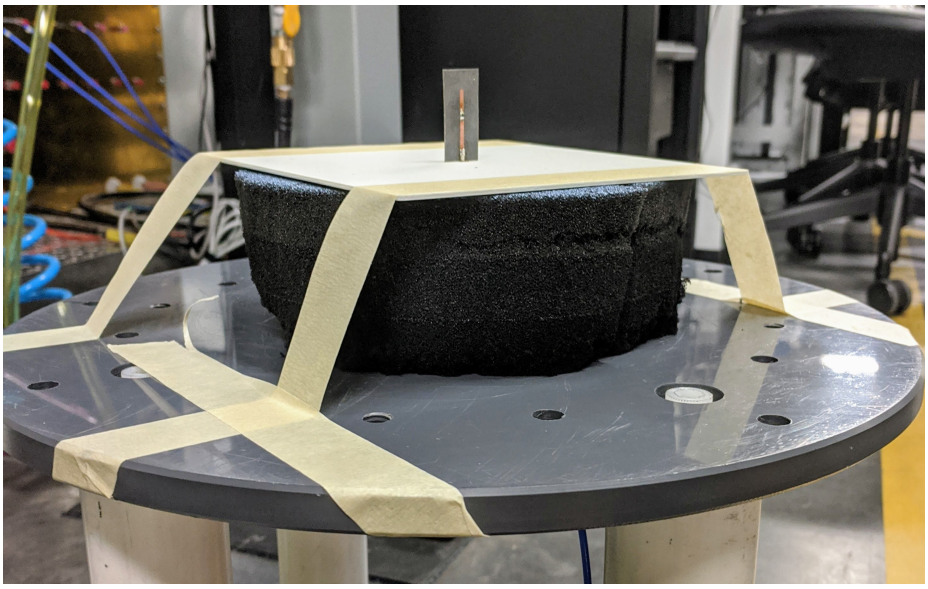


Figure 8.6: Azimuth measurement

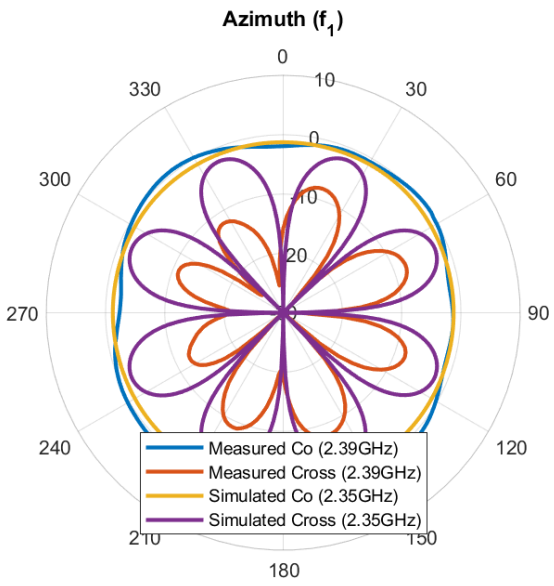


Figure 8.7: Azimuth cut at 2.37 GHz

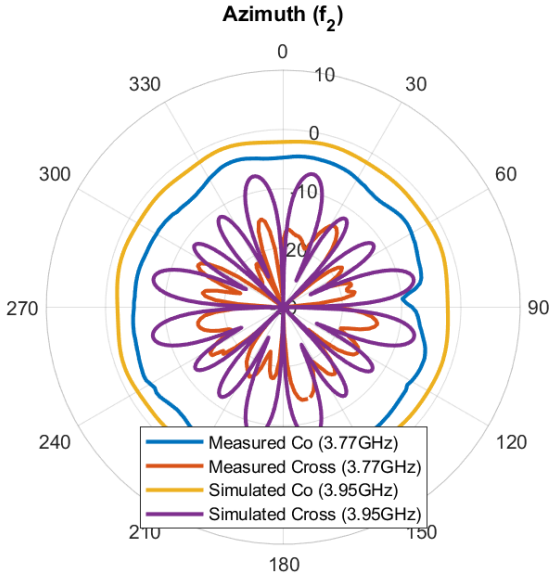


Figure 8.8: Azimuth cut at 3.77 GHz

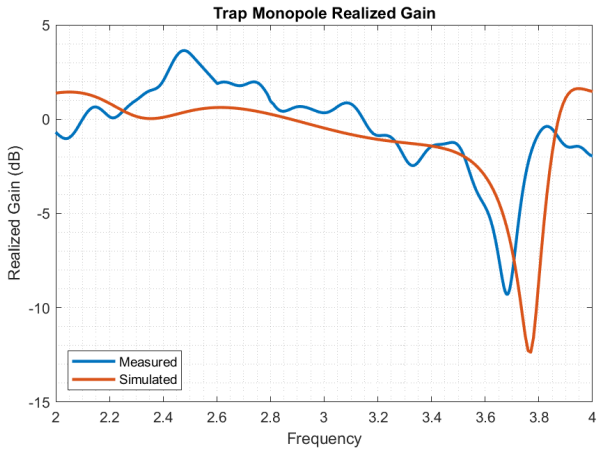


Figure 8.9: Max realized gain over frequency of trap monopole antenna, decrease at 3.78 GHz

with a range of 3+j67 Ω to 8+j114 Ω due to tolerance. The load resonance occurs about 0.513 GHz from the upper impedance match, with a range between 0.651 to 0.385 GHz. The resulting load Q value at 3.776 GHz is about 182. The parallel LC trap is not resonant at the same frequency as the antenna upper operating frequency.

For comparison, Wheeler cap measurements were also taken, and the measured radiation efficiency dips to 16% at 3.72 GHz. The frequency is in near agreement with the measured dip in realized gain.

The first set of measurements proves a significant dip in radiation efficiency near the antenna operating frequency, but not actually at the operating frequency. The measurements also prove that the upper operating frequency is not at the trap resonance.

8.4.1 Time Gating

The far-field measurements were taken in the large chamber at the Radar Innovations Lab, intended for 300 MHz to 30 GHz measurements. At S-band, the expected reflection in the chamber is around -35dB. The monopole measured data dips close to the expected reflection threshold at its lowest values, Figure 8.12. Moreover, looking at the gain across

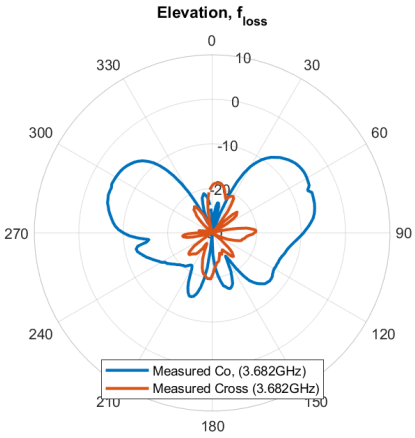


Figure 8.10: Radiation pattern at 3.68 GHz, the frequency at which realized gain is a minimum. The gain at all angles is reduced, indicating increased loss, rather than a change in directivity over angle.

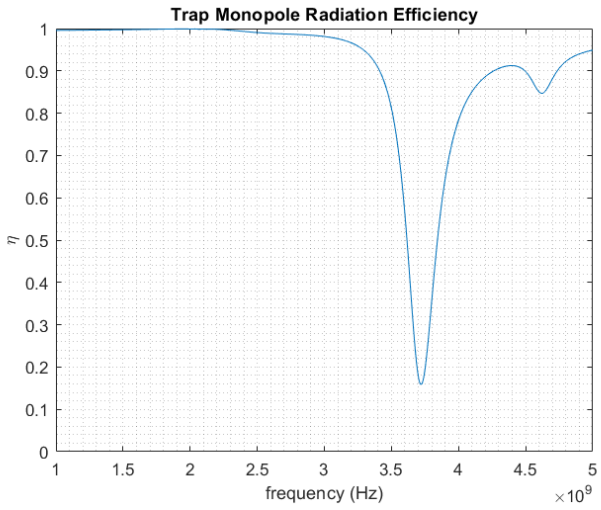


Figure 8.11: Radiation efficiency of trap monopole antenna from Wheeler cap measurement

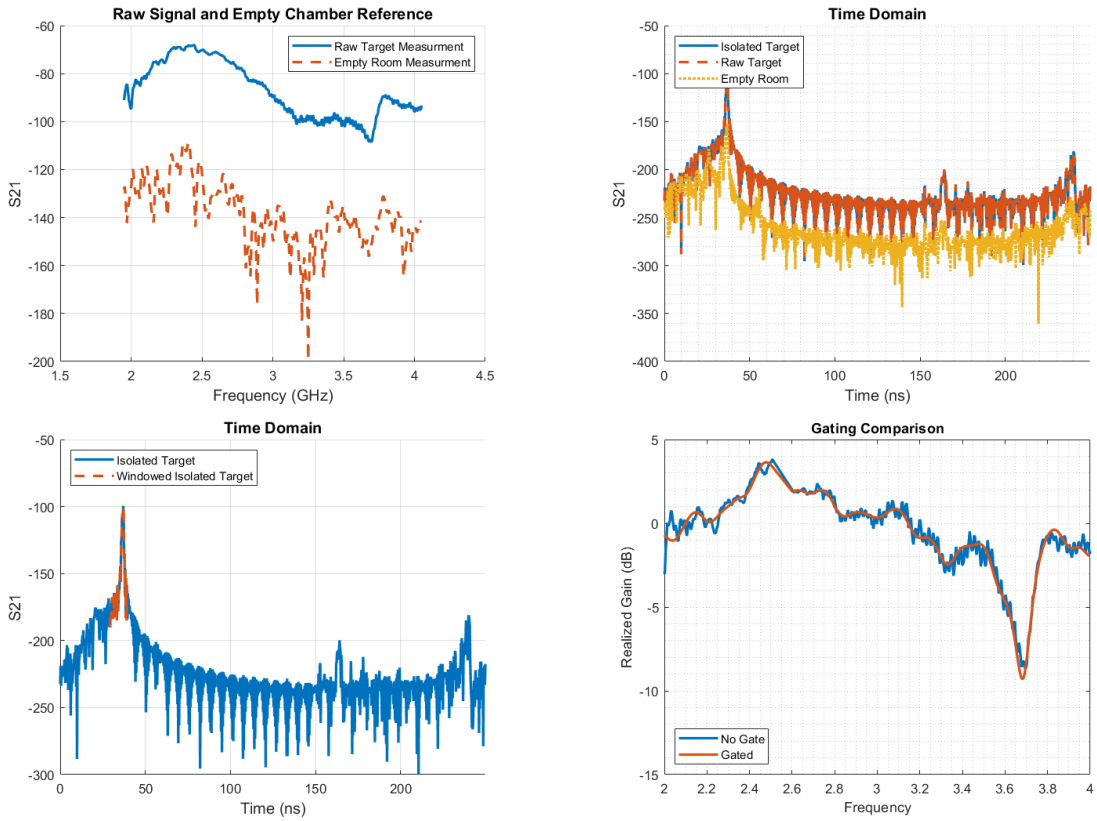


Figure 8.12: a) Uncalibrated monopole gain at maximum gain and at antenna null b) Time domain of antenna return and empty room return c) Time domain of raw data and time gating d) Removed reflections

frequency reveals a large amount of noise, possibly due to reflection. I used a time-domain gating algorithm developed by Rachel Jarvis and based on [83], [84] to remove unwanted ripples in the data due to reflections.

An empty chamber vector subtraction was used in addition to time gating. The empty chamber vector was taken from the measurement of the monopole and gain horns at null angles.

Measuring the broadside realized gain across frequency is a less common measurement and requires careful setup. In the first set of measurements, we used an IF bandwidth of 10kHz and set a frequency resolution of 10 MHz. The data showed noise, and the received signal magnitude was near the chamber's reflection noise floor. The chamber has

an estimated reflection level of about -35 dB in S-band. The measurement system has a built-in 20dB amplifier, and there is about 30dB of cable loss at 0.5dB per foot of cable.

I used time-domain gating to reduce noise from chamber reflections. The measurement frequency resolution sets the time and range bin size. The maximum unambiguous range is defined as

$$R = \frac{v_p}{2\delta f} \tag{8.1}$$

where R is the unambiguous range, the phase velocity v_p varies between free space and the Teflon in the cables, and δf is the frequency step size. Larger range values fold down into a closer range. The chamber has 18.3 m (60 ft) of cable between ports on the network analyzer, and the antenna pedestals are 7.2 m (23.6 ft) apart. The equivalent free space distance, modified by the dielectric constant of Teflon in the cables is 34.3 m. The travel time should be 114 ns between ports on the network analyzer. The travel time between the reference frames of the two pedestals is 24 ns. 4.4 MHz is the largest recommended time step to isolate the target from the main reflection successfully.

A wider IF bandwidth lets in more noise, and the noise is evenly distributed across all frequencies and time. While preferable for noise, a lower IF bandwidth also increases the length of time a measurement takes. Each angle is expected to take about 5 seconds with a frequency resolution of 4 MHz over a 2 GHz sweep. A measurement across frequencies, AUT angle, and both orientations of the measurement horn takes about 30 minutes with these settings. The length of time for measurements sets a lower bound on the frequency step and IF bandwidth.

With the time gating code, I am using square window functions. The windowing tends to distort the edges of the band. To counteract this, I intentionally measured from slightly below 1 GHz or 2 GHz (depending on the antenna), to slightly above 4 GHz, to push the

windowing effects out of band.

8.4.2 Wheeler Cap

A Wheeler cap is a conductive cavity placed around an antenna that effectively shorts out the far-field radiation. With the use of only a network analyzer, the user can separately measure the antenna's input impedance with and without radiation resistance and derive radiation efficiency [85]. The Wheeler cap method was initially used for evaluating the radiation efficiency of electrically small antennas with a backing ground plane. The ideal cap is a conductive half-sphere that shorts to the antenna's ground plane and has a radius of $\lambda/2\pi$ at the antenna operating frequency. The cap walls are spaced away from the antenna at the transition point to the far-field to minimally couple to the antenna, which would change the input impedance beyond just removing the radiation resistance. The cap is also sized small enough to avoid cavity modes at the operating and measurement frequency. This method is ideal for ground plane backed electrically small monopoles measured at a single frequency. Measuring resonant length antennas and measuring over a range of frequencies will typically make it impossible to avoid exciting cavity modes, and several methods have been developed to calibrate out the cavity modes [86]–[88].

The method in [86] is the only one that accommodates multiresonant antennas. Wheeler cap solutions convert the vector reflection measurement to input impedance and then model the antenna resonance as a parallel or series resonance. Cavity resonance effects can be moved out of band in post-processing by rotating the measurement around the Smith chart, effectively adding a transmission line between the antenna and analyzer [87]. Parallel admittances were found to be a better model for multiresonant antennas. The algorithm in [86] combines parallel admittances for each antenna resonance with a rational fitting function to provide a modal decomposition of the input admittance. Equivalent circuits are

constructed for both the free space and Wheeler cap antenna measurements, and the two are combined to create a free space model of the antenna with separately identified loss and radiation resistances. Poles in the admittance of the free space antenna measurement appear substantially at the same frequencies as the Wheeler cap measurement, and additional poles due to cavity resonances are filtered out. The specific RLC component values used in the recreated free space response are determined by using a genetic algorithm for a minimum least-squares fit.

8.5 Series LC Trap Monopole

There are additional problems with designing a trap dipole with a series LC load. A large L/C ratio is required so that the trap can be a short at f_1 and be about 350 jΩ at f_2. Having a larger separation between f_1 and f_2 allows more space for the the reactance to increase from the mandatory 0 jΩ at f_1 to about 350 jΩ at f_2. However, if the ratio of f_2 to f_1 is greater than 3:1, the unloaded $3\lambda/2$ mode is matched at or below f_2. Though this could be used as a third passband if desired, increasing the number of modes makes the analysis more complicated and is undesirable in this demonstration. For a specific design, I have 15 nH inductors that I estimate can be used as high as 3 GHz due to the inductors' self-resonant frequency. I choose f_2 to be about 3 GHz, and choosing f_1 and f_{trap} to be slightly higher than 1 GHz maximizes the reactance at f_2. A 15 nH inductor, combined with a 1 pF capacitor, is resonant at 1.3 GHz and is 230 jΩ at 3 GHz. This reactance is not large enough to create a passband at or near 3 GHz. A larger inductor than 15 nH would have an even lower self-resonant frequency.

To further increase loading within the SRF constraint, I simulated using multiple inductors in series with gaps between the inductors to allow space for soldering. Two 15 nH inductors and a 0.3 pF capacitor with realistic spacing create a dual-band response sim-

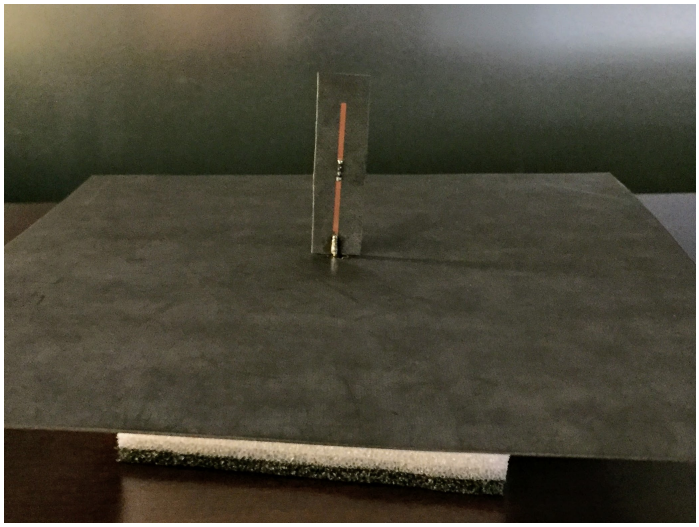


Figure 8.13: Fabricated series LC trap monopole

ulated with -18 dB match at 1.43 GHz and -11 dB match at 3.25 GHz. The fabricated antenna is shown in Figure 8.13, and has operating frequencies at 1.44 GHZ and 3.22 GHz, Figure 8.14.

The series LC trap loaded monopole is a new addition to the literature of trap dipoles. The S parameter measurements confirm that the dipole is dual-band, with the upper operating frequency created by a specific finite trap reactance, rather than a near infinite open circuit commonly assumed to be essential for trap antennas.

The radiation pattern at both frequencies is a typical monopole radiation, as shown in Figures 8.15.

8.6 Inductor Loaded Dual Band Monopole

To further emphasize that the trap dipole is dependent on finite reactive loads rather than infinite opens, an inductor loaded monopole was fabricated. The lower operating frequency is tuned slightly lower because of the inductor, and the upper operating frequency is created by selecting an inductor value that provides the same reactance magnitude as provided by

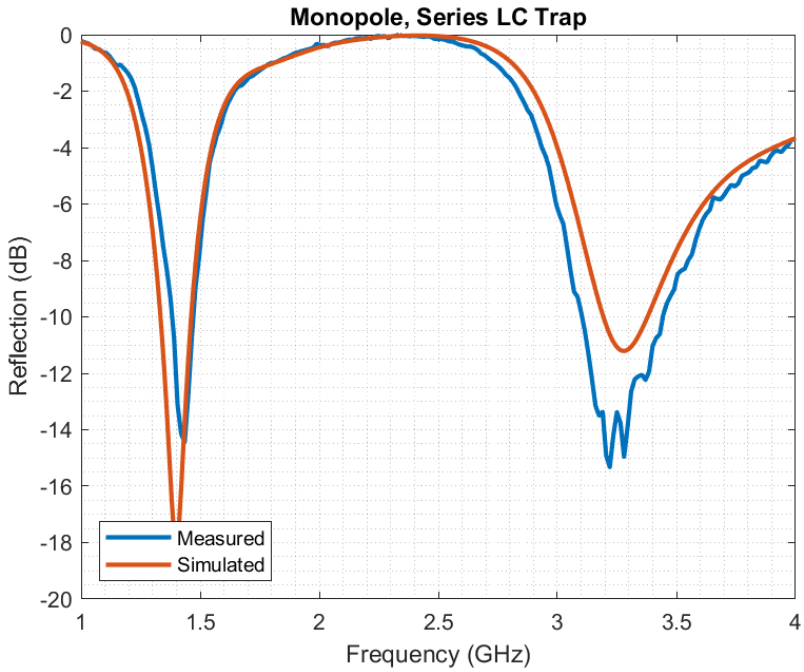


Figure 8.14: Measured and simulated reflection coefficient of dual-band monopole with series LC load. The LC is tuned to be a short at the 1.44 GHz, and provides the same reactance magnitude at 3.22 GHz as a more conventional parallel LC trap, proving that trap dipoles operate at finite reactive loads rather than open circuits.

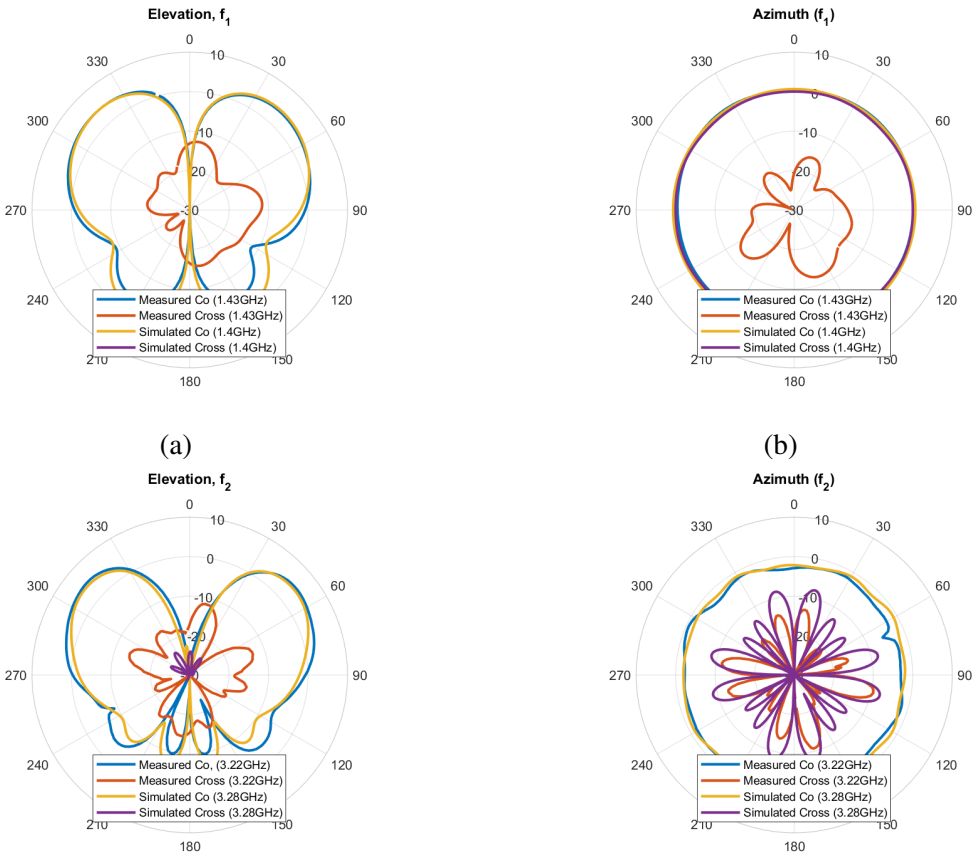


Figure 8.15: Series LC monopole, elevation and azimuth realized gain radiation patterns a) Elevation cut at GHz b) Azimuth cut at GHz c) Elevation cut at GHz d)Azimuth cut at GHz

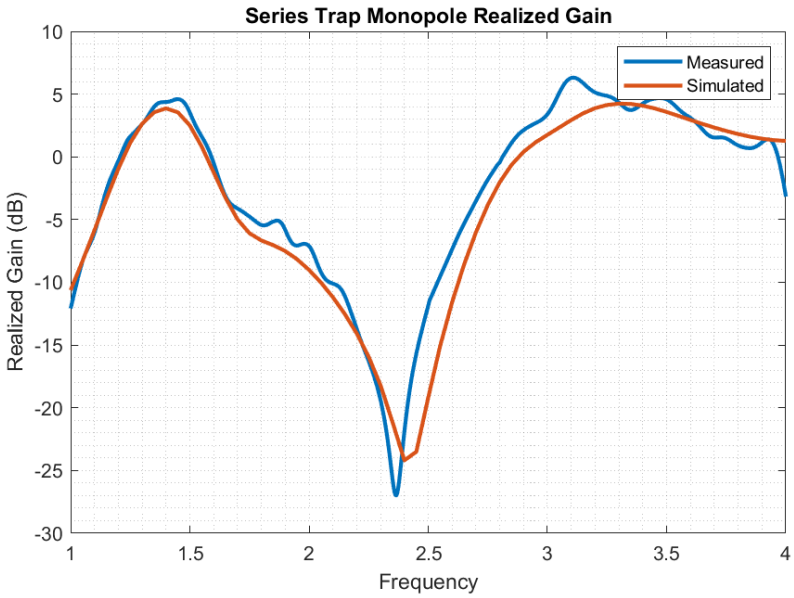


Figure 8.16: Realized gain across frequencies at the angle of maximum directivity, $\theta = -54^{\circ}$

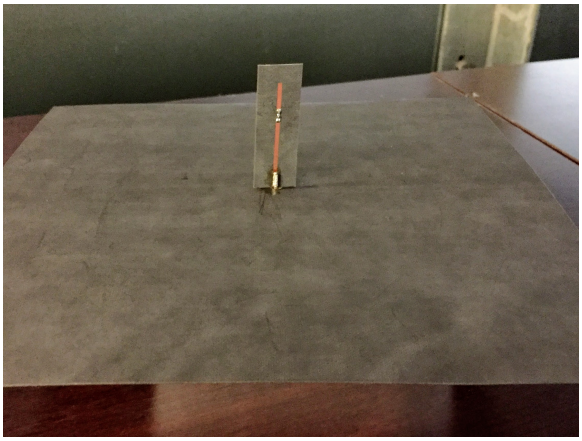


Figure 8.17: Fabricated dual band $\lambda/4$ monopole with inductor load

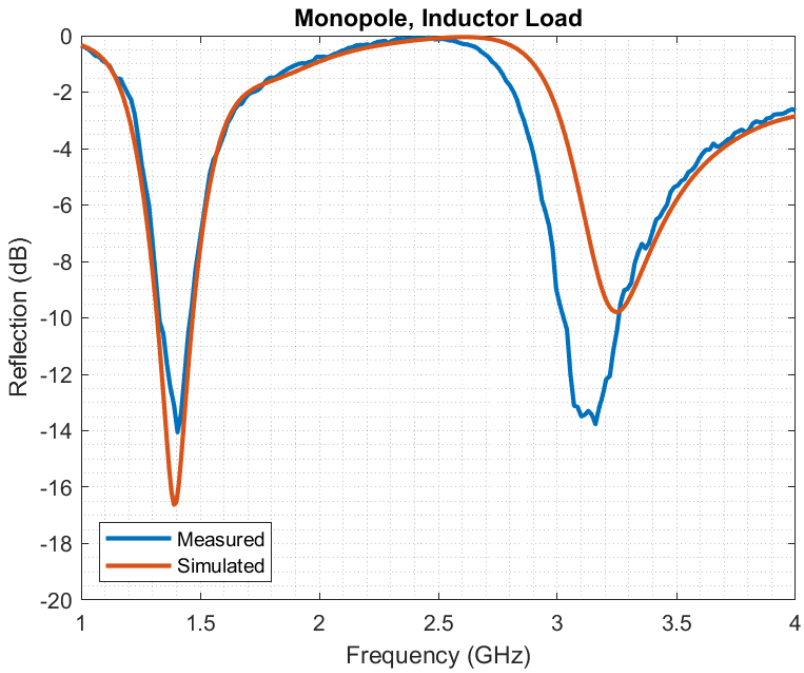


Figure 8.18: Measured and simulated reflection coefficient of dual-band monopole with only an inductor load. The inductor value is chosen to provide the same reactance magnitude at the upper operating frequency as would be caused by a more conventional parallel LC trap, again emphasizing that trap dipoles operate at finite reactive loads rather than at the trap antiresonance open circuit.

a traditional parallel LC trap monopole.

As mentioned previously, electrically small monopoles loaded with inductors are well characterized in the literature. Loading resonant length monopoles with inductors is less common. The theoretical basis for trap dipole design can be used to create a dual-band inductor loaded monopole because trap dipoles are based on finite reactive loading rather than open circuit loading. The fabricated dual-band monopole is shown in Figure 8.17. Two inductors had to be used in fabrication to have a large enough inductance for the design while still operating below the inductors' self-resonant frequency. Larger inductor values usually have lower SRFs. The monopole has operating frequencies at 1.41 GHz and 3.16 GHz.

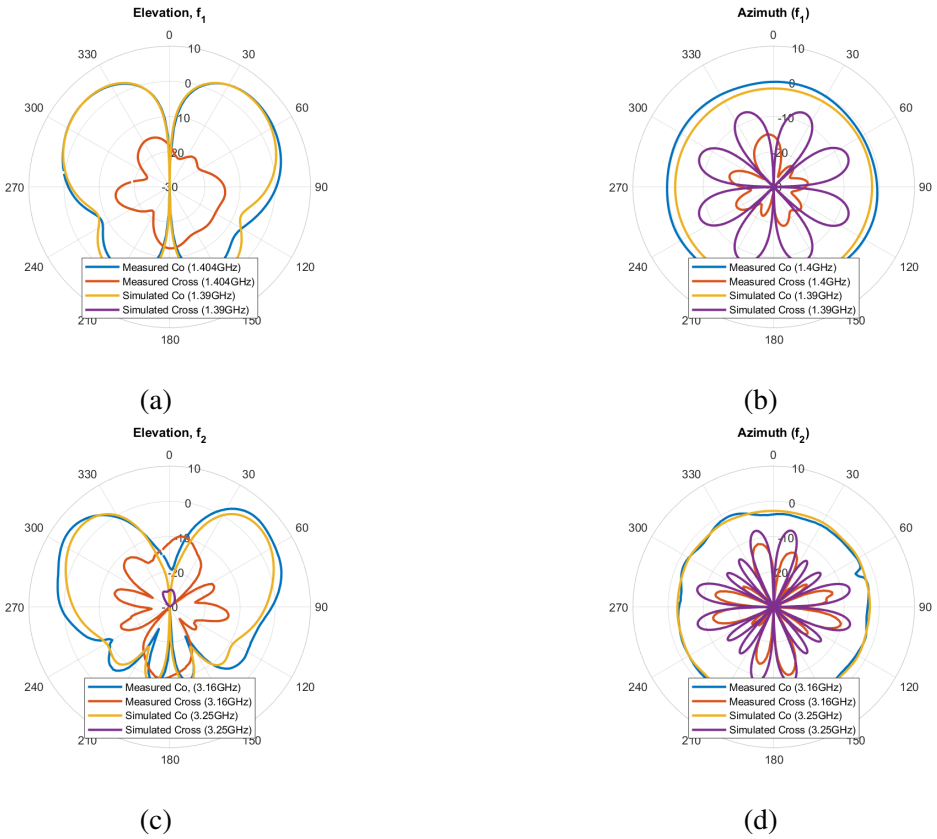


Figure 8.19: Inductor monopole, elevation and azimuth realized gain radiation patterns a) Elevation cut at GHz b) Azimuth cut at GHz c) Elevation cut at GHz d)Azimuth cut at GHz

The antenna operating frequencies have typical monopole radiation patterns, Figure 8.19, which indicates that the radiation is caused by first-mode type current distributions at both frequencies.

The load impedance at 1.405 GHz is 2.6+j183 Ω, with a range of 2.6+j174 Ω to 2.6+j192 Ω due to component tolerance. The load impedance at 3.16 GHz is 7+j514 Ω, with a range of 7+j489 Ω to 7+j540 Ω due to component tolerance. The resulting load Q value at 1.405 GHz is about 71. The inductor loaded monopole has typical monopole radiation patterns at both operating frequencies, shown in Figure 8.19.

The realized gain across frequency has a maximum value of around -54°, varying only a degree or two over the measurement range. A sharp decrease in gain occurs at 2.4 GHz,

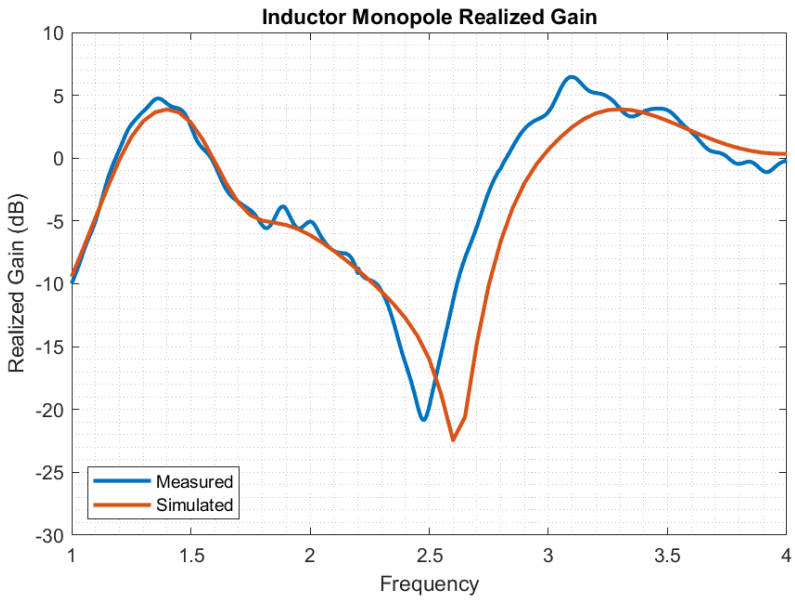


Figure 8.20: Inductor loaded monopole realized gain, sharp decrease in gain at GHz

Figure 8.20. The reference unloaded monopole has no comparable decrease in gain over the range encompassing the first three resonances. The radiation pattern at the minimal realized gain frequency does not show any beam splitting or a shift of directivity, which indicates that the decrease in realized gain is due to increased loss in the antenna at this frequency.

8.7 Series LC Trap Slot Antenna

The ground plane size has less of an impact on the input impedance of a slot than it does on a monopole, but it impacts the slot's radiation pattern. A ground plane with a size of $\lambda/2$ x $3\lambda/4$ has a single lobe above and a single lobe below the ground plane. If the ground plane is made larger but not approaching infinity, beam splitting will occur due to ground edge currents destructively interfering with the slot radiation pattern.

A slot antenna with two series LC traps, Figure 8.21, has operating frequencies at

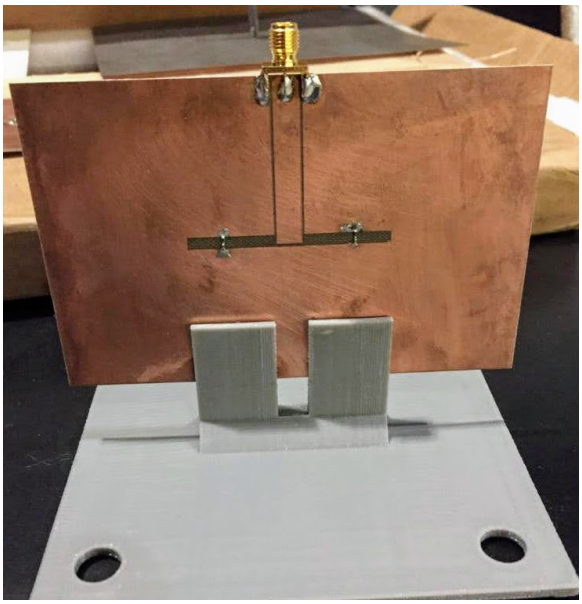


Figure 8.21: Slot antenna with series LC trap loads

2.14 GHz and 3.25 GHz, Figure 8.22. The series LC trap presents a capacitive load at the lower operating frequency. The load impedance at 1.435 GHz is 5-j45 Ω, with a range of 5-j83 Ω to 5-j9 Ω due to component tolerance. The load impedance at 3.22 GHz is 13+j693 Ω, with a range of 13+j640 Ω to 13+j744 Ω due to component tolerance. The load resonance and antenna lower operating frequency have a frequency separation of about 0.104 GHz (range of 0.195 GHz to 0.022 GHz due to tolerance). The resulting load Q value at the lower 1.435 GHz operating frequency is 73.

The trap dipole design principle works for slot antennas, as long as the load values are appropriately chosen.

8.8 Parallel LC Trap Slot Antenna

A slot antenna with two parallel LC traps, Figure 8.25, has operating frequencies at 1.98 GHz and 3.32 GHz, Figure 8.26. The load impedance at 1.976 GHz is 0.1-j0.7 Ω, with a range of tolerances able to vary the true impedance from 0.1-j0.7 Ω to 0.1+j0.7 Ω. The load

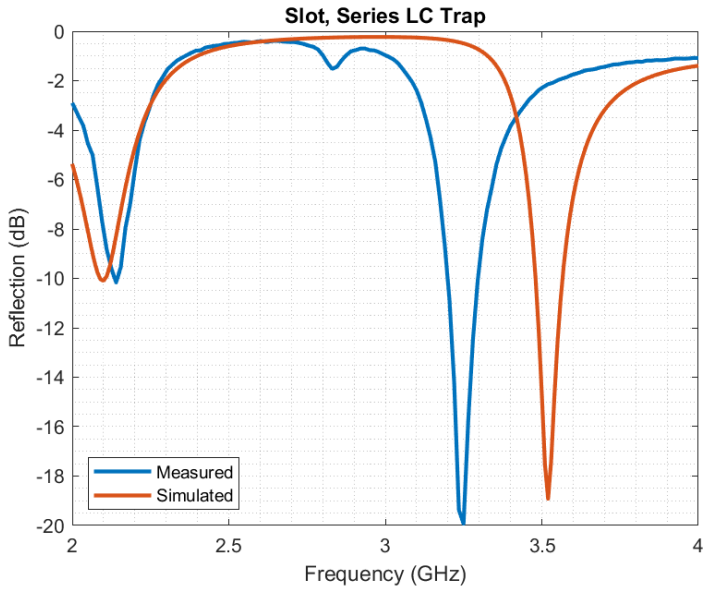
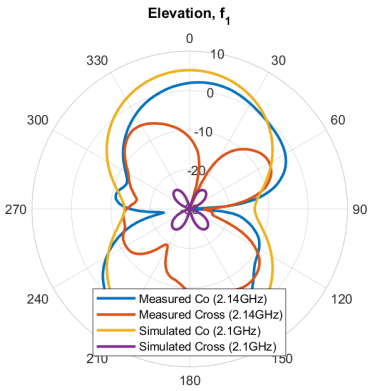


Figure 8.22: Slot antenna with series LC trap loads, operating frequencies at GHz and GHz.

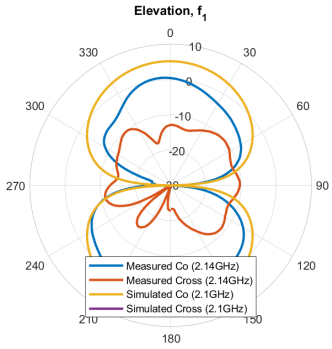
impedance at 3.319 GHz is 0.4-j26 Ω with tolerances able to vary the true impedance from 0.5-j29 Ω to 0.4-j24 Ω. The load resonance ideally occurs 0.19 GHz from the lower impedance match with a range between 0.284 to 0.103 GHz. The resulting load Q value at 1.976 GHz is 92.68 with a range between 84.37 and 101.36.

8.9 Conclusion

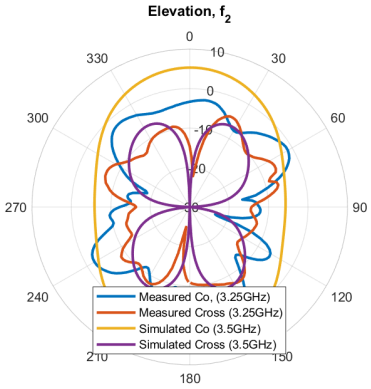
Several trap antennas have been fabricated and measured with good agreement between simulation and measurement. The measurements confirm that trap antennas excite a low radiation efficiency mode near the trap-related operating frequency. The measurements also confirm that the trap related operating frequency is caused by a finite load reactance rather than a true load resonance. Furthermore, new trap antenna designs using series loads, large inductive loads, and slot antennas have been designed and demonstrated with good impedance matching and broad radiation patterns.



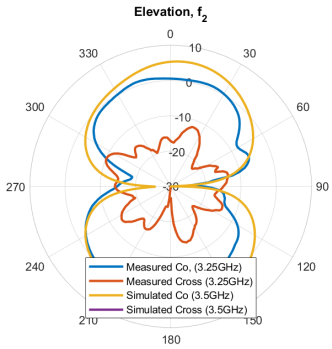
(a)



(b)



(c)



(d)

Figure 8.23: Series LC slot antenna, elevation and azimuth realized gain radiation patterns a) ϕ=0 elevation cut at GHz b) ϕ=90 elevation cut at GHz c) ϕ=0 elevation cut at GHz d) ϕ=90 elevation cut at GHz

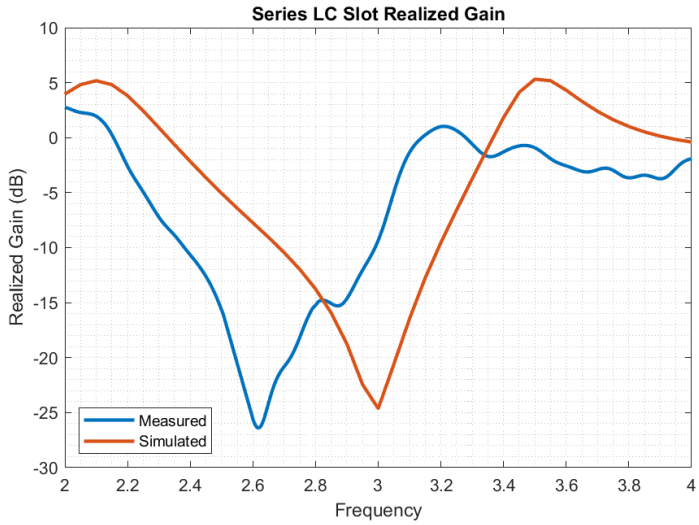


Figure 8.24: Series LC trap slot antenna, realized gain at broadside over frequency



Figure 8.25: Fabricated trap slot antenna with parallel LC loads, 2 nH and 3 pF

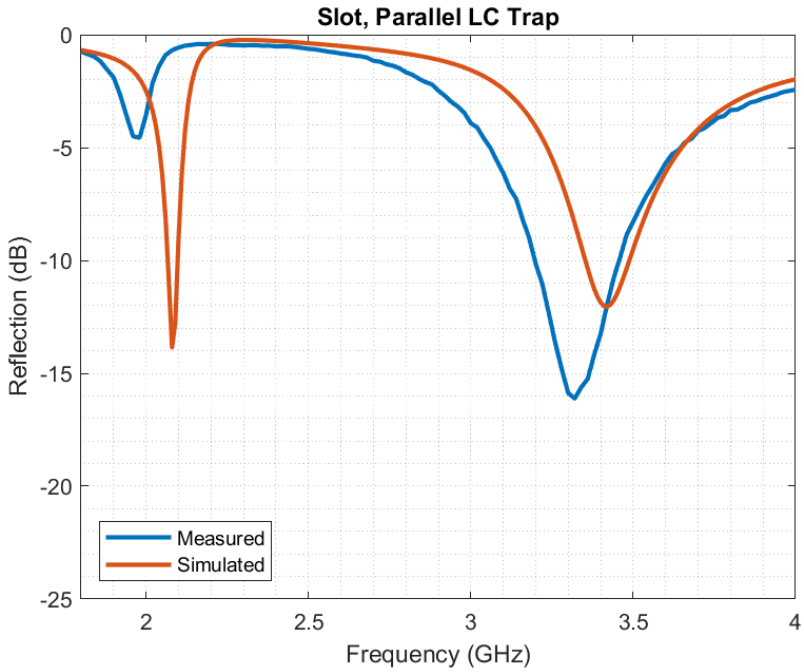


Figure 8.26: Measured reflection of parallel LC loaded slot antenna compared with measurement

Chapter 9

Reconfigurable Trap Antennas

9.1 Introduction

In chapter 3 I simulated a cavity end-loaded slot antenna that was a combination of the ring resonator end-loaded slot antenna and the evanescent mode coax cavity resonator. I did not present a feed structure for the end-loaded slot antenna. Dips in radiation efficiency were near or at the resonance of many of the antenna designs in chapter 3, but the antenna impedance match might not be at exactly the resonance once a feed structure has been added. The actual relationship between loss frequencies and operating frequencies is unknown without a feed structure. However, chapter 5 established that the simulated loss in the designs in chapter 3 is due to a loaded higher order mode not due rather than loss in the resonator. The best designs from chapter 3 can be redesigned with a CPW feed structure.

To create reconfigurable antennas, I moved on from basic trap antennas and demonstrated how to incorporate stubs and more complex resonators in place of simple LC loads. I used the piezo-reconfigurable evanescent mode cavities connected to the slot with CPW stubs to create a slot antenna that can be tuned over S-Band with good power handling and polarization purity. Adding resonant loads to antennas will only increase in popularity

and practicality as filtennas are more often used for their SWaP improvements, better noise performance, and potential for additional degrees of reconfigurability. I was concerned with resolving whether resonant loads introduced excessive loss, based on early simulation experience. The excessive loss occurs because of the excitation of higher-order modes that are also compressed in size, which lowers radiation resistance while the loss resistance remains constant. It is possible to have lossy frequencies overlap with operating frequencies, particularly if the loads are distributed, but in most instances, the lossy frequency was removed from the operating frequencies and did not impact antenna performance.

The parametric study of variable load location on trap dipoles indicates that it is likely that there will be a dual band response with any load location. I expect that any cavity load location will also result in a dual band slot response. For a dipole, a stub can be added that defines an open circuit at the center feed at the lower operating frequency to remove the lower band. The loading from the traps will change the lower frequency. The stub to cancel the lower resonance will change the tuning of the upper resonance.

A length of coaxial line can be offset from the slot's end and soldered across the slot. The exact distance between the end of the slot and the coax determines the impedance match. I will primarily use a CPW to slotline transition with a capacitor gap acting as a coupling impedance transformer. I will start by presenting simulated data of the original end-loaded slot with the new CPW center feed to assess whether the operating frequencies have acceptable radiation efficiency with a feed structure.

9.2 Revised Design Process

The slot antenna outer length should be approximately half a wavelength long at the lower frequency, and the inner dimensions should be approximately half a wavelength long at the upper frequency. If the loading is reconfigurable and the upper frequency is variable,

then the length should be based on the middle value. There's not a clear L/C ratio that is needed from a characteristic impedance standpoint. A series load on a slot is tuned to f_2 and capacitively loads f_1, which lowers the value of f_1. A parallel load on a slot is tuned to f_1 and capacitively loads f_2, which lowers the value of f_2. To counteract the loading effects, the series trap loaded slot should have a shorter than $\lambda/2$ outer length, and the parallel loaded slot should have a shorter than $\lambda/2$ inner length. Alternately, decreasing the characteristic impedance of the trap (ratio of L to C) will decrease the slope of the resonator impedance, which translates to less reactive detuning at the antenna operating frequency not associated with trap resonance. However, the series trap design is more constrained because it has to provide both high and low impedance.

As a general rule, parallel trap designs should have a lower characteristic impedance, and series trap designs should have a higher characteristic impedance. For the series design, the closer f_1 is to f_2, the higher the necessary characteristic impedance. For the parallel design, the closer the operating frequencies are, the lower the necessary characteristic impedance.

To demonstrate, we can start by picking 2 and 4 GHz as our operating frequencies. The operating frequencies will be below the actual trap resonance. For a parallel dipole, an L and C pair is chosen to be resonant at 2.01 GHz and with a low starting Z0 value (10 ohms). The outer length of the slot antenna is calculated to be half a wavelength at 2 GHz, and the inner length is calculated to be half a wavelength at 4 GHz.

I arbitrarily pick 60 mil TMM3 ($\epsilon_r = 3.3$) for the substrate and choose the slot to be 3 mm wide. The characteristic impedance of the slot is 142 Ω, and half a wavelength is 64 mm at 2 GHz. Half a wavelength is 31 mm at 4 GHz, and characteristic impedance has increased to 171 Ω. The preceding numbers are based on slotline modelling, and don't take into account inductive loading at the ends of the slot antenna, or the sizeable impact that the feed type and location has on a slot antenna. Typically, the slot antenna will be resonant

with a smaller than half wavelength slotline.

The capacitively coupled CPW to half wavelength slot can be calculated based on [89]. A CPW feed into a full-wavelength slot is also common, both with center feeding [90] and near end feeding [91]. A microstrip feed coupled to the slot antenna is detailed in [40]. A differential feed across the slot is analyzed in [39].

To substitute a stub for an RLC load, the stub input impedance can be calculated in Matlab if possible, or simulated separately in HFSS. The stub input impedance should match the impedance of the LC load in a working design. The replacement load can be made more complex, as long as the impedance of the load matches the LC load values at the operating frequencies. A cavity terminated stub can be a convenient way of coupling to a cavity from a slot antenna, and can even be closer to ideal point loading than a direct cavity coupling path. If accurate analytical models don't exist for the stubs and loads being used, then isolated full wave simulations are necessary to tune the loads.

9.3 Reconfigurable Trap Dipole and Trap Slot Antennas

One final evolution to the framework for resonator loaded antennas as trap antennas is to design frequency reconfigurable trap antennas. When I was doing my initial MoM based investigation, I was surprised to find that tuning the trap frequency while keeping the load location constant still resulted in creating new antenna second resonances despite the load placement seeming non-optimal. This naturally suggested that trap style antennas are a good candidate for frequency tunable resonator loaded designs, which has not been investigated elsewhere in the literature.

A trap dipole with a static load location and a variable trap resonance was simulated, as seen in Figures 9.1 and 9.2. Generally, the antenna resonance will be tuned over a smaller frequency range than the load resonance. The range of useful load impedances are closer to

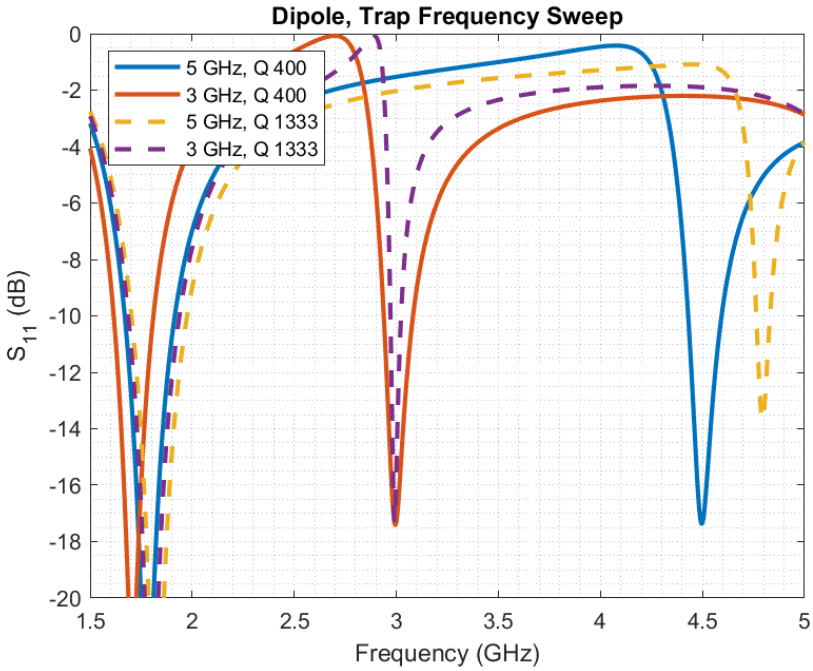


Figure 9.1: Sweeping trap resonance on dipole, higher Q loads tune antenna resonance a higher percentage of the trap resonance sweep

the load resonance for a higher Q load, shown in Figure 9.3 for visual reference. Because of this, a higher Q load will reconfigure the antenna resonance over a wider frequency range than a lower Q load. A higher Q load will reconfigure that dipole resonance more widely than a low Q load. The radiation efficiency is also tuned across frequency. The antenna gain at all angles is decreased at the radiation efficiency minimum. If desired, the radiation efficiency minimum could be tuned to make the antenna an absorptive, non-reflective surface at certain frequencies.

I simulated a trap slot with a static load location and a variable trap resonance, shown in Figure 9.4. A higher Q load will reconfigure the slot resonance more widely than a lower Q load. However, the slot antenna cannot be tuned as widely as the trap dipole. The exact reasons are still unclear, but slot antennas are typically operated at antiresonance and dipoles are typically operated at series resonance. For dipoles and slots, the antiresonance typically

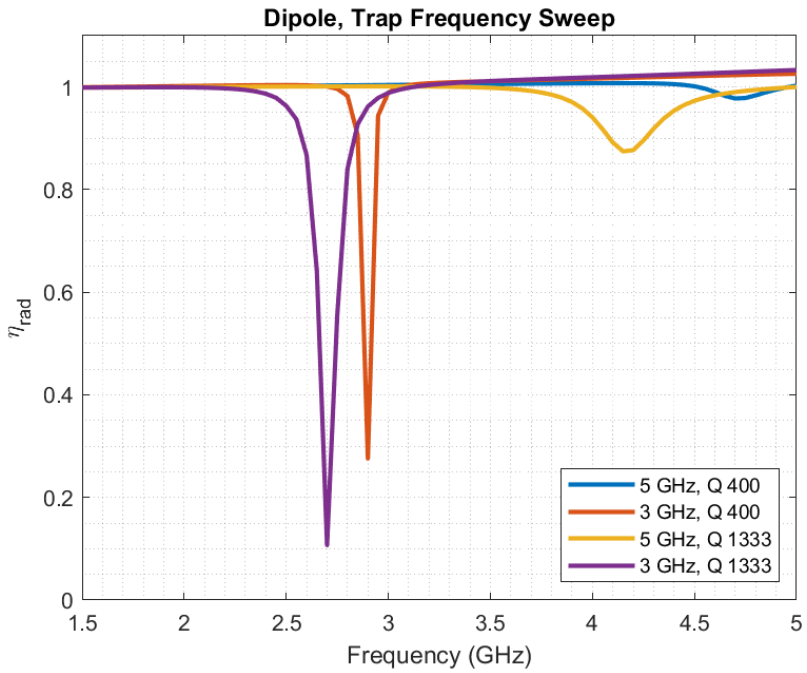


Figure 9.2: Radiation efficiency is also tuned across frequency, still offset from antenna operating frequencies.

has a much higher Q than the series resonance. For the dipole series resonance, there is naturally a very broad band of slowly varying antenna reactance that can be cancelled by the trap load reactance. Around the slot antenna antiresonance, the antenna reactance has a much steeper slope.

9.4 Slot Antenna Loaded with Cavity Terminated Stubs

I previously designed reconfigurable slot antennas by directly aperture coupling the slotline to a reconfigurable cavity. A CPW stub with cavity termination can be added to slot antennas for a reconfigurable stub trap design, as shown in Figure 9.5. Slot's planar structure naturally allows for integration with cavities, piezos and DC bias lines. The antenna capacitively coupled CPW feed impedance matches to the antiresonances of the slot. The stub is loaded with the evanescent mode cavities that can be tuned with DC biased piezo elements.

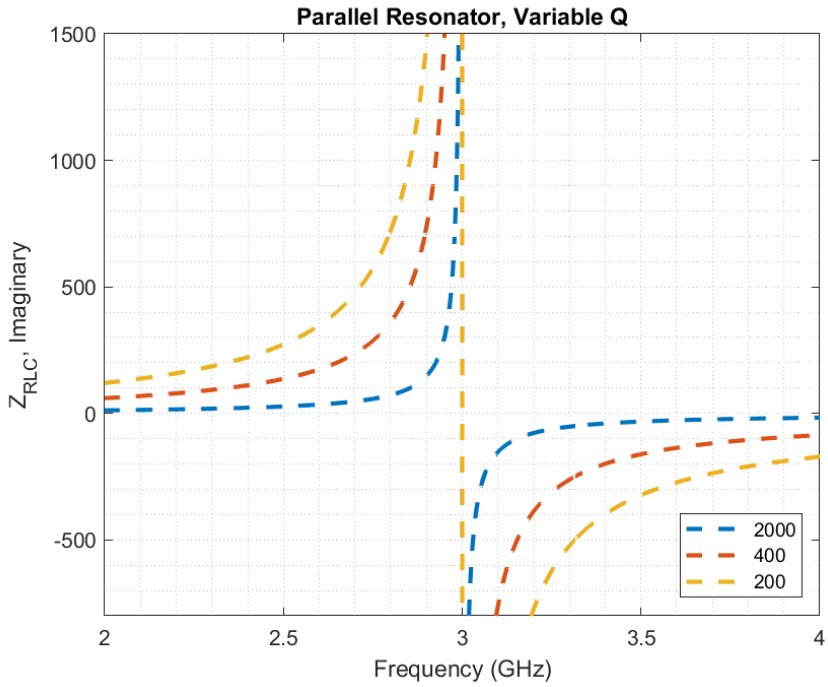


Figure 9.3: Useful range of reactive load values are closer in frequency to load resonance with higher Q loads

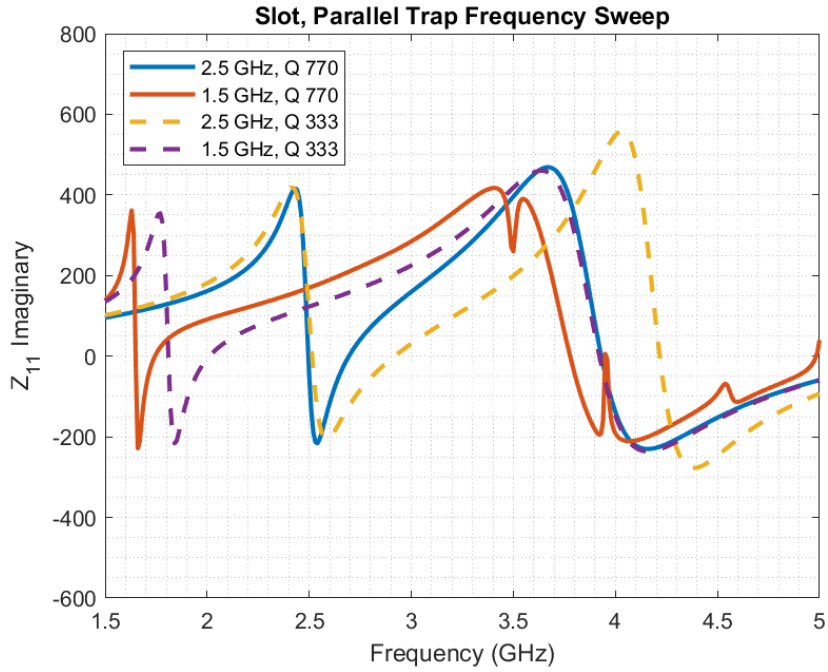


Figure 9.4: Trap slot with static load location, varied load resonance and Q

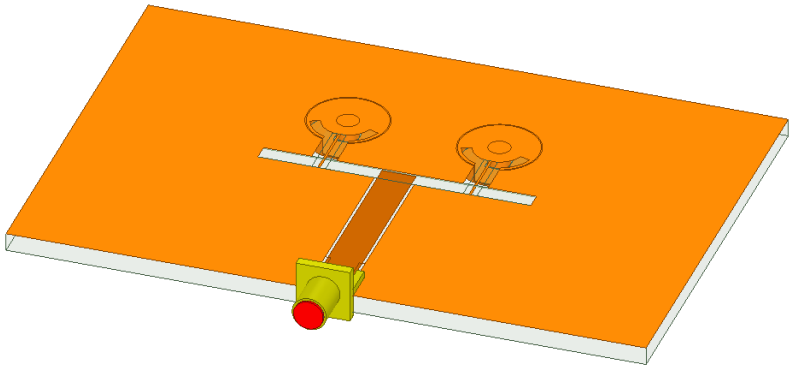


Figure 9.5: Reconfigurable trap slot antenna, trap stub terminated in reconfigurable cavity

The reactance of the stub can be tuned by simulating the CPW and cavity separately, Figure 9.6. Using transmission line stubs better approximates a point load than direct cavity coupling. If the stub is a resonant length, there are possible added harmonic resonances in band. Making the transmission line as short as possible results in a load value that is closer to the resonator input, which simplifies the design.

The stub creates an upper frequency short circuit condition at the slot radiator, and the transition to CPW for the stubs minimally disturbs the radiation pattern. The slot antenna is dual-band, with a static lower resonance and a tunable upper resonance. The lower resonance could be removed with a filter on the feed structure.

The antenna has a static operating frequency at 2.24 GHz, and the upper frequency tunes from 2.52 GHz to 3.41 GHz by tuning the evanescent mode cavities, as shown in Figure 9.7.

The radiation efficiency is consistent with the other trap antennas and cavity loaded antennas presented previously, and has dips in between the two operating frequencies, seen in Figure 9.8. The radiation pattern is a typical slot radiation pattern across tuning, as seen in Figures 9.9 and 9.10. The CPW stubs and coupled cavities minimally disturb the radiation pattern.

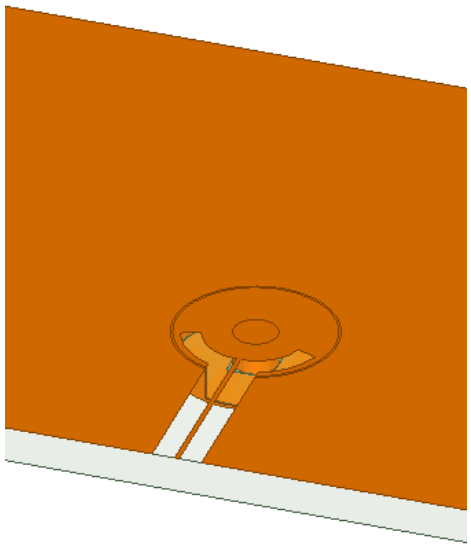


Figure 9.6: The reactance of the cavity terminated stub can be tuned by simulating the CPW and cavity separately to reduce simulation time

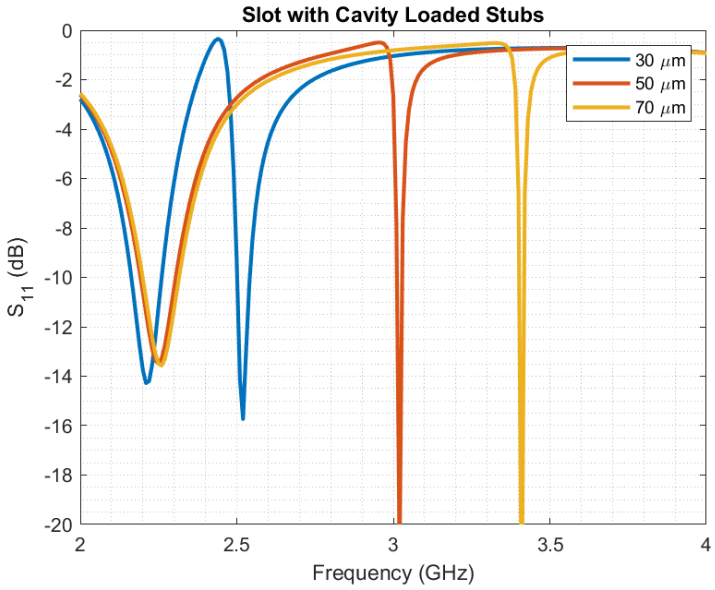


Figure 9.7: S11 of CPW fed slot antenna with cavity end loads, static low frequency at 2.24 GHz, and tunable upper frequency at 2.52 GHz and 3.02 GHz and 3.41 GHz, varying capacitive gap in cavities

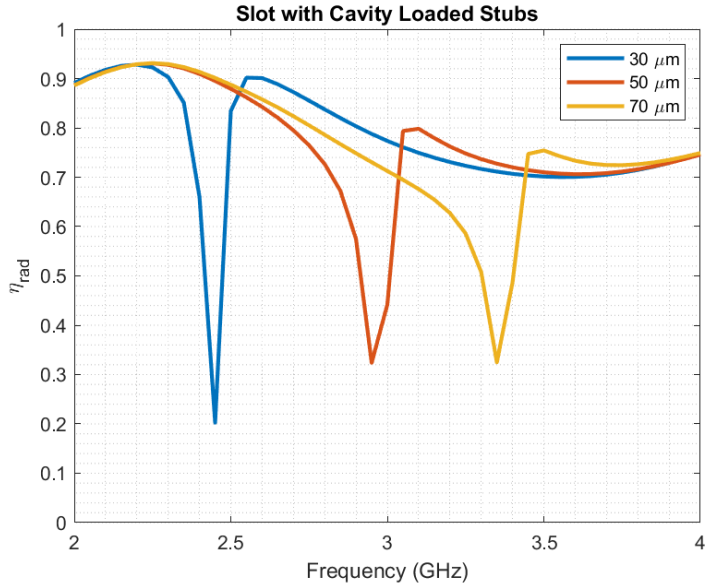


Figure 9.8: Radiation efficiency over 90% at low static frequency, varies from 88% to 59% at the upper frequencies

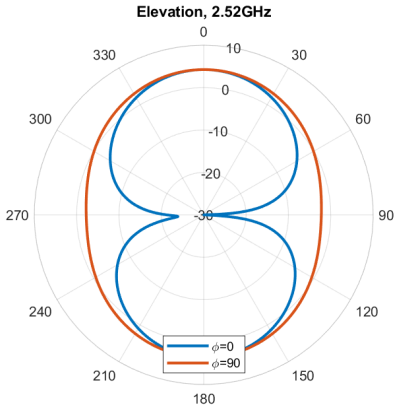


Figure 9.9: 2.52 GHz realized gain pattern, 30 μm capacitive gap

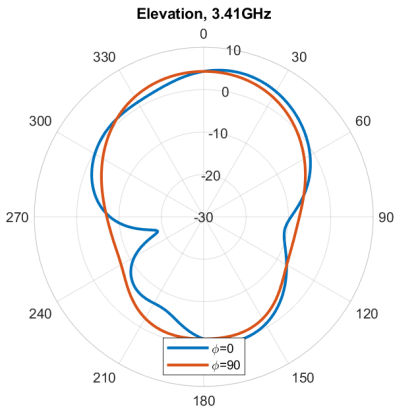


Figure 9.10: 3.41 GHz, 70 μm capacitive gap

This is a practical demonstration of how the revised theory of trap antennas is an effective framework for designing efficient resonator loaded multiband and reconfigurable resonators with a simple design process, and results in desirable radiating field distributions.

9.5 Conclusion

The novel cavity terminated stub loaded slot antenna design is built on the newly expanded framework for trap antenna design. A static lower band exists at the full resonant length of the antenna, while a higher band can be tuned by means of a reconfigurable trap. If a single band of operation is desired, a filter can be integrated into the feed network to eliminate the static lower band.

Trap antennas can be designed to be reconfigurable across frequency by changing the load resonance. The newly developed trap antenna framework can be used to design efficient multiband frequency reconfigurable resonator loaded antennas, and ensures that the antennas will have quasi-first mode responses at both operating frequencies, which results in good radiation patterns. Additionally, there is a tunable null in radiation efficiency that

can potentially be used to make the antenna more absorbtive and less reflective at a certain frequency.

Chapter 10

Conclusions and Future Work

10.1 Conclusions

The goal of this research was to advance the design of resonator loaded antennas. Resonator loaded antennas often suffer from lossy frequencies, which raised an initial question about whether resonator loads are unavoidably lossy. I demonstrated that the loss phenomenon is not due to load resonance, but is actually due to excitation of electrically compressed higher order modes, which can be separated from antenna operating frequencies.

In the process of explaining loss in resonator loaded antennas, I created a new design framework for a class of high efficiency, multiband, and reconfigurable resonator loaded antennas. The design framework is based on the trap dipole, and I significantly revised the traditional analysis of trap antennas before expanding the design principles to a much broader range of antenna designs. The revised trap antenna design ensures not only that the resonator loaded antenna has high radiation efficiency at the operating frequencies, but also ensures that the operating frequencies are quasi first mode distributions, which keeps the radiation pattern free of beam splitting and other distortions. Most of the new trap antennas I demonstrated are loaded with LC resonators, but I demonstrated a final design with cavity

terminated stubs, and the design framework is intended to easily incorporate more complex resonator loads.

Before investigating trap dipoles, I designed several cavity loaded reconfigurable slot antennas with tuning across S-Band. The cavity loaded and cavity backed slot in Chapter 4 was designed to be a widely-tunable array element. The array element can also potentially be tuned to have a higher order filter response through appropriate calibration of the loads.

While investigating the trap dipoles as a simple resonator loaded antenna, I found that the trap load is not resonant at the upper operating frequency of trap dipoles, contrary to the common description of trap antennas. The traps have a finite reactance at the upper operating frequency, and parallel LC loads can be replaced with any other equivalent-reactance resonator. The conventional parallel LC trap dipole was turned into a prototype on which to base more complex resonator loaded antennas. I applied the principles of trap antenna design to create novel multiband trap slot antennas in Chapter 3. I also verified several novel trap antennas in measurement.

In chapter 9, I expanded the trap antenna framework to create reconfigurable trap antennas. I started with basic LC loads and demonstrated how to incorporate stubs and more complex resonators. I used the piezo-reconfigurable evanescent mode cavities connected to the slot with CPW stubs to create a trap slot antenna with a static lower band and a dynamic upper band with 1 GHz of tuning range with good radiation efficiency.

Adding resonant loads to antennas will only increase in popularity and practicality as tunable antennas and filtennas become more widespread. In this dissertation, I demonstrated that resonant loads can introduce lossy modes, and I significantly revised and expanded the theory of the basic trap dipole antenna, which should be a valuable aid in designing resonator loaded antennas with higher degrees of complexity. I demonstrated novel series LC trap dipoles, dual-band inductor loaded trap dipoles, and parallel and series LC trap slots. The newly developed design process also allows for the integration of any kind

of resonator or reactive load to be used to create trap style antennas. A reconfigurable load was also used to demonstrate novel tunable trap antennas. The design procedure is ultimately adaptable to any resonators than can be practically fabricated and physically incorporated into the antenna structure. I contributed significantly to the design of resonator loaded antennas by expanding the simple trap dipole into a much larger framework for trap antennas as a broad new class of high-efficiency multiband and reconfigurable resonator loaded antennas.

10.2 Future Work

The limits to trap slot tunability should be explored further. It seems that the neighboring resonances on either side of the tuned operating resonance will limit the antenna tuning range. It may also be that tuning the antenna further will alter the antenna modal behavior enough so that comparison to the unloaded antenna is no longer a useful reference. The Q of the operating resonance being tuned likely also impacts how widely a tuned load can reconfigure the antenna.

Reconfigurable trap antennas have been demonstrated in simulation and could be fabricated for further demonstration. A reconfigurable LC loaded design could be made reconfigurable with a varactor in place of the capacitor, and the stub-cavity loaded slot antenna could be built as well.

The radiation efficiency minima that occur with resonator loaded designs can potentially be a feature to reduce the antenna reflectivity at a given frequency. This could be especially interesting combined with tunable loads to reconfigure the low reflectivity band.

The trap antenna was demonstrated on both dipoles and slots, but could be expanded to other structures. The reconfigurable trap slot could be cavity backed.

Distributed and asymmetric loading rapidly increases complexity of analysis for the trap

antenna. In my experience, adding distributed loads makes it possible have the radiation efficiency minimum overlap with the antenna operating frequencies, which suggests that the modal excitation changes. It could be possible to asymmetrically tune the loads to increase bandwidth at the cost of radiation pattern symmetry.

Bibliography

[1] D. Schaubert, F. Farrar, A. Sindoris, and S. Hayes, "Microstrip antennas with frequency agility and polarization diversity," *IEEE Transactions on Antennas and Propagation*, vol. 29, no. 1, pp. 118–123, 1981.

[2] D. Pozar and V. Sanchez, "Magnetic tuning of a microstrip antenna on a ferrite substrate," *Electronics Letters*, vol. 24, no. 12, pp. 729–731, 1988.

[3] G. Huff, J. Feng, S. Zhang, and J. Bernhard, "A novel radiation pattern and frequency reconfigurable single turn square spiral microstrip antenna," *IEEE Microwave and Wireless Components Letters*, vol. 13, no. 2, pp. 57–59, 2003.

[4] A.-F. Sheta and S. F. Mahmoud, "A widely tunable compact patch antenna," *IEEE Antennas and Wireless Propagation Letters*, vol. 7, pp. 40–42, 2008.

[5] S. Moon, H. H. Sigmarsson, H. Joshi, and W. J. Chappell, "Substrate integrated evanescent-mode cavity filter with a 3.5 to 1 tuning ratio," *IEEE Microwave and Wireless Components Letters*, vol. 20, no. 8, pp. 450–452, 2010.

[6] L. Szolc, T. Poydence, and J. Ruyle, "Frequency-agile ring resonator end-loaded slot antenna," *Microwave and Optical Technology Letters*, vol. 59, no. 8, pp. 1876–1882, 2017.

[7] S. Saeedi, J. Lee, and H. Sigmarsson, "Prediction of power handling in tunable, high-Q, substrate integrated, evanescent-mode cavity bandpass filters," *Electronics Letters*, vol. 52, no. 10, pp. 846–848, 2016.

[8] H. Joshi, H. H. Sigmarsson, S. Moon, D. Peroulis, and W. J. Chappell, "High-Q fully reconfigurable tunable bandpass filters," *IEEE transactions on microwave theory and techniques*, vol. 57, no. 12, pp. 3525–3533, 2009.

[9] H. H. Sigmarsson, H. Joshi, S. Moon, D. Peroulis, and W. J. Chappell, "Substrate integration of widely tunable bandpass filters," in *Proc. Int. Symp. Microelectronics,*

International Micro-electronics and Packaging Society (IMAPS), 2009, pp. 711–716.

[10] H. H. Sigmarsson, J. Lee, D. Peroulis, and W. J. Chappell, "Reconfigurable-order bandpass filter for frequency agile systems," in *Microwave Symposium Digest (MTT), 2010 IEEE MTT-S International*, IEEE, 2010, pp. 1756–1759.

[11] S. Saeedi, J. Lee, and H. H. Sigmarsson, "Tunable, high-Q, substrate-integrated, evanescent-mode cavity bandpass-bandstop filter cascade," *IEEE Microwave and Wireless Components Letters*, vol. 26, no. 4, pp. 240–242, 2016.

[12] J. Ruyle, C. won Jung, and J. Bernhard, "Reconfigurable stacked patch antenna with beamsteering capabilities," in *Antennas and Propagation Society International Symposium, 2008. AP-S 2008. IEEE*, IEEE, 2008, pp. 1–4.

[13] J. Ruyle and J. Bernhard, "A wideband transmission line model for a slot antenna," *IEEE Transactions on Antennas and Propagation*, vol. 61, no. 3, pp. 1407–1410, 2013.

[14] S. Bass, "Investigation of a frequency and pattern reconfigurable slot array utilizing ring resonator end loads," Master's thesis, University of Oklahoma, 2017.

[15] A. Schaeffer, J. Kennedy, P. Winniford, S. Saeedi, C. Fulton, N. Goodman, H. Sigmarsson, and J. Ruyle, "Investigation of a tunable antenna for high-power phased array applications," in *2018 Antenna Applications Symposium*, 2018, pp. 204–221.

[16] M. Thibodeau, "Theory, design, and fabrication of frequency agile filtennas," 2020.

[17] G. Matthei, "L. young, and em t. jones," *Microwave Filters, Impedance-Matching Networks, and Coupling Structures*,

[18] R. Collin, "Small aperture coupling between dissimilar regions," *Electromagnetics*, vol. 2, no. 1, pp. 1–24, 1982.

[19] R. Harrington and J. Mautz, "A generalized network formulation for aperture problems," *IEEE Transactions on Antennas and Propagation*, vol. 24, no. 6, pp. 870–873, 1976.

[20] N. K. Das and D. M. Pozar, "Multiport scattering analysis of general multilayered printed antennas fed by multiple feed ports. i. theory," *IEEE transactions on antennas and propagation*, vol. 40, no. 5, pp. 469–481, 1992.

[21] N. K. Das, "Generalized multiport reciprocity analysis of surface-to-surface transitions between multiple printed transmission lines," *IEEE transactions on microwave theory and techniques*, vol. 41, no. 6, pp. 1164–1177, 1993.

[22] C.-H. Liang and D. Cheng, "Generalized network representations for small-aperture coupling between dissimilar regions," *IEEE Transactions on Antennas and Propagation*, vol. 31, no. 1, pp. 177–182, 1983.

[23] D. Pozar, "A reciprocity method of analysis for printed slot and slot-coupled microstrip antennas," *IEEE Transactions on Antennas and Propagation*, vol. 34, no. 12, pp. 1439–1446, 1986.

[24] S. B. Cohn, "Microwave coupling by large apertures," *Proceedings of the IRE*, vol. 40, no. 6, pp. 696–699, 1952.

[25] D. M. Pozar, *Microwave engineering*. John Wiley & Sons, 2009.

[26] H. A. Bethe, "Theory of diffraction by small holes," *Physical review*, vol. 66, no. 7-8, p. 163, 1944.

[27] G. Craven, C. Mok, and R. Skedd, "Integrated microwave systems employing evanescent mode waveguide components," in *Microwave Conference, 1969. 1st European*, IEEE, 1969, pp. 285–289.

[28] G. F. Craven and C. Mok, "The design of evanescent mode waveguide bandpass filters for a prescribed insertion loss characteristic," *IEEE Transactions on Microwave Theory and Techniques*, vol. 19, no. 3, pp. 295–308, 1971.

[29] C. Mok, D. Stopp, and G. Craven, "Susceptance-loaded evanescent-mode waveguide filters," in *Proceedings of the Institution of Electrical Engineers*, IET, vol. 119, 1972, pp. 416–420.

[30] C. Mok, "Diaphragms in evanescent waveguides," *Electronics Letters*, vol. 4, no. 3, pp. 43–44, 1968.

[31] A. Schaeffer, J. Kennedy, P. Winniford, M. Thibodeau, S. Saeedi, H. Sigmarsson, and J. Ruyle, "Reconfigurable evanescent-mode cavity loadedslot antenna," in *2019 GOMACTech*, 2019.

[32] H. H. Sigmarsson, A. Christianson, H. Joshi, S. Moon, D. Peroulis, and W. J. Chappell, "In-situ control of tunable evanescent-mode cavity filters using differential

mode monitoring," in *Microwave Symposium Digest, 2009. MTT'09. IEEE MTT-S International*, IEEE, 2009, pp. 633–636.

[33] S. Saeedi, S. Atash-bahar, and H. H. Sigmarsson, "Active tunable substrate integrated evanescent-mode cavity resonator using negative resistance," in *Radio and Wireless Symposium (RWS), 2016 IEEE*, IEEE, 2016, pp. 87–90.

[34] E. J. Naglich, J. Lee, H. H. Sigmarsson, D. Peroulis, and W. J. Chappell, "Intersecting parallel-plate waveguide loaded cavities for dual-mode and dual-band filters," *IEEE Trans. Microw. Theory Techn.*, vol. 61, no. 5, pp. 1829–1838, 2013.

[35] D. K. Cheng *et al.*, *Field and wave electromagnetics*. Pearson Education India, 1989.

[36] S. B. Cohn, "Slot line on a dielectric substrate," *IEEE Transactions on microwave theory and techniques*, vol. 17, no. 10, pp. 768–778, 1969.

[37] R. Garg, I. Bahl, and M. Bozzi, *Microstrip lines and slotlines*. Artech house, 2013.

[38] S. B. Cohn, "Slot-line field components (correspondence)," *IEEE Transactions on Microwave Theory and Techniques*, vol. 20, no. 2, pp. 172–174, 1972.

[39] J. Ruyle, "Small, dual band, placement insensitive antennas," PhD thesis, University of Illinois at Urbana-Champaign, 2012.

[40] M. Himdi and J. Daniel, "Analysis of printed linear slot antenna using lossy transmission line model," *Electronics letters*, vol. 28, no. 6, pp. 598–601, 1992.

[41] S. Bass, *Conversation*, Conversation, Dec. 2018.

[42] M. F. Hagag, M. A. Khater, M. D. Hickle, and D. Peroulis, "Tunable SIW cavity-based dual-mode diplexers with various single-ended and balanced ports," *IEEE Transactions on Microwave Theory and Techniques*, vol. 66, no. 3, pp. 1238–1248, 2017.

[43] D. Sievenpiper, H.-P. Hsu, and R. M. Riley, "Low-profile cavity-backed crossed-slot antenna with a single-probe feed designed for 2.34-ghz satellite radio applications," *IEEE transactions on antennas and propagation*, vol. 52, no. 3, pp. 873–879, 2004.

[44] S. Long, "Experimental study of the impedance of cavity-backed slot antennas," *IEEE Transactions on Antennas and Propagation*, vol. 23, no. 1, pp. 1–7, 1975.

[45] ——, "A mathematical model for the impedance of the cavity-backed slot antenna," *IEEE Transactions on Antennas and Propagation*, vol. 25, no. 6, pp. 829–833, 1977.

[46] H. Hertz, "Ueber einen einfluss des ultravioletten lichtes auf die electrische entladung," *Annalen der Physik*, vol. 267, no. 8, pp. 983–1000, 1887.

[47] M. Bulgerin and A. Walters, "154," *NOLC report*, pp. 67–83, 1954.

[48] H. A. Wheeler, "Fundamental limitations of small antennas," *Proceedings of the IRE*, vol. 35, no. 12, pp. 1479–1484, 1947.

[49] A. Fourie and B. Austin, "Improved HF broadband wire antenna," *Electronics Letters*, vol. 23, no. 6, pp. 276–278, 1987.

[50] R. Hansen, "Efficiency transition point for inductively loaded monopole," *Electronics letters*, vol. 9, no. 5, pp. 117–118, 1973.

[51] C. E. Smith, "A critical study of two broadcast antennas," *Proceedings of the Institute of Radio Engineers*, vol. 24, no. 10, pp. 1329–1341, 1936.

[52] C. Buchanan, "The multimatch antenna system," *QST*, vol. March, pp. 22–23, 130, 1955.

[53] A. Khidre, F. Yang, and A. Z. Elsherbeni, "A patch antenna with a varactor-loaded slot for reconfigurable dual-band operation," *IEEE Transactions on Antennas and Propagation*, vol. 63, no. 2, pp. 755–760, 2014.

[54] N. Behdad and K. Sarabandi, "Dual-band reconfigurable antenna with a very wide tunability range," *IEEE Transactions on Antennas and Propagation*, vol. 54, no. 2, pp. 409–416, 2006.

[55] B. A. Cetiner, G. R. Crusats, L. Jofre, and N. Biyikli, "RF MEMS integrated frequency reconfigurable annular slot antenna," *IEEE Transactions on Antennas and Propagation*, vol. 58, no. 3, pp. 626–632, 2009.

[56] F. Yang and Y. Rahmat-Samii, "Patch antennas with switchable slots (pass) in wireless communications: Concepts, designs, and applications," *IEEE Antennas and propagation Magazine*, vol. 47, no. 2, pp. 13–29, 2005.

[57] Y. Yusuf and X. Gong, "Compact low-loss integration of high-Q 3-D filters with highly efficient antennas," *IEEE transactions on microwave theory and techniques*, vol. 59, no. 4, pp. 857–865, 2011.

[58] D. Smith, "The trap-loaded cylindrical antenna," *IEEE Transactions on Antennas and Propagation*, vol. 23, no. 1, pp. 20–27, 1975.

[59] J. Pemberton, "Multimatch antenna for 'phone," *QST*, vol. December, pp. 24–25, 160, 1955.

[60] J. Hall, "Off-center-loaded dipole antennas," *QST*, vol. September, pp. 28–34, 58, 1974.

[61] R. Hansen, "Efficiency and matching tradeoffs for inductively loaded short antennas," *IEEE Transactions on Communications*, vol. 23, no. 4, pp. 430–435, 1975.

[62] Y. Beers, "Designing trap antennas: A new approach," *Ham Radio*, vol. August, pp. 60–27, 1987.

[63] D. D. Reuster and K. J. Cybert, "A high-efficiency broadband HF wire-antenna system," *IEEE Antennas and Propagation Magazine*, vol. 42, no. 4, pp. 53–69, 2000.

[64] W. O. Coburn and C. Fazi, "A lumped-circuit model for a triband trapped dipole array-part 1: Model description," *IEEE Antennas and Wireless Propagation Letters*, vol. 8, pp. 14–18, 2009.

[65] ——, "A lumped-circuit model for a triband trapped dipole array-part ii: Stacked arrays," *IEEE Antennas and Wireless Propagation Letters*, vol. 7, pp. 648–651, 2008.

[66] F. Parrini, F. Papi, and M. Pieraccini, "Double resonance LC trap for dual-band dipole antenna," in *2014 IEEE Conference on Antenna Measurements & Applications (CAMA)*, IEEE, 2014, pp. 1–4.

[67] P. Taylor, J. C. Batchelor, and E. A. Parker, "Dual-band fss design using LC traps," in *2010 Loughborough Antennas & Propagation Conference*, IEEE, 2010, pp. 405–408.

[68] H. Ayad, A. Khalil, M. Fadlallah, F. Ndagijimana, and J. Jomaah, "Design of MSRR-loaded dual-band dipole PCB antennas," in *ICT 2013*, IEEE, 2013, pp. 1–5.

[69] A. Mirkamali, P. S. Hall, and M. Soleimani, "Reconfigurable printed-dipole antenna with harmonic trap for wideband applications," *Microwave and optical technology letters*, vol. 48, no. 5, pp. 927–929, 2006.

[70] R. Anwar, N. Misran, M. T. Islam, and G. Gopir, "Compact multiband VHF antenna for transient radio telescope," in *2009 International Conference on Space Science and Communication*, IEEE, 2009, pp. 182–185.

[71] A. Mirkamali, P. S. Hall, and M. Soleimani, "Wideband reconfigurable printed dipole antenna with harmonic trap," in *IEEE International Workshop on Antenna Technology Small Antennas and Novel Metamaterials, 2006.*, IEEE, 2006, pp. 188–191.

[72] C. A. Balanis, *Antenna theory: analysis and design*. John Wiley & Sons, 2005.

[73] J. J. Adams and J. T. Bernhard, "A modal approach to tuning and bandwidth enhancement of an electrically small antenna," *IEEE Transactions on Antennas and Propagation*, vol. 59, no. 4, pp. 1085–1092, 2011.

[74] Y. Luo and Z. N. Chen, "Compressed dipoles resonating at higher order modes with enhanced directivity," *IEEE Transactions on Antennas and Propagation*, vol. 65, no. 11, pp. 5697–5701, 2017.

[75] D. L. Smith, "The trap-loaded cylindrical antenna.," 1972.

[76] N. Behdad and K. Sarabandi, "A varactor-tuned dual-band slot antenna," *IEEE Transactions on Antennas and Propagation*, vol. 54, no. 2, pp. 401–408, 2006.

[77] D. Sarkar, K. Saurav, and K. V. Srivastava, "Multi-band microstrip-fed slot antenna loaded with split-ring resonator," *Electronics Letters*, vol. 50, no. 21, pp. 1498–1500, 2014.

[78] K. Van Caekenberghe, N. Behdad, K. M. Brakora, and K. Sarabandi, "A 2.45-ghz electrically small slot antenna," *IEEE Antennas and Wireless Propagation Letters*, vol. 7, pp. 346–348, 2008.

[79] M. C. Scardelletti, G. E. Ponchak, S. Merritt, J. S. Minor, and C. A. Zorman, "Electrically small folded slot antenna utilizing capacitive loaded slot lines," in *2008 IEEE Radio and Wireless Symposium*, IEEE, 2008, pp. 731–734.

[80] J. Li, J. Shi, L. Li, T. A. Khan, J. Chen, Y. Li, and A. Zhang, "Dual-band annular slot antenna loaded by reactive components for dual-sense circular polarization with flexible frequency ratio," *IEEE Access*, vol. 6, pp. 64 063–64 070, 2018.

[81] M. D'Amico and F. M. Fasolo, "Multi-trap CPW-fed wide slot antenna for UWB applications," in *2012 6th European Conference on Antennas and Propagation (EUCAP)*, IEEE, 2012, pp. 1860–1864.

[82] H. Sigmarsson, *Email*, Email, Oct. 2020.

[83] M. A. Richards, *Fundamentals of radar signal processing*. Tata McGraw-Hill Education, 2005.

[84] F. J. Harris, "On the use of windows for harmonic analysis with the discrete fourier transform," *Proceedings of the IEEE*, vol. 66, no. 1, pp. 51–83, 1978.

[85] H. A. Wheeler, "The radiansphere around a small antenna," *Proceedings of the IRE*, vol. 47, no. 8, pp. 1325–1331, 1959.

[86] E. Wilken-Resman, "Measurement of antenna radiation efficiency using improved wheeler cap algorithm," Master's thesis, University of Illinois, 2016.

[87] W. McKinzie, "A modified wheeler cap method for measuring antenna efficiency," in *IEEE Antennas and Propagation Society International Symposium 1997. Digest*, IEEE, vol. 1, 1997, pp. 542–545.

[88] O. Litschke, M. Geissler, M. Martinez, and D. Heberling, "Adaption of the wheeler-cap method for measuring the efficiency of mobile handset antennas," *ITG FACHBERICHT*, pp. 387–390, 2003.

[89] W.-H. Tu, "Analysis and design of coplanar waveguide-fed capacitively coupled slot antennas," in *2015 International Workshop on Antenna Technology (iWAT)*, IEEE, 2015, pp. 265–267.

[90] J.-F. Huang, "A simple model of designing CPW-fed slot antenna," in *2000 5th International Symposium on Antennas, Propagation, and EM Theory. ISAPE 2000 (IEEE Cat. No. 00EX417)*, IEEE, 2000, pp. 577–580.

[91] S. Sierra-Garcia and J.-J. Laurin, "Study of a CPW inductively coupled slot antenna," *IEEE Transactions on antennas and propagation*, vol. 47, no. 1, pp. 58–64, 1999.

[92] T. Le Nadan, J. P. Coupez, and C. Person, "Optimization and miniaturization of a filter/antenna multi-function module using a composite ceramic-foam substrate," in *Microwave Symposium Digest, 1999 IEEE MTT-S International*, IEEE, vol. 1, 1999, pp. 219–222.

[93] A. Abbaspour-Tamijani, J. Rizk, and G. Rebeiz, "Integration of filters and microstrip antennas," in *Antennas and Propagation Society International Symposium, 2002. IEEE*, IEEE, vol. 2, 2002, pp. 874–877.

[94] Y. Yusuf, H. Cheng, and X. Gong, "Co-designed substrate-integrated waveguide filters with patch antennas," *IET Microwaves, Antennas & Propagation*, vol. 7, no. 7, pp. 493–501, 2013.

[95] C.-T. Chuang and S.-J. Chung, "Synthesis and design of a new printed filtering antenna," *IEEE Transactions on Antennas and Propagation*, vol. 59, no. 3, pp. 1036–1042, 2011.

[96] Y. Tawk, J. Costantine, and C. Christodoulou, "A varactor-based reconfigurable filtenna," *IEEE Antennas and wireless propagation letters*, vol. 11, pp. 716–719, 2012.

[97] J. L. Durbin and M. A. Saed, "Tunable filtenna using varactor tuned rings fed with an ultra wideband antenna," *Progress In Electromagnetics Research*, vol. 29, pp. 43–50, 2012.

[98] A. Boag, A. Boag, E. Michielssen, and R. Mittra, "Design of electrically loaded wire antennas using genetic algorithms," *IEEE Transactions on Antennas and Propagation*, vol. 44, no. 5, p. 687, 1996.

[99] W. Edson, "Broadband trapped multiple-wire antennas," in *1981 Antennas and Propagation Society International Symposium*, IEEE, vol. 19, 1981, pp. 586–589.

[100] J. Dong, A. Wang, and H. Lan, "A simple radiation pattern reconfigurable printed dipole antenna," in *2009 3rd IEEE International Symposium on Microwave, Antenna, Propagation and EMC Technologies for Wireless Communications*, IEEE, 2009, pp. 619–622.

[101] W. I. Orr and S. D. Cowan, *The radio amateur antenna handbook*. Radio Publications, 1978, pp. 153–154.

[102] A. Greenberg, "Simple trap construction for the multiband antenna," *QST*, vol. October, no. 40, pp. 18–19, 120, 1956.

[103] D. Shafer, "Four-band dipole with traps," *QST*, vol. October, no. 42, pp. 38–40, 1958.

[104] W. Bell, "A trap collinear antenna," *QST*, vol. August, no. 47, pp. 30–31, 1963.

[105] C. Michaels, "How short can you make a loaded antenna," *Communications Quarterly*, vol. Summer, pp. 73–80, 1992.

[106] D. Nyquist and K.-M. Chen, "The traveling-wave linear antenna with nondissipative loading," *IEEE Transactions on Antennas and Propagation*, vol. 16, no. 1, pp. 21–31, 1968.

[107] L. A. Moxon, *HF Antennas for all Locations*. Radio Society of Great Britian, 1982.

[108] K. A. Obeidat, B. D. Raines, R. G. Rojas, and B. T. Strojny, "Design of frequency reconfigurable antennas using the theory of network characteristic modes," *IEEE Transactions on Antennas and Propagation*, vol. 58, no. 10, pp. 3106–3113, 2010.

[109] E. A. Elghannai, B. D. Raines, and R. G. Rojas, "Multiport reactive loading matching technique for wide band antenna applications using the theory of characteristic modes," *IEEE Transactions on Antennas and Propagation*, vol. 63, no. 1, pp. 261–268, 2015.

[110] H. Kuhlman, "Small aperture coupling between dissimilar regions - example 1," *Unpublished*, 2016.

[111] N. Marcuvitz, *Waveguide handbook*, 21. Iet, 1951.

[112] C. A. Balanis, *Advanced engineering electromagnetics*. John Wiley & Sons, 1999.

[113] R. E. Collin, *Foundations for microwave engineering*. John Wiley & Sons, 2007.

[114] ——, *Field theory of guided waves*. McGraw-Hill, 1960.

[115] K. Chen, H. H. Sigmarsson, and D. Peroulis, "Power handling of high-Q evanescent-mode tunable filter with integrated piezoelectric actuators," in *Microwave Symposium Digest (MTT), 2012 IEEE MTT-S International*, IEEE, 2012, pp. 1–3.

[116] T. Q. Ho and S. M. Hart, "A broad-band coplanar waveguide to slot line transition," NAVAL COMMAND CONTROL, OCEAN SURVEILLANCE CENTER RDT, and E DIV SAN DIEGO CA, Tech. Rep., 1992.

[117] C.-H. Ho, L. Fan, and K. Chang, "New uniplanar coplanar waveguide hybrid-ring couplers and magic-t's," *IEEE Transactions on Microwave Theory and Techniques*, vol. 42, no. 12, pp. 2440–2448, 1994.

[118] S. Saeedi, J. Lee, and H. H. Sigmarsson, "Novel coupling matrix synthesis for single-layer substrate-integrated evanescent-mode cavity tunable bandstop filter design," *IEEE Transactions on Microwave Theory and Techniques*, vol. 63, no. 12, pp. 3929–3938, 2015.

[119] H. Joshi, H. H. Sigmarsson, S. Moon, D. Peroulis, and W. J. Chappell, "High Q narrow-band tunable filters with controllable bandwidth," in *Microwave Symposium Digest, 2009. MTT'09. IEEE MTT-S International*, IEEE, 2009, pp. 629–632.

[120] I. Hunter, *Theory and design of microwave filters*, 48. Iet, 2001.

[121] L. Wedepohl, "Application of matrix methods to the solution of travelling-wave phenomena in polyphase systems," *Electrical Engineers, Proceedings of the Institution of*, vol. 110, no. 12, pp. 2200–2212, 1963.

[122] R. Galloway, W. Shorrocks, and L. Wedepohl, "Calculation of electrical parameters for short and long polyphase transmission lines," *Electrical Engineers, Proceedings of the Institution of*, vol. 111, no. 12, pp. 2051–2059, 1964.

[123] J. A. B. Faria, "A new generalized modal analysis theory for nonuniform multiconductor transmission lines," *Power Systems, IEEE Transactions on*, vol. 19, no. 2, pp. 926–933, 2004.

[124] ——, "A new modal analysis theory for multiconductor nonuniform transmission line structures: Application to the analysis of line junctions," *Power Systems, IEEE Transactions on*, vol. 19, no. 3, pp. 1380–1386, 2004.

[125] J. B. Faria, *Multiconductor transmission-line structures: modal analysis techniques*. John Wiley & Sons, 1993, vol. 16.

[126] F. Croq and D. M. Pozar, "Multifrequency operation of microstrip antennas using aperture-coupled parallel resonators," *IEEE Transactions on Antennas and Propagation*, vol. 40, no. 11, pp. 1367–1374, 1992.

[127] G. Antonini, "A dyadic green's function based method for the transient analysis of lossy and dispersive multiconductor transmission lines," *Microwave Theory and Techniques, IEEE Transactions on*, vol. 56, no. 4, pp. 880–895, 2008.

[128] M. Kirschning and R. H. Jansen, "Accurate wide-range design equations for the frequency-dependent characteristic of parallel coupled microstrip lines," *Microwave Theory and Techniques, IEEE Transactions on*, vol. 32, no. 1, pp. 83–90, 1984.

[129] D. Pavlidis and H. L. Hartnagel, "The design and performance of three-line microstrip couplers," *Microwave Theory and Techniques, IEEE Transactions on*, vol. 24, no. 10, pp. 631–640, 1976.

[130] R. Mongia, I. J. Bahl, and P. Bhartia, *RF and microwave coupled-line circuits*. Artech house, 1999.

[131] V. K. Tripathi, "Asymmetric coupled transmission lines in an inhomogeneous medium," *Microwave Theory and Techniques, IEEE Transactions on*, vol. 23, no. 9, pp. 734–739, 1975.

[132] C. R. Paul, *Analysis of multiconductor transmission lines*. John Wiley & Sons, 2008.

[133] ——, "A brief history of work in transmission lines for EMC applications," *IEEE Transactions on Electromagnetic Compatibility*, vol. 49, no. 2, pp. 237–252, 2007.

[134] S. S. Bedair, "Characteristics of some asymmetrical coupled transmission lines," *IEEE transactions on microwave theory and techniques*, vol. 32, no. 1, pp. 108–110, 1984.

[135] L. A. Pipes, "X. matrix theory of multiconductor transmission lines," *The London, Edinburgh, and Dublin Philosophical Magazine and Journal of Science*, vol. 24, no. 159, pp. 97–113, 1937.

[136] A. Abbosh, "Analytical closed-form solutions for different configurations of parallel-coupled microstrip lines," *IET microwaves, antennas & propagation*, vol. 3, no. 1, pp. 137–147, 2009.

[137] A. M. Abbosh, "Corrections to'analytical closed-form solutions for different configurations of parallel-coupled microstrip lines'," *IET Microwaves, Antennas & Propagation*, vol. 7, no. 3, p. 214, 2013.

[138] A. B. Dalby, "Interdigital microstrip circuit parameters using empirical formulas and simplified model," in *Microwave Symposium Digest, 1978 IEEE-MTT-S International*, IEEE, 1978, pp. 223–226.

[139] R. Garg and I. Bahl, "Characteristics of coupled microstriplines," *IEEE Transactions on microwave theory and techniques*, vol. 27, no. 7, pp. 700–705, 1979.

[140] R. F. Harrington, *Time-harmonic electromagnetic fields*. McGraw-Hill, 1961.

[141] N. Nagai and E. Maekawa, "A new analysis of n-way hybrid power dividers with equiamplitudes," in *In its Equivalent Circuit Representation of Coupled Multiwire Line and Its Appl. p 61-82 (SEE N77-33403 24-33)*, 1977.

[142] M. B. Bazdar, A. R. Djordjevic, R. F. Harrington, and T. K. Sarkar, "Evaluation of quasi-static matrix parameters for multiconductor transmission lines using galerkin's method," *IEEE transactions on microwave theory and techniques*, vol. 42, no. 7, pp. 1223–1228, 1994.

[143] P. Winniford and J. Ruyle, "Expansion of design guidelines for a tightly-coupled microstrip dipole array," *Proc. Allerton Antenna Applications Symposium*, pp. 324–342, 2014.

[144] J. D. Kraus, *Antennas*. McGraw-Hill, 1988.

[145] J. M. Miller, "Electrical oscillations in antennas and inductance coils," *Proceedings of the Institute of Radio Engineers*, vol. 7, no. 3, pp. 299–326, 1919.

Appendix A

Multiline Coupling

A.1 Introduction

Coupled multiline transmission lines (MTLs) are used in many applications, from filters [120], to feed networks and interconnects [132], to radiating elements [126] [143]. Analysis of multiline microstrip transmission lines is often relegated to full-wave approaches [132] [127], which are computationally costly. Additionally, analytical insight into structure behavior is lost with reliance on numerical techniques.

The analysis of multiconductor transmission lines is a topic that has received attention for decades, [133]. Some of the earliest work was focused on high-power transmission lines [135] [121], and the topic continues to expand today with modelling of RF transmission lines [127], [136]. Much of the literature covering analysis of MTLs comes from a time when reducing and simplifying computational cost was a primary concern [121]. Intermediate quantities needed to solve for network parameters, such as modal voltage distribution and characteristic impedance, were included in early papers [121] [141], but have been omitted from recent textbooks which summarize the topic [37] [130]. Furthermore, the intermediate quantities, which give important insight into coupling and transmission behavior, were often simplified in early papers by conventional linear algebra techniques, and converted into terms with no clear meaning beyond serving as a step towards solving for network parameters.

This paper presents a closed form analytical solution for the behavior of multiline microstrip systems. It is based on an eigenanalysis of the system matrix of a microstrip structure. The system matrix is calculated from an analytical closed form solution for the Per-Unit-Length (PUL) capacitance of two coupled microstrip lines found in [128]. To test the accuracy of our solution, we compare it against a commercially available Method of Moments (MoM) package and define percent error across frequency. The authors have found that existing accepted analytic two line solutions [25] [130] [128], calculated over a variety of physical dimensions, have 7.2% error across frequency compared to MoM results for symmetric width lines, and within 14.9% error for asymmetric width lines. Our n-line solution, applied to a wide range of 4 line scenarios, shows a symmetric width error

of 5.1% and asymmetric error of 16.6%. The new multiline solution is within 2.7% of the error of the well accepted analytic two line solutions when both are compared against the commercial MoM solution.

The next section will outline the Telegrapher's Equations for transmission lines. Section 3 expands the Telegrapher's Equations to two coupled microstrip lines. Section 4 covers how to calculate self and mutual capacitance between coupled microstrip lines, and Section 5 explains the general solution of MTL applied to two coupled lines. Section 6 expands the solution to the n-line case, and Section 7 offers conclusions.

A.2 Telegrapher's Equations (TE)

As is well established in RF & microwave theory, [25], the Telegrapher's Equations (TE) describe the behavior of a transmission line. TE has already been applied to two coupled lines and to multiple coupled lines, but has not been applied to a completely closed form solution for coupled microstrip multiline transmission line. In this section we outline basic TE theory applied to a single transmission line using the notation that will be used throughout this paper to orient the method.

Position-dependent voltages, $v(x)$, and currents, $i(x)$, on a transmission line can be found through solving the Telegrapher's Equations [130], which essentially state that the voltage drop is proportionate to the line current [140]

$$\frac{dv(x)}{dx} = -zi(x) \tag{A.1}$$

according to the PUL series impedance, $z = j\omega L + R$. The Telegrapher's Equations also state that the shunt current is proportionate to the line voltage:

$$\frac{di(x)}{dx} = -yv(x) \tag{A.2}$$

according to the PUL shunt admittance, $y = j\omega C + G$. The behavior of a transmission line is characterized by its PUL parameters; any arbitrary structure supporting wave propagation has associated PUL resistance R, conductance G, capacitance C, and inductance L. R and G can simply be omitted for a lossless system. Differentiating both gives the wave equations for $v(x)$ and $i(x)$

$$\frac{d^2v(x)}{dx^2} = \gamma^2 v(x) = zyv(x) \tag{A.3}$$

and

$$\frac{d^2i(x)}{dx^2} = \gamma^2 i(x) = yzi(x) \tag{A.4}$$

with propagation constant

$$\gamma = \sqrt{zy} = \alpha + j\beta \tag{A.5}$$

where α is the wave attenuation coefficient, which should be zero in a lossless system. β is the phase constant and can also defined as

$$\beta = \omega\sqrt{\mu\epsilon} \tag{A.6}$$

where ω is angular frequency.

The solution to the ordinary differential equations (A.3) and (A.4) can be expressed as

$$v(x) = \hat{V}^{+}e^{-\gamma_1 x} + \hat{V}^{-}e^{+\gamma_1 x} \tag{A.7}$$

and

$$i(x) = \hat{I}^{+}e^{-\gamma_1 x} + \hat{I}^{-}e^{+\gamma_1 x}. \tag{A.8}$$

The physical interpretation of this is a forward and backward propagating voltage on a transmission line. Though there is only one mode in this scenario, $\hat{V}$ is our notation to indicate that the voltage is mode specific, and γ_1 is the propagation constant for the first mode. The $+$ and $-$ refer to forward and backward propagating modes. The notation used here is preemptive of the notation necessary to describe a generalized multiline solution with multiple modes due to coupling.

With a voltage and current defined on a line, a characteristic impedance, Z^C is usually defined as [25]

$$Z^C = \frac{\hat{V}^{+}}{\hat{I}^{+}} = \frac{z}{\gamma} = \frac{\gamma}{y} = \sqrt{\frac{z}{y}} = \sqrt{\frac{R + j\omega L}{G + j\omega C}} \tag{A.9}$$

where $\hat{V}^{+}$ and $\hat{I}^{+}$ are the amplitudes of the forward travelling voltage and current waves. For simplicity, R and G will be omitted for a lossless approximation for the remainder of this paper.

The PUL inductance for a lossless microstrip line, or any quasi-TEM transmission line, can be calculated as the inverse of the PUL capacitance for a line with the dielectric replaced with air [25], which can be written as

$$L = \epsilon_0\mu_0 C_0^{-1} \tag{A.10}$$

where C_0 is the capacitance from an equivalent structure with air dielectric. Using C_0 to substitute for the inductance, the characteristic impedance of a single lossless microstrip line can be further rewritten as [25]

$$Z^C = \sqrt{\frac{\epsilon_0\mu_0}{CC_0}}. \tag{A.11}$$

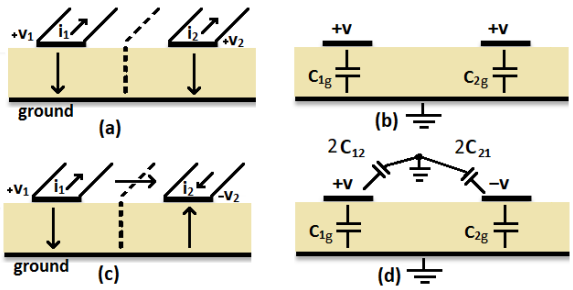


Figure A.1: Even and odd mode excitations for two coupled lines, (a) Even mode excitation and (b) capacitance seen by the lines, and (c) Odd mode excitation and (d) capacitance seen by the lines

A.3 TE for Two Coupled Lines

The Telegrapher Equations are extended in this section to describe two coupled transmission lines, with careful attention being given to our uniquely generalized formulation of the characteristic impedance, which is necessary for solving for network parameters. In [131], Tripathi expresses the system of equations describing coupled microstrip transmission lines in a particularly clear and intuitive way, placing particular emphasis on matrix formatting and characteristic impedances. However, Tripathi's work is meant for two-coupled lines and can't be easily expanded to account for n coupled lines. This paper will retain the clear analytical meaning of Tripathi's work for two lines in a format that is easily generalizable to n lines.

Two parallel microstrip lines in close proximity over a ground plane couple together and mutually induce currents and voltages on each other, shown in Figure A.1. The rate of change of voltage at a particular point on line one is a function of the currents on both lines, and the physically determined impedances seen on both lines, expressed as

$$-\frac{dv_1}{dx} = z_{11}i_1 + z_{12}i_2. \tag{A.12}$$

The same is true for the rate of change of voltage on line two,

$$-\frac{dv_2}{dx} = z_{21}i_1 + z_{22}i_2. \tag{A.13}$$

The rate of change of the current is also linked to the current and shunt admittances on both lines as

$$-\frac{di_1}{dx} = y_{11}v_1 + y_{12}v_2 \tag{A.14}$$

and

$$-\frac{di_2}{dx} = y_{21}v_1 + y_{22}v_2. \tag{A.15}$$

Following the same steps as before, we differentiate the first order Telegrapher's equations and substitute the second order equations into each other as

$$\frac{d^2v_1}{dx^2} = (z_{11}y_{11} + z_{12}y_{21})v_1 + (z_{11}y_{12} + z_{12}y_{22})v_2 \tag{A.16}$$

and

$$\frac{d^2v_2}{dx^2} = (z_{21}y_{11} + z_{22}y_{21})v_1 + (z_{21}y_{12} + z_{22}y_{22})v_2. \tag{A.17}$$

Similar to the single line solution for the Telegrapher's equations, the voltage at any point on the two coupled transmission lines can be expressed as a summation of two distinct modal voltage waves which both have forward and backward propagating components, [130] [131]. A transmission line system consisting of $(n + 1)$ conductors (including the ground plane) will support n modes of forward and backward travelling waves [132]. For the case of two coupled symmetric lines, the modal analysis works out to the common solution of even and odd modes. The voltage and current defined at a particular terminal, or at any position on the system, are a superposition of weighted modal voltage and current waves, where

$$v_1(x) = A_1\hat{V}_{11}e^{-\gamma_1 x} + A_2\hat{V}_{11}e^{+\gamma_1 x} + A_3\hat{V}_{12}e^{-\gamma_2 x} + A_4\hat{V}_{12}e^{+\gamma_2 x}, \tag{A.18}$$

and

$$v_2(x) = A_1\hat{V}_{21}e^{-\gamma_1 x} + A_2\hat{V}_{21}e^{+\gamma_1 x} + A_3\hat{V}_{22}e^{-\gamma_2 x} + A_4\hat{V}_{22}e^{+\gamma_2 x}, \tag{A.19}$$

and where v_1 describes voltage on line 1 and v_2 describes voltage on line 2. Usually each mode has its own unique propagation constant, but there are rare degenerate cases with repeated roots [125]. Equations (A.18) and (A.19) express all of the modal forward and backward propagating voltages with weighting constants, A. The weighting constants, A, used for both voltage and current, are defined by the boundary conditions, which are specific to a particular excitation. $\hat{V}_{ij}$ denotes the mode j voltage on line i, with the direction of propagation given by the sign of γ.

The current can be expressed similarly as

$$i_1(x) = A_1\hat{I}_{11}e^{-\gamma_1 x} - A_2\hat{I}_{11}e^{+\gamma_1 x} + A_3\hat{I}_{12}e^{-\gamma_2 x} - A_4\hat{I}_{12}e^{+\gamma_2 x}, \tag{A.20}$$

and

$$i_2(x) = A_1\hat{I}_{21}e^{-\gamma_1 x} - A_2\hat{I}_{21}e^{+\gamma_1 x} + A_3\hat{I}_{22}e^{-\gamma_2 x} - A_4\hat{I}_{22}e^{+\gamma_2 x} \tag{A.21}$$

where the subscripts on the modal current, $\hat{I}_{ij}$, again indicate mode j on line i. Alternately, since we previously defined a characteristic impedance that related the travelling voltage and current waves, the modal current terms can be replaced with the characteristic impedance divided by the corresponding modal voltage for the same line. Since the propa-

gating modal voltages and currents are mode and line specific, we will need to modify our characteristic impedance to be mode and line specific with the same subscript conventions, such that

$$\hat{I}_{ij} = \hat{V}_{ij}/Z^C_{ij}. \tag{A.22}$$

The modal propagation constant, γ_i, is solved for based on a quadratic equation solution of the coupled Telegrapher's equations. Usually the solution is expressed in terms of a and b terms [131], where

$$a_1 = y_1 z_1 + y_m z_m, \tag{A.23}$$

$$a_2 = y_2 z_2 + y_m z_m, \tag{A.24}$$

$$b_1 = z_1 y_m + y_2 z_m, \tag{A.25}$$

and

$$b_2 = z_2 y_m + y_1 z_m. \tag{A.26}$$

Together these terms combine to define the propagation constants, [131], as

$$\gamma^2_{c,\pi} = \frac{a_1 + a_2}{2} \pm \frac{1}{2}[(a_1 - a_2)^2 + 4b_1 b_2]^{1/2}. \tag{A.27}$$

The c and π subscripts denote the two modes in the notation used in [131].

Writing the mutual impedance terms as z_m works for two lines since the mutual impedance from line one to line two is equivalent to the impedance from line two to line one, or $z_{12} = z_{21}$. To adequately describe a multiline system we will need a more precise nomenclature to keep track of several distinct mutual impedances and admittances. For this reason, we rewrite the a and b terms as

$$a_1 = z_{11} y_{11} + z_{12} y_{21}, \tag{A.28}$$

$$a_2 = z_{21} y_{12} + z_{22} y_{22}, \tag{A.29}$$

$$b_1 = z_{11} y_{12} + z_{12} y_{22}, \tag{A.30}$$

and

$$b_2 = z_{21} y_{11} + z_{22} y_{21}. \tag{A.31}$$

Noticing the symmetry of the subscripts, we can see that the a and b terms arise naturally from the multiplication of the series impedance terms and shunt admittance terms

ordered into matrices,

$$[z][y] = \begin{bmatrix} z_{11} & z_{12} \\ z_{21} & z_{22} \end{bmatrix} \begin{bmatrix} y_{11} & y_{12} \\ y_{21} & y_{22} \end{bmatrix} = \begin{bmatrix} a_1 & b_1 \\ b_2 & a_2 \end{bmatrix}, \tag{A.32}$$

with the self terms on the main diagonal and the mutual terms off axis. For consistency, the previous solution for the propagation constant can be rewritten in an equivalent and much lengthier form as

$$\begin{aligned} \gamma_{1,2}^2 =& \frac{(z_{11}y_{11} + z_{12}y_{21}) + (z_{21}y_{12} + z_{22}y_{22})}{2} \\ & \pm \frac{1}{2}[((z_{11}y_{11} + z_{12}y_{21}) - (z_{21}y_{12} + z_{22}y_{22}))^2 + 4(z_{11}y_{12} + z_{12}y_{22})(z_{21}y_{11} + z_{22}y_{21})]^{1/2}. \end{aligned} \tag{A.33}$$

Since we are focused on presenting a solution that works for n-coupled lines, these expressions have the immediate disadvantage of being difficult to expand to handle more than two lines. Fortunately, the explicit scalar solution for the propagation constant $\gamma_{1,2}^2$ is actually the eigenvalue corresponding to the matrix or polynomial product of the PUL series impedance and PUL shunt admittance, [125]. We will take advantage of this fact later to expand the solution to n-coupled lines.

The propagation constants of the distinct modes of the system corresponds to a specific modal distribution of voltages and currents, and naturally, the eigenvectors associated with the eigenvalue solution are the eignevoltages or eigencurrents, depending on whether the system is formulated as $[z][y]$ or $[y][z]$, respectively, [121], [125]. For the sake of brevity a scalar solution will not be written here for the eigenvoltages or eigensolutions.

To finish describing the behavior of the coupled transmission lines in the transverse plane, a characteristic impedance is needed to define the relationship of the modal voltages to the modal currents. We will use the eigenvoltages or eigencurrents to define the characteristic impedance. Wedepohl offers such a formulation for two lines in [121], although the expressions are unnumbered and go unused in the rest of the paper. The characteristic impedance, with some of the variable notation changed, is

$$Z_{11}^C = \frac{|z|}{\gamma_1[z_{22} - \hat{V}_{21}/\hat{V}_{11}z_{21}]}, \tag{A.34}$$

$$Z_{12}^C = \frac{|z|}{\gamma_2[\hat{V}_{12}/\hat{V}_{22}z_{22} - z_{21}]}, \tag{A.35}$$

$$Z_{21}^C = \frac{|z|}{\gamma_1[\hat{V}_{21}/\hat{V}_{11}z_{11} - z_{12}]}, \tag{A.36}$$

and

$$Z_{22}^{C} = \frac{|z|}{\gamma_2[z_{11} - \hat{V}_{12}/\hat{V}_{22} z_{12}]}. \tag{A.37}$$

Lowercase z still refers to the PUL series impedance of the lines, and $|z|$ is the determinant of the series impedance matrix, $[z]$. With some substitutions and algebraic manipulation the above expressions can be shown to be numerically identical to the corresponding two-line characteristic impedance terms in [131] and [121]. The new generalized n line solution for Z^C will be given later in the paper, but the preceding equations are written in such a way that the reader should already have some intuition as to how to generalize the expressions. Z^C is a characteristic impedance matrix that defines the ratio of voltage to current for a particular mode on a particular line. Since an n line structure generally supports n modes there should be nxn characteristic impedances. For example, with two coupled lines, Z_{21}^{C} is the ratio of mode 1 voltage divided by mode 1 current on line 2.

While it made sense for Tripathi [131] to express characteristic impedance for two coupled lines by way of a voltage ratio term, a multiline solution requires direct knowledge of the normalized modal voltage terms for each line. Similarly, common textbooks citing previous work in coupled multiline transmission lines [25], [37], [130] only show characteristic impedances for a single line or two coupled lines. Our analytical expressions for coupled lines will be generalized into matrix format in Section A.5 and expanded into an n line form in Section A.6. However, before moving forward an analytical method for expressing capacitance matrices must be introduced. In Section A.5 we will connect this mostly scalar analysis of coupled Telegrapher's equations to a matrix analysis centered on the eigenvalue solution.

A.4 Capacitance for Coupled Multiline Microstrip

In this section we will explain how to calculate capacitance and use it to assemble the PUL admittance and impedance matrix. We assume that a multiline structure can be approximated as a superposition of two line structures, and while this idea is simple, we have not seen it used before in the literature.

The capacitance of two coupled microstrip lines over a ground plane is derived by many authors [128], [134], [136]–[139]. In [128], Kirschning and Jansen derive closed form expressions for the capacitances and effective permittivity of two coupled microstrip lines. Expressions for the capacitance between two coupled lines of asymmetric width are given in [134]. Reference [128] has been heavily cited and is used for symmetric width coupled line calculations in this paper, and reference [134] is used for calculating the capacitance between coupled lines of different width. Generally, all of these methods derive the even and odd mode capacitances. The self-capacitance (C^s) of a microstrip line to the ground plane equals the even mode capacitance,

$$C^s = C^{even}, \tag{A.38}$$

and the mutual capacitance (C^m) between two lines is

$$C^m = \frac{C^{odd} - C^{even}}{2}. \tag{A.39}$$

The capacitance is used to define the PUL shunt admittance matrix. For the two line system the shunt admittance matrix can be expressed as

$$[y] = j\omega[C] = j\omega \begin{bmatrix} C_1^s + C_{12}^m & -C_{12}^m \\ -C_{21}^m & C_2^s + C_{21}^m \end{bmatrix} \tag{A.40}$$

where C_1^s and C_2^s are self-capacitances of line 1 and 2 to the ground plane, and C_{12}^m is the mutual capacitance between line 1 and line 2, as illustrated in Figure A.1, [130].

To the best of the authors' knowledge, closed-form calculations for the capacitance between n parallel microstrip lines do not exist. In this paper, rather than relying on computationally intensive numerical approaches, the shunt admittance matrix, Equation (A.40), was expanded to include any number of terms, in the form

$$[y] = j\omega[C] = j\omega \begin{bmatrix} C_{11} & -C_{12}^m & \dots & -C_{1n}^m \\ -C_{21}^m & C_{22} & \dots & -C_{2n}^m \\ \vdots & \vdots & \ddots & \vdots \\ -C_{n1}^m & -C_{n2}^m & \dots & C_{nn} \end{bmatrix} \tag{A.41}$$

with all of the mutual capacitances (C_{ij}^m) approximated by superpositions of two-coupled line capacitance calculations to represent the whole network, as shown in Figure A.2. The main diagonal (C_{ii}) terms are the self-capacitance values of each line plus the summation of the mutual capacitance terms in that row, written as

$$C_{ii} = C_i^s + \sum_{j \neq i} C_{ij}^m. \tag{A.42}$$

Self-capacitance is a measure of the charge and voltage potential on a conductor with reference to ground, but it is still affected by its neighboring conductors since neighboring conductors, even when excited in-phase, will still alter the fringing fields from the conductor in question. In this paper it is assumed that the nearest neighboring conductor will have the greatest impact on the self-capacitance of a conductor to ground, so the self-capacitance calculation used for each line is the self-capacitance from the nearest neighbor pair of lines.

The series impedance of a microstrip transmission line is found by solving for the capacitance of a similar microstrip line with air dielectric, which was expressed in Equation (A.10). The series impedance matrix, populated by PUL inductance values, is found to be

$$[z] = j\omega[L] = j\omega\epsilon_0\mu_0[C_0]^{-1}, \tag{A.43}$$

where C_0 corresponds to the free space, or air dielectric, capacitance.

As stated before, [128] and [134] are used for calculating coupled line capacitance in this paper. The PUL characterization could be replaced with other solutions, such as the

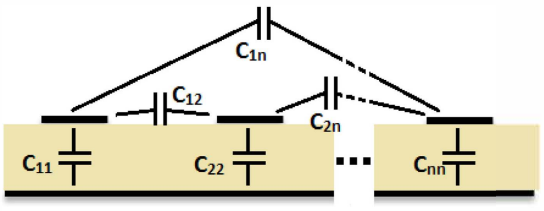


Figure A.2: Superposition of two line capacitance calculations use to approximate an n-line structure

similar closed form solution in [136] or [138], or with a method of moments solution that could take conductor and dielectric loss into account. For a lossy characterization the R and G terms would need to be added into the definitions for series impedance and shunt admittance, and the solution would proceed normally from there.

A.5 Network Parameters for a Two Line System

As mentioned previously, we have been following the solution format for two coupled lines described in [131] and working to expand the method for n-lines. In this section we will apply our form of the solution of network parameters, before demonstrating how to expand this notation and method to the n-line problem in the next section. Since the Telegrapher's Equations for coupled lines turns into a system of equations, the TE are most conveniently represented in matrix form.

In Section A.3, we solved the Telegrapher's equations in terms of scalar solutions, but we did begin to introduce matrix notation into the problem. A centrally important concept to realize with coupled lines is that solving the coupled Telegrapher's equations is an eigenvalue problem [125], [135]. In mathematical terms, the series impedance and shunt admittance, when multiplied together as matrices, form the system matrix ($[z][y]$) of the eigenvalue problem. The square of the propagation constant is the eigenvalue of the system matrix, which is usually a diagonal matrix with distinct roots. The solution for the propagation constant can be expressed as a quadratic for two coupled lines, but the eigenvalue solution doesn't necessarily have an explicit scalar solution for higher order matrices, so we must adopt matrix notation for the whole problem if we wish to characterize multiline coupling. Earlier the authors declined to give a scalar solution for the eigenvoltages of two coupled lines. It is simpler to avoid a scalar solution and instead say that the eigenvectors which lead to each distinct eigenvalue solution are the eigenvoltages for system matrix $[z][y]$, or if the order is reversed it's the eigencurrents for $[y][z]$ [125]. Again, there isn't necessarily any explicit scalar solution for the eigenvectors for more than two lines. Fittingly, the matrix formed from all of the eigenvectors is known as the modal matrix. The eigenvectors are non-unique and usually normalized, but the relationship between the values in each eigenvector signifies the ratio of line voltages or currents for each pure modal

excitation.

Tripathi in [131] chose to define voltages on line 1 of a two coupled line system, and express voltage on line 2 as the line 1 voltage multiplied by modal voltage ratio factors. If all of the modal voltage values on each line can be found, then voltage ratio terms can be avoided.

To solve for the impedance parameters, it is necessary to evaluate Equations (A.18)-(A.21) at $x = 0$ and at $x = l$, where l is line length. For two coupled lines, the first port is chosen to be on line 1 at $x = 0$, so the port voltage is defined as being $V_1 = v_1(x = 0)$. Similarly, the other port voltages are $V_2 = v_2(x = 0)$, $V_3 = v_2(x = l)$, and $V_4 = v_1(x = l)$. The voltages seen at each port are a summation of the propagating voltage modes that satisfy the coupled Telegrapher's equations. Usually the collection of modal contributions to the port voltages have not been defined as a separate matrix variable, but the authors think that it is helpful to assign distinct variable names to these quantities as $[V^{net}]$ and $[I^{net}]$, or the network modal voltage matrix and network modal current matrix. They are identical to Equations (A.18)-(A.21), but packaged in matrix format. They are used below to define the port voltages and currents.

$$(V) = \begin{pmatrix} V_1 \\ V_2 \\ V_3 \\ V_4 \end{pmatrix} = [V^{net}] \begin{pmatrix} A_1 \\ A_2 \\ A_3 \\ A_4 \end{pmatrix} \tag{A.44}$$

where

$$[V^{net}] = \begin{bmatrix} \hat{V}_{11}e^{-\gamma_1 0} & \hat{V}_{11}e^{\gamma_1 0} & \hat{V}_{12}e^{-\gamma_2 0} & \hat{V}_{12}e^{\gamma_2 0} \\ \hat{V}_{21}e^{-\gamma_1 0} & \hat{V}_{21}e^{\gamma_1 0} & \hat{V}_{22}e^{-\gamma_2 0} & \hat{V}_{22}e^{\gamma_2 0} \\ \hat{V}_{21}e^{-\gamma_1 l} & \hat{V}_{21}e^{\gamma_1 l} & \hat{V}_{22}e^{-\gamma_2 l} & \hat{V}_{22}e^{\gamma_2 l} \\ \hat{V}_{11}e^{-\gamma_1 l} & \hat{V}_{11}e^{\gamma_1 l} & \hat{V}_{12}e^{-\gamma_2 l} & \hat{V}_{12}e^{\gamma_2 l} \end{bmatrix} \tag{A.45}$$

The (A) vector is a set of weighting constants that define the voltage and current excitation boundary conditions. Tripathi, [131], defines the voltage on line two as the line one voltage multiplied by a voltage ratio factor, which is also separately defined for each mode. By this convention, for more coupled lines, each line would have its modal voltage components defined by their ratio to the line one modal voltage components. It is simpler to replace modal voltage and current ratios referenced to line one with modal coefficients that are normalized across the whole system . This is simpler because the normalized coefficients already exist in the eigenvoltage and eigencurrent matrices. Following the same pattern as was used for the network voltage matrix, and with the same weighting vector (A), the current at each port can be defined as

$$(I) = \begin{pmatrix} I_1 \\ I_2 \\ -I_3 \\ -I_4 \end{pmatrix} = [I^{net}] \begin{pmatrix} A_1 \\ A_2 \\ A_3 \\ A_4 \end{pmatrix}, \tag{A.46}$$

where

$$[I^{net}] = \begin{bmatrix} \frac{\hat{V}_{11}}{Z_{11}^C}e^{-\gamma_1 0} & -\frac{\hat{V}_{11}}{Z_{11}^C}e^{\gamma_1 0} & \frac{\hat{V}_{12}}{Z_{12}^C}e^{-\gamma_2 0} & -\frac{\hat{V}_{12}}{Z_{12}^C}e^{\gamma_2 0} \\ \frac{\hat{V}_{21}}{Z_{21}^C}e^{-\gamma_1 0} & -\frac{\hat{V}_{21}}{Z_{21}^C}e^{\gamma_1 0} & \frac{\hat{V}_{22}}{Z_{22}^C}e^{-\gamma_2 0} & -\frac{\hat{V}_{22}}{Z_{22}^C}e^{\gamma_2 0} \\ \frac{\hat{V}_{21}}{Z_{21}^C}e^{-\gamma_1 l} & -\frac{\hat{V}_{21}}{Z_{21}^C}e^{\gamma_1 l} & \frac{\hat{V}_{22}}{Z_{22}^C}e^{-\gamma_2 l} & -\frac{\hat{V}_{22}}{Z_{22}^C}e^{\gamma_2 l} \\ \frac{\hat{V}_{11}}{Z_{11}^C}e^{-\gamma_1 l} & -\frac{\hat{V}_{11}}{Z_{11}^C}e^{\gamma_1 l} & \frac{\hat{V}_{12}}{Z_{12}^C}e^{-\gamma_2 l} & -\frac{\hat{V}_{12}}{Z_{12}^C}e^{\gamma_2 l} \end{bmatrix}. \tag{A.47}$$

In the above equations, $\hat{V}_{ij}$ again refers to the mode j voltage on line i, and modal current $\hat{I}_{ij}$ is replaced with $\hat{V}_{ij}/Z_{ij}^C$ since $\hat{V}$ and $\hat{I}$ are both normalized matrices. Z^C was defined in Equations (A.34)-(A.37).

When boundary conditions are applied by means of the (A) modal weights, the network voltage and current matrices are reduced to vectors and are related by impedance parameters as:

$$(V) = [Z](I), \tag{A.48}$$

which can be rewritten as

$$[V^{net}](A) = [Z][I^{net}](A). \tag{A.49}$$

The (A) weighting vector can be cancelled out from both sides, and the impedance parameters can be found as the network voltage matrix multiplied by the inverse of the network current matrix.

$$[V^{net}] = [Z][I^{net}], \tag{A.50}$$

or

$$[Z] = [V^{net}][I^{net}]^{-1}. \tag{A.51}$$

The impedance parameters for two coupled lines can be written symbolically, as seen below in Equations (A.52)-(A.57) which are similar in form to those given in [131] as

$$Z_{11} = \frac{\hat{V}_{22}z_{11}coth(\gamma_1 l)}{|\hat{V}|} + \frac{\hat{V}_{21}z_{12}coth(\gamma_2 l)}{|\hat{V}|}, \tag{A.52}$$

$$Z_{12} = \frac{\hat{V}_{21}\hat{V}_{22}z_{11}coth(\gamma_1 l)}{\hat{V}_{11}|\hat{V}|} - \frac{\hat{V}_{21}\hat{V}_{22}z_{12}coth(\gamma_2 l)}{\hat{V}_{12}|\hat{V}|}, \tag{A.53}$$

$$Z_{13} = \frac{\hat{V}_{21}\hat{V}_{22}z_{11}}{\hat{V}_{11}|\hat{V}|sinh(\gamma_1 l)} - \frac{\hat{V}_{21}\hat{V}_{22}z_{12}}{\hat{V}_{12}|\hat{V}|sinh(\gamma_2 l)}, \tag{A.54}$$

$$Z_{14} = \frac{\hat{V}_{22}z_{11}}{|\hat{V}|sinh(\gamma_1 l)} - \frac{\hat{V}_{21}z_{12}}{|\hat{V}|sinh(\gamma_2 l)}, \tag{A.55}$$

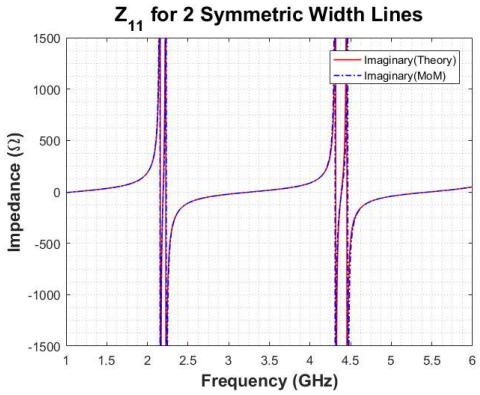


Figure A.3: New closed-form analytical calculation compared to commercially available MoM solver, for two lines. s=2.286mm, w=2.286mm, l=50mm, h=0.762mm, ϵ_r=2.2. Zero crossings with less than 0.3% error compared to a MoM solution.

$$Z_{22} = \frac{\hat{V}_{12} z_{21} coth(\gamma_1 l)}{|\hat{V}|} + \frac{\hat{V}_{11} z_{22} coth(\gamma_2 l)}{|\hat{V}|}, \tag{A.56}$$

and

$$Z_{23} = \frac{(\hat{V}_{21})^2 \hat{V}_{22} z_{11}}{(\hat{V}_{11})^2 |\hat{V}| sinh(\gamma_1 l)} - \frac{\hat{V}_{21} (\hat{V}_{22})^2 z_{12}}{(\hat{V}_{12})^2 |\hat{V}| sinh(\gamma_2 l)}. \tag{A.57}$$

The impedance parameters derived by the authors agree exactly with those given by Tripathi [131] with some substitution and algebraic manipulation. The terms developed by the authors, are slightly more complicated to write in scalar form than those developed by Tripathi in [131], but they have the significant advantage of being completely adaptable to matrix form, allowing for the solution of impedance parameters for n coupled lines.

The results are compared numerically against those from a commercial Method of Moments solver in Figure A.3. In the results, s is the spacing between microstrip lines (measured between nearest edges), w is the width of each line, l is the length of the system, and h is the height or thickness of the substrate. The authors' results for symmetric coupled lines are within 7.2% error tolerance over a wide range of dimensions and substrate materials compared against those calculated in a commercially available Method of Moments (MoM) solver. The accuracy of the solutions significantly depend on the calculation of PUL capacitance. Kirschning and Jansen, in [128], state that their two line capacitance calculations for symmetric microstrip lines have less than 4% error over the range $0.1 < w/h < 10$ and $0.1 < s/h < 10$ and $1 < \epsilon_r < 18$.

Asymmetric coupled line calculations depend on the asymmetric line capacitance calculations from [134], which don't have any stated bounds over what range of design parameters an accurate result can be expected. The authors have found the theoretical results

to be within 14.9% error tolerance compared against the MoM solution over a similarly wide range of design parameters. Improved accuracy depends on use of a more accurate calculation of PUL capacitance. Both the symmetric and symmetric two line solution are well-established in the literature [25], [130], [131], so they may be taken as a baseline to compare multiline accuracy against.

A lossless system assumption has been made for the calculations ($R, G = 0$), resulting in purely reactive values for the impedance parameters. Conductor and dielectric loss could be easily taken into account by inserting the PUL resistance and conductance into the series impedance and shunt admittance matrices, the calculations for which are available in [132]. The next section will demonstrate our new closed form analytical solution for n-coupled microstrip lines.

A.6 Network Parameters for n-Coupled Line System

The solution for network parameters of more than two lines requires use of an eigen-analysis of the system matrix, $[z][y]$, which yields the eigenvoltages, $[\hat{V}]$, as the modal matrix or eigenvectors, and the square of the modal propagation constants, $[\gamma^2]$, as the eigenvalues. As before, $[z]$ is the matrix of PUL series impedance, and $[y]$ is the matrix of PUL shunt admittance. For a 2x2 matrix a scalar expression often exists for the eigenvalues, but for larger matrices this is usually not the case. The eigenvalue problem for coupled transmission lines, based on the the PUL series impedances and shunt admittances is

$$[z][y][\hat{V}] = [\gamma^2][\hat{V}]. \tag{A.58}$$

The eigenvalue matrix $[\gamma^2]$ is a diagonal matrix, where each term is the propagation constant for a separate mode. The eigencurrents could be similarly found from the matrix $[y][z]$. Since both the eigencurrents, $[\hat{I}]$, and the eigenvoltages, $[\hat{V}]$, are normalized quantities, the ratio of $[\hat{I}]$ to $[\hat{V}]$ is not meaningful. For that reason, it is necessary to substitute $\hat{I}_{ij} = \hat{V}_{ij}/Z^C_{ij}$ for the modal currents, as

$$v_i(x) = \sum_j A_j \hat{V}_{ij} e^{\pm\gamma_j x}, \tag{A.59}$$

and

$$i_i(x) = \sum_j A_j \hat{I}_{ij} e^{\pm\gamma_j x} = \sum_j A_j \frac{\hat{V}_{ij}}{Z^C_{ij}} e^{\pm\gamma_j x}. \tag{A.60}$$

An example calculation of eigenvoltages is given in Table A.1 for a coupled 4 line system of asymmetric width.

The characteristic impedance, or relation of current to voltage on each line for each mode can be solved for as the propagation constant divided by shunt admittance (similar to the the form in Equation (A.9), scaled to each mode and line by the modal currents where

Table A.1: Example eigenvoltage calculation for a system of four coupled lines defined as $w_1 = w_2 = w_4 = 0.2286mm$, $w_3 = 2.286mm$, $s_1 = s_2 = s_3 = 0.2286mm$, $h = 2.286mm$, $\epsilon_r = 2.2$

	Line 1	Line 2	Line 3	Line 4
Mode 1	-0.9	-0.34	0.56	0.26
Mode 2	-0.35	0.02	0.32	-0.95
Mode 3	0.26	-0.09	0.63	-0.06
Mode 4	-0.11	0.94	0.42	0.18

$$[\psi^z] = [y]^{-1}[\hat{I}][\gamma], \tag{A.61}$$

and

$$Z_{ij}^C = \psi_{ij}^z / \hat{I}_{ij}. \tag{A.62}$$

The concept of characteristic impedance is sometimes awkward to express because it depends on both matrix and scalar data to represent the mode and line specific voltage-current ratios that stem from the eigenanalysis of the system matrix $[z][y]$, so the term $[\psi^z]$ has been added just as an intermediate term to simplify the expressions. A symbolically different, but numerically identical expression for n-line characteristic impedance exists as an unlabelled equation in an appendix of [121], but to the best of the authors' knowledge our symbolic formulation is new to the literature and the older formulation went unused in subsequent literature. In the authors' opinion, this expression is also much simpler symbolically than the one found in [121]. Similarly, the characteristic admittance can be also be found as

$$[\psi^y] = [z]^{-1}[\hat{V}][\gamma] \tag{A.63}$$

and

$$Y_{ij}^C = \psi_{ij}^y / \hat{V}_{ij}. \tag{A.64}$$

It was shown in Equations (A.48)-(A.51) that solving for impedance parameters depends on finding the network voltage and current matrices. In Figure A.4 the voltages and currents for four coupled lines are labelled appropriately.

The vector of terminal voltages, (V), can be constructed by multiplying the network voltage matrix $[V^{net}]$ by the vector of weights for the propagating waves, (A), where

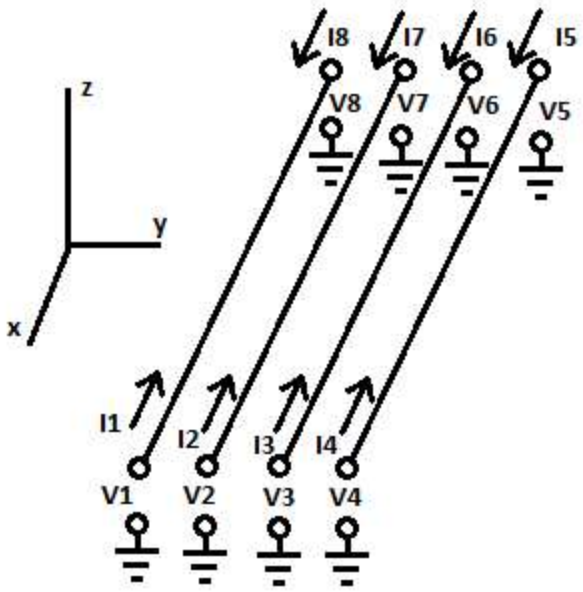


Figure A.4: Port currents and voltages labelled for four coupled lines

$$[V^{net}] = \begin{bmatrix} \hat{V}_{11}e^{-\gamma_1 0} & \hat{V}_{11}e^{\gamma_1 0} & \dots & \hat{V}_{1n}e^{-\gamma_n 0} & \hat{V}_{1n}e^{\gamma_n 0} \\ \hat{V}_{21}e^{-\gamma_1 0} & \hat{V}_{21}e^{\gamma_1 0} & \dots & \hat{V}_{2n}e^{-\gamma_n 0} & \hat{V}_{2n}e^{\gamma_n 0} \\ \vdots & & & & \\ \hat{V}_{n1}e^{-\gamma_1 0} & \hat{V}_{n1}e^{\gamma_1 0} & \dots & \hat{V}_{nn}e^{-\gamma_n 0} & \hat{V}_{nn}e^{\gamma_n 0} \\ \hat{V}_{n1}e^{-\gamma_1 l} & \hat{V}_{n1}e^{\gamma_1 l} & \dots & \hat{V}_{nn}e^{-\gamma_n l} & \hat{V}_{nn}e^{\gamma_n l} \\ \vdots & & & & \\ \hat{V}_{21}e^{-\gamma_1 l} & \hat{V}_{21}e^{\gamma_1 l} & \dots & \hat{V}_{2n}e^{-\gamma_n l} & \hat{V}_{2n}e^{\gamma_n l} \\ \hat{V}_{11}e^{-\gamma_1 l} & \hat{V}_{11}e^{\gamma_1 l} & \dots & \hat{V}_{1n}e^{-\gamma_n l} & \hat{V}_{1n}e^{\gamma_n l} \end{bmatrix}. \tag{A.65}$$

The vector of terminal currents, (I), can be defined similarly to the terminal voltages, but with the substitution of defining the modal currents as $\hat{I}_{ij} = Y_{ij}^{C}\hat{V}_{ij}$. The impedance parameters are ultimately calculated by multiplying the network voltage matrix by the inverse of the network current matrix where

$$[Z] = [V^{net}][I^{net}]^{-1}. \tag{A.66}$$

The multiline techniques have been tested against AWR over a range of parameters for four line coupled systems. Figures A.5 and A.6 are representative plots of Z_{11} for four line systems, with line width and spacing, substrate thickness and material, and line length given in the figure captions. For symmetric line widths over a wide range of line widths, spacings,

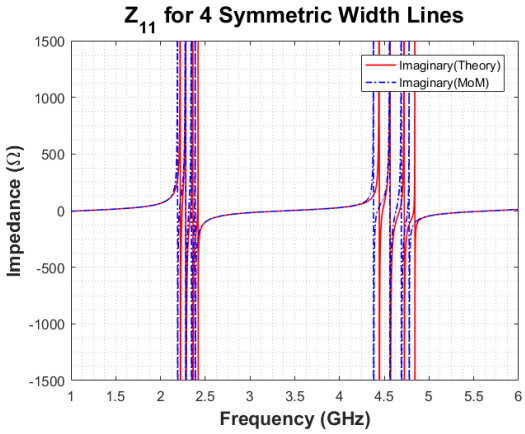


Figure A.5: Z11 for 4 coupled symmetric width lines, $w = 2.286mm$, $s = 2.286mm$, $h = 0.762mm$, $\epsilon_r = 9.2$, $l = 25mm$, showing a frequency shift of less than 1.4% frequency shift error compared to MoM calculation

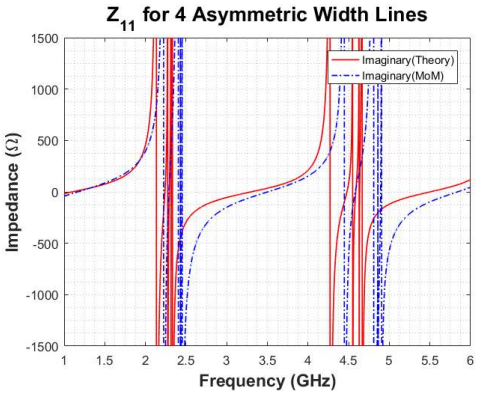


Figure A.6: Z11 for 4 coupled asymmetric lines, $w_1 = w_2 = w_4 = 0.2286mm$, $w_4 = 2.286mm$, $s_1 = s_2 = s_3 = 0.2286mm$, $h = 2.286mm$, $\epsilon_r = 2.2$, $l = 50mm$, showing a frequency shift of less than 5.9% error compared to MoM calculation

substrate heights and dielectric constants, the method is within 5.1% error, which is slightly better accuracy than the well accepted methods for two symmetric line calculations (within 7.2%).

There aren't stated accuracy bounds for the method of calculating the capacitance of asymmetric coupled microstrip lines in [134], and the method of moments solution diverges from the author's theory based calculation as the coupling weakens. With tight coupling, the method of moments solution shows clusters of 4 asymptotic responses, coming from the contributions of the four modes, but as line spacing increases the contribution of the fourth mode often disappears. For a similarly broad range of design parameters, asymmetric line calculations are within 16.6% error compared to the MoM solution, which is 2.7% worse than the existing asymmetric two line solutions (within 13.9% error) that are widely accepted in the literature. As was stated in the discussion of two line results, greater accuracy will depend on a more accurate calculation of the PUL capacitance of the coupled lines.

The authors' calculation of multiline parameters have been shown to be in excellent agreement with MoM results and analytical two line results from the literature. A simple and physically realizable system of tightly coupled microstrip lines wasn't fabricated because the spacing required to fit SMA connectors on and leave clearance room for high-quality cables and a torque wrench prevents close line spacing. More significantly, common deembedding techniques such as TRL [25] would be needed to remove connector performance, but such techniques are undefined for multiport systems. Similarly, line bends can't be used to transition spaced out connectors to a tightly coupled multiline system due to the same unavailability of multiport deembedding techniques. With this in mind, the agreement of existing two line literature and commercial MoM calculations has been taken to be an authoritative reference.

A.7 Conclusions and Future Work

A new matrix solution for the network parameters of coupled multiline transmission line, here applied to microstrip, has been derived. The solution was shown to achieve the same accuracy levels as existing well-established analytical two line solutions, compared against the MoM solution. The primary boundaries placed on this method depend on the accuracy bounds of the calculation of the PUL system characteristics. New to this solution is an assumption that coupled multiline capacitance is a superposition of simple two line capacitances, and a new formulation of the multiline and multimode characteristic impedance has also been used. The value of the solution is not just in its accuracy, but in its simplicity, and as a tool for analytical insight into the modal behavior of coupled transmission lines of symmetric and asymmetric line widths.

Appendix B

Measurement Calibration and Accreditation

NSI MI's current accreditation is not from NIST's NVLAP (National Voluntary Laboratory Accreditation Program) but is from A2LA (American Association for Laboratory Accreditation). Both programs are to accredit a lab to the ISO 17025 standard for Testing/Calibration Laboratories. In the documentation provided from NSI-MI about OEWG calibration, no claim to NIST traceability is made, but the A2LA certificate includes a statement of measurement uncertainty for different frequency ranges and measurement types. For some of the measurements, they rely on the Three Antenna Method for establishing Calibration and Measurement Capability Uncertainty (CMC), which is possibly something that can be done locally (although ISO 17025 certification is still external). Supposedly the three antenna method is harder to do accurately. The provided certificate was issued on April 13, 2018 and is valid until November 30, 2019, so this accreditation is frequently renewed. It's possible that A2LA is cheaper than NIST.

The ARRC can technically self-calibrate and document their own calibration for near-field probes. Laboratory accreditation is a significant recurring cost to officially recognize our documentation.

NSI-MI provide Gain calibration data for an additional $4000.00 per probe. The NSI-MI A2LA scope of accreditation is posted here https://www.nsi-mi.com/images/PDFs/NSI-MI-A2LA-Accreditation-2019.pdf .